Phosphate Glass Microspheres as Cell Microcarrier Substrates for Bone Tissue Engineering Applications

Thesis submitted by

Nilay Jayant Lakhkar

For the degree of
DOCTOR OF PHILOSOPHY

Division of Biomaterials and Tissue Engineering
UCL Eastman Dental Institute
University College London
256 Gray's Inn Road
London
WC1X 8LD

-2014-

Declaration

I, Nilay Jayant Lakhkar, confirm that the work presented in this thesis is my own. Where information has been derived from other sources, I confirm that this has been indicated in the thesis.

For Aaji, Appa and Baba (My Late Grandparents)

Acknowledgements

The number of people to whom I am indebted for their help with my studies at UCL and with living in London is too numerous for me to possibly acknowledge everyone within the confines of a thesis acknowledgements section. However, I endeavour to include here all those individuals and organizations that have made possible the research reported in this thesis.

First of all, I am most grateful to the UCL Graduate School for their financial support in the form of the Graduate Research Scholarship and Overseas Research Scholarship, as well as additional research grants and conference travel grants. A significant portion of this research was also supported by the WCU program through the National Research Foundation of Korea (NRF) funded by the Ministry of Education, Science and Technology (No. R31-10069).

Sincere thanks go to my supervisors Prof. Jonathan Knowles and Dr. Vehid Salih who have been brilliant in their roles as teachers, mentors, colleagues and friends. It has been an honour and a pleasure to work with them, and if my future work receives favourable responses for reasons relating to creativity, organisation, thoroughness, professionalism and team work, I will owe it entirely to their able tutelage and mentorship.

I am thankful for the guidance and support from our research technicians Drs. George Georgiou, Graham Palmer, Nicky Mordan and Mohamed Parker who have been very helpful in my experiments and with other research-related aspects. The other staff members as well as students and postdocs in the department have of course provided valuable guidance at various points in my research. Our division at UCL Eastman Dental Institute is a tight-knit, social group and everyone has contributed to making my time here an enjoyable one, be it through journal club meetings, department outings and events, Christmas meals, lunch-time discussions or Friday evenings at the pub.

Outside the department, I would like to gratefully acknowledge Drs. Ivan Wall (Department of Biochemical Engineering) and Richard Day (UCL Division of Medicine) for their guidance with my cell culture experiments and Ms. Katarzyna Ludka-Stempien (UCL Medical School) for her help with statistical analyses of my results. Outside UCL, I would like to thank Dr. John Hanna and Mr. Scott King

(University of Warwick) and Dr. Richard Martin (Aston University) for kindly carrying out NMR and XANES experiments on my samples respectively and for analysing the results and arranging for visits to the Solid State NMR facility at Warwick and the Diamond Light Source in Didcot, Oxfordshire. The contributions of Mr. Jeong-Hui Park (Dankook University, Korea) vis-à-vis some of the images used in this thesis are gratefully acknowledged. I also wish to thank Dr. Wojciech Chrzanowski (University of Sydney, Australia) who provided me with opportunities to publish some of my work in the form of an invited review article for a special issue in *Advanced Drug Delivery Reviews* and an invited book chapter for a forthcoming book titled *Biointerfaces: Where Material Meets Biology*. In addition, I am grateful to various co-authors in our papers published thus far for their contributions and helpful discussions.

Finally, none of this would have been possible without the undying support of my family back home in India, especially my parents who have been pillars of support all through my life, and I dedicate this thesis to the memory of my grandparents, three of whom passed away in the months before my PhD began. I am where I am today thanks to all their sacrifices and constant leadership by example.

Abstract

Phosphate glasses have demonstrated a high degree of suitability for use as biomaterials in a wide range of biomedical applications involving both hard and soft tissue regeneration. This study focused on the use of these glasses as substrate microcarrier materials for three-dimensional bone tissue formation. For this purpose, the successful production of phosphate glass microspheres in the ~10–200 µm size range was demonstrated using a simple, inexpensive and industrially scalable process. Microspheres made out of two different series of phosphate glass compositions were investigated: (a) iron phosphate glasses $0.5P_2O_5$–0.4CaO–(0.1 – x)Na_2O–xFe_2O_3 where x = 0.00, 0.01, 0.03 and 0.05 mole fraction and (b) titanium phosphate glasses $0.5P_2O_5$–0.4CaO–(0.1 – x)Na_2O–$xTiO_2$ where x = 0.00, 0.01, 0.03, 0.05 and 0.07 mole fraction. Investigations of the microsphere physicochemical properties revealed the densification of the glass structure with increased metal oxide incorporation in the glass. Glass structural characterisation studies provided valuable information relating the physicochemical properties to glass structural arrangements at the glass phase and atomic levels. Cell culture studies involving culture of the microspheres with MG63 osteosarcoma cells and human mesenchymal stem cells indicated that microspheres made of glasses containing 3–7 mol% metal oxides, and particularly those containing 5 mol% TiO_2, showed favourable characteristics in terms of cell attachment, viability, proliferation and release of proteins related to cell differentiation and metabolism under both static conditions in culture well plates and dynamic conditions in spinner flask bioreactors. Taken together, the results provide evidence of the potential of the investigated glass microspheres to function as effective microcarrier substrates for bone tissue engineering applications.

List of contents

Title page		**1**
Declaration		**2**
Acknowledgements		**4**
Abstract		**6**
List of contents		**7**
List of tables		**14**
List of figures		**16**
Chapter 1.	**Introduction and review of the literature**	**35**
1.1.	Phosphate glasses at a glance	35
1.2.	Organisation of the review	37
1.3.	Primary research motivation: Bone tissue engineering	38
1.4.	Basic concepts of phosphate glass structure	41
1.5.	Phosphate glass synthesis routes	44
1.5.1.	Melt-quenching	44
1.5.2.	Sol-gel synthesis	45
1.6.	Phosphate glass processing and applications	46
1.6.1.	Phosphate glass fibres	46
1.6.2.	Phosphate glass microspheres	47
1.7.	Probing the structure of phosphate glasses	49
1.7.1.	Fourier transform infrared and Raman spectroscopies	50
1.7.2.	X-ray diffraction	51

1.7.3.	Magic angle spinning nuclear magnetic resonance	54
1.7.4.	Ti *K*-edge X-ray absorption near edge structure	57
1.8.	Phosphate glass degradation and ion release	57
1.9.	Phosphate glass biocompatibility	64
1.10.	Research hypotheses	68
Chapter 2.	**Glass/microsphere physicochemical properties**	**70**
2.1.	Introduction	70
2.2.	Materials and methods	70
2.2.1.	Materials for glass production	70
2.2.2.	Precursor amount calculations	71
2.2.3.	Preparation of glass microparticles	73
2.2.4.	Design of flame spheroidisation apparatus	74
2.2.5.	Preparation of glass microspheres	75
2.2.6.	Particle size distribution	75
2.2.7.	Density measurement	76
2.2.8	Differential thermal analysis	76
2.2.9.	Short-term weight loss measurement by time lapse technique	76
2.2.10.	Long-term weight loss measurement using conventional weight loss model	77
2.2.11.	pH measurement	78
2.2.12.	Ion release measurement	78
2.2.12.1.	Anion release	78
2.2.12.2.	Cation release	79

2.2.12.3.	Transition metal ion release	80
2.2.12.4.	Inductively coupled plasma–mass spectroscopy	80
2.3.	Results	80
2.3.1.	Particle size distribution	80
2.3.2.	Density measurement	83
2.3.3.	Differential thermal analysis	85
2.3.4.	Short-term weight loss measurement by time lapse technique	87
2.3.5.	Long-term weight loss measurement using conventional weight loss model	92
2.3.6.	pH measurement	94
2.3.7.	Ion release measurement	96
2.3.7.1.	Anion release	96
2.3.7.2.	Cation release	101
2.3.7.3.	Transition metal ion release	104
2.4.	Discussion	105
Chapter 3.	**Glass structural characterisation**	**112**
3.1.	Introduction	112
3.2.	Materials and methods	112
3.2.1.	Fourier transform infrared spectroscopy	112
3.2.2.	X-ray diffraction	113
3.2.2.1.	Ambient temperature X-ray diffraction	113
3.2.2.2.	High temperature X-ray diffraction	113
3.2.3.	Solid state magic angle spinning nuclear magnetic resonance	113

3.2.3.1.	^{31}P MAS NMR	113
3.2.3.2.	^{23}Na MAS NMR	114
3.2.4.	Ti *K*-edge X-ray near edge absorption	114
3.3.	Results	115
3.3.1.	Fourier transform infrared spectroscopy	115
3.3.2.	X-ray diffraction	117
3.3.2.1.	Ambient X-ray diffraction	117
3.3.2.2.	High temperature X-ray diffraction	121
3.3.3.	Solid state magic angle spinning nuclear magnetic resonance	127
3.3.3.1.	^{31}P MAS NMR	127
3.3.3.2.	^{23}Na MAS NMR	137
3.3.4.	Ti *K*-edge X-ray near edge absorption	138
3.4.	Discussion	142
Chapter 4.	**Interactions between microspheres and MG63 osteosarcoma cells**	**148**
4.1.	Introduction	148
4.2.	Materials and methods	148
4.2.1.	Preparation of MG63 cells	148
4.2.2.	Cell culture on microspheres under static conditions	149
4.2.2.1.	Seeding in mesh well inserts	149
4.2.2.2.	Seeding in ultra-low attachment plates	150
4.2.3.	Cell culture on microspheres under dynamic conditions	150
4.2.4.	Scanning electron microscopy imaging	151

4.2.5.	Confocal laser scanning microscopy imaging	152
4.2.6.	Cell proliferation assay	152
4.2.7.	Statistical analysis	153
4.3.	Results	153
4.3.1.	Initial screening: static MG63 cell–microsphere interactions for Fe- and Ti-PGMs	153
4.3.1.1.	Scanning electron microscopy imaging	154
4.3.1.2.	Confocal laser scanning microscopy imaging	156
4.3.1.3.	Cell proliferation assays	157
4.3.2.	Bioreactor-mediated MG63 cell proliferation: dynamic MG63 cell–microsphere interactions for titanium PGMs	162
4.3.2.1.	Scanning electron microscopy and confocal laser scanning microscopy imaging	162
4.3.2.2.	Cell proliferation assays	164
4.4.	Discussion	167
Chapter 5.	**Interactions between microspheres and human mesenchymal stem cells**	**172**
5.1.	Introduction	172
5.2.	Materials and methods	173
5.2.1.	Preparation of hMSCs	173
5.2.2.	Cell culture on microspheres under static conditions	173
5.2.3.	Cell culture on microspheres under dynamic conditions	173
5.2.4.	Scanning electron microscopy and confocal laser scanning microscopy imaging	174
5.2.5.	Cell proliferation assay	174
5.2.6.	Alizarin Red S assay	174

5.2.7.	ELISA assays for bone morphogenetic protein-2 and osteopontin	175
5.2.8.	Statistical analysis	176
5.3.	Results	176
5.3.1.	Investigating stem cell growth and differentiation potential: static hMSC–microsphere interactions for Ti-PGMs	176
5.3.1.1.	Scanning electron microscopy imaging	176
5.3.1.2.	Confocal laser scanning microscopy imaging	177
5.3.1.3.	Cell proliferation assays	179
5.3.1.4.	Alizarin Red S assay	185
5.3.1.5	ELISA assays for bone morphogenetic protein-2 and osteopontin	186
5.3.2.	Investigating bioreactor-mediated hMSC proliferation: dynamic hMSC–microsphere interactions for Ti-PGMs	190
5.3.2.1.	Time course experiment	190
5.3.2.2.	Cell proliferation assays	191
5.3.2.3.	Scanning electron microscopy imaging	193
5.4.	Discussion	194
Chapter 6.	**Summary: General discussion and future directions**	**201**
	References	**207**
	Appendices	**222**
A.1.	Procedure for carrying out the time lapse and image analysis procedures for microsphere diameter measurements	222

A.1.1.	Materials	222
A.1.2.	Equipment	222
A.1.3.	Procedure	223
A.2.	Box-and-whisker plots for bar charts provided in Chapter 4	226
A.3.	AlamarBlue® cell proliferation assay	228
A.3.1.	Materials and methods	228
A.3.2.	Results	228
A.4.	Box-and-whisker plots for bar charts provided in Chapter 5	230
A.5.	List of publications	233
A.6.	List of conferences	234

List of tables

Chapter 2. Glass/microsphere physicochemical properties

Table 2.1. Glass compositions, codes and melting temperatures (MT, °C) and times (t, h) used. 71

Table 2.2. Amounts of precursors used (g) to prepare the investigated glasses. 73

Table 2.3. Glass transition temperatures T_g (°C) for the investigated iron and titanium phosphate glass microspheres. 85

Table 2.4. Short-term and long-term degradation rates (%.mm^{-2}.h^{-1} and %.h^{-1} respectively) and ion release rates (ppm.h^{-1}) of the investigated microspheres. These values are determined from the slopes of the linear fit between degradation or ion release values against time. 91

Table 2.5. Average values of short-term and long-term degradation rates (%.mm^{-2}.h^{-1} and %.h^{-1} respectively) and ion release rates (ppm.h^{-1}) for iron and titanium phosphate glass microsphere series obtained by averaging the values listed in Table 2.4 111

Chapter 3. Glass structural characterisation

Table 3.1. Wave numbers (cm^{-1}) and absorbance intensities (a.u.) of peaks obtained from the FTIR spectra of iron and titanium phosphate glasses. 117

Table 3.2. Phases present in crystalline XRD samples as identified by Crystallographica Search-Match software in conjunction with ICDD database volumes 1 to 42. 121

Table 3.3. Values of ^{31}P isotropic chemical shifts, linewidths and relative intensities for the investigated titanium phosphate glasses. 132

Table 3.4. Summary of chemical shift and quadrupolar coupling constant values for the investigated titanium phosphate glasses. 138

List of figures

Chapter 1. Introduction and review of the literature

Figure 1.1. The phosphate anion PO_4^{3-} tetrahedron. 42

Figure 1.2. The four different representations of the PO_4^{3-} tetrahedron. 42

Figure 1.3. Plots of data from differential thermal analysis, ambient X-ray diffraction and high temperature X-ray diffraction combined together to form combination graphs. These combination plots are for quaternary P_2O_5–CaO–Na_2O–SrO glasses containing (a) 0 mol% SrO and (b) 1 mol% SrO (Lakhkar et al., 2010). 54

Figure 1.4. ^{31}P MAS NMR spectra for glass samples of compositions (a) 45 mol% P_2O_5 8mol% CaO 47mol% Na_2O, (b) 45mol% P_2O_5 12mol% CaO 43mol% Na_2O, (c) 45mol% P_2O_5 35mol% CaO 20mol% Na_2O and (d) 45mol% P_2O_5 40mol% CaO 14mol% Na_2O. The change in the Q^1:Q^2 ratio can clearly be seen. The asterisks denote spinning sidebands (Kiani et al., 2012(b)). 56

Figure 1.5. Example of an anion chromatogram for phosphate species collected using a Dionex ICS 2500 system, showing the presence of PO_4^{3-}, $P_2O_7^{4-}$, $P_3O_9^{3-}$ and $P_3O_{10}^{5-}$ and higher phosphates (Lakhkar et al., 2013). 58

Chapter 2. Glass/microsphere physicochemical properties and bulk characterisation

Figure 2.1. Schematic diagram of flame spheroidisation apparatus. 74

Figure 2.2. Particle size distribution of microspheres obtained from (a) iron-doped and (b) titanium-doped phosphate glass compositions. The microsphere diameters range from 7 µm to 214 µm with approx. 80% of the particles having 82

diameters of 120 μm or less.

Figure 2.3. Light microscopy images of phosphate glass microspheres (Ti7 glass) for different size ranges (bar: 100 μm). Visual examination reveals the microsphere yield (proportion of glass particles that form microspheres) is maximum at microsphere diameters of 63–106 μm. 83

Figure 2.4. Glass density as a function of the (a) Fe_2O_3 content and (b) TiO_2 content for iron and titanium phosphate glass microspheres respectively. The glass density undergoes an increase with the metal oxide content of the glass. 84

Figure 2.5. DTA traces of phosphate glass microspheres with different (a) Fe_2O_3 and (b) TiO_2 contents. An increase in the metal oxide content generally leads to an increase in the T_g, T_c and T_m values. 86

Figure 2.6. Time lapse acquisition images showing the degradation of Fe0, Fe1, Fe3 and Fe5 microspheres at 0, 20, 40 and 60 hours for each composition. The Fe0 microspheres degrade at much higher rates than the Fe1–5 microspheres. 87

Figure 2.7. Time lapse acquisition images showing the degradation of Ti0, Ti1, Ti3, Ti5 and Ti7 microspheres at 0, 20, 40 and 60 hours for each composition. The Ti0 microspheres degrade at much higher rates than the Ti1–7 microspheres. 88

Figure 2.8. Short-term degradation of (a) iron and (b) titanium phosphate glass microspheres by the time lapse method. Data are presented as cumulative weight loss per unit surface area ($\%\mu m^{-2}$) of microspheres as a function of time. The degradation rate of the microspheres is inversely proportional to the metal oxide content of the microspheres 90

for both glass series.

Figure 2.9. Long-term degradation of (a) iron and (b) titanium phosphate glass microspheres as determined by the conventional weight loss method. Data are presented as percentage weight loss (%) of microspheres as a function of time. Similar to the short-term degradation results, the long-term results show that in general the microsphere degradation rate decreases as the metal oxide content increases. 93

Figure 2.10. pH change in deionised water as a function of time for (a) iron and (b) titanium phosphate glass microspheres. For most of the investigated compositions, the pH shows an initial sharp decrease followed by a more gradual decrease. 95

Figure 2.11. Average release (ppm) of (a) PO_4^{3-}, (b) $P_3O_9^{3-}$, (c) $P_2O_7^{4-}$ and (d) $P_3O_{10}^{5-}$ ions as a function of time for iron phosphate glass microspheres. In general, the amount of phosphate ions released decreases with an increase in the metal oxide (Fe_2O_3) content. 98

Figure 2.12. Average release (ppm) of (a) PO_4^{3-}, (b) $P_3O_9^{3-}$, (c) $P_2O_7^{4-}$ and (d) $P_3O_{10}^{5-}$ ions as a function of time for titanium phosphate glass microspheres. Similar to the case of the iron phosphate glass microspheres, the amount of phosphate ions released generally decreases with an increase in the metal oxide (TiO_2) content. 100

Figure 2.13. Average release (ppm) of Na^+ ions as a function of time for (a) iron and (b) titanium phosphate glass microspheres. In general, the amount of Na^+ ions released generally decreases with an increase in the metal oxide content. 102

Figure 2.14. Average release (ppm) of Ca^{2+} ions as a function of time 103

for (a) iron and (b) titanium phosphate glass microspheres. As with the Na^+ and phosphate ions, the amount of Ca^{2+} ions released generally decreases with an increase in the metal oxide content, although it is difficult to observe this trend clearly in the figures.

Figure 2.15. Average release (ppm) of Fe^{3+} ions as a function of time for the investigated iron phosphate glass microspheres. In general, the amount of Fe^{3+} ions released undergoes a sharp initial increase up to 170 hours followed by a gradual decrease over the rest of the study period. 104

Figure 2.16. Average release (ppm) of Ti^{4+} ions as a function of time for the investigated titanium phosphate glass microspheres. In general, the amount of Ti^{4+} ions released decreases with an increase in the TiO_2 content. 105

Chapter 3. Glass structural characterisation

Figure 3.1. Fourier transform infrared spectra obtained for the investigated (a) iron and (b) titanium phosphate glasses. In both cases, a slight broadening of the spectrum and a small shift towards lower wave number values are observed as the metal oxide content is increased. 116

Figure 3.2. Ambient XRD plots of as-prepared glass powder samples of (a) iron and (b) titanium phosphate glasses. All the spectra are free from any detectable crystalline phases. 118

Figure 3.3. Ambient XRD plots of crystallised samples of (a) iron and (b) titanium phosphate glasses. Peaks 1–5 in (a) and 1–7 in (b) correspond to different phases in the glass. [a] Calcium phosphate, [b] sodium calcium phosphate, [c] sodium iron phosphate and [d] titanium phosphate. As the metal oxide content of the glass is increased, the intensities of the peaks undergo changes. 120

Figure 3.4. Combination plots of (a) Fe0, (b) Fe1, (c) Fe3 and (d) Fe5 glasses where DTA trace, ambient XRD spectrum and contour HTXRD plot are included in the same graph. The correlation between three distinct sets of experimental data can be observed. As the Fe_2O_3 content is increased, the HTXRD peaks are observed at higher temperatures and are fewer in number. 124

Figure 3.5. Combination plots of (a) Ti1, (b) Ti3, (c) Ti5 and (d) Ti7 glasses where DTA trace, ambient XRD spectrum and contour HTXRD plot are included in the same graph. As with the iron phosphate glasses, the correlation between three distinct sets of experimental data can be observed, with an increase in the TiO_2 content leading to a decrease in the number of HTXRD peaks which are observed at higher temperatures. 126

Figure 3.6. ^{31}P MAS NMR spectra obtained for the investigated titanium phosphate glass samples. Spinning sidebands are indicated by asterisks. No significant changes in the spectra can be discerned with an increase in the TiO_2 content. 127

Figure 3.7. Relative abundance of Q^1 and Q^2 units in titanium phosphate glasses as a function of the TiO_2 content. Squares (■) denote Q^1 species and diamonds (♦) denote Q^2 species. Errors in Q^1 and Q^2 relative intensities are ±1% for all compositions as obtained from multiple fits of the ^{31}P NMR data using Dmfit software. Irrespective of the TiO_2 content, the glass structure is predominantly comprised of Q^2 species. 128

Figure 3.8. Isotropic chemical shift of (a) Q^1 and (b) Q^2 species as a function of the TiO_2 content of the investigated titanium phosphate glasses. (c) Relative isotropic chemical shift of Q species. Squares (■) denote Q^1 species and diamonds 130

(♦) denote Q^2 species. Errors in Q^1 and Q^2 chemical shifts are ±0.5 ppm for all compositions as obtained from multiple fits of the ^{31}P NMR data using Dmfit software. The chemical shifts associated with both Q^1 and Q^2 species show upfield movement towards more negative values as the TiO_2 content is increased.

Figure 3.9. Variation in linewidth of (a) Q^1 and (b) Q^2 species as a function of the TiO_2 content of the investigated titanium phosphate glasses. (c) Relative variation in linewidth of Q species. Squares (■) denote Q^1 species and diamonds (♦) denote Q^2 species. Errors in linewidth values are ±0.5 ppm for all compositions as obtained from multiple fits of the ^{31}P NMR data using Dmfit software. The linewidths associated with the Q^1 and Q^2 groups generally increase with the TiO_2 content. 132

Figure 3.10. Variation in (a) chemical shift and (b) relative intensity of Q^1 species as a function of the TiO_2 content for titanium phosphate glasses containing 45 and 50 mol% P_2O_5 (data for 45 mol% P_2O_5 glass obtained from (Kiani et al., 2010); errors not shown for clarity). Both glass series show an upfield movement in the Q^1 chemical shift towards more negative values as the TiO_2 content is increased. The Q^1 relative intensity shows a net downward trend in the 45 mol% P_2O_5 glass but remains relatively constant in the 50 mol% P_2O_5 glass. 134

Figure 3.11. Variation in (a) chemical shift and (b) relative intensity of Q^2 species as a function of the TiO_2 content for titanium phosphate glasses containing 45, 50 and 55 mol% P_2O_5 (data for 45 and 55 mol% P_2O_5 glass obtained from (Kiani et al., 2010) and (Kiani et al., 2012a) respectively; errors not shown for clarity). As the TiO_2 content of the glass is increased, all three glass series exhibit upfield movement in the Q^2 chemical shift towards more negative values but 136

show contrasting behaviour in terms of the abundance of Q^2 units in the glass structure.

Figure 3.12. ^{23}Na MAS NMR spectra and simulations acquired for the investigated titanium phosphate glasses at (a) 9.4 T and (b) 14.1 T. The simulations were performed using QuadFit. All the spectra show a single, broad, slightly asymmetric peak lacking in any recognisable resolution with no appreciable change as the TiO_2 content is increased. 138

Figure 3.13. (a) Titanium *K*-edge X-ray absorption near edge structure spectra of the investigated titanium phosphate glasses (the data sets are offset for clarity). (b) Magnified view of pre-peak between 4965 and 4980 eV. Two small peaks are observed at 4968 and 4970 eV with normalized intensities of 0.08 and 0.05 respectively, indicating the Ti atom occupies a six-fold coordinated (TiO_6) environment in all the glasses. 140

Figure 3.14. (a) Titanium *K*-edge X-ray absorption near edge structure spectra of titanium phosphate glasses having P_2O_5 contents of 45, 50 and 55 mol% and constant TiO_2 content of 5 mol% (the data sets are offset for clarity). (b) Magnified view of pre-peak between 4965 and 4980 eV. The peaks at 4968 and 4970 eV with normalized intensities of 0.08 and 0.05 respectively imply a six-fold coordinated (TiO_6) environment for the Ti atom in all the glasses. 141

Chapter 4. Interactions between microspheres and MG63 osteosarcoma cells

Figure 4.1. Scanning electron microscopy images showing MG63 cells growing on iron phosphate glass microspheres in Transwell® inserts at time points of 1 and 7 days. The Fe0 microspheres (a, b) and Fe1 microspheres (c, d) show no cell growth on account of excessive degradation. The Fe3 155

and Fe5 microspheres show individual cells (sometimes with flat morphology) growing on the surface at day 1 (e, g). Higher magnifications are used to view these cells more clearly; the positions of cells are denoted by arrows. By day 7, the cells have formed aggregates around groups of microspheres (f, h).

Figure 4.2. Scanning electron microscopy images showing MG63 cells growing on titanium phosphate glass microspheres in Transwell® inserts at 7 days post seeding (images for day 1 not shown since the images obtained are similar to those obtained for iron phosphate glass microspheres in terms of cell attachment). Similar to the Fe1 microspheres, the Ti1 microspheres show considerable surface degradation with no cells visible on the surface (a). The Ti3, Ti5 and Ti7 microspheres show similar cell growth features. A non-uniform distribution of cells on different microspheres is observed with some microspheres showing no cell growth while other microspheres show many cells growing on the surface (Ti3 microspheres in (b)). At higher magnifications, the proliferation of cells on the microspheres and the linkages between cells by means of processes can be more clearly discerned (Ti5 microspheres in (c, d) and Ti7 microspheres in (e, f)). 156

Figure 4.3. Confocal laser scanning microscopy images of MG63 cells attached to titanium phosphate glass microspheres in Transwell® inserts at 7 days post culture. Phalloidin stains the actin filaments of the cytoskeleton green while propidium iodide stains the nuclei red. As in the case of the SEM micrographs, the CLSM images of Ti3 (a), Ti7 (b) and Ti5 (c, d) microspheres show similar cell growth features. The actin filaments align themselves along the curved surface, indicating good cell adhesion. Cells on two or more microspheres are joined to each other and form larger sized fragments of cell–microsphere aggregates (a– 157

c). Individual microspheres are also completely covered by a layer cells (d).

Figure 4.4. Standard curve of MG63 cell growth plotted as absorbance values versus number of cells after carrying out a CCK-8 assay at 1 day post seeding. The absorbance values are obtained at a wavelength of 450 nm. Error bars represent ±SD (n = 6). 158

Figure 4.5. Bar charts showing the proliferation of MG63 cells on iron phosphate glass microspheres in ultra-low attachment cell culture plates at time points of 1, 4 and 7 days as determined using the CCK-8 assay. The control comprises silica glass microspheres (Polysciences Inc.). Error bars represent ±SD and n = 2. The symbols ** and *** indicate $p < 0.01$ and $p < 0.001$ respectively. (a) For all the compositions and the control, a significant increase in cell numbers is observed between all the time points (*** $p < 0.001$). (b) At all the time points, the cell populations of Fe3 are significantly lower than those of the control, while those of Fe5 are significantly lower than those of the control only at day 7; further, Fe5 shows significantly greater cell numbers than Fe3 at days 1 and 4 (*** $p < 0.001$). 159

Figure 4.6. Bar charts representing MG63 cell proliferation on titanium phosphate glass microspheres in ultra-low attachment cell culture plates at time points of 1, 4 and 7 days as determined using the CCK-8 assay. The control comprises silica glass microspheres (Polysciences Inc.). Error bars represent ±SD and n = 2. The symbols ** and *** indicate $p < 0.01$ and $p < 0.001$ respectively. (a) As with the iron phosphate glass microspheres, statistically significant increases in cell growth between days 1, 4 and 7 can be observed for all the compositions and the control (*** $p < 0.001$). (b) At days 1 and 7, the cell populations of all the 161

compositions are significantly higher than the control (*** p < 0.001), but no statistically significant differences in cell populations can be observed on day 4 (p > 0.008, Bonferroni correction).

Figure 4.7. Scanning electron microscopy images showing MG63 cells attached to (a, b) Ti5 and (c, d) control glass microspheres at 4 days post seeding as well as (e, f) Ti5 and (g, h) control glass microspheres at 7 days post seeding after culture under dynamic conditions in spinner flask bioreactors. Left images are at lower magnifications (100x or 200x) while right images are at higher magnifications (1500x or 2000x). Fewer MG63 cells are observed to be attached to the control microspheres in comparison with the Ti5 microspheres at both time points. Furthermore, with regard to the Ti5 microspheres, more cells are observed at day 7 (e) than at day 4 (b). Mostly individual cells with a 'torn' appearance are visible on both the Ti5 and control microspheres, although cells with a flattened morphology are visible (b, d), as are groups of cells on adjacent microspheres which are joined to each other by means of processes (h). 163

Figure 4.8. Confocal laser scanning microscopy images of MG63 cells growing on Ti5 and control microspheres in spinner flask bioreactors at 4 days post culture (a, c) and 7 days post culture (b, d) respectively. Phalloidin stains the actin filaments of the cytoskeleton green while propidium iodide stains the nuclei red. As with the SEM images in Figure 4.7, more cells are visible on the Ti microspheres (a, b) than on the control microspheres (c, d) at both time points. The cells mostly exhibit a torn appearance on the surfaces of both the Ti5 and control microspheres, although the alignment of cytoskeletal filaments along the surface curvature can be discerned in some cases (as indicated by white arrows in the images). 164

Figure 4.9. Bar chart showing the proliferation of MG63 cells on Ti5 and control glass microspheres at time points of 1, 4 and 7 days in ultra-low attachment cell culture plates under static conditions, as determined using the CCK-8 assay. The control comprises silica glass microspheres (Polysciences Inc.). Error bars represent ±SD where n = 2. The symbols ** and *** indicate $p < 0.01$ and $p < 0.001$ respectively. Note the difference in the growth profile of Ti5 and control microspheres between this figure and Figure 4.6. The differences in cell growth between the Ti5 and control microspheres are not statistically significant on days 1, 4 or 7 ($p > 0.016$, Bonferroni correction). Ti5 microspheres show significantly greater cell proliferation on days 4 and 7 in comparison with day 1 (*** $p < 0.001$). The difference in cell numbers on control microspheres is statistically significant between days 1 and 4 and between days 4 and 7 (** $p < 0.01$). With reference to an initial seeding density of 50,000 cells per well, the increase in cell numbers for the Ti5 microspheres is 8-fold. 165

Figure 4.10. Bar chart showing the proliferation of MG63 cells on Ti5 and control glass microspheres at time points of 1, 4 and 7 days in spinner flask bioreactors under dynamic conditions, as determined using the CCK-8 assay. The control comprises silica glass microspheres (Polysciences Inc.). Error bars represent ±SD where n = 2 (note that for simplicity, statistical significance is not shown in the graph). In the dynamic environment, the difference in cell growth between the Ti5 and control microspheres at all the investigated time points is highly significant (*** $p < 0.001$). The Ti5 microspheres show a considerable increase in cell numbers between days 1, 4 and 7 (*** $p < 0.001$). In the control microspheres, the cell numbers at days 4 and 7 are significantly higher than at day 1 (*** $p < 0.001$) but the difference between days 4 and 7 is not statistically 166

significant ($p > 0.016$, Bonferroni correction). With reference to an initial seeding density of 50,000 cells per well, the increase in cell numbers for the Ti5 microspheres is 24-fold under dynamic culture.

Chapter 5. Interactions between microspheres and human mesenchymal stem cells

Figure 5.1. Scanning electron microscopy images showing hMSCs attached to (a, b) Ti5 and (c, d) control glass microspheres when cultured in ultra-low attachment plates at 7 days post seeding (DMEM is used as the culture medium). In comparison with the number of MG63 cells attached to the microspheres in earlier experiments, much fewer hMSCs are found attached to both the Ti5 and control microspheres, with most microspheres not covered with cells. Individual cells are visible on the Ti5 microspheres, which have either a torn appearance (a) or a reasonably flattened morphology with spread out features (b). The control microspheres show groups of cells on adjacent microspheres that are joined together by means of processes. As with the cells on the Ti5 microspheres, those on the control have either a somewhat flattened structure (c) or a torn appearance (d). 177

Figure 5.2. Confocal laser scanning microscopy images of hMSCs growing on the control microspheres (a, b) and Ti5 microspheres (c, d) in ultra-low attachment plates at 7 days post culture. DMEM is used as the culture medium. Phalloidin stains the actin filaments of the cytoskeleton green while propidium iodide stains the nuclei red. More cells are visible on the control microspheres than on the Ti microspheres. The alignment of the actin filaments along the microsphere curvature is visible (indicated by white arrows in the images), which implies favourable cell adhesion. Clusters of cells covering groups of microspheres are observed in the control microspheres (a, 178

b), whereas smaller clusters or individual cells are found to cover the Ti5 microsphere (c, d).

Figure 5.3. Standard curve of hMSC growth plotted as absorbance values versus number of cells after carrying out a CCK-8 assay at 1 day post seeding. The absorbance values are obtained at a wavelength of 450 nm. Error bars represent ±SD (n = 6). 179

Figure 5.4. Figure 5.4. Bar chart representing the results of a CCK-8 assay to quantify hMSC proliferation on Ti5 and control microspheres in ultra-low attachment cell culture plates at time points of 1, 4 and 7 days when DMEM and a commercially available mesenchymal stem cell growth medium DXF (Promocell GmbH, Germany) are used as the culture medium. The control comprises silica glass microspheres (Polysciences Inc.). Error bars represent ±SD and n = 2. The symbols ** and *** indicate $p < 0.01$ and $p < 0.001$ respectively. DMEM produces a significant increase in cell numbers on both the Ti5 and control microspheres between day 1 and day 7 (*** $p < 0.001$). DXF produces a significant increase in cell numbers on the control microspheres but causes a significant decrease in cell numbers on the Ti5 microspheres from day 1 to day 7 (*** $p < 0.001$). 180

Figure 5.5. Bar chart comparing hMSC proliferation on Ti5 and control microspheres in ultra-low attachment cell culture plates at time points of 1, 4 and 7 days when (a) DMEM and (b) DXF are used as the culture medium. The control comprises silica glass microspheres (Polysciences Inc.). Error bars represent ±SD and n = 2. The symbols ** and *** indicate $p < 0.01$ and $p < 0.001$ respectively. When DMEM is used, the Ti5 microspheres show significantly greater cell proliferation than the control microspheres at all the time points (*** $p < 0.001$). When commercial DXF 182

is used, the Ti5 microspheres show significantly greater cell proliferation than the control microspheres at days 1 and 4 (*** $p < 0.001$) but not at day 7 where the difference is statistically insignificant ($p > 0.05$).

Figure 5.6. Bar charts comparing the effects of DMEM and commercial DXF cell culture media on hMSC proliferation in the case of (a) Ti5 and (b) control microspheres in ultra-low attachment cell culture plates at time points of 1, 4 and 7 days. The control comprises silica glass microspheres (Polysciences Inc.). Error bars represent ±SD and n = 2. The symbols ** and *** indicate $p < 0.01$ and $p < 0.001$ respectively. Ti5 microspheres exhibit a positive effect towards DMEM but a negative effect towards commercial DXF with statistically significant differences at all the time points (*** $p < 0.001$). Control microspheres exhibit a positive effect towards both DMEM and DXF but the differences are statistically insignificant ($p > 0.05$). 184

Figure 5.7. Bar chart representing the differentiation of hMSCs into bone cells on Ti5 and control glass microspheres as quantified by the extent of mineralisation on the microsphere surface using an Alizarin Red S assay. The assay was carried out at time points of 7, 14 and 21 days and absorbance measurements were carried out at 540 nm. Error bars represent ±SD where n = 2. The symbols ** and *** indicate $p < 0.01$ and $p < 0.001$ respectively. Significantly higher absorbance values are obtained for the control microspheres in comparison with the Ti5 microspheres at every time point (** $p < 0.01$; *** $p < 0.001$). Statistically significant differences are observed in the control microspheres between days 7 and 14 and between days 7 and 21 (*** $p < 0.001$). For the Ti5 microspheres, the differences in the absorbance values are not statistically significant between any of the time points ($p > 0.016$, Bonferroni correction). 185

Figure 5.8. Bar chart showing the variation in the cumulative secretion of human bone morphogenetic protein–2 (BMP-2) by hMSCs at time points of 7, 14 and 21 days when cultured on Ti5 and control microspheres in osteogenic medium, as quantified using a mammalian BMP-2 ELISA assay. Prior to the assay, a standard curve of optical density versus human BMP-2 concentration (pg/ml) was plotted (a). Error bars represent ±SD where n = 2. hMSCs cultured on Ti5 microspheres secrete higher levels of BMP-2 at all the investigated time points. 187

Figure 5.9. Bar chart showing the variation in the cumulative secretion of human osteopontin (OPN) by hMSCs at time points of 7, 14 and 21 days when cultured on Ti5 and control microspheres in osteogenic medium, as quantified using a mammalian OPN ELISA assay. Prior to the assay, a standard curve of optical density versus human OPN concentration (ng/ml) was plotted (a). Error bars represent ±SD where n = 2. hMSCs cultured on Ti5 microspheres produce considerably higher levels of OPN than those cultured on the control at all the investigated time points. 189

Figure 5.10. Bar chart comparing the variations in the secretion of human BMP-2 and OPN by hMSCs as obtained from Figures 5.8 and 5.9. Error bars represent ±SD where n = 2. The secretion of OPN from the Ti5 microspheres is considerably higher than that from the control microspheres or the secretion of BMP-2 from the Ti5 and control microspheres. 190

Figure 5.11. Scatter plot showing the percentage of unattached cells remaining at time points of 2, 4, 6 and 8 hours after culture of Ti5 and control microspheres with hMSCs; the number of unattached cells was determined using a Vi-CELL cell viability analyser. Error bars represent ±SD and n = 2. By 4 hours post seeding, approx. 10% unattached cells 191

remain for both the Ti5 and control microspheres, indicating that approx. 90% of the seeded cells have attached to the microsphere surface.

Figure 5.12. Bar chart showing the number of hMSCs on Ti5 microspheres at time points of 4 and 7 days in spinner flask bioreactors under dynamic conditions, as determined using the CCK-8 cell proliferation assay. DMEM is used as the culturing medium. Error bars represent ±SD where n = 2. The Ti5 microspheres show greater cell proliferation at day 7 than at day 4 but the difference is not statistically significant ($p > 0.05$). 192

Figure 5.13. Bar chart showing the number of hMSCs on Ti5 microspheres at time points of 10 and 15 days in spinner flask bioreactors under dynamic conditions, as determined using the CCK-8 cell proliferation assay. Osteogenic inductive medium is used as the culturing medium. Error bars represent ±SD where n = 2. The symbol *** indicates $p < 0.001$. The Ti5 microspheres show significantly lesser numbers of cells at day 15 than at day 10 (*** $p < 0.001$). 193

Figure 5.14. Scanning electron microscopy images showing hMSCs attached to Ti5 microspheres at (a, b) 10 days and (c, d) 15 days post seeding when cultured in a dynamic environment within spinner flask bioreactors. Osteogenic inductive medium is used as the culture medium. Very few hMSCs, if at all, are found attached to the Ti5 microspheres, with almost all the microspheres showing no signs of cell coverage. Some fragments, which may correspond to cells, are visible on the Ti5 microspheres; the fragments seem to be peeling off the microspheres. No differences can be observed between the microspheres on days 10 and 15 with regard to the number of cells or their morphology. 194

Chapter 6. Summary: General discussion and future directions

Figure 6.1. A conventional powder spray torch. The use of a powder canister above the torch eliminates the need for an external feed. 202

Figure 6.2. Schematic diagram of a perfusion bioreactor system. Media is perfused in a closed loop through a growth chamber containing substrate material and seeded cells (Yeatts and Fisher, 2011). 205

Appendices

Figure A.1. Screenshots of Multi–dimensional Acquisition and Snap/Live windows in µManager software. 224

Figure A.2. Box-and-whisker plot representing MG63 cell proliferation on iron phosphate glass microspheres in ultra-low attachment cell culture plates at time points of 1, 4 and 7 days as determined using the CCK-8 assay (corresponding to bar charts in Figure 4.5). Note that circles indicate outliers (values more than the interquartile range) while asterisks indicate extreme outliers (values more than three times the interquartile range). 226

Figure A.3. Box-and-whisker plot representing MG63 cell proliferation on titanium phosphate glass microspheres in ultra-low attachment cell culture plates at time points of 1, 4 and 7 days as determined using the CCK-8 assay (corresponding to bar chart in Figure 4.6). Note that circles with numbers next to them indicate outliers. 226

Figure A.4. Box-and-whisker plot showing the proliferation of MG63 cells on Ti5 and control glass microspheres at time points of 1, 4 and 7 days in ultra-low attachment cell culture plates under static conditions, as determined using the CCK-8 assay (corresponding to bar chart in Figure 4.9). 227

Note that circles with numbers next to them indicate outliers.

Figure A.5. Box-and-whisker plot showing the proliferation of MG63 cells on Ti5 and control glass microspheres at time points of 1, 4 and 7 days in spinner flask bioreactors under dynamic conditions, as determined using the CCK-8 assay (corresponding to bar chart in Figure 4.10). Note that circles with numbers next to them indicate outliers. 227

Figure A.6. (a) Standard curve of cell growth plotted as absorbance values versus number of cells. (b) Bar chart showing the proliferation of MG63 cells on titanium phosphate glass microspheres in Transwell® inserts at time points of 1, 4 and 7 days as determined using the alamarBlue® assay. The control comprises the mesh of the Transwell® insert. Error bars represent ±SD and n = 2. For all the compositions and the control, a significant increase in cell numbers is observed between day 1 and day 7. 229

Figure A.7. Box-and-whisker plots representing the results of a CCK-8 assay to quantify hMSC proliferation on Ti5 and control microspheres in ultra-low attachment cell culture plates at time points of 1, 4 and 7 days when DMEM and a commercially available mesenchymal stem cell growth medium DXF (Promocell GmbH, Germany) are used as the culture medium. The control comprises silica glass microspheres (Polysciences Inc.). (a) and (b) correspond to bar charts in Figures 5.6(a) and 5.6(b) respectively. Note that circles indicate outliers (values more than the interquartile range) while asterisks indicate extreme outliers (values more than three times the interquartile range). 230

Figure A.8. Box-and-whisker plot representing the differentiation of hMSCs into bone cells on Ti5 and control glass 231

microspheres at time points of 7, 14 and 21 days as quantified by the extent of mineralisation on the microsphere surface using an Alizarin Red S assay (corresponding to bar chart in Figure 5.7). Note that circles with numbers next to them indicate outliers.

Figure A.9. Box-and-whisker plot showing the proliferation of hMSCs on Ti5 microspheres at time points of 4 and 7 days in spinner flask bioreactors under dynamic conditions, as determined using the CCK-8 cell proliferation assay (corresponding to bar chart in Figure 5.12). Note that circles with numbers next to them indicate outliers. 231

Figure A.10. Box-and-whisker plot showing the proliferation of hMSCs on Ti5 microspheres at time points of 10 and 15 days in spinner flask bioreactors under dynamic conditions when osteogenic inductive medium is used as the culturing medium, as determined using the CCK-8 cell proliferation assay (corresponding to bar chart in Figure 5.13). 232

Chapter 1. Introduction and review of the literature

1.1. Phosphate glasses at a glance

In recent years, phosphate glasses have been studied extensively as potential candidate materials for a number of biomedical applications such as dental, maxillofacial and orthopaedic implants; scaffolds for bone tissue engineering; and vehicles for the delivery of antimicrobial ions (Knowles, 2003, Abou Neel et al., 2009d). These materials were originally conceptualized for application as achromatic optical elements on account of their low dispersion and relatively high refractive indices (Kreidl and Weyl, 1941) but have since been studied for use in fields ranging from semiconductor and sensor design to nuclear waste encapsulation (Marasinghe et al., 2000, Brow, 2000). Phosphate glasses have elicited considerable interest among biomaterials researchers for two major reasons. First, the degradation of phosphate glasses in various solubilising media is highly controllable. Glasses which degrade over periods ranging from 2–3 hours to 1 year or longer can easily be synthesized in the laboratory; for instance, modification of ternary P_2O_5–Na_2O–CaO glasses through the addition of suitable metal oxides to form quaternary or higher order systems can decrease the glass solubility by several orders of magnitude. Second, the main elemental constituents of phosphate glasses (e.g. Na, Ca and P) are found in the inorganic mineral phase of bone. This is a highly important point when investigating the interactions between phosphate glass materials and bone cells under both *in vitro* and *in vivo* conditions and is particularly essential from the viewpoint of developing bioactive implants, wherein by definition a chemical reaction occurs between the implant surface and the surrounding tissue, leading to the formation of a bond between the implant and the host tissue (Anselme, 2000).

In terms of the composition, the basic starting point is a glass made of pure P_2O_5; however, the highly reactive and hygroscopic nature of vitreous P_2O_5 precludes any use of this glass for biological applications (Hudgens et al., 1998). The earliest research on phosphate glass biomaterials focused on the addition of oxides such as Na_2O and CaO to form ternary P_2O_5–Na_2O–CaO phosphate glass systems (Burnie et al., 1981, Burnie et al., 1983). The composition of the ternary P_2O_5–Na_2O–CaO glass system can be varied to control the rate at which the glass degrades; for example, an increase in the CaO content at the expense of Na_2O leads to a

decrease in the degradation rate and vice versa. However, the dissolution rate of most compositions within the above ternary system is still relatively high and their biocompatibility is poor mainly due to large pH changes, so more recent studies have focused on controlling the degradation rate of phosphate glasses by the addition of other metal oxides to the glass system to achieve the objectives of controlled dissolution and improved cell response. To date, the metal oxides used for this purpose include Fe_2O_3 (Reis et al., 2002, Karabulut et al., 2003, Ahmed et al., 2004a), CuO (Shih et al., 1998, Mulligan et al., 2003a, Abou Neel et al., 2005b), CoO (Lee et al., 2013b), Al_2O_3 (Shah et al., 2005), TiO_2 (Navarro et al., 2003b, Abou Neel et al., 2007a, Rajendran et al., 2007), MgO (Franks et al., 2002, Lee et al., 2013a), ZnO (Meyer, 1997, Moss et al., 2010), AgO (Mulligan et al., 2003b, Ahmed et al., 2006, Valappil et al., 2007), Ga_2O_3 (Pickup et al., 2009, Valappil et al., 2009) and SrO (Lao et al., 2008, Lakhkar et al., 2009, Hesaraki et al., 2010, O'Donnell and Hill, 2010). The purposes of metal oxide addition to the glass structure may be two-fold. First, metal oxides serve as the most effective means to control the degradation rate by increasing the covalent nature of the bonds within the glass structure. Second, the metal ions released from such glasses can exert a biological function such as an antimicrobial effect and/or positively impact on cell proliferation and tissue regeneration.

The appeal of phosphate glasses in biomedical research derives essentially from the strong inter-relationships between three sets of factors: (a) the glass chemistry and glass network structure, (b) the glass physicochemical properties and (c) the interactions between glasses and living cells or tissues. The link between the first two factors is that subtle changes in glass chemistry through variations in glass composition can bring about significant changes in glass physicochemical properties such as the glass transition temperature, glass density or glass dissolution rate in solubilising media. For instance, a ternary P_2O_5–Na_2O–CaO glass not containing TiO_2 may disappear completely in a matter of a few hours when immersed in deionized water, whereas a quaternary P_2O_5–Na_2O–CaO–TiO_2 glass containing 5 mol% TiO_2 may take several months to degrade completely. In turn, the glass properties greatly influence the ability of the glass surface to provide a stable substrate for cells to attach and proliferate and, in the case of stem cells, to possibly differentiate down a specific lineage, for example osteogenic or chondrogenic pathways. Using the same example as above, the rapid degradation of the former glass would lead to considerable fluctuations in the solution pH which would be detrimental to cells under *in vitro* cell culture conditions, while the latter glass would

provide the stable surface required for the cells to flourish.

1.2. Organisation of the review

Before embarking on a review of the literature pertaining to the topic of research, it is worth mentioning at the outset that researchers have investigated the use of glasses in biomedical applications for several decades before phosphate glasses were envisioned as biomaterials; silicate glasses have been studied for a significantly longer period since Larry Hench reported on the now famous 45S5® Bioglass composition in the late 1960s, and consequently far more literature exists on the properties and biomedical applications of silicate glasses in comparison with phosphate glasses (Hench et al., 1972, Hench, 1991, Kokubo et al., 2003, Hench, 2006, Rezwan et al., 2006). However, the amount of research on biological phosphate glasses suggests that they have now emerged as a distinct class of biomaterials in their own right.

The present research focuses on phosphate glass microspheres from the perspectives of three major areas of study: (1) the production of phosphate glass microspheres and their physicochemical properties, (2) the underlying structural features of the glass network from which the glass and microsphere properties arise and (3) the interactions between the microspheres and bone cells (MG63 cells) as well as human mesenchymal stem cells (hMSCs) under static and dynamic environments, which are dependent on the microsphere physicochemical properties and which ultimately lead to applications of the microspheres for cell-based therapies and tissue engineering. It should again be emphasised that although all three areas of research are quite distinct in terms of the underlying principles as well as the research methodologies and techniques used, the results obtained from experiments conducted in all three areas are closely interlinked.

The literature review elaborates upon these areas of study in the following order: the primary research motivation, i.e. tissue engineering, is outlined and the basics of phosphate glass structure are provided, after which the methods used to prepare phosphate glasses and the processing techniques utilised in order to achieve different forms such as glass fibres and glass microspheres are examined. Next, the techniques that can be used to probe the glass structure at different levels of resolution are explained. The review then moves on to the glass physicochemical properties in terms of phosphate glass degradation and release of various ions.

Subsequently, the biocompatibility aspects of phosphate glasses are discussed. Finally, the hypothesis and objectives of the present study are presented. The metal oxide dopants used for the glasses in the present study are iron oxide (Fe_2O_3) and titanium oxide (TiO_2); therefore, wherever appropriate, the review mainly highlights studies carried out on phosphate glasses containing Fe_2O_3 or TiO_2 as the metal oxide dopants.

1.3. Primary research motivation: Bone tissue engineering

Considering what is known about the strong links between structure, properties and cell–material interactions, research into phosphate glasses at present is focused on the development of specific biomedical applications of these glasses in the dental, maxillofacial and orthopaedic realms. A major objective in such research is to process the bulk glass into forms that can satisfy two seemingly disparate requirements: (a) to be suitable in terms of size and morphology for use either within the human body or within engineered devices that support an active biological environment and (b) to be reproducible using rapid, inexpensive and easily scalable industrial techniques. Thus far, phosphate glasses have been processed in the form of monoliths, discs, granules, cloths and tubes in the macroscopic size range as well as powders and fibres in the micro- and nano-sized ranges (Gilchrist et al., 1991). The applications examined in the current research involve using phosphate glass microspheres as a substrate material for the *in vitro* formation of viable bone tissue for the treatment of critical sized bone defects (a few millimetres in size). The development of such substrate materials involves the investigation of the interactions between cells and glass systems, firstly within static systems such as culture well plates and subsequently within dynamic systems such as spinner flasks and perfusion bioreactors.

At this stage, it is useful to explain some of the underlying concepts governing tissue engineering and other research areas such as *in vitro* cell expansion (also known as cell scale up) in order to understand how phosphate glasses can play a key role in these applications. In the years since Langer and Vacanti first reported on the field of tissue engineering as one that combines concepts from biology and engineering in the development of functional substitutes for damaged tissue (Langer and Vacanti, 1993), the tissue engineering approach—which essentially involves the combined use of cells, engineered materials and biochemical and physicochemical factors to develop viable structures for tissue repair or replacement—has emerged as a key research area in the biomedical realm and has been used in the *in vitro*

production of several tissue types including liver (Dvir-Ginzberg et al., 2003, Shakesheff, 2007), bone (Meinel et al., 2004, Yu et al., 2004, El Haj and Cartmell, 2010), cartilage (Hutmacher, 2000, Suh and Matthew, 2000, Hunziker, 2002), cardiac muscle (Laflamme and Murry, 2005, Ott et al., 2008, Radisic et al., 2008), tendon and ligament (Woo et al., 1999, Mikos et al., 2006, Sahoo et al., 2006) and nerve (Hadlock et al., 2000, Holmes et al., 2000, Yang et al., 2004). In the context of bone tissue engineering, the main requirements are cells capable of forming bone tissue (such as osteoblasts or mesenchymal stem cells), matrices or scaffold structures that are osteoconductive in nature and osteogenic growth factors that aid in cell adhesion and proliferation or, in the case of stem cells, differentiation along osteogenic pathways (Rauh et al., 2011).

Conventional tissue engineering paradigms commonly subscribe to the so-called 'top-down approach' in which cells seeded on a scaffold create the required extracellular matrix and microarchitecture when cultured in a bioreactor that provides the necessary biochemical and mechanical stimuli. However, one of the problems encountered when using this approach is the existence of a concentration gradient of biologically relevant molecules (e.g. oxygen, glucose, amino acids, metabolic products etc.) between the outer surface and the centre of the construct, thereby leading to preferential cell proliferation and extracellular matrix formation at the outer surface (up to about 200–250 μm in depth), nutrient deprivation and subsequent cell death at the core; as a result, restrictions exist in the dimensions of the tissue engineering constructs thus formed (generally in the millimetre range) (Ishaug et al., 1997, Ishaug-Riley et al., 1998, Holy et al., 2000, Muschler et al., 2004). These limitations are particularly problematic for the repair of macroscopic defects which are commonly found in bone injury.

In recent years, the so-called 'bottom up' tissue engineering approach has gained attention as a viable alternative to the top-down approach. This approach envisages the initial development of microscopic building blocks of structures that mimic the natural tissue composition and architecture, followed by the assembly of these building blocks to form larger tissue constructs (Nichol and Khademhosseini, 2009). This approach can potentially facilitate the development of 3D tissue engineered constructs with high cell density and overcome the size limitation of the top-down approach (Fernandez and Khademhosseini, 2010, Liu et al., 2010, Yanagawa et al., 2011). Several designs have been investigated as micro-scale cell-based building blocks, including self-assembled cell aggregates (Kelm et al., 2006, Jakab et al.,

2008), cell-laden microgels (Du et al., 2008), cell sheets (Yang et al., 2005, Ohashi et al., 2007) and cell-seeded microcarriers or microspheres (Martin et al., 2011). The present research aims to apply the cell-seeded microsphere design to bone tissue engineering applications.

A large variety of microcarriers have been developed for tissue engineering applications. Commercially available microcarriers (and the materials used to make them) include Biosilon® by Nunc (polystyrene), Cellagen® by MP Biomedicals (collagen), Cultispher® by Percell Biolytica (gelatin), Cytodex® by GE Healthcare (dextran, positively charged or gelatin coated), Hillex® by SoloHill (dextran with surface coating) and so on, while non-commercial microcarriers developed for specific applications include those made of materials such as cellulose, chitosan, polycaprolactone, poly(L-lactide) etc. (Martin et al., 2011). The common features of these microcarriers are their diameters, which are in the range of 100–400 μm, and the presence of porosity, which increases the available surface area considerably and allows cell penetration into the microcarrier bulk, thereby leading to favourable cell adhesion and proliferation. However, one of the challenges involved in the use of these microcarriers is the harvesting of the expanded cells at the end of the culture process, particularly considering that trypsinisation may not be the optimal method to dislodge the maximum number of cells from the microspheres.

For *in vitro* bone cell expansion and bone tissue engineering, glass microspheres can offer some unique advantages over other surfaces. For instance, in comparison with tissue culture plastic, they (as well as the abovementioned microcarriers) can provide a considerably larger surface area for cell proliferation. Furthermore, this surface area is easily and accurately quantifiable as opposed to the case of microscopic glass powders or porous microcarriers. In addition, since glass microspheres do not have any porosity, cell harvesting by trypsinisation may be facilitated. All these factors assume significant importance in the context of industrial scale-up of the cell expansion process for providing a large quantity of cells that can be used in cell-based therapies or for high throughput screening. The cell-seeded microspheres thus obtained can be assembled into larger tissue via methods such as packing into perfusion bioreactors, stacking of layers or direct assembly (Urciuolo et al., 2012). The perfusion bioreactor approach has already been investigated with some success; for instance, the development of modular bone tissue constructs using microcarriers laden with human amniotic stem cells has been reported (Chen et al., 2011).

It should be noted that the behaviour of cells in contact with the material surface is one of the fundamental factors determining the success of the abovementioned tissue engineering approaches, or indeed that of any biomedical application that involves contact between biomaterials and cells under *in vitro* or *in vivo* conditions. Cell adhesion plays a major role in various physiological functions ranging from embryogenesis to three-dimensional tissue assembly and maintenance of tissue structure, wound healing, immune response and metastasis, and it is a highly dynamic process involving several mechanisms that facilitate the translation of basic genetic information into complex three-dimensional cellular patterns present in tissue structures (Gumbiner, 1996, Anselme, 2000). In the orthopaedic field, bone cell adhesion to a biomaterial involves both short-term and long-term phenomena. The short term phenomena comprise cell attachment whereby physicochemical linkages occur between cells and materials through ionic forces, van der Waal's forces and so on. The longer term phenomena comprise the cell adhesion process, which involves three types of multiprotein complexes: extracellular matrix proteins (including both collagenic and non-collagenic proteins), cytoskeleton proteins and adhesion molecules (including integrins and catechins which govern cell-substrate and cell-cell adhesion processes respectively). It is interesting to note that the adhesion of bone cells to materials is governed by various characteristics of the material surface such as the topography, chemistry and surface energy; furthermore, these characteristics play major roles not only in bone cell adhesion but also in bone cell proliferation and differentiation on the material surface (Boyan et al., 1996).

1.4. Basic concepts of phosphate glass structure

There are three main types of oxides that can be used to form any glass in general: network-forming oxides, network-modifying oxides and intermediate oxides (Zachariasen, 1932). Network-forming oxides are those that can form glasses on their own. In the case of phosphate glasses, the network-forming oxide is P_2O_5, which as previously mentioned can form a highly hygroscopic glassy material, although various other materials such as oxides of Si, Ge, B, As and Sb have also been found to possess the same property. Network-modifying oxides are those that modify the glass structure through disruption of the glass network, thereby changing the glass properties. They are generally oxides of alkali and alkali-earth metals; for instance, in the case of ternary P_2O_5–Na_2O–CaO phosphate glasses, Na_2O and CaO function as network-modifying oxides, and their influence on the glass structure is based on various factors such as the ionic charge, ionic radius, bond

length, bond enthalpy, electronegativity and so on. Intermediate oxides are those of elements such as Al, Ga, Ti, C, V, Bi, Mo, W, S, Se and Te that are unable to form glasses by themselves but can be substituted in the place of network formers to some extent. It is noteworthy that the distinctions between these three categories of oxides are sometimes not entirely clear; for instance, the role of TiO_2 in glasses as a network former or a network modifier is at present a matter of debate and TiO_2 is sometimes referred to as a conditional network former under certain circumstances (Kiani et al., 2010, Kiani et al., 2012a).

Phosphate glasses can essentially be considered as inorganic polymers comprised of the tetrahedral phosphate anion PO_4^{3-} (Figure 1.1) as the basic units which are linked to form a three-dimensional network (Hoppe, 1996, Brow, 2000).

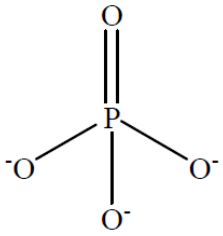

Figure 1.1. The phosphate anion PO_4^{3-} tetrahedron.

The linkages between the PO_4^{3-} tetrahedra occur through covalent bonds with oxygen atoms which are known as bridging oxygens (BOs). On the basis of the number of BOs shared between the phosphate units, the phosphate tetrahedra can be classified using Q^i terminology where Q denotes the P atom bonded to four O atoms to form the phosphate tetrahedron while 'i' refers to the number of BOs per tetrahedron and can take integer values ranging from 0 to 3 (Kirkpatrick and Brow, 1995b, Brow, 2000, Walter et al., 2001)**.** Thus, there are 4 possible structures for the PO_4^{3-} tetrahedron as shown in Figure 1.2.

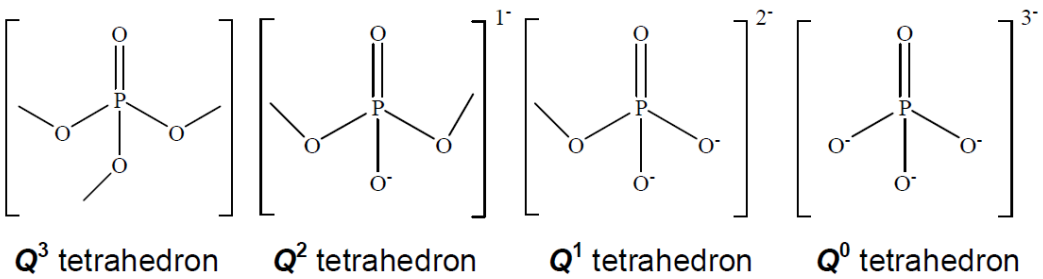

Figure 1.2. The four different representations of the PO_4^{3-} tetrahedron.

Within this framework, it is understood that the structure of vitreous P_2O_5 comprises only Q^3 phosphate tetrahedra which are linked to form a three-dimensional network. The addition of modifying oxides (e.g. Na_2O and/or CaO) causes the cleavage of P–O–P bonds and formation of negatively charged non-bridging oxygens (NBOs) at the expense of BOs, with both processes leading to depolymerisation of the glass network. As per the model proposed by Kirkpatrick and Brow (Kirkpatrick and Brow, 1995a), the depolymerisation process occurs in conjunction with changes in the *Q* speciation according to the following sequence: $Q^3 \rightarrow Q^2 \rightarrow Q^1 \rightarrow Q^0$. Assuming the addition of a monovalent oxide M_2O to vitreous P_2O_5, the changes in the *Q* species can be expressed in the form of the following chemical reactions:

$$2Q^3 + M_2O \rightarrow 2Q^2$$
$$2Q^2 + M_2O \rightarrow 2Q^1$$
$$2Q^1 + M_2O \rightarrow 2Q^0$$

The NBOs coordinate the modifier cations such that the cations attain their preferred coordination number with respect to oxygen (Kirkpatrick and Brow, 1995b, Brow, 2000, Walter et al., 2001). It follows that variations in the modifier oxide content of the glass have a direct effect on the O/P ratio, which can be used to determine the average number of BOs per PO_4^{3-} tetrahedron and consequently identify the dominant *Q* species in the glass.

On the basis of the glass composition $(M_{2/V}O)_x(P_2O_5)_{1-x}$ where $0 \leq x \leq 1$ and v denotes the valency of the cation in the modifying oxide, the phosphate glasses can be classified into three broad types: ultraphosphate, metaphosphate and polyphosphate glasses. Ultraphosphate glasses lie in the region $0 \leq x < 0.5$ and their O/P ratio is in the range $2.5 \leq O/P < 3.0$. These glasses are characterised by the presence of mainly Q^3 and Q^2 units in the glass structure; at $x < 0.25$, the glass structure may begin to approximate that of vitreous P_2O_5 with a predominantly Q^3-based structure. Metaphosphate glasses have $x = 0.5$ and $O/P = 0.3$. In these glasses, the glass structure is typified by the predominance of Q^2 units that form long phosphate chains linked through ionic bonds between the modifying cations and terminal NBOs provided by Q^1 units. The transition from vitreous P_2O_5 to a metaphosphate glass composition can be considered as the transformation from a Q^3-based cross-linked structure to a Q^2-based chain-like structure, with ultraphosphate glasses showing a mixture of both cross-linked and chain structures

in ratios that depend on the P_2O_5 content. Polyphosphate glasses have x > 0.5 and O/P > 0.3 with a glass structure comprising mainly Q^2 chain units and chain-terminating Q^1 units. Polyphosphate glasses with x = 0.67 and O/P = 3.5 are referred to as pyrophosphate glasses; the network structure of these glasses mainly consists of Q^1 units linked by a single BO. Polyphosphate glasses with x = 0.75 and O/P > 3.5 are referred to as orthophosphate glasses and have a structure mainly comprised of Q^0 units. The present study focuses on the production, physicochemical properties, glass structure and biocompatibility of metaphosphate glasses so that all the investigated glass compositions have a constant P_2O_5 content of 50 mol% i.e. x = 0.5 with O/P = 0.3. It is worth noting that while metaphosphate and polyphosphate glasses have been the focus of many studies, ultraphosphate glasses are relatively less studied on account of their highly hygroscopic and volatile nature (Brow, 2000).

1.5. Phosphate glass synthesis routes

1.5.1. Melt-quenching

The low fusion temperatures and relative ease of glass formation without vitrification mean that phosphate glasses can be synthesised by simple conventional melt-quench routes. In the melt-quench process, the required oxide precursors are mixed and melted in a furnace at temperatures in excess of 1000°C (the exact melting temperature depends on the glass composition). The homogeneous melt thus formed can either be poured on to a steel plate so that it cools suddenly to room temperature to form a glass. Alternatively, the molten glass can be poured into preheated moulds to form different shapes such as rods or plates; in such cases, to remove any residual stresses, the mould with the molten glass is placed in an annealing furnace and the glass is cooled slowly to room temperature. P_2O_5—the main component of these glasses—is highly hygroscopic. Therefore, the inclusion of phosphorus in the glass structure without using excessive amounts of P_2O_5 becomes a significant technical challenge, and the presence of small amounts of water can promote crystallisation (Brow et al., 1990). A good way to overcome this challenge is to (a) add some proportion of phosphorus in the form of a stable oxide that includes one of the modifying cations, e.g. $CaHPO_4$ or NaH_2PO_4, and then (b) add any remaining minimal amount as P_2O_5. Water uptake (and also P_2O_5 loss due to volatilisation) can be minimised by melting in ampoules or covered crucibles.

1.5.2. Sol-gel synthesis

The sol-gel method serves as a useful alternative to the conventional melt-quench process for producing glasses. The main advantages of this method—which involves the mixing of inorganic alkoxide and metal chloride precursors to form a colloid through hydrolysis and polycondensation reactions and subsequent thermal treatment to yield a dense, porous, glassy material—are its high level of adaptability and the low temperatures involved (up to an order of magnitude lower than in the melt-quench process). The process of reacting from a liquid allows sol-gel glasses to be deposited as thin films on a substrate, drawn into fibres, or produced as micrometre- or nanometre-sized spherical particles. The low processing temperature has direct implications for drug delivery applications since it allows the incorporation of some active biological ingredients such as proteins, antibiotics and chemotherapeutic molecules into the glass structure. At the same time, questions exist regarding the residual organics that may reside in a sol-gel derived glass, some of which can be toxic in nature.

Silica-based sol-gel glasses have been studied extensively by biomaterials researchers (Gill and Ballesteros, 2000, Schottner, 2001, Kokubo et al., 2003). However, few studies have focused on the synthesis of phosphate glasses by the sol-gel route for biomedical applications; even fewer studies exist on the synthesis of biological sol-gel phosphate glasses containing titanium and almost none on those containing iron. This can mainly be attributed to the highly challenging chemistry involved in phosphate sol-gel synthesis and the lack of readily available precursor chemicals. Alkyl phosphates undergo hydrolysis at considerably slower rates than alkyl silicates, and the times required for synthesis and subsequent drying are of the order of several weeks. Nonetheless, several studies have investigated the synthesis of sol-gel phosphate glasses with encouraging results. For instance, a recent study reported the incorporation of Cisplatin into a sol-gel derived P_2O_5–Na_2O–CaO glass and subsequent controlled release into an aqueous salt solution (Pickup et al., 2012). Cisplatin—a commonly used cytotoxic drug in the treatment of cancers of the lung, head and neck—tends to remain stable at temperatures above 200°C, which is the temperature at which the sol gel was dried. After a sample preparation process (including drug incorporation) of about 2 weeks in duration, Pt L_{III}-edge extended X-ray absorption fine structure (EXAFS) spectroscopy was used to confirm the successful incorporation of Cisplatin within the sol-gel matrix. The sustained release of the encapsulated Cisplatin into an aqueous medium over a period of approx. 160 hours was then verified by means of

UV-visible spectroscopy. The results highlighted the capability of sol-gel derived phosphate glasses to function as Cisplatin delivery devices for cancer therapy as well as delivery carriers for other drugs and active molecules.

With regard to titanium phosphate glasses, the phosphate precursor of choice for these sol-gels is $PO(OH)_{3-x}(OR)_x$ (R = alkyl group) which, at a basic level, can be reacted with a titanium alkoxide to yield a clear sol at equimolar P/Ti ratios; ^{31}P magic angle spinning nuclear magnetic resonance (MAS NMR) results reveal the presence of P–O–Ti bonds without the occurrence of precipitation at the expense of gelation (Livage et al., 1992, Noda et al., 1997). The comparison of binary P_2O_5–TiO_2 glasses of the same composition prepared by sol-gel and melt-quench routes provides several interesting results (Tang et al., 2004). For instance, in the sol-gel glass, the Ti^{4+} ion has an average coordination number of 6 and tends to form TiO_6 octahedra, whereas in the melt-derived glass, the same ion has an average coordination number of between 4 and 5 since it exists predominantly in the 4- and 5-fold coordination states as TiO_4 tetrahedral and TiO_5 pyramidal units respectively, while only a small number of Ti^{4+} ions having 6-fold coordination states are present as TiO_6 octahedra. The higher coordination number in the sol-gel glass coincides with its higher refractive index and density as compared to the melt-quenched glass. Furthermore, the Ti–O bond length in the melt-derived glass is slightly smaller than that in the sol-gel glass; this may possibly be attributed to the presence of TiO_5 pyramidal units in the melt-derived glass in addition to the TiO_4 tetrahedral and TiO_6 octahedral units. Thus, sol-gel synthesis provides a more consistently ordered structure than is possible by melt-quenching, although the effect of such differences on the biocompatibility of the resulting glasses has not been studied. It is noteworthy that no reports exist in the literature regarding similar comparisons for ternary P_2O_5–CaO–TiO_2 or quaternary P_2O_5–CaO–Na_2O–TiO_2 glasses; considering the wealth of data available for melt-quenched quaternary titanium glasses, it would be quite interesting for future studies to particularly focus on the sol-gel synthesis of quaternary P_2O_5–CaO–Na_2O–TiO_2 glasses.

1.6. Phosphate glass processing and applications

1.6.1. Phosphate glass fibres

The potential range of biomedical applications of glass fibres encompasses the fields of muscle and ligament tissue engineering and nerve regeneration; this is mainly because the morphology and chemistry of glass fibres can be conducive to the growth of anisotropic tissue such as muscle or neuronal cells along the

longitudinal axis of the fibre. Several studies have investigated the production of phosphate glass fibres containing metallic oxides such as Fe_2O_3 and CuO as dopants (Ahmed et al., 2004a, Ahmed et al., 2004c, Bitar et al., 2005, Abou Neel et al., 2005a, Abou Neel et al., 2005b, Shah et al., 2005, Abou Neel et al., 2007b, Munoz et al., 2008, Vitale-Brovarone et al., 2012). Quaternary P_2O_5–CaO–Na_2O–Fe_2O_3 glasses have shown themselves to be amenable to glass fibre production using a fibre-rig that comprises a top-loading furnace with a platinum/10% rhodium (Pt/10% Rh) crucible having a bushing with a 1 mm hole and 15 mm long tip. Glass left to melt and homogenize in the furnace can then be subsequently cooled by decreasing the furnace temperature to achieve the right melt viscosity, after which it is drawn onto a steel drum that rotates at speeds that can be varied to achieve different fibre diameters; a higher rotating speed gives rise to smaller fibre diameters (Ahmed et al., 2004a, Ahmed et al., 2004c). Biocompatibility studies using murine muscle cells revealed that fibres made from glasses containing 4–5 mol% Fe_2O_3 show favourable cell attachment and differentiation, with myotubes formed along the fibre axis.

Very few studies, however, have studied the fabrication of glass fibres made from phosphate glasses incorporating titanium oxide. One such study produced P_2O_5−CaO−MgO−Na_2O−TiO_2 fibres by the preforming technique at 600–620°C at a pull rate of 6 m.minute^{-1} (Brauer et al., 2008). These fibres were then combined with a macromer/HEMA (methacrylic acid 2-hydroxyethylester) mixture to form degradable fibre reinforced polymer composite matrices. The similarities between the matrices and cortical bone in terms of bending strengths and elastic moduli and the favourable biocompatibility of the matrices as evidenced by *in vitro* cell culture studies demonstrated the promise of these fibre composites for use in bone fixation devices. Proof of concept for the fabrication of P_2O_5−30CaO−9Na_2O−3SiO_2−3MgO−K_2O−TiO_2 glass fibres by the preform approach was shown (Vitale-Brovarone et al., 2011). Fibres free from crystallisation were successfully obtained at diameters in the range 37–173 mm, although the biocompatibility of these fibres was not reported.

1.6.2. Phosphate glass microspheres

Glass microspheres show considerable potential for use in a whole host of biomedical applications including cancer radiotherapy and thermotherapy, drug and protein delivery, and bone filler materials (Kawashita et al., 2003, Cacaina et al., 2006, Cacaina et al., 2008, Sene et al., 2008, Martinelli et al., 2010, Wu et al.,

2010). Thus far, the biggest application of glass microspheres is in the field of oncology, where Y^{90} microspheres have been used as internal brachytherapeutic tools to combat hepatic malignancies (Ho et al., 1998, Kennedy et al., 2004, Salem and Thurston, 2006). Some of the earliest work in this area was carried out by Day's research group at University of Missouri-Rolla who investigated the production of glass microspheres in the 20–30 μm size range containing either ^{31}P or ^{89}Y isotopes that could undergo activation by neutron bombardment to form ^{32}P or ^{90}Y for treatment of liver tumours through intra-arterial radiotherapy (Ehrhardt and Day, 1987, Erbe and Day, 1993, White and Day, 1994). Many research groups are also engaged in the development of mesoporous microspheres that can serve as scaffolds for bone tissue engineering or as vehicles for drug and protein delivery (Arcos et al., 2009, Li et al., 2010, Lei et al., 2010).

The production of microspheres from melt-quenched glasses takes place using a technique generally known as *flame spheroidisation* or *flame spheronisation*; both names belie the innate simplicity of the underlying principle, which is essentially the 'moulding' of glass microparticles into spherical form via surface tension forces whilst in the molten state. Interestingly, initial studies by Gerhardt and Day focused on the materials that would be amenable to such processing to form microspheres (Ehrhardt and Day, 1987). For this purpose, powdered samples were passed through a fluidised bed powder feed into a flame sprayer, and the spheroidisation product was collected in a stainless steel drum. It was observed that whereas silicon–phosphorus alloys commonly used in the semiconductor industry were poorly suited to such processing and showed poor chemical durability, Y_2O_3–Al_2O_3–SiO_2 glasses were able to provide flame spheroidised particles with a high degree of sphericity and uniformity; leaching experiments showed satisfactorily small levels of ^{90}Y leaching from the microspheres (less than 0.07% leaching of ^{90}Y in 24 hours from $0.4Y_2O_3$–$0.2Al_2O_3$–$0.4SiO_2$ glass microspheres) following immersion in a 1% EDTA solution at pH 6.

Various experimental designs and apparatuses for this procedure have been described in the literature, the basic components of which are (a) a high-temperature jet, (b) a feed assembly and (c) collectors, with particles travelling along the jet axis as they undergo spheroidisation. The high-temperature jet can be a gas/oxygen flame, with the gas being acetylene or liquid petroleum gas, or it can be a radio frequency plasma flame (Gu et al., 2004, Cacaina et al., 2006, Cacaina et al., 2008, Sene et al., 2008, Martinelli et al., 2010); a high-temperature flame can

also be produced by using methyl**a**cetylene-**p**ropadiene **p**ropane (MAPP) and can be used for heating, soldering, brazing and welding due to its high flame temperature of 2925°C in air (Lakhkar et al., 2012). An alternative to the gas flame is a vertical tubular electric furnace, in which particles dropped at the top end of the furnace are transformed into microspheres as they fall through the furnace under the effect of gravity (Sene et al., 2008, Martinelli et al., 2010, Ward et al., 2010). It is worth noting that the choice of the high-temperature jet depends on the required particle size; stronger jets generated at higher temperatures can spheroidise particles with a larger grain size. The particles to be spheroidised can be fed to the flame either manually or using an automated feed assembly. The microspheres can be collected in air or on water in standard glass containers. Other techniques for producing glass microspheres are based on processing techniques that complement the sol-gel method, as described in the review by Park et al. (Park et al., 2013). Silicate glasses are far more amenable to such processing than phosphate glasses, with tetraethyl orthosilicate (TEOS) being the silica precursor of choice, and various microsphere morphologies such as solid or hollow microspheres with or without surface porosity can be obtained (Kawashita et al., 2003, Li et al., 2010, Wu et al., 2010, Poorbaygi et al., 2011a, Poorbaygi et al., 2011b, Wu et al., 2011), as opposed to the flame spheroidisation process which is used to produce non-porous solid microspheres.

1.7. Probing the structure of phosphate glasses

One of the major avenues of glass research is to understand the glass structure by means of a variety of characterisation techniques. It is worth mentioning here that ongoing research in glass systems is being driven by developments in the available characterisation techniques, which allows us to obtain information at various size scales from the macroscopic level down to the atomic level. Thus, for instance, glass bulk properties such glass density and surface free energy can be investigated using relatively simple techniques and equipment, and at the same time information about the local environments and connectivity of constituent atoms such as P and Ti can be obtained by highly specialised techniques such as ^{31}P MAS NMR and Ti *K*-edge X-ray absorption near edge structure (XANES) spectroscopy. The vibrational techniques of Fourier transform infrared (FTIR) and Raman spectroscopies are widely used in order to obtain information on the presence of chemical groups and changes in the intensity of peaks corresponding to these groups with variations in the glass composition. Conventional X-ray diffraction (XRD), which yields information about broad features existing in the disordered

structure, can confirm the presence of any crystalline components through the presence of any sharp diffraction peaks. X-ray spectroscopic (XAS) techniques are element specific and the spectral features reflect the nature of the local coordination. Among the most advanced techniques available today for glass structural probing are neutron and X-ray scattering techniques, which can provide information about atom type, atomic distances, coordination numbers and various thermal parameters. However, it should be argued that all these techniques are clustered at either end of the length scale in terms of the glass structure. Thus, methods exist for measuring bulk properties such as thermal analysis methods on the one hand and for examining specific nuclei and their local environment on the other. A large knowledge gap exists in the middle of the scale where information can at present only be inferred from other measurement techniques.

1.7.1. Fourier transform infrared and Raman spectroscopies

Fourier transform infrared and Raman spectroscopies, which are commonly used techniques for investigating the various structural units present in glasses, are based on absorption and scattering of electromagnetic radiation at different wavenumbers due to resonance vibrations of different chemical groups of a molecule. Both techniques allow a deeper understanding of the variation in the thermophysical properties of phosphate glasses as a function of the composition. To elaborate, absorption of IR radiation causes transitions in the resonant vibrational and rotational states associated with the ground electronic state of a molecule. These resonant modes of the bonds are either stretches (changes in bond length) or bends (changes in bond angles), which are typically observable in the infrared part of the spectrum. Peaks at various wavenumbers in an FTIR spectrum can readily be assigned to chemical groups because each bond or group of atoms has different vibrational energies (Drake, 1994). The wavenumber in a Raman spectrum, however, is obtained by subtracting the wavenumber of the scattered radiation from that of the laser (called the Raman shift). As laser radiation hits a molecule, a proportion of the deflected photons emerge with slightly different wavenumbers. This is due to the absorption or emission of the energy by the molecule under the influence of laser radiation as a result of interactions with bond vibrations (Stevens, 1999).

Although relevant information from the Raman and FTIR spectra of phosphate glasses is obtained generally in two main regions (600–1500 cm^{-1} and 0–600 cm^{-1}), data related to the characteristics of the phosphate network—mainly corresponding

to the stretching vibrations of anions—can be obtained only in the high-wavenumber 600–1500cm^{-1} region. Within this region, the 1000–1400 cm^{-1} band corresponds to the terminal P–O stretching vibrations and the 600–850 cm^{-1} band to bridging stretching modes (Reis et al., 2002, Le Saout et al., 2002). The complementarity of FTIR and Raman spectra lies in the fact that peak(s) corresponding to a particular chemical group are present in both spectra at the same wavenumber(s). In a molecule with a centre of symmetry, those vibrations symmetrical about the centre of symmetry are active in the Raman and inactive in the IR; on the other hand, asymmetric vibrations are inactive in the Raman and usually active in the IR. Hence, strongly absorbed peaks in the mid FTIR region show weak absorption in the Raman region and vice versa (Stevens, 1999).

FTIR/Raman studies on various binary, ternary and more complex phosphate glasses have consistently revealed shifts in the υ_s(P–O–P), υ_s(PO_2) and υ_{as}(PO_2) vibrations with variations in the metal oxide content, thereby implying the phosphate chains undergo depolymerisation when the metal oxide content is increased (Pemberton et al., 1991, Meyer, 1997, Hudgens et al., 1998, Meyer, 1998, Shih et al., 1999, Brow, 2000, Peitl et al., 2001, Shih, 2003, Karabulut et al., 2003, Carta et al., 2007b, Shih and Shiu, 2007, Abou Neel et al., 2009a, Valappil et al., 2009, Lucacel et al., 2010, Tiwari et al., 2011); These shifts in phosphate chains occur in agreement with the corresponding *Q* species changes observed in NMR studies. FTIR studies on titanium metaphosphate glasses have revealed that with an increase in the TiO_2 content, the intensity of the bands associated with Q^2 groups at ~1270 and 900 cm^{-1} decreases relative to those associated with Q^1 groups at ~1100 and 1000 cm^{-1}. A small shift in the υ_{as}(P–O–P) band to a higher energy with an increase in the Ti^{4+} content was also observed (Abou Neel et al., 2009a). Furthermore, it has been observed that an increase in the TiO_2 content of the glass occurs in conjunction with a shift in symmetric stretching band of P–O–P towards higher frequencies. The higher wavenumber of the P–O–P band is due to the smaller P–O–P bond angle, which results from either shorter phosphate chain length or smaller metal cation size (Shih, 2003).

1.7.2. X-ray diffraction

X-ray diffraction is a powerful technique that provides information regarding the structure of solids and the molecules that form part of the solid structure. At the most fundamental level, it can be used to investigate and quantify the separation of

atomic layers within a solid as well as the locations of the atoms. The basic principle of the technique is founded on the interaction between a monochromatic X-ray beam and a solid substance. When an X-ray beam is focused on the solid, the electrons around the atoms that make up the solid begin to oscillate at frequencies equal to that of the incident beam, producing secondary spherical waves that emanate from the electron. In most cases, these secondary waves cancel each other out since they are out of phase, so that no energy leaves the sample. However, in a few cases, the waves are in phase and will reinforce each other so that well-defined X-ray beams leave the sample and can be detected and further analysed. These beams form the so-called 'diffraction pattern' which serves as a fingerprint of the solid sample. This is especially true for crystalline samples since every crystalline substance is associated with a unique diffraction pattern; it is also true in the case of a solid comprising different crystalline phases, since each phase will be associated with its own diffraction pattern (Hull, 1919).

Thus, XRD analysis is of great use in the study of crystalline materials which exhibit atoms arranged in a regular pattern; the XRD spectra of crystalline substances comprise a series of well-defined peaks which are unique to the substance. Glasses, however, are amorphous substances, meaning that the constituent atoms are randomly arranged. As a result, the XRD spectra of glasses exhibit a pattern with very broad peaks. This can often be a useful means to determine the success of the glass production process, since the presence of any sharp peaks will indicate phase crystallisation within the bulk glass. The crystallisation temperature of the glass (also known as the T_c value) can be obtained from techniques such as differential thermal analysis (DTA) or differential scanning calorimetry (DSC). Thus, in a glass sample crystallised by heating close to the T_c value, the crystal phases present in the glass can be identified by XRD experimentation and subsequent phase identification using appropriate software that references a database of known diffraction patterns e.g. International Centre for Diffraction Data (ICDD); furthermore, the effect of changes in glass composition on the crystalline phases can be investigated (Abou Neel et al., 2005b, Ahmed et al., 2007, Carta et al., 2007a, Valappil et al., 2007, Abou Neel and Knowles, 2008, Qiu et al., 2008a, Kiani et al., 2012a).

In ternary P_2O_5–CaO–Na_2O glasses (both melt-quenched and sol-gel derived), XRD analysis of phosphate glasses has generally revealed the main and secondary phases to be phosphate compounds containing Na and/or Ca e.g. $NaCa(PO_3)_3$,

$Na_4Ca(PO_3)_6$, $NaPO_3$, $Ca_2P_2O_7$ etc. (Ahmed et al., 2004b, Carta et al., 2007a). The relative concentrations of Na and Ca in these phases are dependent on the glass composition, so it can be expected that an increase in the CaO content of the glass at the expense of Na_2O will, at some threshold concentration, probably give rise to phases that do not contain Na; the same principle holds true if Na_2O is added to the glass at the expense of CaO. In quaternary or higher order glasses containing transition metal oxides, the main phase remains a phosphate compound containing Na and/or Ca at low metal oxide contents; however, as the metal oxide content is increased, it is possible that metal-containing phases may arise. For instance, in quaternary glass systems where the metal oxide dopant used is Cu_2O, SrO, ZnO, or TiO_2, phases such as $NaCu(PO_4)$, $Sr_3(PO_4)_2$, $NaZn(PO_3)_3$ and TiP_2O_7 have been observed as secondary phases at metal oxide contents of 5 mol% or higher (Abou Neel et al., 2005b, Abou Neel et al., 2008a, Abou Neel and Knowles, 2008, Abou Neel et al., 2008b, Abou Neel et al., 2009b, Kiani et al., 2010).

High-temperature XRD (HTXRD) is a useful technique that combines conventional XRD equipment with a stage heater in order to acquire XRD spectra as the sample is heated to an elevated temperature. The spectra thus obtained can be viewed in the form of contour maps that show the various peaks obtained at increasing temperatures as ‘events’. The results obtained from HTXRD experiments can be combined with those from ambient XRD and DTA experiments and DTA-XRD-HTXRD combination plots can be prepared (Figure 1.3), which provide interesting insights into the close correlations between three distinct sets of experimental data (Pickup et al., 2007b, Lakhkar et al., 2010).

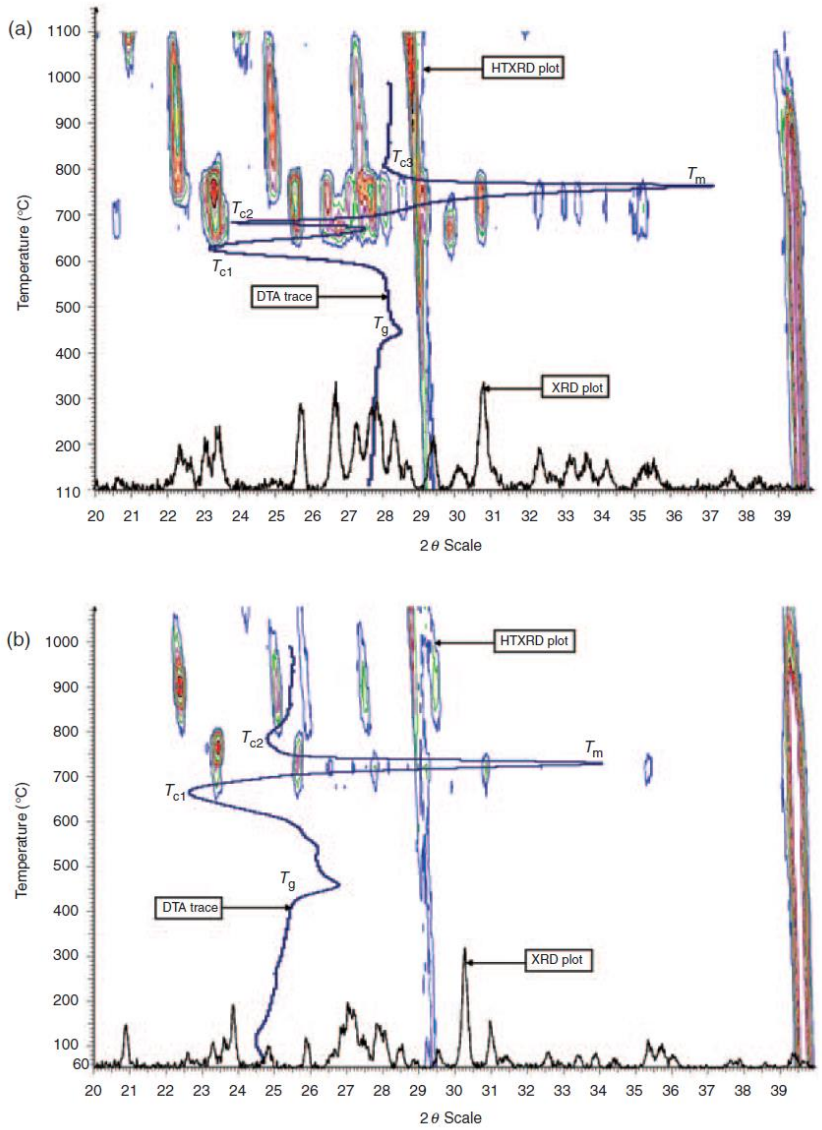

Figure 1.3. Plots of data from differential thermal analysis, ambient X-ray diffraction and high-temperature X-ray diffraction combined together to form combination graphs. These combination plots are for quaternary P_2O_5–CaO–Na_2O–SrO glasses containing (a) 0 mol% SrO and (b) 1 mol% SrO (Lakhkar et al., 2010).

1.7.3. Magic angle spinning nuclear magnetic resonance

Solid state NMR has been used extensively as a spectroscopic technique to probe the structure of phosphate glasses. In this context, ^{31}P NMR can be considered as the logical starting point since the glass structure is predominantly comprised of phosphate units. ^{31}P NMR spectra are relatively easy to obtain and process because of the sensitivity of the ^{31}P isotope, which has 100% natural abundance and possesses a large magnetic moment and consequently a high receptivity (Mackenzie and Smith, 2002b). ^{31}P is strongly influenced by the chemical shielding interaction on account of being a spin-1/2 nucleus; the chemical shielding interaction arises when the magnetic field experienced by the nucleus is modified by

the electronic density around the nucleus. This leads to a change in the resonance frequency of the nucleus and is referred to as the chemical shift; the chemical shift is usually expressed in units of ppm to remove the magnetic field dependence. The spatial dependence of this interaction means that a powder sample gives rise to a broadened powder lineshape that reflects the local environmental symmetry.

In the presence of multiple phosphorus sites corresponding to different *Q* species, severe overlap between the different environments occurs because of the broadening caused by the anisotropy, due to which unambiguous resolution of sites corresponding to different *Q* species becomes difficult. This problem is commonly overcome by using magic angle spinning (MAS); the 'magic angle' in this case is the angle of 54.7° between the axis of rotation of the powder sample and the main static magnetic field direction. When the powder sample is rotated rapidly under MAS conditions at values in the kHz range, the anisotropy is eliminated and the resolution is thereby greatly improved. As a result, it becomes possible to distinguish between the different Q^n species on the basis of their differing isotropic chemical shifts. The MAS technique splits the static lineshapes into the isotropic line and a series of spinning sidebands which are separated from the isotropic line by multiples of the spinning rate as shown in Figure 1.4. The intensity contribution from the spinning sidebands must be included in determining the relative abundance of each site.

^{31}P MAS NMR experiments offer direct information about the Q^n speciation and consequently the variation in the network environment (Figure 1.4) and have been utilised in binary, ternary and more complex systems (Tang et al., 2004, Pickup et al., 2008b). However, the isotropic chemical shifts yield additional information on the changing local arrangements in the glass due to the bonding effects of different metals in the system that coordinate to the phosphate network. The shift ranges and the effects on ^{31}P are well defined (Kirkpatrick and Brow, 1995b, Brow, 2000, Mackenzie and Smith, 2002b, Carta et al., 2007b, Carta et al., 2007a, Pickup et al., 2007a). Phosphate glasses are usually characterised by a binary model wherein only two consecutive Q^n species are found at any given composition. An alternative description of the network connectivity N_{P-O-P} is given by

$$N_{P-O-P} = \sum_{n=0}^{3} n f_n$$

where f_n is the fractional intensity of that Q^n species (Pickup et al., 2007a).

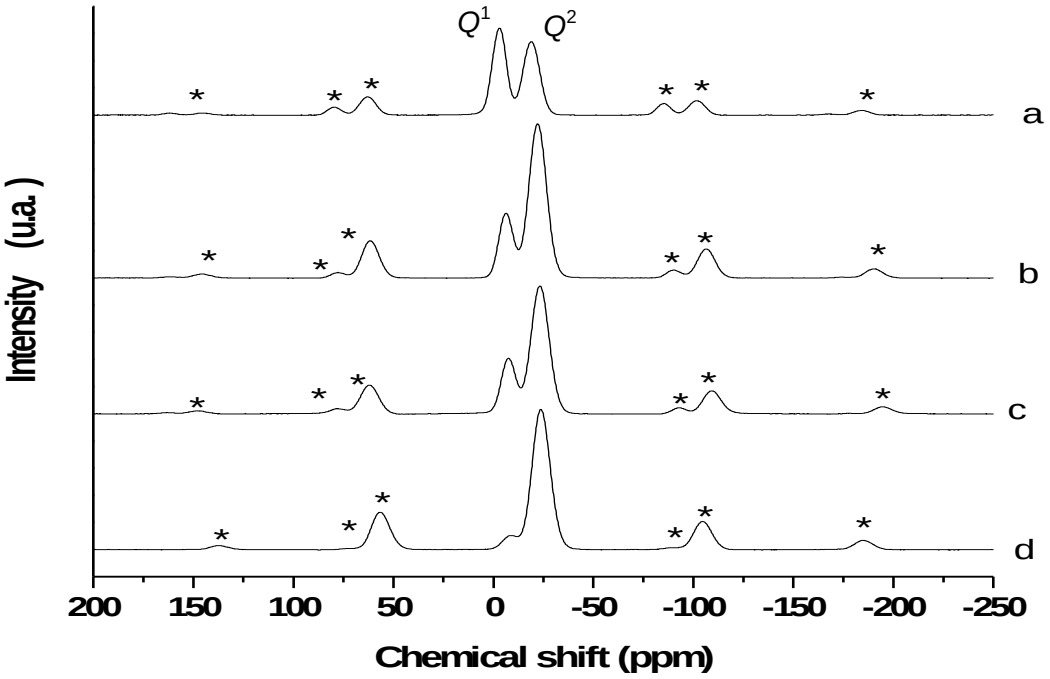

Figure 1.4. ^{31}P MAS NMR spectra for glass samples of compositions (a) 45 mol% P_2O_5 8mol% CaO 47mol% Na_2O, (b) 45mol% P_2O_5 12mol% CaO 43mol% Na_2O, (c) 45mol% P_2O_5 35mol% CaO 20mol% Na_2O and (d) 45mol% P_2O_5 40mol% CaO 14mol% Na_2O. The change in the Q^1:Q^2 ratio can clearly be seen. The asterisks denote spinning sidebands (Kiani et al., 2012b).

^{23}Na is another isotope that is accessible to probing by MAS NMR techniques. Like ^{31}P, ^{23}Na also has 100% abundance, but in contrast to the spin-1/2 nucleus of ^{31}P, ^{23}Na has a spin-3/2 nucleus so it experiences the nuclear quadrupolar interaction (Smith and van Eck, 1999), thereby complicating the interpretation of the ^{23}Na MAS NMR spectra, although additional information on the coordination environments associated with neighbouring network formers and modifiers can be obtained (Deffontaines et al., 1991, Stebbins et al., 1992). The quadrupolar interaction introduces a magnetic field dependent effect through the second-order perturbation interaction (Smith and van Eck, 1999, Mackenzie and Smith, 2002b). Hence, by recording spectra at multiple applied magnetic fields and either simulating the spectra using computer programmes such as Quadfit (Kemp and Smith, 2009a) or by plotting the change in the centre of gravity position of the lineshape, the interactions can be deduced (Kohn et al., 1989, Kohn et al., 1998, Kiani et al., 2010, Kiani et al., 2012a).

The other nuclei in these systems are much less accessible to solid state MAS NMR. For instance, the NMR active isotope ^{17}O has a natural abundance of only 0.037 % with I = 5/2 i.e. it is a quadrupolar nucleus. ^{17}O MAS NMR usually requires isotopic enrichment with higher fields and faster MAS rates and the costs involved

mean that limited reports exist on ^{17}O MAS NMR in phosphate glasses (Mackenzie and Smith, 2002b, Ashbrook and Smith, 2006). Nuclei such as ^{43}Ca and $^{47,49}Ti$ are yet more difficult to process using MAS NMR; both are quadrupolar nuclei with small magnetic moments (Smith, 2001). ^{43}Ca has low natural abundance (0.135%) and therefore requires isotropic enrichment like ^{17}O, while the ^{47}Ti and ^{49}Ti NMR-active isotopes in $^{47,49}Ti$ are only separated by a few kHz which means the lineshapes of the two isotopes often overlap.

1.7.4. Ti *K*-edge X-ray absorption near edge structure

Titanium *K*-edge XANES is a widely used technique for understanding the local coordination environment of tetravalent Ti(IV) in materials such as titanosilicate and titanophosphate glasses (Farges et al., 1996, Farges et al., 1997). Ti *K*-edge XANES data usually exhibit three peaks at energies of that just before the main absorption edge which are assigned to different transitions in the atomic state (Poumellec et al., 1991, Fronzoni et al., 2006). The lowest energy peak among these is highly sensitive to changes in the Ti coordination environment, shifting to a lower energy and becoming more intense as the Ti coordination changes from six- to five- to four-fold (Farges et al., 1997). This peak is therefore usually the focus of structural analysis. Ti *K*-edge XANES investigations of metaphosphate P_2O_5–CaO–Na_2O–TiO_2 glass systems have shown that the titanium ions occupy an octahedral structural environment with minimal distortion in all the glass compositions. (Pickup et al., 2008a). Degradation of the glass by immersion in distilled water for various times was found to have no effect on the pre-edge feature, suggesting that the titanium environment does not change in water over long periods of time.

1.8. Phosphate glass degradation and ion release

Many studies have demonstrated that phosphate glasses exhibit degradation behaviours that make them ideal candidate materials for applications requiring a temporary device and involving the controlled release of therapeutic ions. As mentioned previously, the glass degradation behaviour is closely linked to the glass chemistry so that alteration of the glass composition allows control of the degradation rate over several orders of magnitude (Knowles, 2003, Abou Neel et al., 2009d). The weight loss of phosphate glasses and also the concurrent ion release are, in general, highly linear functions of the immersion time in the solubilising medium for a wide range of glass compositions and types (Franks et al., 2000, Navarro et al., 2003a, Brauer et al., 2006, Ahmed et al., 2008, ElBatal et al., 2009, Khor et al., 2011). This linearity in the degradation and ion release offers a

major advantage over the degradation behaviour of silicate glasses since the ion release is sustained as long as the glass is present in the medium. An interesting observation in phosphate glass ion release studies is the differing ranges and levels of phosphate species released. These range from the orthophosphate to linear and cyclic phosphates and much larger phosphate groups (Ahmed et al., 2005b). An example of the type of chromatogram obtained with some peak assignments is shown in Figure 1.5.

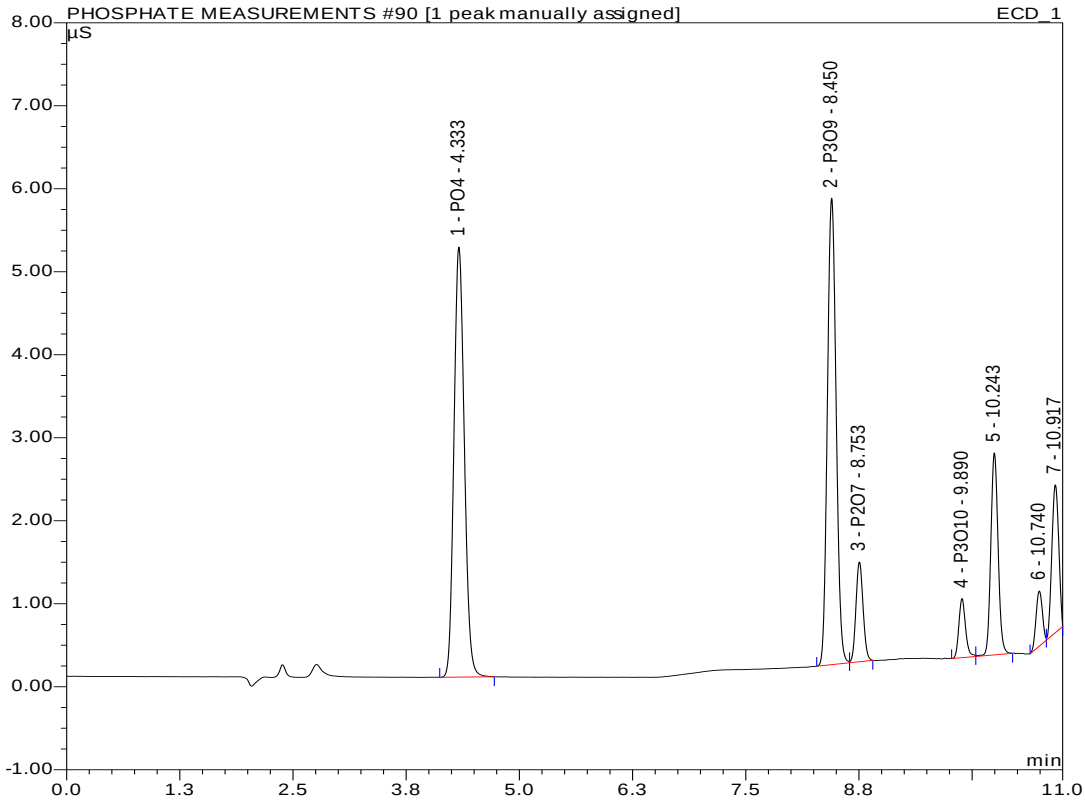

Figure 1.5. Example of an anion chromatogram for phosphate species collected using a Dionex ICS 2500 system, showing the presence of PO_4^{3-}, $P_2O_7^{4-}$, $P_3O_9^{3-}$ and $P_3O_{10}^{5-}$ and higher phosphates (Lakhkar et al., 2013).

Phosphate glass degradation in a solubilising medium occurs in two stages, namely an initial slow degradation stage and subsequent uniform degradation stage, which show exponential and linear variation with time respectively. In the slow degradation stage, H_2O molecules diffuse into the glass and cover the entire surface layer, whereas in the uniform degradation stage, the completely hydrated surface layer separates from the underlying partially hydrated layers and leaches into the surrounding medium. Transition from the first to the second stage is dependent on several factors which can be classified as internal and external factors (Gao et al., 2004). Internal factors include those such as the glass composition and thermal history. External factors include solution pH (glass degradation is greater in acidic

environments than in basic ones), solution temperature (glass degradation is greater at higher temperatures), extent of saturation of the solution (a highly saturated solution inhibits glass degradation) and surface area to volume ratio (Bunker et al., 1984). It is considered that the phosphate glass degradation process is governed by three types of chemical reactions: (1) acid-base reactions, which serve to disrupt the glass chain ionic interactions and are controlled by the pH at the glass surface and acid/base consumption; (2) hydrolysis reactions, which involve the cleavage of P–O–P bonds and destruction of the glass network to yield PO_4^{3-} ions; and (3) hydration reactions, which involve the hydration of entire phosphate chains as opposed to the cleavage of individual P–O bonds.

Studies on the release of phosphate groups from phosphate based glasses have become much more common on account of the development of ion chromatography methods. The main phosphate groups of interest are orthophosphate (PO_4^{3-}), linear species such as pyrophosphate ($P_2O_7^{4-}$) and tripolyphosphate ($P_3O_{10}^{5-}$) and cyclic species such as cyclic trimetaphosphate ($P_3O_9^{3-}$). It is considered that higher phosphate species (P_4 and higher) may be released by these glasses but these have not been studied in detail due to the lack of calibration standards containing these species, and the identification of the higher species by chromatography or mass spectroscopy would be a significantly complex task. The main techniques used thus far to measure polyphosphate distributions (mainly in food products) include chromatography techniques such as high performance liquid chromatography and ion chromatography along with other approaches such as modified end group titration; among these techniques, ion chromatography was shown to be the simplest and most effective at least for the smaller molecular weight phosphates (Baluyot and Hartford, 1996).

As with the release of other ions from the phosphate glass, phosphate release from phosphate glasses generally continues with time until full dissolution of the glass. For instance, in ternary $0.45P_2O_5$–xCaO–$(0.55 - x)Na_2O$ glass systems where x = 0.30, 0.40 and 0.45 mole fraction, all four phosphate species are released continuously over the study period (Ahmed et al., 2005c). The release of the orthophosphate and linear species is straightforward in that these species are released at rates that decrease with the increase in the CaO content, whereas the release rate of the cyclic metaphosphate ions first decreases from x = 0.30 to x = 0.35 and then increases again at x = 0.40, thereby partially mirroring the trend shown for the cations Na^+ and Ca^{2+}. It has been suggested that crosslinking with

cationic species, and consequently the content of cationic oxides in the glass, plays a role in determining linear phosphate ion release, as does the presence of single or multiple phases in the glass and the proximity of the glass composition to a eutectic point in phase diagrams. The extent of crosslinking between the branched linear phosphates and the Ca^{2+} ions is proportional to the CaO content (Ahmed et al., 2005b); furthermore, the chelates formed by the Ca^{2+} ions and the complexing abilities of these chelates are an influencing factor. As the P_2O_5 content in the glasses is increased further to 50 and 55 mol%, the only species that undergoes release with a significant trend is the cyclic $P_3O_9^{3-}$ ion, which is released at rates that increase with the CaO content of the glass; the other species are released at amounts that are too low for any particular trend to be discernible (Ahmed et al., 2005a). The phosphate ion release trends observed for the 50 and 55 mol% P_2O_5 are in agreement with the model proposed by Bunker et al. (Bunker et al., 1984) which takes into account the occurrence of three types of reactions between the glass and the surrounding water: acid/base reactions, hydrolysis and hydration. Interestingly, in all three glass systems, the amount of cyclic $P_3O_9^{3-}$ released is generally the highest among all the investigated phosphate species. From this observation, it can be inferred that the cyclic species dominates the structure of these glasses.

As further dopants such as metal oxides are added to ternary glasses to form quaternary and higher order glass systems, the metal ions would be expected to exert their own influence on the phosphate ion release based on several factors including metal ion valency and atomic radius. In quaternary glasses containing metal oxides with metal valencies of 3+ or higher, the overall trend is for the phosphate ion release to mirror the degradation profile so that glasses that degrade at slower rates release smaller amounts of all phosphate species. For example, in fibres made out of glasses of the composition $0.5P_2O_5$–$0.3CaO$–$(0.2 - x)Na_2O$–xFe_2O_3 where x = 0.0 to 0.05 mole fraction, it was observed that fibres with the highest Fe_2O_3 content have the lowest degradation rates as well as the lowest release rates of different phosphate species (Abou Neel et al., 2005a). The same trend is observed for quaternary glasses containing oxides of gallium and titanium as well (in which the metal ions have a valency of +3 and +4, respectively) (Abou Neel et al., 2008a, Valappil et al., 2008). However, such a trend is not clearly seen in glasses containing divalent metal oxides; for instance, P_2O_5–CaO–Na_2O–ZnO glasses with different ZnO contents release phosphate ions at roughly similar rates, whereas in P_2O_5–CaO–Na_2O–SrO glasses, there is no particular consistency in

terms of the overall trend of phosphate release (Salih et al., 2007, Abou Neel et al., 2009b).

With regard to the other ions released from phosphate glasses, specifically cations such as Na^+ and Ca^{2+}, release studies on ternary P_2O_5–CaO–Na_2O glasses containing 45 or 55 mol% P_2O_5 have generally shown that these cations are released at rates that are inversely proportional to the CaO content of the glass; this is to be expected since it corresponds to the finding that the addition of CaO to the ternary glass serves to densify the glass network and consequently reduce glass solubility and ion release (Ahmed et al., 2004b, Ahmed et al., 2004c, Ahmed et al., 2005c, Ahmed et al., 2005a). The same inverse relationship in Na^+ and Ca^{2+} release is observed with an increase in the metal oxide content in the case of quaternary phosphate glasses where the charge of the metal ion added is greater than +2, for instance Fe_2O_3, Al_2O_3 or TiO_2 (Ahmed et al., 2004a, Abou Neel et al., 2005a, Abou Neel et al., 2008a, Abou Neel et al., 2009a, Abou Neel and Knowles, 2008, Kiani et al., 2010, Kiani et al., 2012b), indicating that among various factors, the difference in ionic charge between the dopant ion and the ion being replaced (generally Ca^{2+} or Na^+) plays a significant role in determining the glass network structure.

However, exceptions to this relationship can be found. For instance, ternary P_2O_5–CaO–Na_2O glasses containing 55 mol% P_2O_5 show a direct relationship between CaO content and Ca^{2+} ion release (Ahmed et al., 2005a), suggesting differences in the cation release dynamics between ultraphosphate glasses on one hand and metaphosphate or polyphosphate glasses on the other. In quaternary phosphate glasses containing metal oxides with 2+ charge, e.g. MgO, SrO or ZnO, there may be no trend in Na^+ and Ca^{2+} release or the trend may not be as straightforward as it is for 3+ charge metal oxides (Franks et al., 2002, Salih et al., 2007, Abou Neel et al., 2009b, Lee et al., 2013a); in these glasses, the divalent metal ion is often incorporated in the glass structure at the expense of the equivalently charged Ca^{2+} ion, indicating the role of more subtle factors such as ionic radius, electronegativity, bond lengths and so on in determining the glass structure.

With regard to Fe^{3+} and Ti^{4+}, the same broad trends as those mentioned for Na^+ and Ca^{2+} release are applicable. It is worth noting that the titanium release can be further modulated by the incorporation of additional metal oxides. The incorporation of SrO or ZnO in titanium phosphate glasses at the expense of CaO to form five-component P_2O_5–CaO–Na_2O–TiO_2–SrO or P_2O_5–CaO–Na_2O–TiO_2–ZnO glasses

leads to an increase in titanium ion release with the SrO or ZnO content, respectively (Abou Neel et al., 2009c, Lakhkar et al., 2010, Lakhkar et al., 2009). For instance, Lakhkar et al. investigated the degradation behaviour of $0.5P_2O_5$–$0.17Na_2O$–$0.03TiO_2$–$(0.3 - x)CaO$–$xSrO$ where x = 0, 0.01, 0.03 and 0.05 mole fraction They found that the addition of just 1 mol% SrO increased the cumulative titanium release rate by one order of magnitude from 0.0053 $ppm.h^{-1}$ for the 0 mol% SrO glass to 0.0617 $ppm.h^{-1}$ for the 1 mol% SrO glass (Lakhkar et al., 2009). Clearly the addition of SrO or ZnO disrupts the stability of the quaternary P_2O_5–CaO–Na_2O–TiO_2 glass network and causes the glass properties to more closely resemble those of ternary P_2O_5–CaO–Na_2O glasses.

At this point, it should be noted that while the present study focuses only on iron and titanium phosphate glasses of the metaphosphate type, with a constant P_2O_5 content of 50 mol% maintained throughout all the investigated glass compositions, ultraphosphate glasses with P_2O_5 content of less than 50 mol% have also been extensively studied as biomaterials for similar biomedical applications. For instance, studies on ternary P_2O_5–CaO–Na_2O glasses containing 45 mol% P_2O_5 revealed the biocompatibility of these glasses by the formation of brushite precipitates (a precursor to apatite formation), although extracts from only the less soluble glasses with higher CaO contents were found to beneficially impact MG63 and human osteoblast cell growth and antigen expression (Franks et al., 2000, Salih et al., 2000). Further investigations were carried out on the glass structure and physicochemical properties of discs and fibres made from three series of ternary P_2O_5–CaO–Na_2O glasses having P_2O_5 contents of 45, 50 and 55 mol% (Ahmed et al., 2004b, Ahmed et al., 2004c). In the 45 mol% P_2O_5 glasses, NMR studies revealed the predominance of Q^1 and Q^2 species in the glass structure as expected, while XRD studies revealed the existence of $Na_4Ca(PO_3)_6$ and CaP_2O_6 as the main phase at lower and higher CaO contents respectively. The non-linear nature of the solubility and thermal data at higher CaO contents was considered to be influenced by the glass packing density of the 45 mol% P_2O_5 glasses. However, it was not possible to produce fibres from the 45 mol% P_2O_5 glasses, with the low values of glass cross-link density, network connectivity and chain length being considered the likely reasons.

With regard to titanium phosphate glasses, several studies have examined the glass structure, physicochemical properties and biocompatibility of titanium pyrophosphate glass compositions. One of the first such studies was carried out by

Navarro et al. who investigated the physicochemical, mechanical and structural characteristics of $0.445P_2O_5$–$0.445CaO$–$(0.11 – x)Na_2O$–$xTiO_2$ glasses where x = 0.00, 0.03, 0.05 and 0.08 mole fraction when subjected to degradation in simulated biological fluid (Navarro et al., 2003a). In general, an increase in chemical durability and elastic modulus was observed as the TiO_2 content of the glass was increased. The structural changes brought about by the incorporation of titanium ions in the phosphate glass network were considered to be responsible for these modifications in the glass properties. Raman spectra revealed the presence of increasing numbers of TiO_5 and TiO_6 units in the glass structure with an increase in the TiO_2 content, with consequent formation of Ti–O–P cross-links in the glass structure which served to strengthen the glass network. Similar results were obtained in studies on glass systems such as $0.45P_2O_5$–$0.24CaO$–$(0.31 – x)Na_2O$–$xTiO_2$ where x = 0.00–0.25 and $0.47P_2O_5$–$0.305CaO$–$(0.225 – x)Na_2O$–$xTiO_2$ where x = 0.00–0.025 (Rajendran et al., 2007, Devi et al., 2010). In a study by Navarro et al. (Navarro et al., 2003b), the cellular responses to titanium pyrophosphate glasses was shown to be dependent on the glass solubility characteristics, although interestingly it was also noted that the testing procedure used (culturing with glass extracts versus direct culture on glass surfaces) may be in itself an influencing factor. To elaborate, cell behaviour during direct culture on glass surfaces is determined by substratum properties such as surface morphology, free energy and charge; however, these factors are absent when cells are cultured with glass extracts. Also it should be considered that in direct culture on glass surfaces, the local conditions can undergo significant local variations from the surface, where ions diffuse into the liquid medium, to the bulk medium itself. In contrast, cells cultured in extracts are exposed to a more homogeneous environment with more uniform ionic concentrations. The authors inferred that these circumstances would have played a role in the somewhat contradictory nature of the cell culture results, whereby a glass with higher solubility showed greater toxicity to the cells under direct culture but no toxicity under glass extract culture.

Recent research in ultraphosphate glass compositions has begun to focus on glasses containing 40 mol% P_2O_5 since it is considered that these glasses may provide further improved control over the glass dissolution and biocompatibility characteristics. For instance, Haque et al. studied the physicochemical, mechanical and thermal properties of $40P_2O_5$–$24MgO$–$16CaO$–$16Na_2O$–$4Fe_2O_3$ phosphate glass fibres (Haque et al., 2013a). Mechanical testing of the fibres when subjected to environmental aging over a 6 month period revealed the durability of the fibres.

The degradation rate of the glass fibres was measured over a 12 week period when the fibres were immersed in deionised water with pH adjusted to around 7.4 at 37°C. The degradation rate was determined to be 4.9×10^{-8} g.cm^{-2}.min^{-1} for the first 72 hours of the experiment, after which it reduced to 4.5×10^{-9} g.cm^{-2}.min^{-1} at 6 weeks and then finally decreased to 8.0×10^{-10} g.cm^{-2}.min^{-1} from 8 until 12 weeks. The surface morphology of the degraded glass fibres revealed the scatter of flaws on the fibre surface over the 12 week study period, with a thin hydrated layer on the fibre surface undergoing degradation without degradation of the remaining fibre bulk. The degradation rate of these glasses was found to be lower than that of the quaternary ultraphosphate glass $40P_2O_5$–$24MgO$–$16CaO$–$20Na_2O$ (Cozien-Cazuc et al., 2008, Cozien-Cazuc et al., 2009); thus, the addition of Fe_2O_3 was found to be a major factor that influenced the decrease in the fibre dissolution rate.

1.9. Phosphate glass biocompatibility

In studies on the biocompatibility of phosphate glasses in general and titanium/iron phosphate glasses in particular, most researchers have used one or more of the following three approaches: (a) *in vitro* evaluation following immersion in artificially prepared fluids such as citric acid, Tris buffer, Tris-HCL or simulated biological fluid (SBF); (b) *in vitro* cell culture and subsequent assays to estimate cell viability, adhesion, proliferation, differentiation and toxicity as well as gene expression; and (c) *in vivo* implantation in various animal models and subsequent histological studies.

The first approach is by far the most commonly used, especially in titanium phosphate glasses. In particular, SBF—a mixture of Na^+, K^+, Mg^{2+}, Ca^{2+}, Cl^-, HCO^{3-}, HPO_4^{2-}, and SO_4^{2-} ions in ion-exchanged and distilled water at concentrations approximately equal to those in human plasma—affords the easy initial evaluation of bioactivity via qualitative and quantitative assessment of apatite formation on the material surface in contact with the fluid. Kasuga et al. investigated SBF-induced apatite formation on the surface of phosphate glasses doped with TiO_2; their investigated $0.6CaO$–$0.3P_2O_5$–$0.07Na_2O$–$0.03TiO_2$ glass showed evidence of a calcium phosphate phase on the surface at 2–4 weeks post immersion, whereas a simultaneously studied $0.6CaO$–$0.3P_2O_5$–$0.07Na_2O$–$0.03MgO$ glass did not, thereby implying the relatively superior bioactivity of the TiO_2-containing glass and the underlying link between the chemical composition of the glass and the observed biological properties (Kasuga et al., 1999). Another study reported apatite formation for $0.47P_2O_5$–$0.305CaO$–$(0.225 - x)Na_2O$–$xTiO_2$ (x = 0–0.025 mol%) (Devi et al.,

2010). On the other hand, several studies reported the absence of an apatite layer following SBF immersion. For instance, Abou Neel et al. observed that none of the four compositions $0.5P_2O_5$–$(0.2 – x)Na_2O$–$0.3CaO$–$xTiO_2$ (x = 0–0.05 mol fraction) formed an apatite layer following incubation in SBF for 14 days at 37°C (Abou Neel et al., 2007a). A similar lack of apatite layer formation was observed in the case of $0.45P_2O_5$–$0.24CaO$–$(0.31 – x)Na_2O$–$xTiO_2$ (x = 0–0.025 mol fraction) (ElBatal et al., 2009) and $xTiO_2$–$(1 – x)[CaO.P_2O_5]$ (x = 0.005 and 0.01 mol fraction) (Lucacel et al., 2010). It should be noted that the lack of apatite formation for a particular glass composition upon SBF immersion need not be strictly indicative of a lack of bioactivity; indeed, some materials can directly bond with bone tissue without apatite formation (Kokubo and Takadama, 2006, Lee et al., 2006). It is possible that any layer formed on the glass surface under SBF immersion is a hydrated layer formed as a result of the glass degradation process as opposed to a precipitate layer arising from the solution. Thus, although SBF immersion studies have been used a means to confirm that a material is bioactive, further cell culture studies are generally required to gain a better understanding of material biocompatibility.

In vitro cell culture studies represent the logical next step in understanding material biocompatibility since they provide valuable qualitative and quantitative data regarding the ability of cells to adhere and proliferate on the material surface. In iron phosphate glass biocompatibility studies, Ahmed et al. investigated the culture of H-2KbtsA58 murine muscle cells on fibres made of P_2O_5–Na_2O–CaO-Fe_2O_3 glasses of various compositions (Ahmed et al., 2004a). It was found that fibres made of glasses containing 4–5 mol% Fe_2O_3 showed good cell adhesion and cell differentiation through formation of myotubes along the axis of the fibres. Another *in vitro* study on P_2O_5–Na_2O–CaO-Fe_2O_3 fibres using primary human osteoblasts and fibroblasts showed that fibres made of glasses containing 3 mol% Fe_2O_3 showed a well spread cell morphology and considerable proliferation over a 21 day study period, as evidenced by fluorescent immunolabeling studies, as well as committed cell differentiation by both cell types, as revealed in the results of real-time quantitative polymerase chain reaction (rtQ-PCR) analysis (Bitar et al., 2005). In both cases, the reduced solubility of fibres containing higher Fe_2O_3 contents was cited as a major factor underpinning the favourable biocompatibility of the fibres.

With regard to titanium phosphate glasses, Del Valle and co-workers cultured MC3T3-E1 preosteoblast cells on P_2O_5–CaO–Na_2O–TiO_2 glasses and investigated their growth and differentiation at the cell–material interface over a 37 day period;

the DNA, RNA, and total protein concentrations were indicative of normal proliferation and differentiation rates (Del Valle et al., 2003). In a more comprehensive study, Navarro et al. used human skin fibroblasts to study cell toxicity, adhesion and proliferation for glasses with the composition $0.445P_2O_5$–$0.445CaO$–$(0.11 - x)Na_2O$–TiO_2 (x = 0 and 0.05 mol fraction) (Navarro et al., 2003a). For each composition, a WST toxicity assay was carried out using cells cultured both on glass discs and in glass extract solutions over a 48 hour period, while ELISA adhesion and proliferation tests were carried out on glass discs over a 96 hour period. The toxicity test results revealed that a significantly greater effect was exerted by the glass discs than by the glass extracts; in addition, the less soluble 5 mol% TiO_2 glass showed greater cell viability. On the other hand, the more soluble 0 mol% TiO_2 glass showed greater cell adhesion and proliferation. The reasons for these apparently contradictory results were not entirely clear, but the authors indicated that the results were linked to the glass composition and solubility.

More clear-cut results were obtained by Dias et al. and Brauer et al. who concluded that TiO_2-containing glasses with lesser solubility were more favourable from a biocompatibility viewpoint on account of their greater levels of cell adhesion, growth and proliferation (Dias et al., 2005, Brauer et al., 2006). In addition, Brauer et al. studied the effect of porosity on cell adhesion, using an MTT assay to investigate the proliferation of MC3T3-E1.4 murine preosteoblasts on P_2O_5–CaO–Na_2O–MgO–X (X = TiO_2 or SiO_2) glasses over a 72 hour period. For the investigated compositions, the cell proliferation rates of nonporous specimens were comparable, whereas those of the porous specimens showed significant variations depending on the glass composition. In general, the sample topography and roughness of the porous specimens played a major role in initially inhibiting cell proliferation up to about 24 hours, although by 72 hours, extensive cell growth had occurred on both porous and nonporous specimens.

The present authors' research division at UCL Eastman Dental Institute has carried out a series of studies on the biocompatibility of TiO_2-doped phosphate glasses using *in vitro* cell culture approaches. Initial investigations focused on glasses of the composition $0.5P_2O_5$–$(0.2 - x)Na_2O$–$0.3CaO$–$xTiO_2$ (x = 0.00, 0.01, 0.03 and 0.05 mol fraction) (Abou Neel and Knowles, 2008). MG63 human osteosarcoma cells were cultured on the surfaces of glass discs of each composition over a 7 day period, with confocal microscopy and scanning electron microscopy (SEM) being used to assess cell viability and cell attachment, respectively. It was observed that

the glasses doped with 3 and 5 mol% TiO_2 were considerably favourable from both viability and attachment perspectives in comparison with the TiO_2-free glass; the authors attributed this increased biocompatibility to the lower degradation rate of the 3 and 5 mol% TiO_2 glasses and also correlated the similar cell responses of the two glasses with their structural similarities as evidenced by their DTA profiles. In another study, the authors attempted to further improve the biocompatibility by increasing the TiO_2 content to 15 mol% (Abou Neel et al., 2008a). As in the previous study, the TiO_2-containing glasses—especially at concentrations of 3 mol% or higher—showed enhanced biocompatibility in comparison with the TiO_2-free glass. The study does not contain quantitative data regarding the effect of increasing the TiO_2 content from 5 mol% to 15 mol% on the glass biocompatibility; however, it was observed that the glasses containing 10 mol% and 15 mol% TiO_2 did not elicit a significantly enhanced cell response in comparison with the glass containing 5 mol% TiO_2.

The $0.5P_2O_5$–$(0.2 - x)Na_2O$–$0.3CaO$–$xTiO_2$ (x = 0.00–0.05 mol fraction) glasses were then subjected to more detailed quantitative *in vitro* analyses, with cell proliferation and gene expression levels being studied over a 14 day period by means of an Alamar Blue assay and rtQ-PCR experiments, respectively (Abou Neel et al., 2007a). The 3 and 5 mol% TiO_2 glasses revealed significant upregulation of COLIA1, alkaline phosphatase, osteonectin and Cbfa-1 gene expression, thereby confirming their favourable properties with regard to cell proliferation and differentiation. Subsequent studies have focussed on incorporating additional metal oxides with proven antimicrobial properties such as ZnO and SrO into the quaternary P_2O_5–Na_2O–CaO–TiO_2 glasses, with interesting results obtained with regard to the structural characteristics, degradation behaviour and biocompatibility of the resulting five-component glasses (Abou Neel et al., 2009c, Lakhkar et al., 2009, Lakhkar et al., 2010).

In comparison with the above *in vitro* approaches, the *in vivo* implantation approach has been the subject of relatively fewer studies, which is to be expected in the context of challenges with regulatory and ethical approvals. Either rat models or rabbit models have been used, with the defect site being filled with glass granules of predefined size, and histological samples have been viewed using light microscopy or polarized microscopy following implantation timelines in the range of 5–12 weeks. Implantation of $0.45CaO$–$0.45P_2O_5$–$0.05MgO$–$0.05K_2O$ and $0.45CaO$–$0.37P_2O_5$–$0.05MgO$–$0.13TiO_2$ glass granules in rabbit tibiae revealed a considerable effect of

glass solubility on *in vivo* glass behaviour, with the former glass being degraded to a much greater extent than the latter (Dias et al., 2006). Furthermore, while granules of the latter glass were fully surrounded by new bone tissue, those of the former showed some empty spaces. A combination of solution-mediated and cell-mediated processes was suggested to be the driving force behind *in vivo* glass degradation. In another study involving implantation of P_2O_5–Na_2O–CaO–TiO_2 glasses of various compositions in rabbit models, it was revealed that incorporation of 0.5 mol% TiO_2 in the glass yielded optimal results in terms of bone cell growth whereas higher TiO_2 concentrations were associated with decreased bioactivity (Monem et al., 2008). Abou Neel et al. implanted particles of four different compositions into defects drilled in the calvarium of male rats (Abou Neel et al., 2007a). They found that bone tissue formation was significant only for the glass with the highest TiO_2 content i.e. 5 mol%.

Thus, a considerable number of *in vitro* and some *in vivo* studies encompassing various approaches have been conducted on iron and titanium phosphate glasses. From an overall perspective, the results of these studies clearly indicate the biocompatible nature of the glasses and also suggest a significant link between the glass composition, degradation behaviour and biocompatibility. In comparison with glasses of other compositions, those containing TiO_2 have largely been found to degrade much more slowly both in simulated *in vitro* environments and in *in vivo* physiologic animal models; this makes the glasses more favourable from the viewpoints of cell attachment, growth, proliferation, and differentiation. These favourable results have now provided the impetus for researchers to conduct further studies focusing on the development of medical applications of phosphate glasses.

1.10. Research hypothesis

On the basis of the literature review carried out thus far, the following hypotheses have been proposed for the present research:

1. Phosphate glass microspheres of different compositions, i.e. containing different metal oxide contents, can be manufactured by using a process that is inexpensive, rapid and industrially scalable.
2. The developed microspheres have physicochemical properties that vary consistently with the glass composition, or in particular, the metal oxide content.
3. The physicochemical properties of the microspheres are strongly linked to the glass structure, which can be studied by means of commonly used as

well as state-of-the-art techniques that provide information about glass network bonding features, phase transitions and ionic local environments.

4. The developed microspheres elicit favourable responses from bone cells as well as human mesenchymal stem cells and as such can be proposed as carriers for bone tissue engineering.

It is anticipated that the results of the studies conducted to verify these hypotheses will provide the reader with an in-depth perspective of the strong links between the microsphere properties, glass structure and cell–microsphere interactions.

Chapter 2. Glass/microsphere physicochemical properties

2.1. Introduction

The initial objectives of the research were to investigate the production of glass microspheres of different compositions by flame spheroidisation. A total of eight glass compositions comprising three different glass series were prepared: (a) a ternary P_2O_5–CaO–Na_2O glass, (b) three P_2O_5–CaO–Na_2O–Fe_2O_3 iron phosphate glasses and (c) four P_2O_5–CaO–Na_2O–TiO_2 titanium phosphate glasses. Emphasis was laid on the development of a flame spheroidisation apparatus that was easily reproducible, relied on inexpensive components, produced microspheres at high rates and with high yields (ratio of microspheres to nonspheroidised particles post spheroidisation), and could be appropriately scaled up for industrial production. The effect of glass composition on microsphere size was studied and the parameters required for optimum microsphere yield were empirically obtained. After the microspheres were produced, the properties of the microspheres such as the microsphere density and glass transition temperature were investigated. The degradation behaviour of the microspheres when immersed in deionised water was studied in detail using conventional weight loss models as well as a novel time lapse imaging technique. Ion release profiles for anionic phosphate species, cationic species such as Na^+ and Ca^{2+} and transition metal ions such as Fe^{3+} and Ti^{4+} were obtained using ion chromatography and inductively coupled plasma–mass spectroscopy (ICP-MS) techniques. The effects of metal oxide addition in general on the glass properties were highlighted, as were the differential effects of Fe_2O_3 addition vis-à-vis TiO_2 addition, and the morphological effects on the microsphere properties were examined by comparing the microsphere properties with previously reported properties of glass discs and glass fibres having similar compositions.

2.2. Materials and methods

2.2.1. Materials for glass production

The following precursors were used without further purification in the production of both Fe- and Ti-doped phosphate glasses: phosphorus pentoxide (P_2O_5), calcium carbonate ($CaCO_3$) and sodium dihydrogen orthophosphate (NaH_2PO_4). Iron(III) oxide (Fe_2O_3) was used in the Fe-doped glasses while titanium(IV) oxide (TiO_2) was used in the Ti-doped glasses. All the precursors had purities of >98% and were obtained from VWR-BDH, Poole, UK.

2.2.2. Precursor amount calculations

Three iron-containing glasses (P_2O_5–CaO–Na_2O–Fe_2O_3) and four titanium-containing glasses (P_2O_5–CaO–Na_2O–TiO_2) were prepared along with one ternary glass (P_2O_5–CaO–Na_2O) free of metal ions. The glass codes and molar compositions are listed in Table 2.1.

Table 2.1. Glass compositions, codes and melting temperatures (MT, °C) and times (t, h) used.

Glass series	Glass code	Glass composition (mol%)					MT/*t* (°C/h)
		P_2O_5	CaO	Na_2O	Fe_2O_3	TiO_2	
Ternary phosphate glass	Fe0/Ti0	50	40	10	0	-	1100/1
Iron-doped phosphate glasses	Fe1	50	40	9	1	-	1100/1
	Fe3	50	40	7	3	-	1100/1
	Fe5	50	40	5	5	-	1100/1
Titanium-doped phosphate glasses	Ti1	50	40	9	-	1	1300/3
	Ti3	50	40	7	-	3	1300/3
	Ti5	50	40	5	-	5	1300/3
	Ti7	50	40	3	-	7	1400/5

The amounts of precursors used to manufacture the glasses were calculated as follows, using the Fe1 and Ti1 glasses as examples (P_2O_5 = 50 mol%; CaO = 40 mol%; Na_2O = 9 mol%; Fe_2O_3/TiO_2 = 1 mol%).

A. Sodium dihydrogen orthophosphate (NaH_2PO_4)

	$2NaH_2PO_4$	→	Na_2O	+	P_2O_5	+	$2H_2O$
Mol. wt. ($g.mol^{-1}$)	240		62		142		36
Relative mol. wt. ($g.mol^{-1}$)			0.26		0.59		0.15

Here, amount of NaH_2PO_4 to be added in order to obtain 9 mol% Na_2O
= [(mol. fraction of Na_2O) × (mol. wt. of Na_2O)]/(relative mol. wt. of Na_2O)

= (0.09 × 62)/(0.26) = **21.46 g**

B. Phosphorus pentoxide (P_2O_5)

Amount of P_2O_5 produced in the above reaction

= (amount of NaH_2PO_4 required) × (relative mol. wt. of P_2O_5)

= 21.46 × 0.59 = 12.66 g

Amount of P_2O_5 required to produce 50 mol% P_2O_5

= 0.50 × 142 = 71.00 g

Therefore, actual amount of P_2O_5 to be added

= 71.00 – 12.66 = **58.34 g**

C. Calcium carbonate ($CaCO_3$)

	$CaCO_3$	→	CaO	+	CO_2
Mol. wt. ($g.mol^{-1}$)	100		56		44
Relative mol. wt. ($g.mol^{-1}$)			0.56		0.44

Amount of $CaCO_3$ to be added in order to obtain 40 mol% CaO

= (0.4 × 56)/0.56 = **40.00 g**

D. Titanium(IV) dioxide (TiO_2) or iron(III) oxide (Fe_2O_3)

Mol. wt. of TiO_2 = 47.90 + (2 × 16) = 79.9

Mol. wt. of Fe_2O_3 = (55.8 × 2) + (16 × 3) = 159.6

Amount of TiO_2 to be added in order to obtain 1 mol% TiO_2

= 0.01 × 79.9 = **0.80 g**

OR

Amount of Fe_2O_3 to be added in order to obtain 1 mol% Fe_2O_3

= 0.01 × 159.6 = **1.60 g**

The amounts of precursors required in the other compositions have been similarly calculated and are listed in Table 2.2.

Table 2.2. Amounts of precursors used (g) to prepare the investigated glasses.

Glass series	Glass code	Amounts of precursors used (g)				
		P_2O_5	CaO	NaH_2PO_4	Fe_2O_3	TiO_2
Ternary phosphate glass	Fe0/Ti0	56.85	26.67	24.00	-	-
Iron-doped phosphate glasses	Fe1	58.34	26.67	21.46	1.60	-
	Fe3	61.03	26.67	16.81	4.80	-
	Fe5	63.89	26.67	12.02	8.00	-
Titanium-doped phosphate glasses	Ti1	58.34	26.67	21.46	-	0.80
	Ti3	61.03	26.67	16.81	-	2.40
	Ti5	63.89	26.67	12.02	-	4.00
	Ti7	66.73	26.67	7.21	-	5.60

2.2.3. Preparation of glass microparticles

The required amounts of all precursors except P_2O_5 were weighed and then mixed in a Seward Stomacher®400 Circulator (Wolf Laboratories, York, UK) at 200 rpm for 1 minute. Because P_2O_5 is highly hygroscopic, care was taken to weigh the P_2O_5 precursor separately and add it quickly to the already mixed $CaCO_3$, NaH_2PO_4 and metal oxide precursors, followed by further mixing for 1 minute. The precursor mix was then poured into a Pt/10% Rh type 71040 crucible (Johnson Matthey, Royston, UK) and the crucible was placed in a Carbolite RHF 1500 furnace (Carbolite, Sheffield, UK) preheated at 700°C. The precursors were first heated at 700°C for 30 minutes to remove H_2O and CO_2 and then melted at the temperatures and times listed in Table 2.1. After melting for the required period, the glasses were rapidly quenched by pouring on to a steel plate at room temperature and then allowed to cool overnight. The glasses thus obtained were broken into fragments using a mortar and pestle and the fragments were further ground to form microparticles using a Retsch MM301 milling machine (Retsch, Germany). Whenever microparticles of particular size fractions were required, the microparticles were passed through sieves of appropriate mesh sizes (Endecotts Ltd., London, UK) on a Fritsch Spartan sieve shaker (Fritsch GmbH, Germany).

2.2.4. Design of flame spheroidisation apparatus

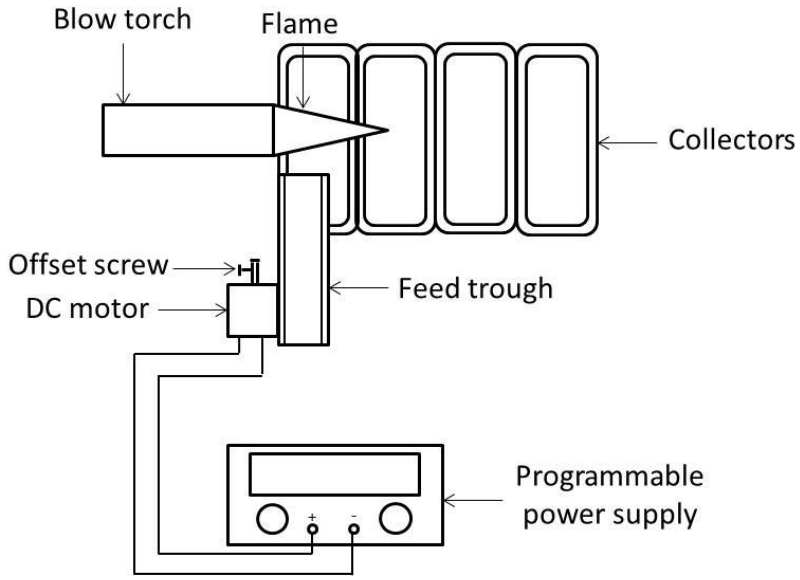

Figure 2.1. Schematic diagram of flame spheroidisation apparatus.

The flame spheroidisation apparatus comprised the following component assemblies: (1) blow torch, (2) feed and (3) collectors (see Figure 2.1). The blow torch assembly consisted of a Rothenberger Super Fire 2 gas torch (Rothenberger Werkzeuge GmbH, Kelkheim, Germany) fitted to a 453 g yellow MAP-PLUS gas cylinder (Today's Tools, UK). Both the gas torch and cylinder are widely available commercially. MAP-PLUS gas is a generic substitute for the trademarked MAPP gas (**m**ethyl**a**cetylene-**p**ropadiene **p**ropane) and can be used for heating, soldering, brazing and welding due to its high flame temperature of 2925°C in oxygen. The blow torch assembly was positioned in such a way that the flame of the gas torch was horizontal.

The feed assembly comprised an aluminium trough with dimensions of 200 × 20 × 30 mm, with the edge of the free end positioned approximately 10 mm above the outlet of torch at a slight angle to the horizontal. A DC motor (15800 rpm, 4.5–15V, 35.8 mm dia; RS components, Corby, UK) was attached to the other end of the trough and was connected to an ISO-TECH IPS-405 programmable power supply (RS Components, Corby, UK) by wires fitted with the required connectors (4 mm banana test plug connectors for the power supply and alligator test connectors for the motor). A metal screw connected to the axle of the motor served as an off set to generate vibration when the motor was in operation so that the particle feed for microsphere production was distributed over the surface of the trough before the

particles entered the flame. The output power from the programmable power supply was varied during operation in order to obtain optimum particle distribution in the trough.

The collectors consisted of four rectangular glass boxes with dimensions of 275 × 150 × 60 mm placed with their longer edges in contact with each other. The first collector was placed directly below the flame so as to collect particles that did not pass through the flame.

2.2.5. Preparation of glass microspheres

The glass microparticles thus produced (either with or without sieving) were then passed through the flame spheroidisation apparatus to produce microspheres in the approximate size range of 10–220 μm that fell into the collectors. During operation, as they passed into the flame, the microparticles travelled along the flame axis (or at varying angles to the flame axis) and underwent spheroidisation due to surface tension forces; the microspheres particles were then collected in the glass boxes placed one after the other below the flame. The microspheres from each collector were separately visualised by light microscopy. The material present in the collector immediately below the torch outlet was discarded since it usually contained a mixture of glass microspheres along with a significant proportion of non-spherical particles; the material in the remaining glass boxes contained very few non-spherical particles, if any, and was therefore collected and stored for further investigation.

2.2.6. Particle size distribution

For determining the particle size distribution of the obtained microspheres, glass fragments of approximately equal sizes with a combined weight of 2 g were crushed in the milling machine for 2 minutes at a frequency of 10 Hz. The crushed particles were then spheroidised in the flame spheroidisation assembly and the material from all four glass boxes was collected. A small quantity of the material was then added to a drop of Fractoil synthetic immersion oil (VWR, Poole, UK) placed on a microscope slide and the material was manually dispersed in the oil by means of a spatula. A cover slip was placed on top of the slide and the slides were then imaged on an Olympus BX50 microscope (Olympus Corporation, Japan) using a CoolSNAP-Pro cf camera (Photometrics, USA). Image analysis and microsphere diameter measurements were carried out using Image-Pro Plus version 5.0 software (Media Cybernetics, USA).

Based on the results of the particle size distribution experiments, microspheres in the size range 63–75 µm were used in subsequent experiments involving microspheres. These microspheres were obtained by passing the feed particles through 75 µm and 63 µm sieves (Endecotts Ltd., London, UK) on a Fritsch Spartan sieve shaker (Fritsch GmbH, Germany).

2.2.7. Density measurement

Density measurements were carried out on the basis of Archimedes' principle using triplicate samples of glass fragments. An analytical balance (Mettler Toledo, UK) with a density measurement kit was used for this purpose. Absolute ethanol was used instead of water as the immersion liquid since the glasses are water-soluble in nature. The following formula was used to calculate the glass density (ρ_{glass}):

$$\rho_{glass} = [M_{air}/(M_{air} - M_{ethanol})] \times \rho_{ethanol} \quad (1)$$

where M_{air} and $M_{ethanol}$ are the masses of the sample in air and ethanol (g), respectively, and $\rho_{ethanol}$ is the density of ethanol at ambient temperature ($g.cm^{-3}$).

2.2.8. Differential thermal analysis

Differential thermal analysis (DTA) studies were performed on glass microspheres using a Setaram differential thermal analyser (Setaram, France). Approximately 60 mg of glass microspheres was placed in a 10 µl platinum crucible which was then placed in the analyser. DTA experiments were carried out by heating the sample from room temperature to 1000°C at a heating rate of $20°C.minute^{-1}$ using air as the purge gas; an empty platinum crucible was used as a reference. The parameters measured in DTA were the glass transition temperature (T_g), crystallisation temperature (T_c) and melting temperature (T_m).

2.2.9. Short-term weight loss measurement by time lapse technique

Degradation studies on the glass microspheres over a time period of 80 hours were carried out using a novel time lapse imaging method. Approximately 100 mg of glass microspheres was added to a 25 cm^2 cell culture flask containing 10 ml of ultrapure high-purity deionised water (resistivity = 18.2 $M\Omega.cm^{-1}$) obtained from a PURELAB UHQ-PS (Elga Labwater, Marlow, UK). Prior to the addition of microspheres and water, the bottom inner surface of the flask had been scraped with a brush in order to provide surface roughness so that the microspheres would remain reasonably stationary during the experiment. Care was taken to wash the

flask 2-3 times with deionised water before adding the microspheres so as to wash away any debris generated by the scraping action. The flask was then placed on the stage of a Leica DMIRB microscope (Leica Microsystems CMS GmbH, Germany) fitted with a Solent Scientific incubator system (Solent Scientific Ltd., Segensworth, UK) that had been maintained at a temperature of 37°C. Time lapse images of the microspheres were acquired at intervals of 1 hour over an 80 hour period using a Tucsen TCA-10.0-N camera (Tucsen Image Technology Inc., China) running on µManager microscopy open source software (Ron Vale Lab, University of California–San Francisco, USA); subsequent image analysis and diameter measurements were carried out using ImageJ (National Institutes of Health, USA; a more detailed procedure for time lapse acquisition and image analysis is provided in Appendix A.1). For each glass composition, the diameters of six microspheres were measured and the mass of the microsphere was obtained by the following equation:

$$m_{sphere} = \rho_{glass} \times v_{sphere} = [\rho_{glass} \times 4\pi(r_{sphere})^3]/3 \quad (2)$$

where m_{sphere} is the mass of the microsphere (µg); ρ_{glass}, the density of the glass obtained from the previous density measurement (µg.µm^{-3}); v_{sphere}, the volume of the microsphere (µm^3); and r_{sphere}, the radius of the microsphere (µm).

The percentage weight loss per unit surface area of the microsphere at each time point was calculated by the following equation:

$$[(m_{sphere(0)} - m_{sphere(t)})/m_{sphere(0)}A_t] \times 100 \quad (3)$$

where $m_{sphere(0)}$ is the mass of the microsphere at time t = 0 (µg); $m_{sphere(t)}$, the mass of the microsphere at time t (µg); and A_t, the surface area of the microsphere at time t (µm^2).

2.2.10. Long-term weight loss measurement using conventional weight loss model

Degradation studies were carried out on the basis of a weight loss method in a simple aqueous model. Measurements were carried out in triplicate and a fresh batch of samples was prepared for each time point. The following time points were used for the iron phosphate glass microspheres (Fe-PGMs): 0, 25, 75, 170, 314 and 484 hours (corresponding to days 0, 1, 3, 7, 13 and 20). The time points used

for the titanium phosphate glass microspheres (Ti-PGMs) were 0, 22, 70, 163, 307 and 476 hours (corresponding to days 0, 1, 3, 7, 13 and 20). For each sample, approximately 100 mg of glass microspheres was weighed and then immersed in plastic containers holding 10 ml of high-purity deionised water (resistivity = 18.2 $M\Omega.cm^{-1}$) obtained from a PURELAB UHQ-PS (Elga Labwater, Marlow, UK). Prior to immersion, the pH of the deionised water had been adjusted to 7 ± 0.2 by means of NH_4OH and/or HCl. Immersion in deionised water was followed by incubation at 37 ± 1°C. At each time point, the solution was removed from the incubator, stored in Sterilin bottles and refrigerated for use in further analyses (pH and ion release measurements), and the microspheres were dried at 60°C for 1 day and then weighed. The collected data was plotted in the form of average percentage degradation as a function of time for microspheres of each investigated glass composition by using the following equation:

$$(m_0 - m_t)/m_0 \times 100 \quad (4)$$

where m_0 and m_t are the sample mass at time t = 0 (mg) and at time t (mg) respectively.

2.2.11. pH measurement

The pH of the solution obtained at each time point from the long-term weight loss experiment was measured using an Orion pH meter (Thermo Scientific, UK) fitted with a pH glass electrode. At all the time points, the pH meter was calibrated using colourkey standard solutions of pH 4, 7 and 10 (BDH, Poole) before use.

2.2.12. Ion release measurement

2.2.12.1. Anion release

The release of phosphate anions from the glass microspheres was analysed over a sample run time of 25 minutes using a Dionex ICS-2500 ion chromatography system (Dionex, Surrey, UK) incorporating a 25 µl injection loop within a gradient pump. The following phosphate ions were measured: orthophosphate (PO_4^{3-}), pyrophosphate ($P_2O_7^{4-}$), cyclic trimetaphosphate ($P_3O_9^{3-}$) and linear polyphosphate or ultraphosphate ($P_3O_{10}^{5-}$). Prior to performing the analysis at each time point, calibration of the ion chromatograph was carried out against a five-point calibration curve with the help of a predefined calibration program. The sample solutions were eluted without any pre-processing through a 4 × 250 mm Ion Pac® AS16 anion-exchange column packed with anion exchange resin. A Dionex Anion Self-

Regenerating Suppressor (ASRS®) was used at a current of 223 mA, in combination with a Dionex EG40 eluent generator equipped with a potassium hydroxide (KOH) cartridge; the eluent generator serves the purpose of eliminating baseline shifts caused by hydroxide gradients and providing enhanced retention time reproducibility. The KOH gradient program was configured so that the sample run time of 25 minutes was divided as follows: maintain at 30 mM KOH for 10 minutes, increase from 30 to 60 mM KOH for 12 minutes, maintain at 60 mM KOH for 1 minute, decrease from 60 to 30 mM KOH for 1 minute, maintain at 30 mM KOH for 1 minute. The Chromeleon® software package was used for data analysis. Note that it was necessary to dilute some of the samples 10-fold (especially at the later time points) so as to ensure that the measured phosphate ion release was within the measurement range of the instrument.

Standard solutions were prepared using sodium phosphate, trisodium trimetaphosphate, pentasodium tripolyphosphate (Sigma–Aldrich, Dorset, UK) and tetrasodium pyrophosphate (BDH, Poole, UK) as the reagents. A 100 ppm working solution containing all the four reagents was prepared and then serially diluted to 50, 25, 10 and 5 ppm standard solutions. Deionised water was used in both solution preparation and dilution.

2.2.12.2. Cation release

Na^+ and Ca^{2+} ion release measurements were performed on a Dionex ICS-1000 ion chromatography system (Dionex, Surrey, UK) using 30 mM methanesulphonic acid (Fluka, Dorset, UK) incorporating a 4 × 250 mm Ion Pac® CS12A separator column and a sample loop of 25 µl. Similar to the anion release measurements, the system was calibrated against a five-point calibration curve using a previously developed routine before carrying out the sample run for each time point. The separator column possesses high sensitivity to phosphate species; hence, the samples were pre-processed by passing them through a Dionex OnGuard IIA cartridge prior to injection through the column. As in the anion release measurements, the Chromeleon® software package was used for data analysis.

Sodium chloride (Sigma–Aldrich, Dorset, UK) and calcium chloride (BDH, Poole, UK) were used as reagents to prepare a 100 ppm stock solution containing both the reagents. The stock solution was serially diluted to produce 50, 25, 10 and 5 ppm standard solutions. As in the anion standards, deionised water was used to prepare the stock solution and to dilute it to form the standards.

2.2.12.3. Transition metal ion release

A Dionex ICS-2500 ion chromatography system (Dionex, UK) consisting of a 25 µl sample loop was used to measure the release of Fe^{3+} ions from the Fe-PGMs with a sample run time of 10 minutes. Elution of the post degradation media containing the released Fe^{3+} transition metal ions was performed using an IonPac® CS5A cation ion exchange column in combination with a CG5Aguard column, which is used for the determination of transition and lanthanide metals. The eluent concentrate employed was MetPac® PDCA (Dionex, UK), in which pyridine-2,6-dicarboxylic acid (PDCA) functions as a complexing agent for metal complex separation via anion exchange. The MetPac® PAR Post Column Reagent Diluent was added through a reaction coil as a diluent for 4-(2-pyridylazo) resorcinol (PAR). This diluent has a controlled pH and low metal contamination and reacts with a wide range of metals, allowing detection limits in the parts per billion (ppb) range. The Fe^{3+} concentration was measured by absorbance detection at 530 nm. Prior to carrying out sample measurements, the instrument was calibrated using iron(III) chloride (Sigma–Aldrich, UK) as a reagent. A 100 ppm stock solution was prepared and then serially diluted to 50, 25, 10 and 5 ppm using deionized water throughout.

2.2.12.4. Inductively coupled plasma–mass spectroscopy

Titanium Ti^{4+} ion release measurements were carried out using ICP-MS. A Spectromass 2000 ICP mass spectrometer (Spectro, Germany) with a minimum detection limit of 1–10 ppt was used for this purpose. Prior to conducting the measurements, the instrument was calibrated using TraceCERT® titanium standard for ICP (Fluka, UK) that had been diluted to a range of 10–1000 ppb in deionised water containing 2% HNO_3 (60% Ultrapur® for trace analysis); the Ti^{4+} concentration in the ultrapure water was set to 0 ppb. All the samples were prepared in a 2% HNO_3 acid matrix. Note that it was necessary to dilute most of the samples 100-fold so as to ensure that the measured titanium ion release was within the range of the instrument.

2.3. Results

2.3.1. Particle size distribution

Figure 2.2 shows the particle size distributions of the microspheres obtained for the investigated iron and titanium phosphate glass compositions. Glass microspheres were successfully obtained for all the investigated compositions over a size range of between approx. 7 µm and 214 µm for the ternary P_2O_5–CaO–Na_2O, between 10 µm and 200 µm for the iron phosphate glasses and between 9 µm and 195 µm for

the titanium phosphate glasses. For all the compositions, a minimum of 80% of microspheres had sizes of 120 μm or less. There was no significant difference between the particle size distributions for the different glass compositions in both the iron and titanium phosphate glasses; thus, the microsphere production process was independent of the glass composition.

The results obtained from the particle size distribution were further confirmed by light microscopy images of the microspheres obtained for particles of different size fractions. Taking the Ti7 microspheres as a representative example, it was observed that at particle sizes of 45–63 μm, very few microspheres were obtained (Figure 2.3). During the flame spheroidisation process, the feed particles tended to aggregate together on the feed trough and it was difficult to ensure adequate particle separation on the trough before the particles entered the flame; inside the flame, the particle aggregates tended to break up into the constituent particles without significant microsphere formation.

At particle sizes of 106–150 μm, a significant number of particles were too large and the particle residence time in the flame was too short for the particles to undergo spheroidisation; consequently, microsphere samples in this size range tended to contain large numbers of non-spherical particles. The proportion of non-spherical particles was minimal at particle sizes of 63–75 and 75–106 μm; therefore, a size range of 63–106 μm was considered to be the optimal particle size for microsphere production using the developed apparatus. In subsequent experiments, a particle size range of 63–75 μm was adopted for microsphere production so as to minimise the effect of microsphere size on the experimental results.

(a)

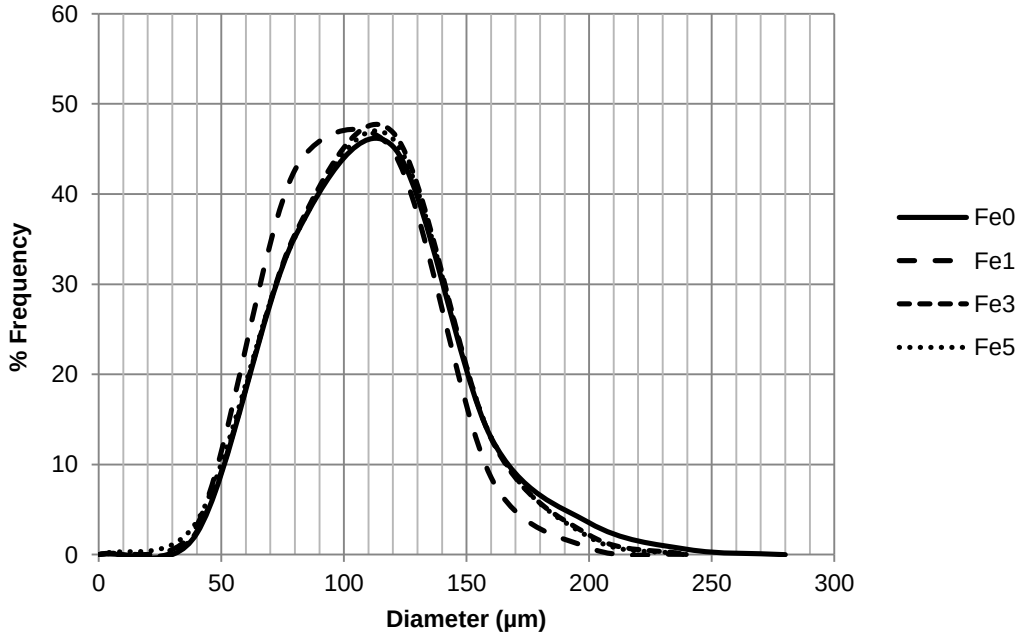

(b)

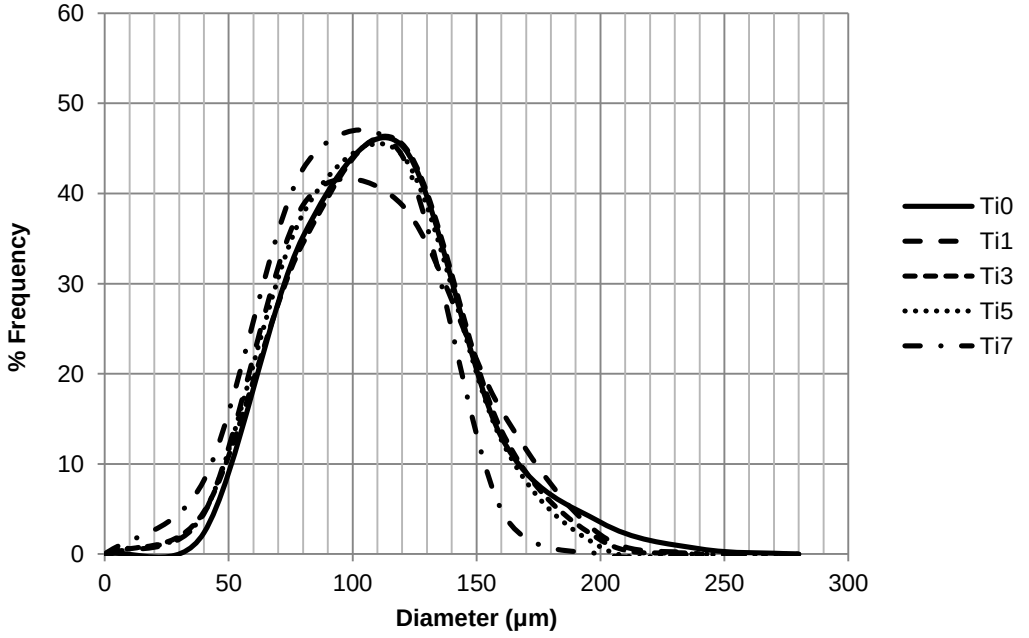

Figure 2.2. Particle size distribution of microspheres obtained from (a) iron-doped and (b) titanium-doped phosphate glass compositions. The microsphere diameters range from 7 µm to 214 µm with approx. 80% of the particles having diameters of 120 µm or less.

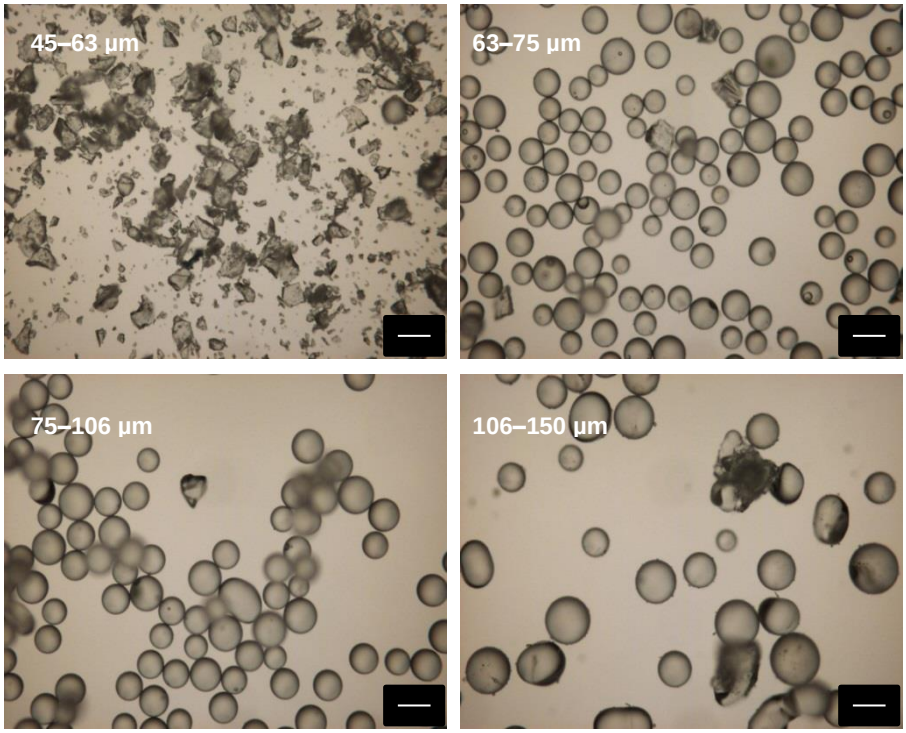

Figure 2.3. Light microscopy images of phosphate glass microspheres (Ti7 glass) for different size ranges (bar: 100 µm). Visual examination reveals the microsphere yield (proportion of glass particles that form microspheres) is maximum at microsphere diameters of 63–106 µm.

2.3.2. Density measurement

Figure 2.4 shows plots of the density of the investigated glass compositions as a function of the metal oxide content of the glasses. The glass density was observed to increase with the incorporation of metal oxide in the glass composition. In the Fe-PGMs, the glass density increased from 2.6290 ± 0.0007 g/cm^3 for the ternary Fe0/Ti0 glass to 2.6470 ± 0.0105 g/cm^3 for the Fe1 glass and subsequently to 2.7334 ± 0.0008 g/cm^3 for the Fe5 glass. Similarly the density values increased from 2.6290 ± 0.0007 g/cm^3 for the Fe0/Ti0 glass to 2.6318 ± 0.0010 g/cm^3 for the Ti1 glass and finally 2.6714 ± 0.0021 g/cm^3 for the Ti7 glass.

(a)

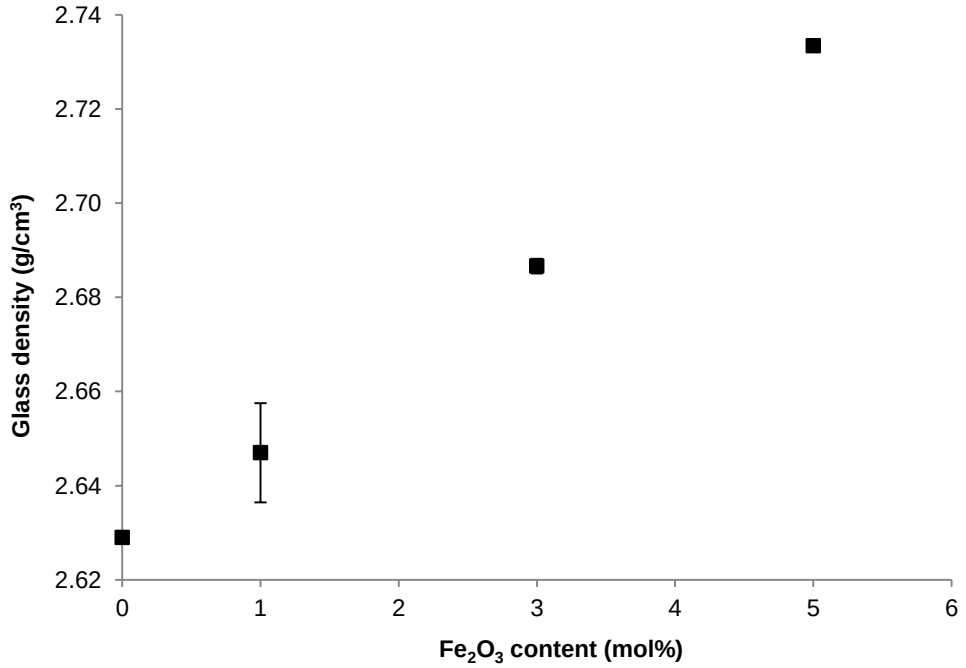

(b)

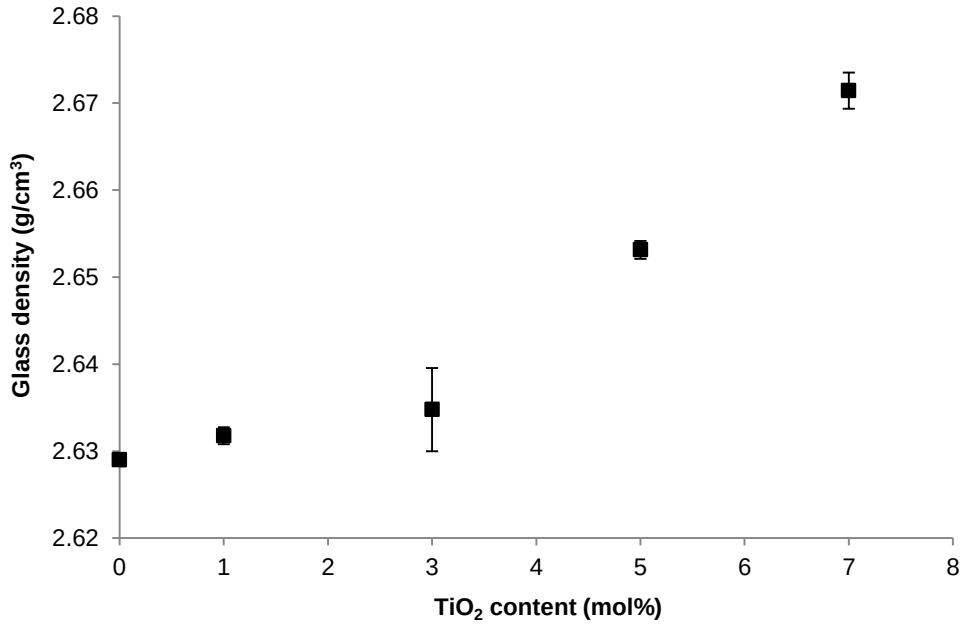

Figure 2.4. Glass density as a function of the (a) Fe_2O_3 content and (b) TiO_2 content for iron and titanium phosphate glass microspheres respectively. The glass density undergoes an increase with the metal oxide content of the glass.

2.3.3. Differential thermal analysis

Table 2.3 lists the T_g values of the investigated glass compositions. The addition of increasing amounts of metal oxides Fe_2O_3 or TiO_2 led to an appreciable increase in the T_g value of the glass from 452°C for the Fe0/Ti0 glass to 505°C for the Fe5 glass and 529°C for the Ti7 glass.

Table 2.3. Glass transition temperatures T_g (°C) for the investigated iron and titanium phosphate glass microspheres.

Glass code	Fe0/Ti0	Fe1	Fe3	Fe5	Ti1	Ti3	Ti5	Ti7
T_g (°C)	452	462	479	505	467	489	510	529

The DTA traces of the glass microspheres are shown in Figure 2.5. The DTA trace of the Fe0/Ti0 glass microspheres revealed a single sharp crystallisation peak at T_c = 593°C. In the Fe-PGMs, the incorporation of 1 and 3 mol% Fe_2O_3 in the glass led to an increase in the T_c value to 620 and 660°C, respectively. When the Fe_2O_3 content was increased further to 5 mol%, the single crystallisation peak was transformed into two peaks with T_{c1} and T_{c2} values of 675 and 726°C respectively. All four compositions showed the presence of two melting peaks with T_{m1} and T_{m2} values in ranges of 742–820°C and 808–862°C respectively. Although no discernible trend was noticeable in the T_{m1} values, the T_{m2} values increased with the Fe_2O_3 content.

The addition of 1 mol% TiO_2 to the Fe0/Ti0 glass gave rise to two broader crystallisation peaks at 620°C and 650°C that appeared to overlap with each other. Two broad overlapping peaks were also observed for the Ti5 glass at 720°C and 751°C, although the DTA trace of the Ti3 glass exhibited only a single large peak at 679°C and a significantly smaller peak adjacent to it; the same was true for the Ti7 glass which showed a large peak at 739°C with an adjacent smaller peak, thereby indicating a higher degree of overlap between the two crystallisation peaks in these compositions. Thus, there was an increase in the T_c values with the TiO_2 content of the glass. The Ti0 and Ti1 glasses showed two distinct melting peaks at similar T_m values (742°C and 808°C for Ti0; 739°C and 811°C for Ti1). However, the Ti3–7 glasses showed only single melting peaks at 878, 905 and 921°C respectively. Thus, an increase in the metal oxide content of the glass was generally associated

with an increase in the T_g, T_c and T_m values.

(a)

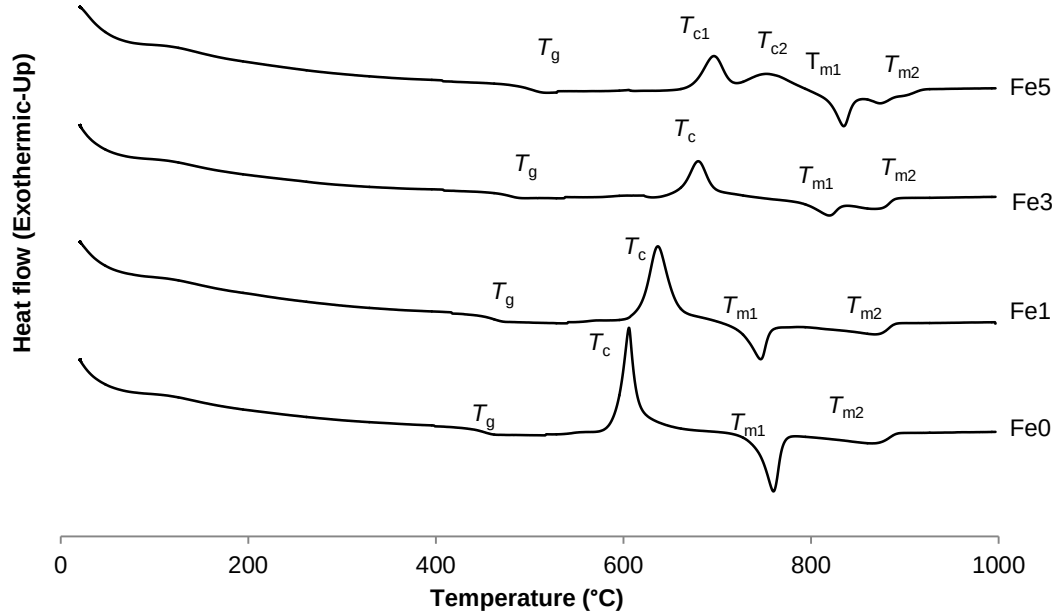

(b)

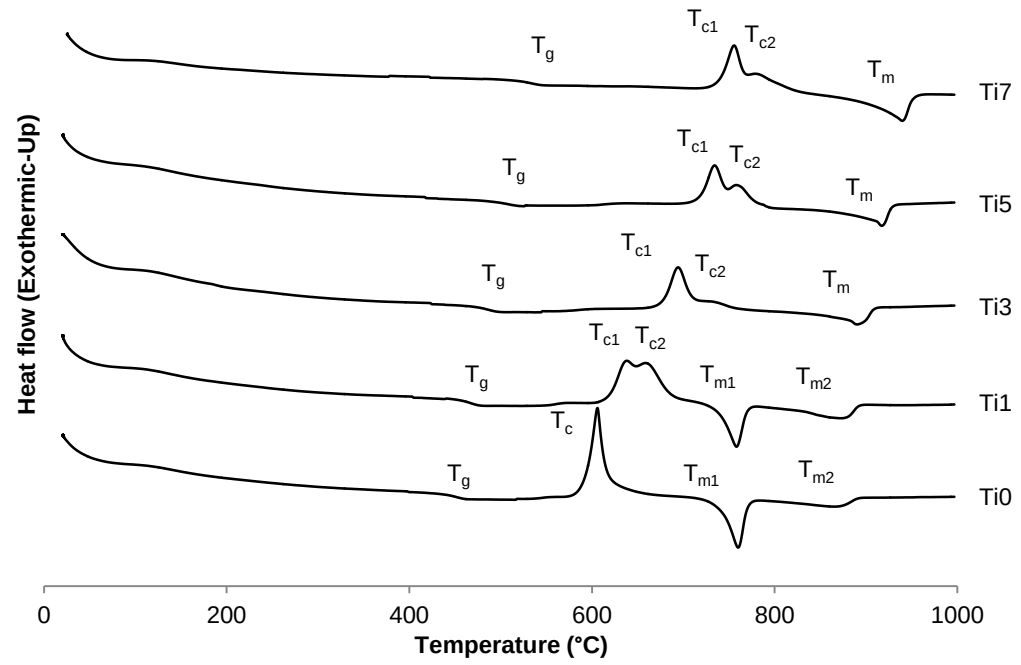

Figure 2.5. DTA traces of phosphate glass microspheres with different (a) Fe_2O_3 and (b) TiO_2 contents. An increase in the metal oxide content generally leads to an increase in the T_g, T_c and T_m values.

2.3.4. Short-term weight loss measurement by time lapse technique

Figures 2.6 and 2.7 show time lapse images acquired for the investigated Fe- and Ti-PGMs, respectively, from 0 to 60 hours at intervals of 20 hours. The images revealed that the Fe0/Ti0 ternary glass microspheres underwent degradation at a considerably more rapid rate than both Fe- and Ti-PGMs.
By t = 20 hours, a hydrated layer began to form on the outer surface of most of the microspheres and the microspheres continued to degrade inside this structure. As it degraded within the layer, each microsphere became increasingly irregular in shape and constantly changed its position inside the structure. In some cases, the hydrated layers of adjacent microspheres came in contact and fused together, with the microspheres continuing to degrade inside the newly formed larger layer. By t = 60 hours, almost all the microspheres had degraded completely, leaving behind only the transparent structures. Under these circumstances, it was not possible for the image analysis software to distinguish between the actual microsphere boundary and the outer boundary of the hydrated layer and measure the microsphere diameter.

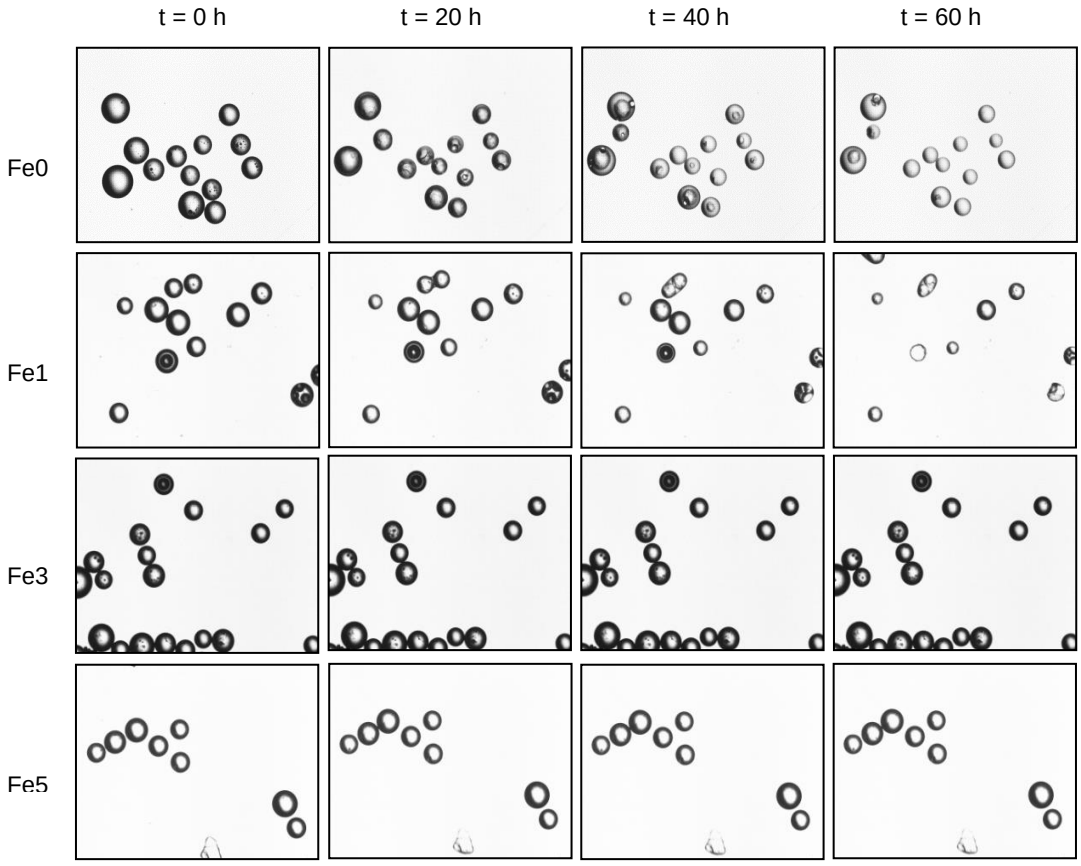

Figure 2.6. Time lapse acquisition images showing the degradation of Fe0, Fe1, Fe3 and Fe5 microspheres at 0, 20, 40 and 60 hours for each composition. The Fe0 microspheres degrade at much higher rates than the Fe1–5 microspheres.

The Fe1–5 and Ti1–7 microspheres degraded at a much slower rate than the Fe0/Ti0 microspheres. The Fe1 and Ti1 microspheres showed some evidence of transparent structure formation similar to the Fe0 microspheres; however, for most of the microspheres, the microsphere boundary could easily be identified by the software, which was then able to automatically measure the microsphere diameter. For the Fe3–5 and Ti3–7 microspheres, only minimal differences in microsphere size if at all could be discerned with the naked eye from one image to the next.

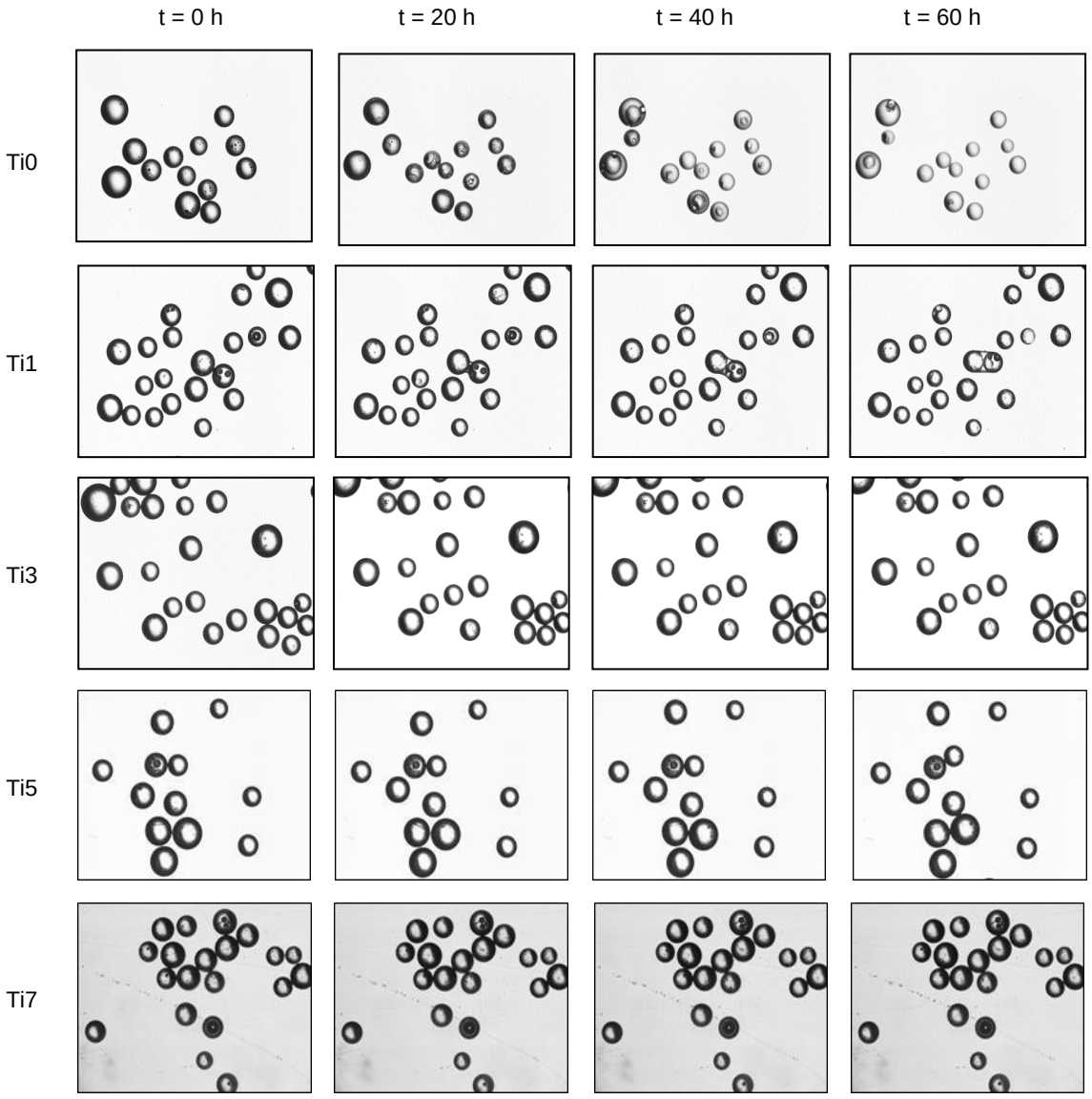

Figure 2.7. Time lapse acquisition images showing the degradation of Ti0, Ti1, Ti3, Ti5 and Ti7 microspheres at 0, 20, 40 and 60 hours for each composition. The Ti0 microspheres degrade at much higher rates than the Ti1–7 microspheres.

Figure 2.8 shows the percentage cumulative weight loss per unit surface area of the microspheres as a function of the degradation time for the investigated Fe- and Ti-PGMs. Note that for the reasons mentioned in the previous paragraph, it was not possible to plot the data for the Fe0/Ti0 microspheres over the 80 hour time scale used for the degradation study. Therefore, the degradation graphs contain data only for the metal oxide–containing glasses.

In both degradation plots, it was observed that the microspheres underwent increased degradation with time. A clear correlation between the metal oxide content and the degradation rate was observed, whereby as the metal oxide content increased, the glass microspheres degraded to a lesser extent. The slope of the linear fit of the degradation data against time provides the degradation rate of the glass (Table 2.4; note that the degradation rate values thus obtained are used only to rank the degradation behaviour of microspheres of different compositions and should not be considered as representative of linear degradation behaviour). As the Fe_2O_3 content was increased from 1 to 3 mol%, the degradation rate decreased considerably by a factor of 6 (i.e. 6-fold) from 105.9624×10^{-5} $\%.mm^{-2}.h^{-1}$ to 17.6671×10^{-5} $\%.mm^{-2}.h^{-1}$. However, increasing the Fe_2O_3 content from 3 to 5 mol% resulted in only a 1.45-fold decrease in the degradation rate to 12.1623×10^{-5} $\%.mm^{-2}.h^{-1}$. In the case of the Ti-PGMs, the corresponding decreases in the degradation rate from 1 to 3 to 5 to 7 mol% TiO_2 were 2.63-, 2.95- and 1.15-fold respectively. Thus, the trend in the short-term degradation rates for the Fe- and Ti-PGMs could be represented as follows: Fe0 >> Fe1 >> Fe3 > Fe5 and Ti0 >> Ti1 > Ti3 > Ti5 > Ti7. The error bars of the data points in the graph were reasonably small, indicating the reliability of the methodology.

(a)

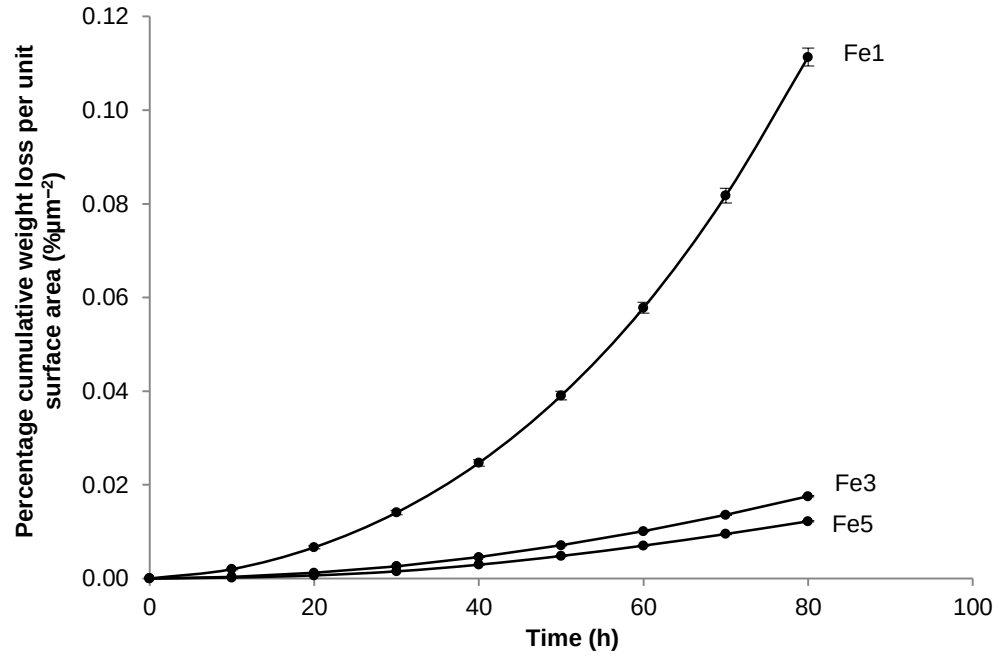

(b)

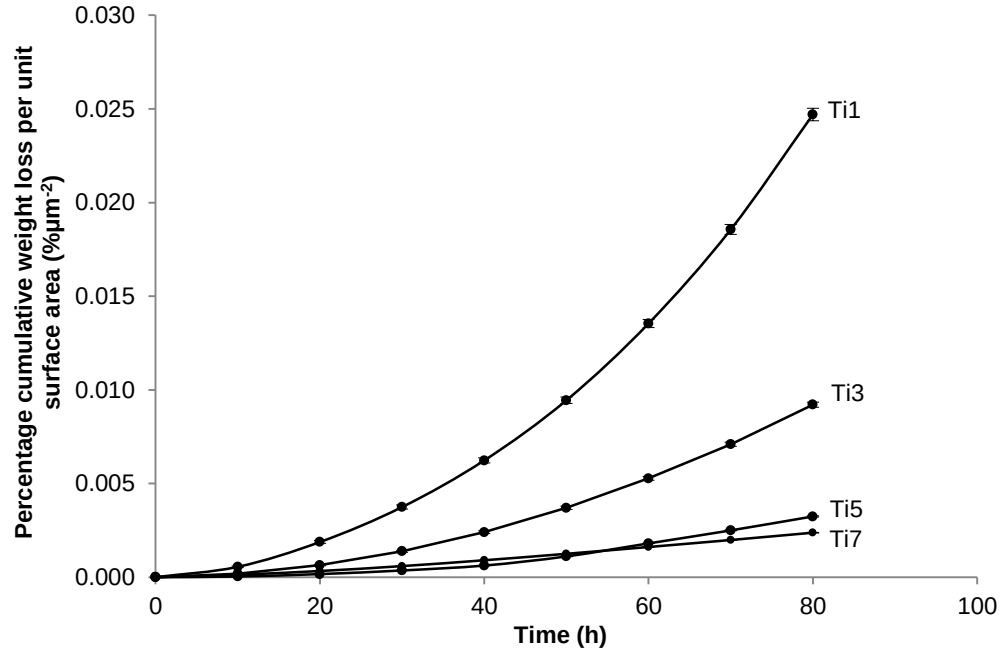

Figure 2.8. Short-term degradation of (a) iron and (b) titanium phosphate glass microspheres by the time lapse method. Data are presented as cumulative weight loss per unit surface area (%µm^{-2}) of microspheres as a function of time. The degradation rate of the microspheres is inversely proportional to the metal oxide content of the microspheres for both glass series.

Table 2.4. Short-term and long-term degradation rates (%.mm^{-2}.h^{-1} and %.h^{-1} respectively) and ion release rates (ppm.h^{-1}) of the investigated microspheres. These values are determined from the slopes of the linear fit between degradation or ion release values against time.

Glass code	Short term deg.* (%.mm^{-2}.h^{-1} × 10^{-5})	Long term deg. (%.h^{-1})	Anion (ppm.h^{-1})				Cation (ppm.h^{-1})		Fe^{3+} (ppm.h^{-1})	Ti^{4+} (ppm.h^{-1})
			PO_4^{3-}	$P_3O_9^{3-}$	$P_2O_7^{4-}$	$P_3O_{10}^{5-}$	Ca^{2+}	Na^{+}		
Fe1	105.9624	0.2366	8.2910	5.7921	2.1792	2.8005	0.3766	0.4496	0.2023	-
Fe3	17.6671	0.0933	8.2741	3.6601	1.3865	1.7466	0.1712	0.0881	0.1907	-
Fe5	12.1623	0.0458	2.2307	0.6135	0.2240	0.2719	0.1409	0.0458	0.1567	-
Ti1	24.3457	0.2314	5.8313	6.4382	1.7149	2.9705	0.0319	0.0936	-	0.1307
Ti3	9.2584	0.0842	1.5191	2.1129	0.4654	0.6874	0.0287	0.0393	-	0.1357
Ti5	3.1295	0.0204	0.2657	0.4301	0.0894	0.1667	0.0175	0.0097	-	0.0413
Ti7	2.7067	0.0162	0.1373	0.2348	0.0811	0.1424	0.0148	0.0052	-	0.038

***Note that all these rate values were used only to rank the degradation behaviour of microspheres of different compositions and are not representative of linear degradation behaviour. For this reason, trend lines have not been shown in the corresponding graphs.**

2.3.5. Long-term weight loss measurement using conventional weight loss model

Figure 2.9 shows the percentage weight loss of the microspheres as a function of the degradation time for the investigated Fe- and Ti-PGMs. Similar to the short-term degradation results, the microspheres underwent increased degradation with time, and an increase in the metal oxide content coincided with a decrease in the extent of degradation. With regard to the degradation rates (Table 2.4), it was observed that for the Fe-PGMs, the progressive increase in the Fe_2O_3 content from 1 to 3 to 5 mol% led to 2.53- and 2.04-fold decreases in the degradation rates; the corresponding values for the Ti-PGMs from 1 to 3 to 5 to 7 mol% TiO_2 were 2.75-, 4.13- and 1.26-fold, thereby implying that an increase in the TiO_2 content from 3 to 5 mol% resulted in a considerable decrease in the degradation rate, while the effect of the increase from 5 to 7 mol% was not as marked. Thus, the trend in the long-term degradation rates for the Fe- and Ti-PGMs could be represented as follows: Fe0 >> Fe1 > Fe3 > Fe5 and Ti0 >> Ti1 > Ti3 > Ti5 > Ti7. One interesting observation was the difference between the shapes of the curves obtained from the short- and long-term degradation studies, whereby the former appeared more exponential in nature while the latter appeared more plateau-shaped.

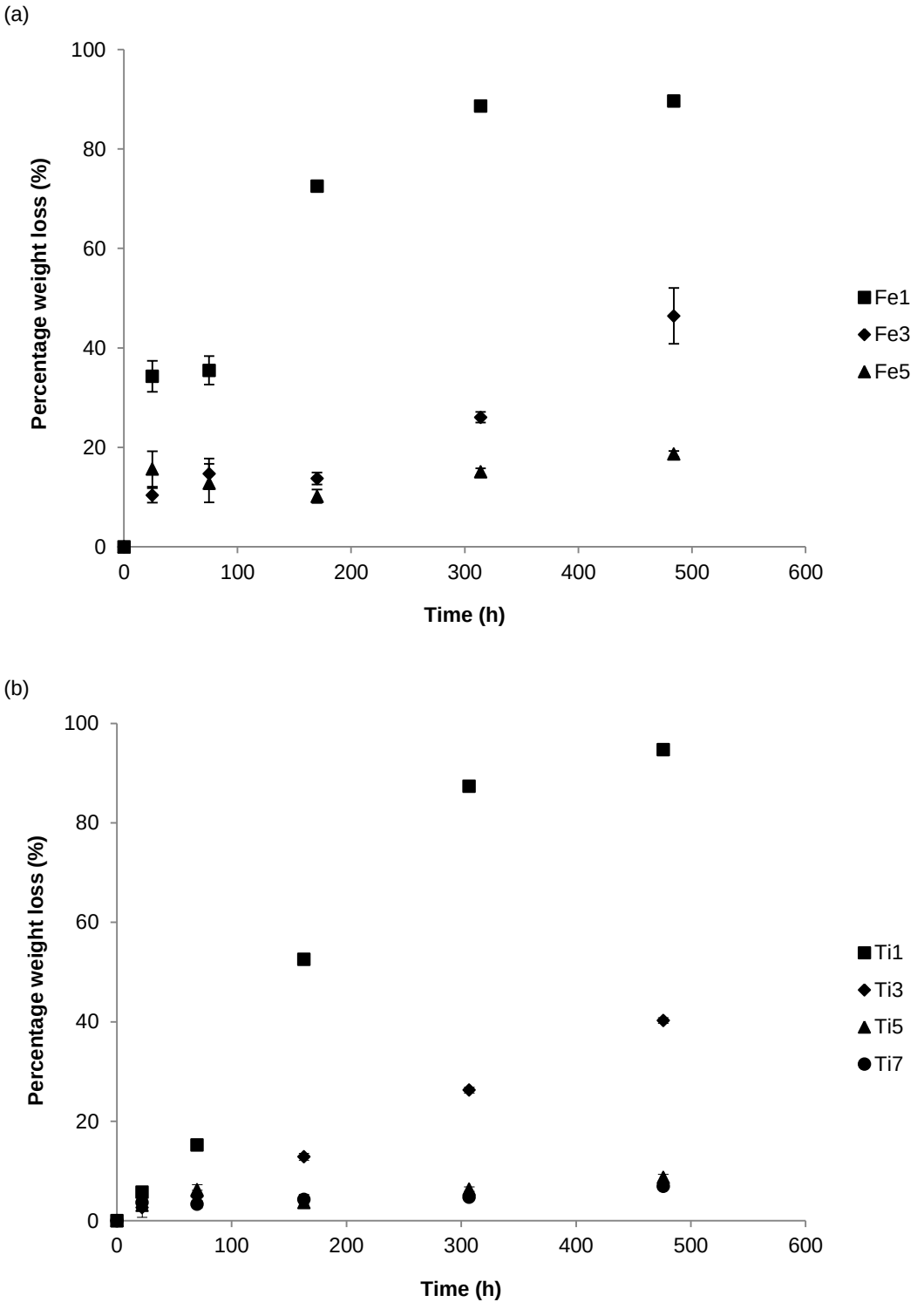

Figure 2.9. Long-term degradation of (a) iron and (b) titanium phosphate glass microspheres as determined by the conventional weight loss method. Data are presented as percentage weight loss (%) of microspheres as a function of time. Similar to the short-term degradation results, the long-term results show that in general the microsphere degradation rate decreases as the metal oxide content increases.

2.3.6. pH measurement

Figure 2.10 shows the variation in pH values with time for the investigated microspheres immersed in deionised water over the 20 day study period. In both series of microspheres, a decrease in pH was observed over the course of the study. The steepest decrease in pH was observed from day 0 to day 1 for most compositions; however, the pH decrease became progressively more gradual over the rest of the immersion time. The only composition that showed a different trend was Ti5, where the pH values showed the steepest decrease between days 3 and 7. The range of pH values observed for the Fe-PGMs over the study period was 3.67–4.76, 3.65–5.32 and 3.70–5.42 for Fe1, Fe3 and Fe5 respectively; the corresponding values for the Ti-PGMs were 3.63–4.76, 3.33–5.01, 3.83–6.75 and 3.91–6.08 for Ti1, Ti3, Ti5 and Ti7 respectively (the first value in each range is the final pH at day 20 while the second value is the initial pH at day 1). Thus, the solutions obtained for the Fe5 and Ti5 compositions were found to be the least acidic in nature.

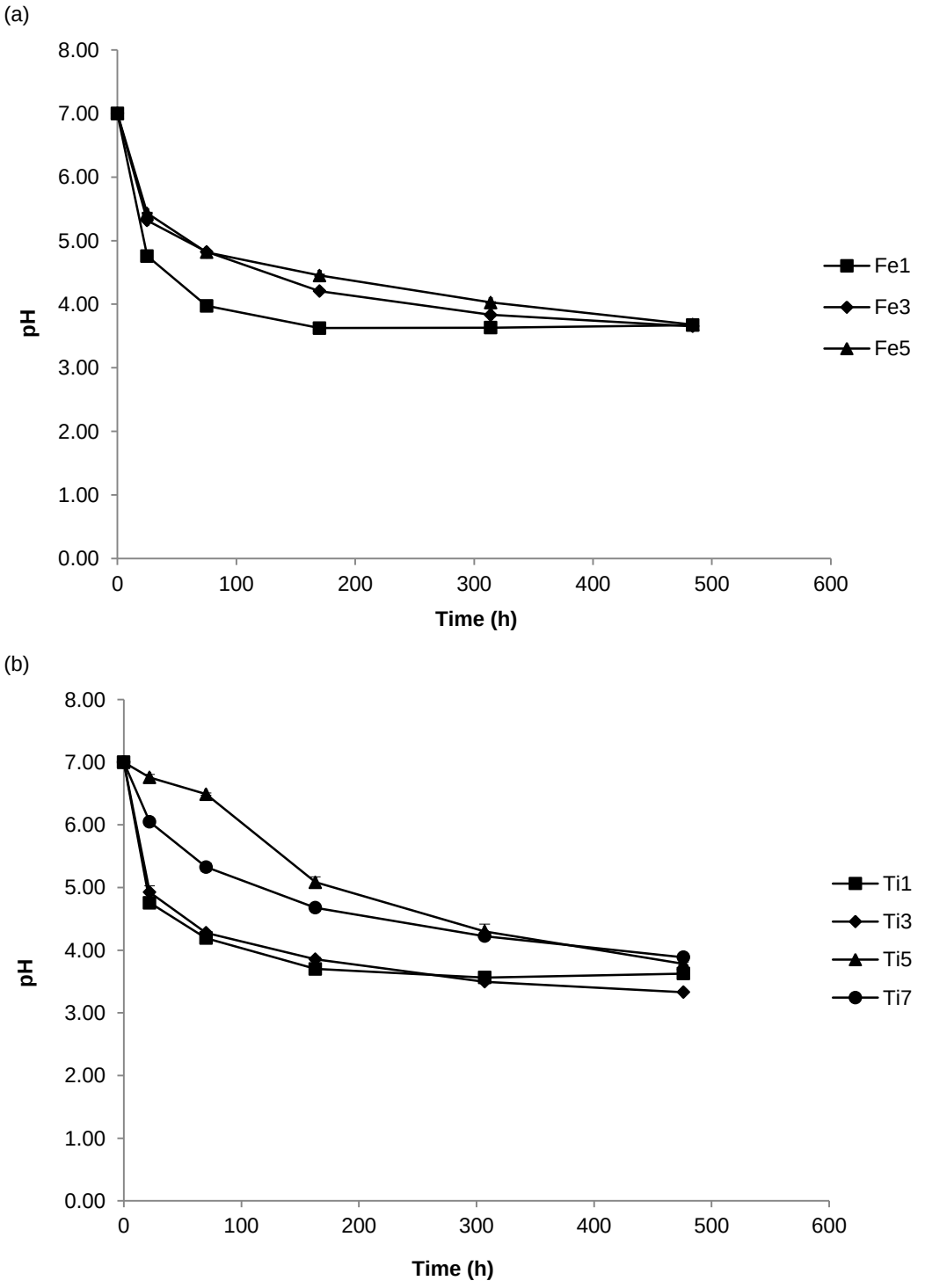

Figure 2.10. pH change in deionised water as a function of time for (a) iron and (b) titanium phosphate glass microspheres. For most of the investigated compositions, the pH shows an initial sharp decrease followed by a more gradual decrease.

2.3.7. Ion release measurement

2.3.7.1. Anion release

Figures 2.11 and 2.12 show the release of phosphate species from the Fe-PGMs and Ti-PGMs, respectively, as a function of time over the duration of the 20 day study period. Similar to the degradation results, the release of phosphate ions from all the microsphere samples increased with time and the amount of ions released was inversely proportional to the metal oxide content. In the Fe-PGMs (Figure 2.11), significant differences were noted between the release profiles of different compositions for all the phosphate species, aside from the release of orthophosphate PO_4^{2-} ions where the Fe1 and Fe3 release curves were close together; this was further confirmed from the calculated ion release rates (Table 2.4) where the Fe1 and Fe3 microspheres yielded almost equivalent release rates (Fe1 = 8.2910 ppm.h^{-1} and Fe3 = 8.2741 ppm.h^{-1}). In the Ti-PGMs (Figure 2.12), for all four phosphate species, there was a significant difference between the release profiles and release rates of the Ti1 and Ti3 microspheres and, to a lesser extent, between the Ti3 and Ti5 microspheres, while there was little difference in the release profiles and rates between the Ti5 and Ti7 microspheres. Thus, the trends in the phosphate release profiles could be algebraically expressed as Fe1 > Fe3 > Fe5 and Ti1 > Ti3 > Ti5 ≈ Ti7 for the Fe-PGMs and Ti-PGMs respectively. In both microsphere series, the amount of PO_4^{2-} ions released was the largest among all four phosphate species.

(a)

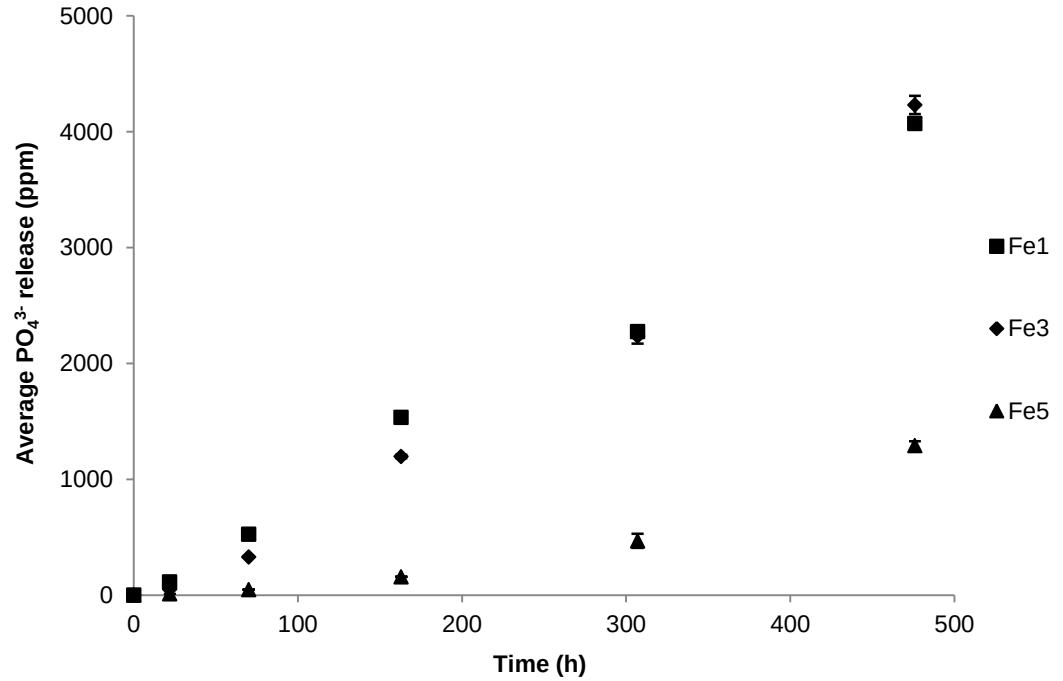
5000
4000
3000
2000
1000
0
Average PO_4^{3-} release (ppm)
0
100
200
300
400
500
Time (h)
Fe1
Fe3
Fe5

(b)

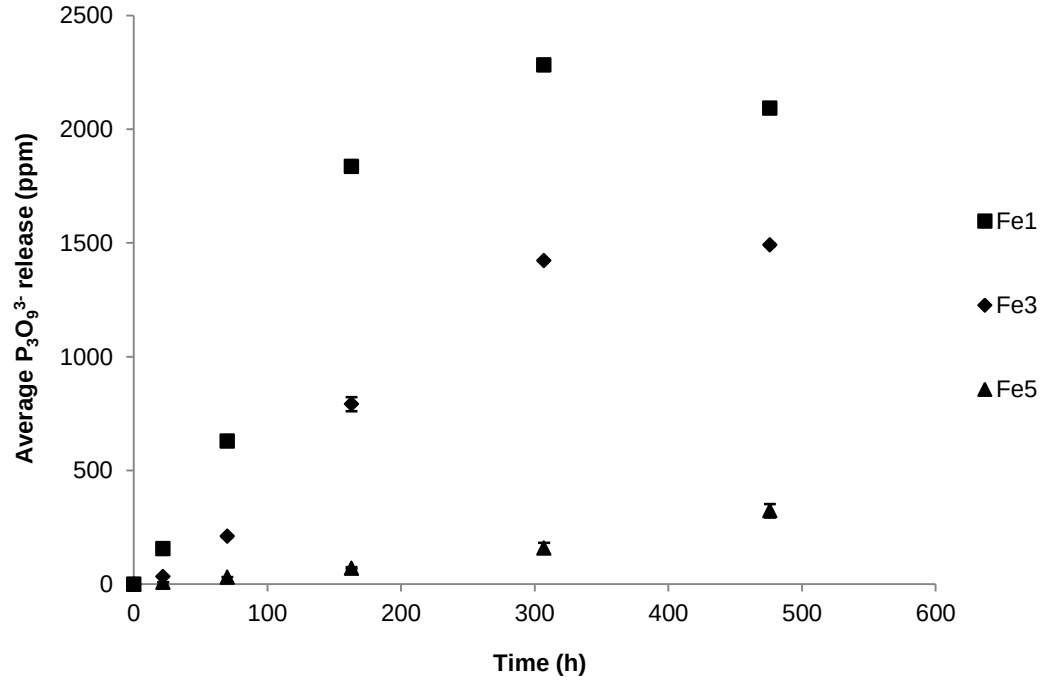
2500
2000
1500
1000
500
0
Average $P_3O_9^{3-}$ release (ppm)
0
100
200
300
400
500
600
Time (h)
Fe1
Fe3
Fe5

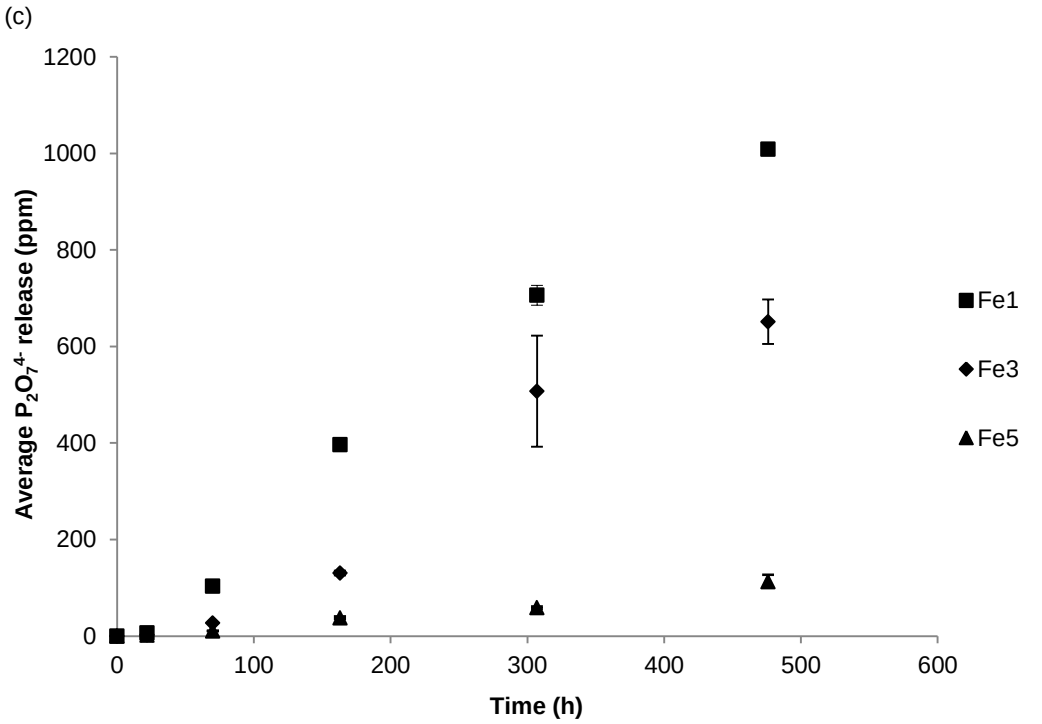

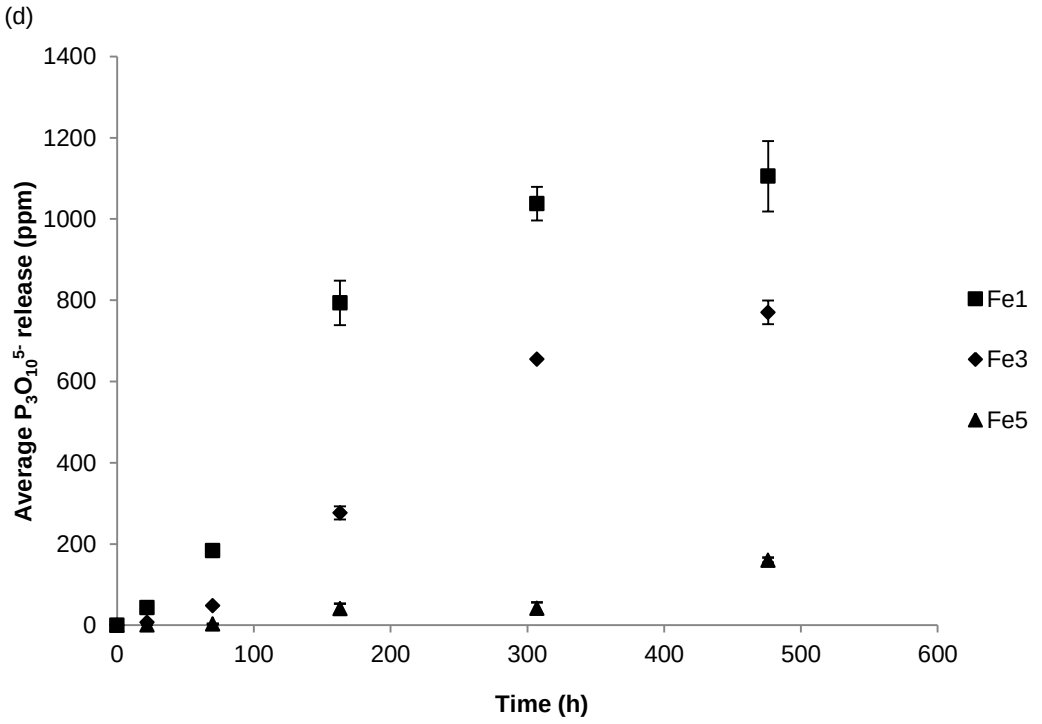

Figure 2.11. Average release (ppm) of (a) PO_4^{3-}, (b) $P_3O_9^{3-}$, (c) $P_2O_7^{4-}$ and (d) $P_3O_{10}^{5-}$ ions as a function of time for iron phosphate glass microspheres. In general, the amount of phosphate ions released decreases with an increase in the metal oxide (Fe_2O_3) content.

(a)

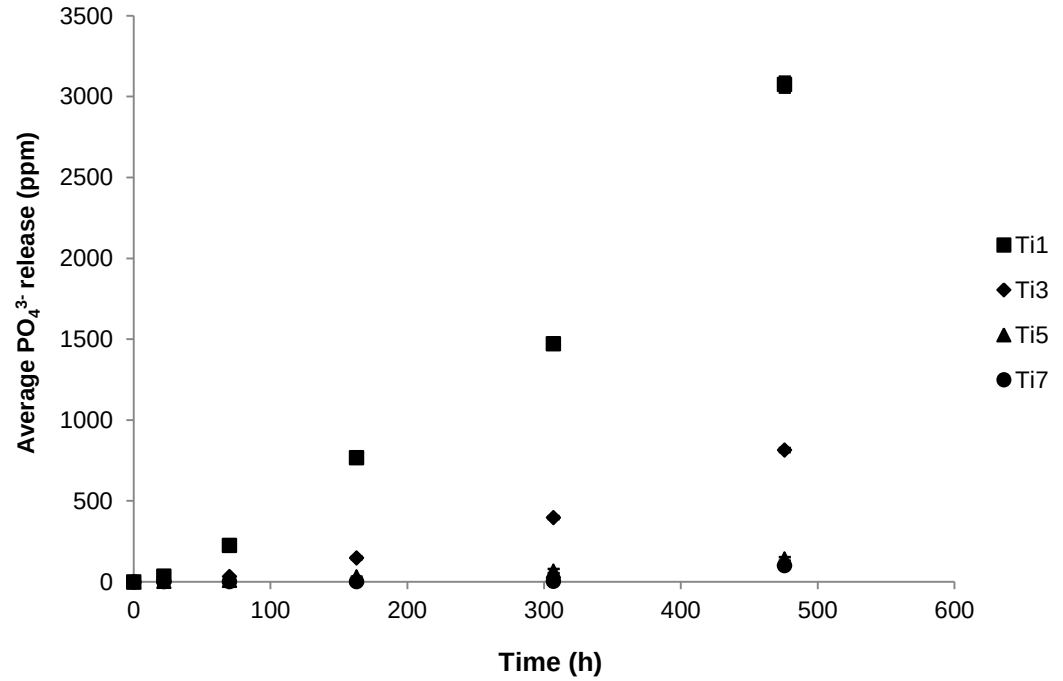
3500
3000
2500
2000
1500
1000
500
0
Average PO_4^{3-} release (ppm)
0
100
200
300
400
500
600
Time (h)
Ti1
Ti3
Ti5
Ti7

(b)

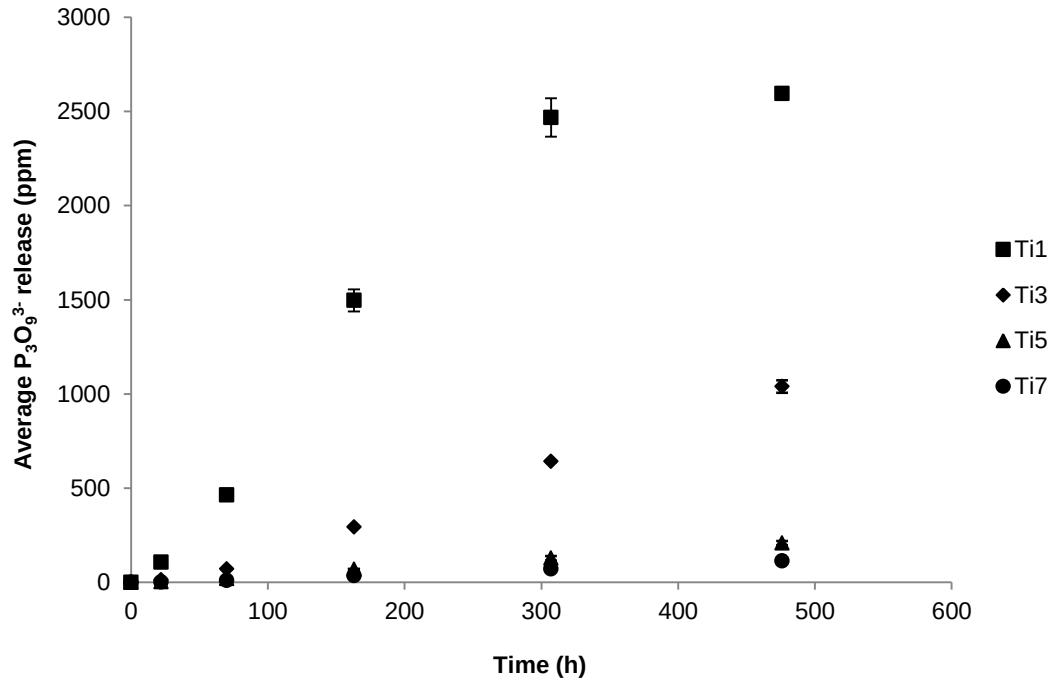
3000
2500
2000
1500
1000
500
0
Average $P_3O_9^{3-}$ release (ppm)
0
100
200
300
400
500
600
Time (h)
Ti1
Ti3
Ti5
Ti7

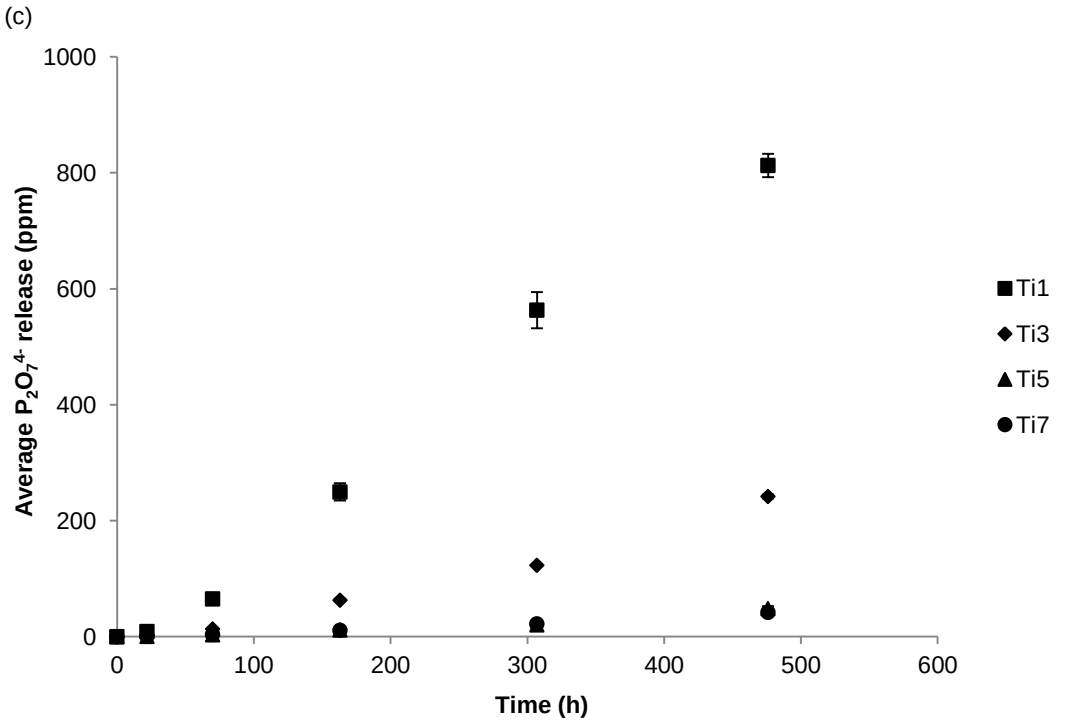

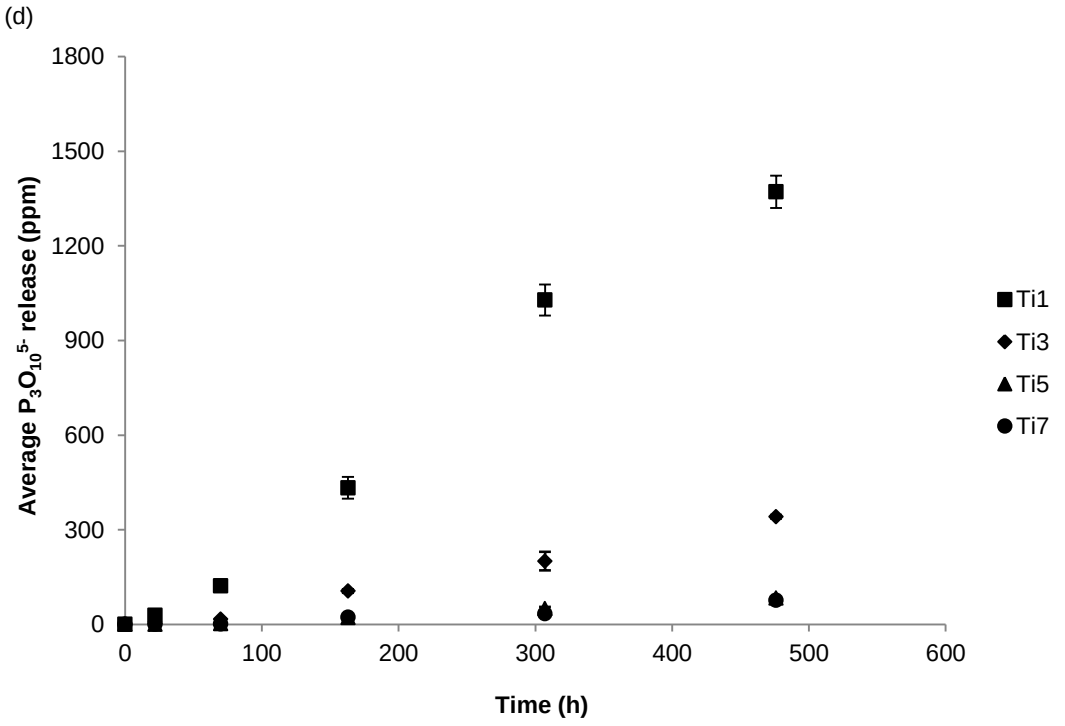

Figure 2.12. Average release (ppm) of (a) PO_4^{3-}, (b) $P_3O_9^{3-}$, (c) $P_2O_7^{4-}$ and (d) $P_3O_{10}^{5-}$ ions as a function of time for titanium phosphate glass microspheres. Similar to the case of the iron phosphate glass microspheres, the amount of phosphate ions released generally decreases with an increase in the metal oxide (TiO_2) content.

2.3.7.2. Cation release

Figures 2.13 and 2.14 show the variation in the average release of Na^+ and Ca^{2+} ions from the Fe-PGMs and Ti-PGMs, respectively, with time over the duration of the 20 day study period. As expected, the release of both ions from all the investigated microsphere samples generally increased with time. With regard to Na^+ release, the observed trends were broadly similar to those for phosphate release, whereby there was a significant decrease in the release rate with an increase in the metal oxide content from 1 to 3 mol% and to a lesser extent from 3 to 5 mol%; the Ti5 and Ti7 release rates were close to each other. As regards the Ca^{2+} release, there was a general decrease in the release rate as the metal oxide content was increased (Table 2.4), although it was more difficult to discern this trend clearly in the release profiles on account of the large error bars (Figures 2.14).

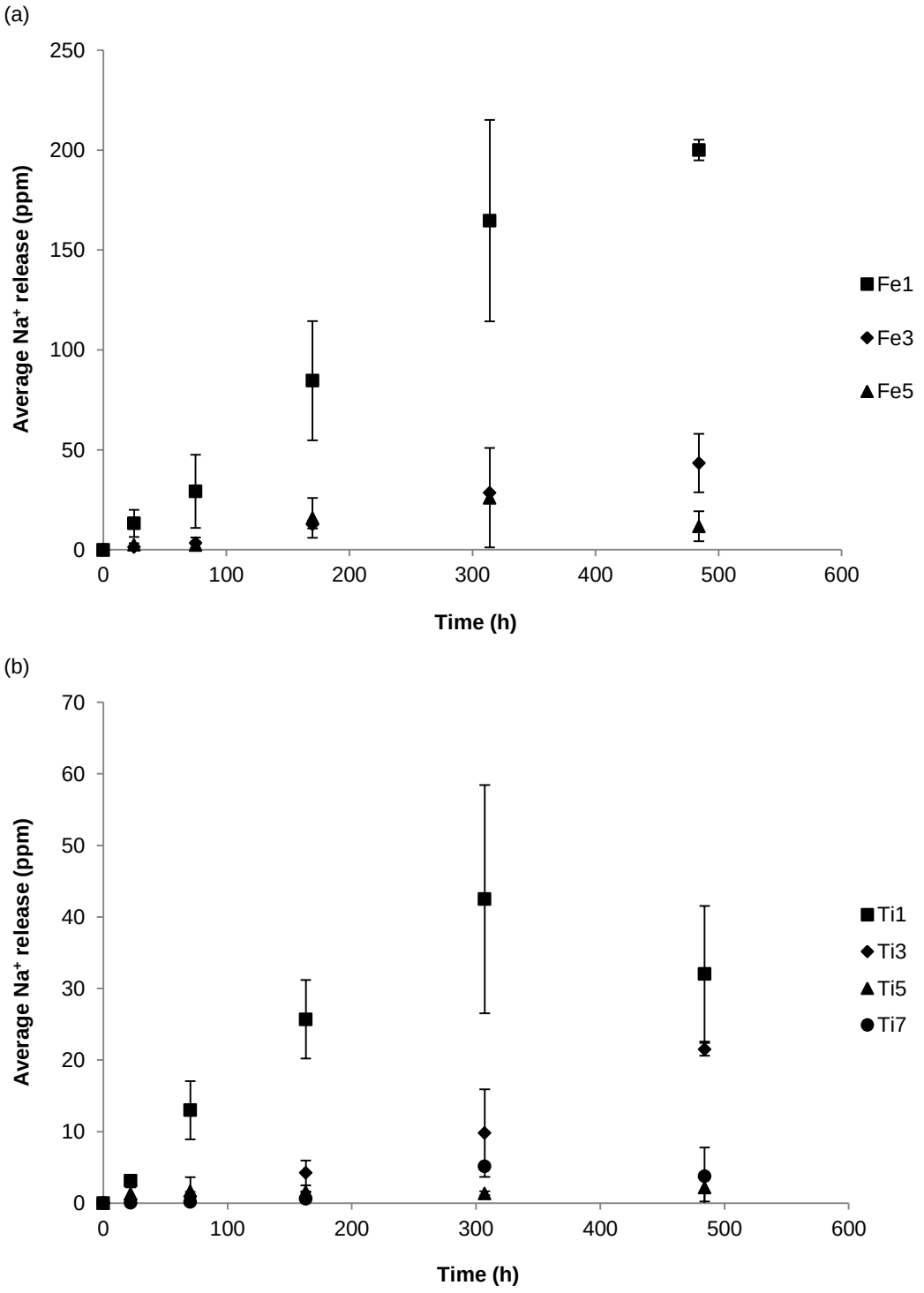

Figure 2.13. Average release (ppm) of Na^+ ions as a function of time for (a) iron and (b) titanium phosphate glass microspheres. In general, the amount of Na^+ ions released generally decreases with an increase in the metal oxide content.

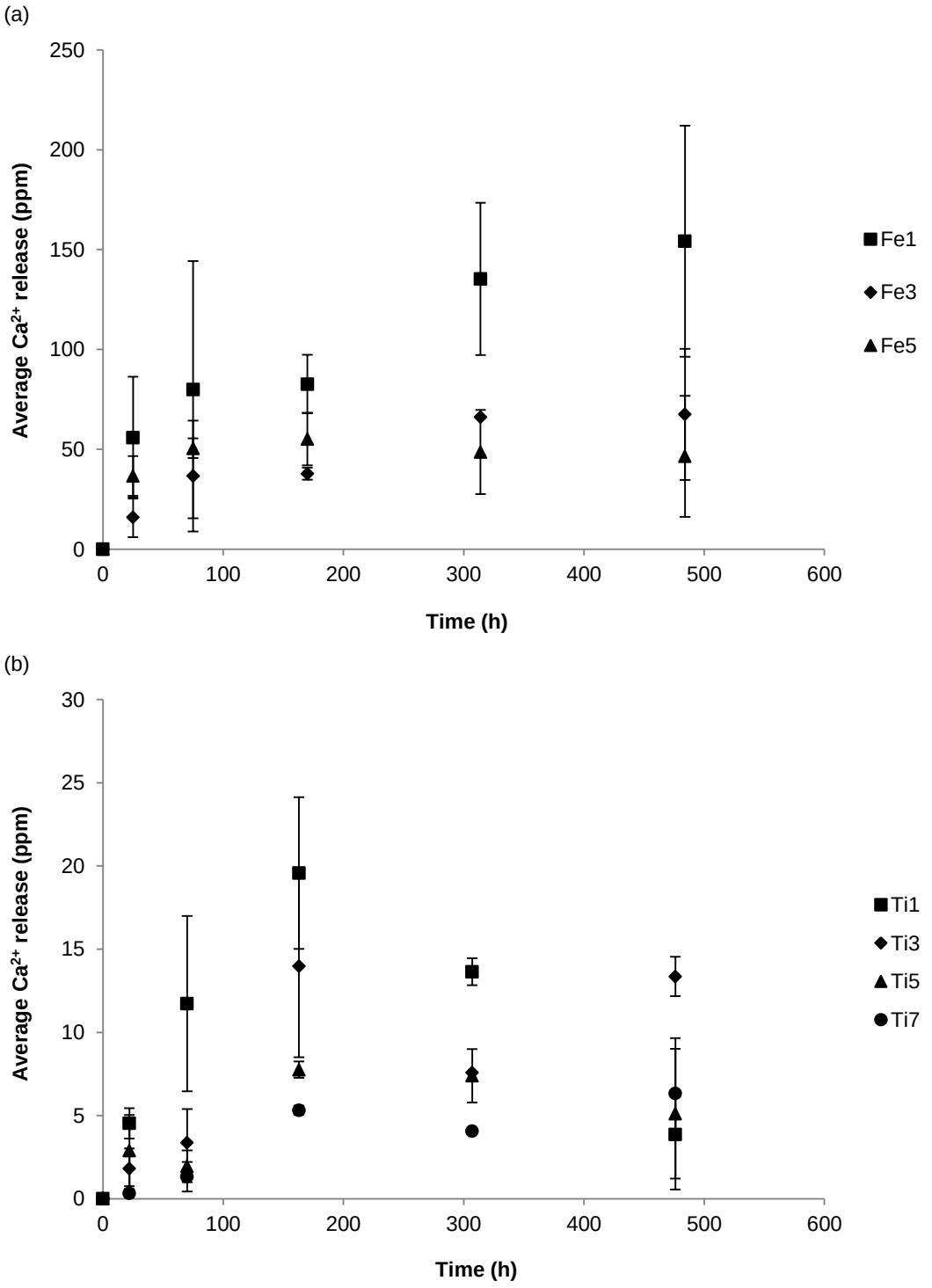

Figure 2.14. Average release (ppm) of Ca^{2+} ions as a function of time for (a) iron and (b) titanium phosphate glass microspheres. As with the Na^{+} and phosphate ions, the amount of Ca^{2+} ions released generally decreases with an increase in the metal oxide content, although it is difficult to observe this trend clearly in the figures.

2.3.7.3. Transition metal ion release

Figures 2.15 and 2.16 show the release profile of Fe^{3+} and Ti^{4+} ions from the Fe- and Ti-PGMs, respectively, over the course of the 20 day study period. In the Fe-PGMs, a sharp increase in Fe^{3+} release was observed up to 170 hours post immersion, after which the amount of Fe^{3+} ions released underwent a more gradual decrease (Figure 2.15). However, in the Ti-PGMs, the amount of Ti^{4+} ions released increased with time throughout the study period (Figure 2.16). The rates of release of both ions were found to decrease with an increase in the metal oxide content of the glass microspheres, although the Ti5 and Ti7 microspheres showed almost equivalent release rates (Table 2.4).

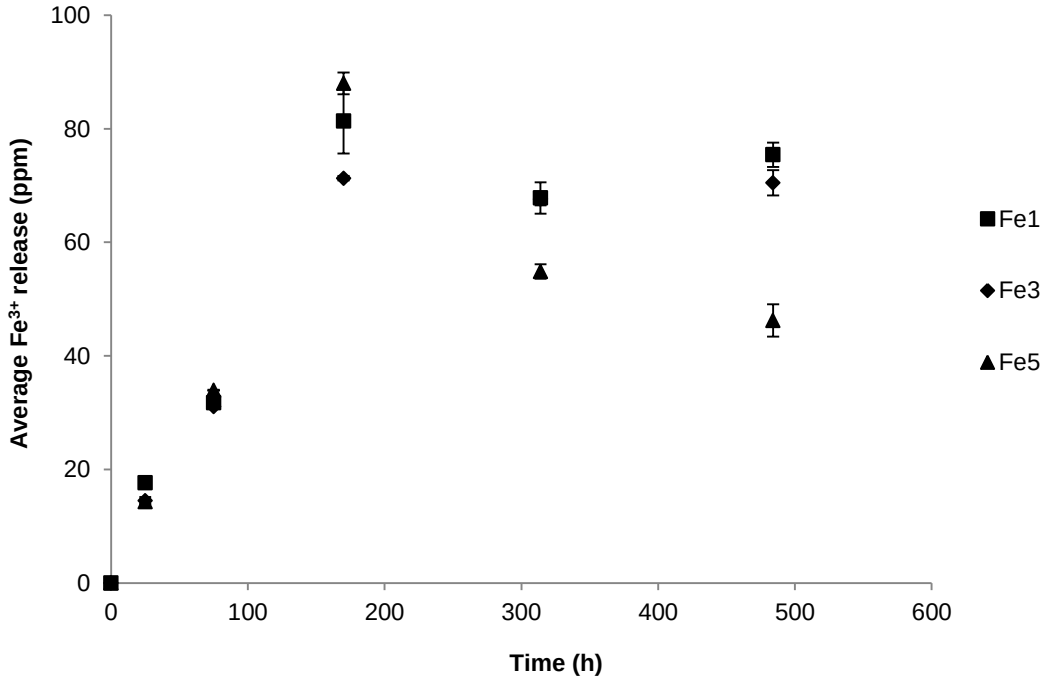

Figure 2.15. Average release (ppm) of Fe^{3+} ions as a function of time for the investigated iron phosphate glass microspheres. In general, the amount of Fe^{3+} ions released undergoes a sharp initial increase up to 170 hours followed by a gradual decrease over the rest of the study period.

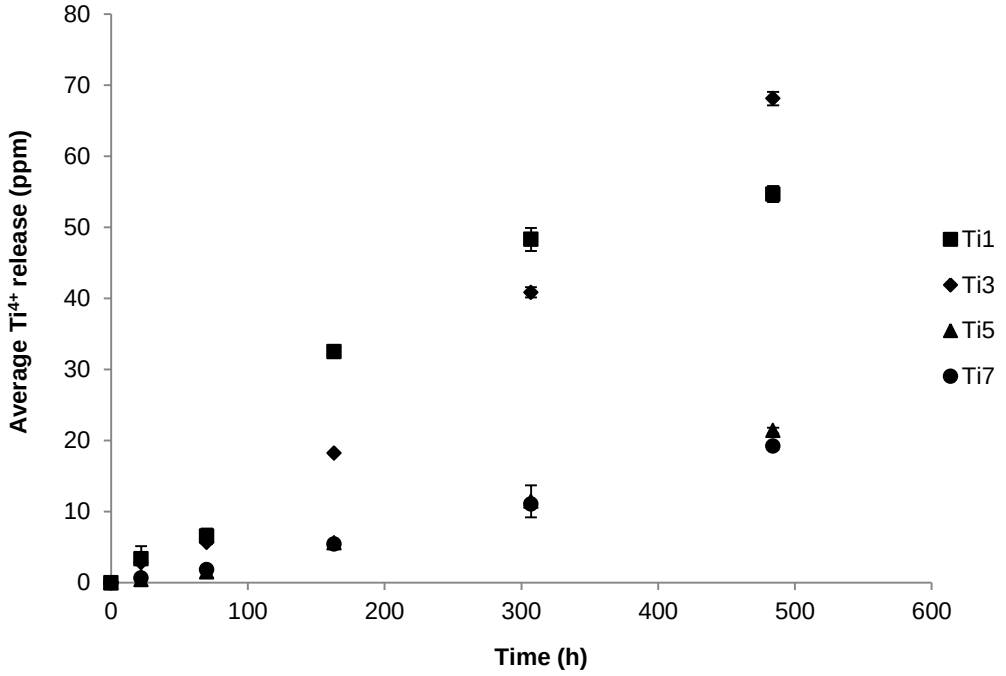

Figure 2.16. Average release (ppm) of Ti^{4+} ions as a function of time for the investigated titanium phosphate glass microspheres. In general, the amount of Ti^{4+} ions released decreases with an increase in the TiO_2 content.

2.4. Discussion

The major objectives of this part of the research were to demonstrate the successful production of microspheres for all the studied glass compositions using the described flame spheroidisation method and to investigate the microsphere properties so as to identify trends that correlate the microsphere properties to the glass composition.

The particle size distribution experiment was carried out to investigate whether the glass composition can affect the size of microspheres obtained from the flame spheroidisation apparatus. At the outset, it should be noted that the present method relied on a combination of image analysis and visual examination, and the microsphere diameter measurements were carried out manually. In order to minimise the effects of human error, the sizes of at least 500 microspheres were measured for each composition. It is considered that the sample population used here is sufficiently large so that any measurement errors would not significantly affect the overall results. At the same time, a quicker and more efficient means to carry out particle size distribution measurements would be to use a particle size analyser which would automatically measure microsphere sizes over the entire size spectrum.

The present particle size distribution results the revealed that the microsphere size was independent of the glass composition; this is a favourable result since it implies that a wider range of microsphere sizes can be obtained by suitably modifying the various parameters of the flame spheroidisation set up, for instance, the flame temperature, particle residence time in the flame, frequency of vibration of feed assembly etc. The present set up yielded microspheres in the size range of ~10–210 μm. At the lower end of this range, particle agglomeration in the feed apparatus and subsequent dispersal of the agglomerates in the flame considerably restricted the number of glass microspheres with sizes of <45 μm. This problem can possibly be overcome by dispersing the feed particles in a suitable liquid dispersant prior to introduction in the flame. On the other hand, at the higher end of the range, microsphere numbers were limited because the residence time of the particles in the flame was inadequate for achieving complete spheroidisation. This problem can be resolved by generating a flame of greater length and higher temperature to provide a greater residence time under hotter conditions. A larger blow torch connected to a gas–oxygen source may be used for this purpose, as has been implemented in several previous glass microsphere studies (Cacaina et al., 2006, Cacaina et al., 2008, Sene et al., 2008, Martinelli et al., 2010). As such, the flame spheroidisation apparatus used in the present study was found to yield maximum proportion of spherical particles over a size range of 63–106 μm, and the smallest possible sub-range for which appropriate sieves were available was 63–75 μm; as a result, all microsphere-related experiments were conducted using microspheres within this size range so as to minimise the effects of particle size on the experimental results.

From an overall perspective, the characterisation results are broadly in agreement with those of previous studies on metal oxide–containing quaternary phosphate glasses (Navarro et al., 2003a, Rajendran et al., 2007, Abou Neel et al., 2008a, Abou Neel and Knowles, 2008, Pickup et al., 2008a, Abou Neel et al., 2009a, Kiani et al., 2010, Abou Neel et al., 2005a, Ahmed et al., 2004a). For instance, the microsphere densities and glass transition temperatures are approximately equal to those obtained for glass discs, powders or fibres of the similar compositions. The microspheres degrade at increasing rates in the same way as the other morphologies and the degradation rates and ion release for all the morphologies are inversely proportional to the metal oxide content. Thus, the same structural changes are occurring with increased metal oxide incorporation regardless of the sample morphology. Yet, there are several important differences that can be ascribed to the

morphological differences between the samples being studied (e.g. glass microspheres vs. glass powders vs. glass fibres vs. glass discs). In subsequent paragraphs, these morphological aspects will be compared and contrasted wherever applicable.

The characterisation studies yielded several sets of results that can be correlated to provide a detailed overall view of changes in the glass properties with the incorporation of increasing amounts of metal oxides. Thus, an increase in the metal oxide content occurred in conjunction with (A) an increase in the glass density, (B) shift in T_g towards higher values, (C) decrease in the short- and long-term degradation rates, (D) an increase in the pH values of the solution and (E) a decrease in the ion release rate for most anionic, cationic and transition metal species. Many of these results can be discussed independently and thereby have their own implications, but one common indication from all of them is the increased densification of the glass structure as the metal oxide content of the glass is increased.

The increase in the glass structural densification with the metal oxide content has been observed in many previous studies on metal oxide–doped phosphate glasses (Abou Neel et al., 2005a, Abou Neel et al., 2008a, Abou Neel et al., 2009a, Abou Neel and Knowles, 2008, Navarro et al., 2003a, Rajendran et al., 2007). There are several factors that play a role in determining the strength of the glass structure when metal oxide dopants are added at the expense of one of the components of the ternary P_2O_5–Na_2O–CaO glass system. Some of these factors include the ionic charge, atomic weight and ionic radius of the ions that are substituted in the glass structure as well as the bond enthalpies i.e. the energy required to break the bonds formed between the constituent ions. In the P_2O_5–Na_2O–CaO–Fe_2O_3 and P_2O_5–Na_2O–CaO–TiO_2 glass systems, trivalent Fe^{3+} and tetravalent Ti^{4+} ions are respectively added at the expense of univalent Na^+ ions. The higher ionic charge of Fe^{3+} or Ti^{4+} as compared to Na^+ implies that the addition of these metal ions to the glass would increase the atomic packing and thereby strengthen the glass structure.

In the case of glass density, the atomic weight and ionic radius of the constituent ions are considered to play important roles. The relative atomic weights of iron (55.845) and titanium (47.867) are more than twice that of sodium (22.989) (Wieser et al., 2013). At the same time, the ionic radii of Fe^{3+} (69–78.5 pm) and Ti^{4+} (74.5 pm) are lower than that of Na^+ (116 pm) (Shannon, 1976). A higher atomic weight is

associated with a larger sample mass, and a lower atomic radius is associated with reduced inter-atomic spacing; both effects concurrently lead to an increase in the glass density. In other words, the replacement of a lighter ion having a larger ionic radius (Na^{+}) with a heavier ion having a smaller ionic radius (Fe^{3+} or Ti^{4+}) would lead to an increase in the glass density.

With reference to the DTA results, the T_g value of the glass is associated with the linkage strength of the glass, which can be expressed in terms of the bond enthalpy and consequently the bond length; the smaller the bond length, the stronger the bond formed between the constituent atoms and the higher the energy required to break the bond (Hoppe, 1996). The bond enthalpies of the Ti–O bond (672.4 ± 9.2 KJ/mol) and Fe–O bond (390.4 ± 17.2 KJ/mol) are both higher than that of the Na–O bond (256.1 ± 16.7 KJ/mol). Thus, Fe^{3+} and Ti^{4+} bonds are stronger than Na^{+} bonds and require more energy for bond breakage which results in a higher T_g value. It is worth noting that for glasses having the same composition, differences exist between the DTA profiles of glass microspheres and glass powders; this is particularly true for the DTA data obtained for microspheres and nonspheroidised powders of titanium phosphate glasses having the same composition (Abou Neel et al., 2009a). The differences are mainly in terms of the presence of additional crystallisation or melting peaks. These differences may be dependent on the particle sizes of the samples being analysed. The present study utilised glass microspheres in the size range 63–106 µm, whereas it is probable that powdered samples containing particles of smaller sizes were used for DTA analyses in the previous study. The differences in the particle sizes may have preferentially promoted surface nucleated phases during the course of the experiment.

When discussing the results of the short-term degradation study, it is worth mentioning that to the best of our knowledge, the use of a time lapse imaging technique to obtain degradation data for glass microspheres has not been reported previously; thus, this novel technique allows us to understand more accurately how glass microspheres degrade when immersed in a liquid. As will be demonstrated in later chapters, the formation of a hydrated layer on the microsphere surface has important implications for interactions between microspheres and cells *in vitro*. The degradation profile obtained in the present study is influential for the development of microsphere-based biomedical applications, since the degradation of the microspheres *in vivo* would be considered to follow a similar profile. Over the same time scale, differences exist in the shapes of the degradation graphs between the

Ti-PGMs in this study and titanium phosphate glass discs investigated in previous studies which show a more linear profile (Abou Neel et al., 2008a). This difference can possibly be attributed to differences in morphology; for equivalent weights of glass microsphere and glass disc samples, the microsphere samples would possess a much larger surface area, which would lead to differences in degradation rates as well as in the local environments of the samples undergoing degradation.

The pH trends observed in the study are in agreement with the results of previous studies on glass discs of similar compositions (Abou Neel et al., 2009a, Abou Neel et al., 2005a); the decrease in pH values is linked to the formation of phosphoric acid in the deionised water arising from the dissociation of hydrated phosphate chains released from the glass. The pH decrease is more rapid at earlier time points (e.g. between days 1 and 7) but becomes more gradual at later time points, suggesting the establishment of a balance between the hydration and dissociation processes. The amount of phosphoric acid formed is proportional to the phosphate release; thus, more soluble glasses (such as Fe1 or Ti1) which release more phosphate ions experience a sharper drop in pH as compared to less soluble glasses (such as Fe5 or Ti5).

With regard to the ion release results, the increase in the metal oxide content in both the Fe- and Ti-PGMs is generally found to correlate with a decrease in the microsphere dissolution rates (both short-term and long-term) and release rates of all the studied ions such as PO_4^{3-}, $P_2O_7^{4-}$, $P_3O_9^{3-}$, $P_3O_{10}^{5-}$, Na^+, Ca^{2+}, Fe^{3+} and Ti^{4+}. The amount of PO_4^{3-} ions released is the largest out of all the investigated ions, thereby possibly indicating that linear PO_4^{3-} ions form the largest proportion of the glass structure. It is difficult to clearly discern a trend in the Ca^{2+} release from both Fe-PGMs and Ti-PGMs and the error values obtained are larger than for any of the other ions (Figure 2.14), but this may possibly be attributed to the quality of the cartridges used to remove the phosphate species from the samples; along with the removal of phosphate species, the blocking of some proportion of the total Ca^{2+} ions released cannot be ruled out.

With regard to the iron release profile from the Fe-PMGs, it is worth mentioning that in ionic form, iron can exist in the +2 and/or +3 oxidation states. However, it has been shown by Fe *k*-edge X-ray absorption spectroscopy studies that iron phosphate glasses with 50 mol% P_2O_5 contain iron only in the +3 oxidation state with octahedral coordination (Qiu et al., 2008b). Therefore, the iron release

experiments in the present study focused only on Fe^{3+} ion release with iron(III) chloride used as the measurement standard. Among all the ion release profiles investigated, the Fe^{3+} ion release seems anomalous on account of the decrease observed at later time points (days 13 and 20 in Figure 2.15). A similar trend has been observed previously in iron phosphate glass fibres (Abou Neel et al., 2005a) and although the occurrence of a precipitation process in the medium as degradation occurs was identified as a possible cause, the exact reason for this behaviour remains unclear. A commonly observed trend in the Ti-PGMs is the lack of significant differences in the degradation and ion release rates between the Ti5 and Ti7 glasses. It is possible that the addition of 5 mol% TiO_2 to the glass serves to saturate the glass structure, and any further TiO_2 that may be added has a reduced effect on the glass network. Another possibility is that differences may exist between the calculated composition of the 7 mol% TiO_2 glass and the actual composition of the glass prepared by the melt quench technique. To further investigate this observation, it would be useful to carry out energy-dispersive x-ray (EDX) analysis which would provide an accurate elemental analysis of the glass samples. EDX analysis has been conducted on a range of phosphate glass compositions in previous studies, and it has generally been shown that the difference between the calculated composition and the composition as measured by EDX is generally no more than 1–2 mol% in a glass with satisfactory homogeneity (Ahmed et al., 2008, Ahmed et al., 2010, Hasan et al., 2012, Shaharuddin et al., 2012, Haque et al., 2013b, Shash and Ahmed, 2013, Boroica et al., 2013, Sava et al., 2013, Goh et al., 2014). Similar observations have been made previously in the author's research laboratory. It is possible that the difference between the calculated and measured composition may be higher or lower in the 7 mol% TiO_2 glass. In this context, future studies should ensure that EDX analysis of the prepared phosphate glasses is carried out so as to confirm the actual composition of the investigated glass compositions.

It is worth noting that differences exist between the properties and behaviours of Fe-PGMs and Ti-PGMs. As illustrated in Table 2.5, the Fe-PGMs possess higher values than the Ti-PGMs for both short- and long-term degradation rates as well as all the ion release rates. In particular, the short-term degradation values of Fe-PGMs are approx. 5 times higher, the PO_4^{3-} values are 3 times higher, and the Na^+ and Ca^{2+} values are respectively 10 and 5 times higher than the corresponding values for the Ti-PGMs.

Table 2.5. Average values of short-term and long-term degradation rates (%.mm^{-2}.h^{-1} and %.h^{-1} respectively) and ion release rates (ppm.h^{-1}) for iron and titanium phosphate glass microsphere series obtained by averaging the values listed in Table 2.4.

Glass series	Iron phosphate glass	Titanium phosphate glass
Short term deg. (%.mm^{-2}.h^{-1} × 10^{-5})	45.264	9.8601
Long term deg. (%.h^{-1})	0.1252	0.0881
PO_4^{3-} (ppm.h^{-1})	6.2652	1.9384
$P_3O_9^{3-}$ (ppm.h^{-1})	3.3552	2.3040
$P_2O_7^{4-}$ (ppm.h^{-1})	1.2632	0.5877
$P_3O_{10}^{5-}$ (ppm.h^{-1})	1.6063	0.9918
Na^+ (ppm.h^{-1})	0.2296	0.0232
Ca^{2+} (ppm.h^{-1})	0.1945	0.0370
Fe^{3+} (ppm.h^{-1})	0.1832	-
Ti^{4+} (ppm.h^{-1})	-	0.0864

Clearly, Ti^{4+} incorporation in a ternary P_2O_5–CaO–Na_2O glass serves to strengthen the glass to a greater extent than Fe^{3+} incorporation. Many of the same factors as those influencing the glass structure and properties when metal oxides are added at the expense of Na_2O (e.g. ionic charge, coordination, ionic radius, bond enthalpy etc.) are considered to play a role here as well. In particular, the higher values of ionic charge (+4 vs. +3) and bond enthalpy (672.4 ± 9.2 KJ/mol vs. 390.4 ± 17.2 KJ/mol) imply a more pronounced strengthening effect when the glass structure is modified by Ti^{4+} doping. Thus, the successful production of microspheres from phosphate glasses containing Fe_2O_3 and TiO_2 has been demonstrated using the flame spheroidisation technique and several interesting trends which correlate the microsphere properties with the glass composition and highlight the effect of metal oxide addition have been observed. These results offer possibilities for studying the glass structure at lower size scales so as to reveal how metal oxide addition can impact structural arrangements at the phase and atomic levels. Several techniques such as Fourier transform infrared (FTIR) spectroscopy, X-ray diffraction (XRD), magic angle spinning nuclear magnetic resonance (MAS NMR) and X-ray absorption near edge structure (XANES) exist for this purpose; indeed, on-going research in glass systems is being driven by further developments in the available characterisation techniques, which allows us to obtain information at various size scales from the macroscopic level down to the atomic level. The next chapter focuses on studies using these techniques to facilitate a deeper understanding of the structure of the investigated glass systems.

Chapter 3. Glass structural characterisation

3.1. Introduction

In this chapter, the structure of the previously prepared glasses was probed using several techniques that provide detailed information on glass structural variations from the phase level to the atomic level. The following four techniques were employed: Fourier transform infrared spectroscopy (FTIR), X-ray diffraction (XRD), ^{31}P and ^{23}Na magic angle spinning nuclear magnetic resonance (MAS NMR) and Ti *K*-edge X-ray absorption near edge structure (XANES) spectroscopy. FTIR spectra provide information about the effects of metal oxide addition on various chemical groups present in the glass structure such as PO_2^-, PO_3^{2-} and P–O–P. XRD spectra provide a better understanding of changes in the glass structure at the phase level; ambient XRD analyses of crystallised glass samples allow the understanding of the different phases present in the glass as the metal oxide content is increased, whereas high-temperature XRD (HTXRD) analyses highlight the phase transitions that occurred in the glasses as a function of both chemistry and also temperature. ^{31}P and ^{23}Na MAS NMR are powerful techniques for elucidating the local environments of P and Na atoms present in the glass structure since they allow the mapping of the structural connectivities of the phosphate network as well as the neighbouring network formers and modifiers. Ti *K*-edge XANES, considered among the most advanced characterisation techniques available, is a suitable tool for in-depth examination of the local Ti environment and coordination. In this study, the FTIR and XRD techniques were carried out on both iron and titanium phosphate glasses, whereas the MAS NMR and XANES techniques were used for the titanium phosphate glasses alone. The data obtained from all these techniques constitute a detailed account of the glass structural characteristics.

3.2. Materials and methods

3.2.1. Fourier transform infrared spectroscopy

The FTIR spectra were obtained in the absorption mode using a Perkin Elmer System 2000 spectrometer (Perkin Elmer, USA) equipped with a Specac Golden Gate Attenuated Total Reflectance unit (Specac, Orpington, UK). Crushed microsphere samples were used, and scanning was carried out in the range 4000–450 cm^{-1} with a resolution of 4 cm^{-1}. Each spectrum was the result of summing 10 scans.

3.2.2. X-ray diffraction

3.2.2.1. Ambient temperature X-ray diffraction

XRD analyses were carried out using powder forms of both the original as-prepared glass and crystallised glass. In the case of the crystallised samples, crystallisation of the glass was carried out by heating the glass powder in a Lenton furnace (Lenton, Hope Valley, UK) at a ramp heating rate of 7°C.minute^{-1} to approximately 8–10°C above the crystallization temperature (T_c) obtained from DTA (refer to section 2.3.3), followed by maintaining the temperature at T_c + 10°C for 3 hours; overnight cooling to ambient temperature at a ramp rate of 7°C.minute^{-1}; and crushing of the crystallised glass samples to powder. The XRD analysis was carried out using a Brüker D8 Advance Diffractometer (Brüker, Coventry, UK) in flat plane geometry with Ni-filtered Cu *K*α radiation; the diffractometer was fitted with a LynxEye detector (Brüker, Coventry, UK). Data was collected from 2θ = 10° to 100° at a step size and count time of 0.02° and 0.1 seconds, respectively. For phase identification, the Crystallographic Search-Match (CSM) software (Oxford Cryosystems, Oxford, UK) was utilized in conjunction with the International Centre for Diffraction Data (ICDD) database volumes 1 to 42.

3.2.2.2. High temperature X-ray diffraction

The same Brüker D8 Advance Diffractometer as that used for ambient XRD studies was used for HTXRD studies as well. In addition to the abovementioned LynxEye detector, an Anton Paar HTK 1600 heated stage (Anton Paar, Austria) fitted with a platinum electrode was used for the HTXRD experiments. The HTXRD data were collected at 2θ values in the range 20–40° for a step size and count time of 0.02° and 0.1 seconds per point, respectively. As in the normal XRD experiments, the radiation used was Ni-filtered Cu *K*α radiation at a voltage of 35 kV and current of 45 mA. The temperature range applied for data collection was 30–1100°C at a heating rate of 21°C.minute^{-1}, and helium was used as the purge gas.

3.2.3. Solid state magic angle spinning nuclear magnetic resonance

These experiments were carried out at the Solid State NMR facility located in Warwick University.

3.2.3.1. ^{31}P MAS NMR

Solid state ^{31}P MAS NMR experiments were undertaken at 9.4 T using a Bruker DSX-400 spectrometer operating at a Larmor frequency of 161.92 MHz. All measurements were facilitated using a Bruker 4 mm dual channel probe in which

MAS frequencies of 12.5 kHz were implemented. All ^{31}P MAS NMR data were acquired using single pulse experiments where pulses of 2.5 microsecond duration (corresponding to π/4 flip angles) were employed with recycle delays of 240 seconds to achieve a quantitative survey of the P speciation. ^{31}P chemical shifts were referenced against the primary IUPAC standard of 85% H_3PO_4 (δ 0.0 ppm) via a secondary solid reference of $(NH_4)[H_2PO_4]$ (δ 1.0 ppm). Each spectrum was processed with Bruker TOPSPIN software, with the spectral deconvolutions performed using the DmFit software package (Massiot et al., 2002).

3.2.3.2. ^{23}Na MAS NMR

Solid state ^{23}Na MAS NMR studies were conducted at Larmor frequencies of 132.29 and 158.67 MHz on Bruker AV-500 (11.75 T) and Bruker AV-600 (14.1 T) spectrometers, respectively, with a 4 mm Bruker triple-resonance probe having a spinning frequency of 10 kHz being utilised for both fields. At each field, ^{23}Na data were obtained by carrying out a one pulse experiment. Non-selective (solution) π/2 pulse times of ~6 microseconds were calibrated on solid NaCl from which selective (solid) θ pulse times of ~1 microsecond were employed to ensure quantitative estimates and to avoid lineshape distortions. A recycle delay of 20 seconds and 100 transients per sample were common to all measurements. All ^{23}Na spectra were referenced against 1 M NaCl via a secondary reference of solid NaCl (δ 7.2 ppm). Spectral deconvolutions were performed using the QuadFit software package (Kemp and Smith, 2009b).

3.2.4. Ti *K*-edge X-ray near edge absorption

The Ti *K*-edge XANES studies were conducted in collaboration with Dr. Richard Martin of Aston University. All measurements were carried out at the Diamond Light Source located in the Harwell Science and Innovation Campus in Didcot, Oxfordshire. The Ti *K*-edge XANES data were collected in fluorescence mode using the micro-focus beam-line I18. Spectra were collected from 80 eV below the edge to 220 eV above the edge in order to allow an accurate background subtraction. The spectra were collected in three step sizes; a 5 eV step size was used for the pre-edge (4900–4940 eV), a 0.25 eV step size was used over the pre-peak and edge (4940–5000 eV) and a 2 eV step size was used after the edge (5000–5200 eV). All measurements were conducted at room temperature. The spectra were normalized to have an edge step of one. Metallic Ti foil was used as the standard in order to calibrate the energy shift. Furthermore, the following compounds containing Ti^{4+} ions in different coordinate environments were used as standards: cristobalite (four-

fold), Na_2TiSiO_5 (five-fold) and anatase, rutile and $CaTiSiO_5$ (all six-fold). Comparison between signals from the reference standards and the titanium phosphate glass samples was carried out using ATHENA software (Ravel and Newville, 2005) in order to determine the Ti environment in the glasses.

3.3. Results

3.3.1. Fourier transform infrared spectroscopy

Figure 3.1 shows the FTIR spectra obtained for the investigated glass compositions. In accordance with a previous study on glass powders of similar compositions (Abou Neel et al., 2009a), the peaks at 1270 and 1100 cm^{-1} were assigned to the asymmetric stretching of PO_2^- ($\nu_{as}(PO_2^-)$) and PO_3^{2-} ($\nu_{as}(PO_3^{2-})$) groups which were associated with Q^2 and Q^1 species respectively. The peak at 900 cm^{-1} was assigned to the asymmetric stretching of P–O–P chains (ν_{as}(P–O–P)), which was associated with Q^2 species. A broad peak with the maximum value located from 780 cm^{-1} to 720 cm^{-1} (not highlighted in the figures) was assigned to the symmetric stretching of P–O–P chains (ν_s(P–O–P)). Only peaks relating to phosphate groups were observed in the FTIR spectra.

In both the iron and titanium glasses, a slight broadening of the spectrum was generally observed as the metal oxide content of the glass was increased. This was associated with a small shift towards lower wavenumber values for the $\nu_{as}(PO_2^-)$ and $\nu_{as}(PO_3^{2-})$ peaks along with a slight shift towards higher wavenumber values for the ν_{as}(P–O–P) peak (Table 3.1). For instance, the $\nu_{as}(PO_3^{2-})$ peak shifted by a small value from 1082 cm^{-1} for Fe0/Ti0 to 1072 cm^{-1} for Fe5 and 1071 cm^{-1} for Ti5, while the corresponding shifts for the ν_{as}(P–O–P) peak were from 884 cm^{-1} for Fe0/Ti0 to 892 cm^{-1} for Fe5 and 888 cm^{-1} for Ti7. The $\nu_{as}(PO_3^{2-})$ peak was not evident in the Ti7 glass. In the titanium phosphate glasses, the absorbance intensity for all three peaks showed an increasing trend with the metal oxide content e.g. from 0.0812 a.u. for Ti1 to 0.1186 a.u. for Ti7 when considering $\nu_{as}(PO_2^-)$. Such a trend was not observed in the iron phosphate glasses.

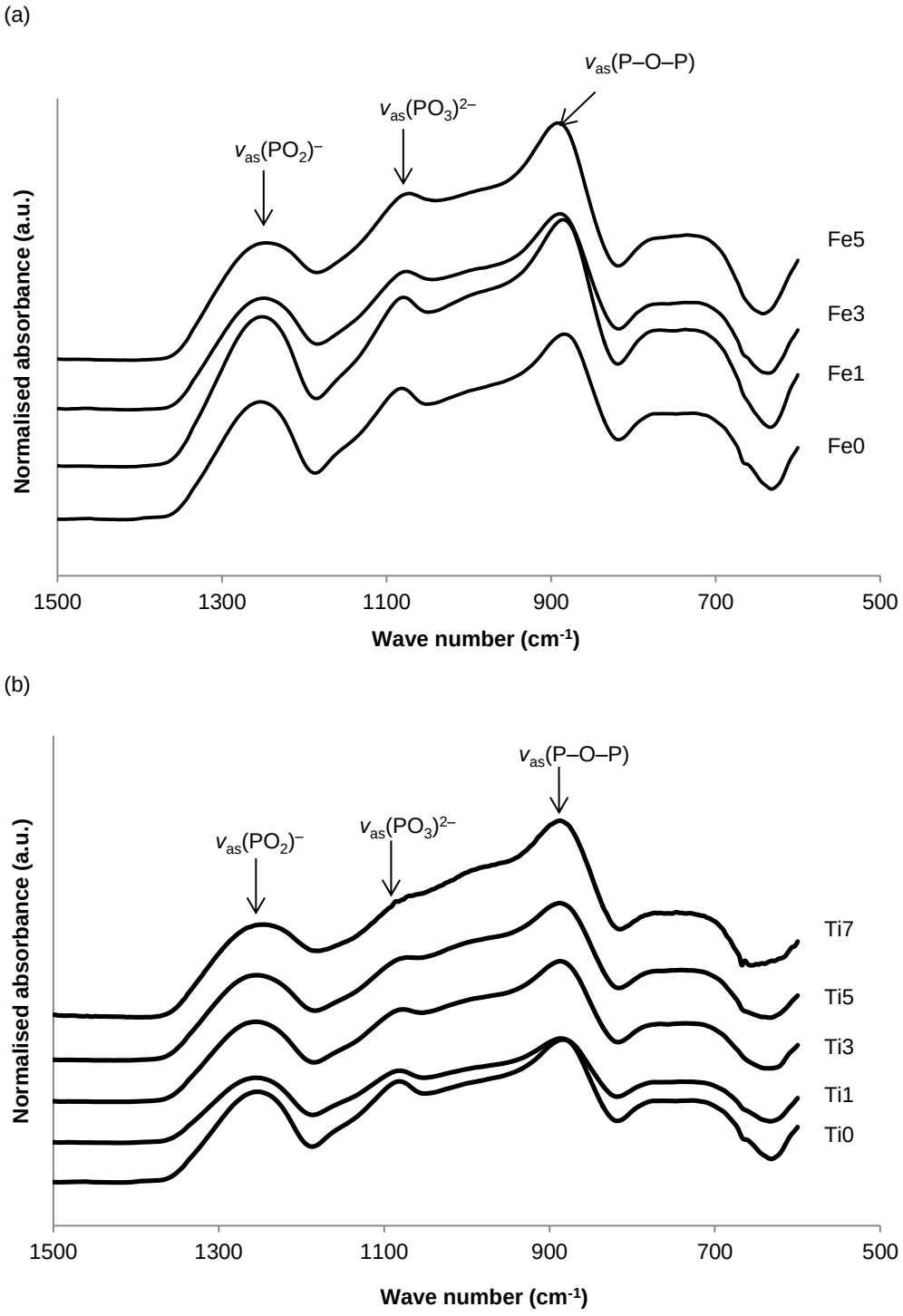

Figure 3.1. Fourier transform infrared spectra obtained for the investigated (a) iron and (b) titanium phosphate glasses. In both cases, a slight broadening of the spectrum and a small shift towards lower wave number values are observed as the metal oxide content is increased.

Table 3.1. Wave numbers (cm^{-1}) and absorbance intensities (a.u.) of peaks obtained from the FTIR spectra of iron and titanium phosphate glasses.

Glass code	$\nu_{as}(PO_2^-)$		$\nu_{as}(PO_3^{2-})$		ν_{as}(P–O–P)	
	Wave number (cm^{-1})	Absorbance intensity (a.u.)	Wave number (cm^{-1})	Absorbance intensity (a.u.)	Wave number (cm^{-1})	Absorbance intensity (a.u.)
Fe0/Ti0	1253	0.1140	1082	0.1268	884	0.1779
Fe1	1251	0.1443	1080	0.1625	886	0.2358
Fe3	1250	0.1118	1076	0.1370	888	0.1914
Fe5	1246	0.1140	1072	0.1605	892	0.2270
Ti1	1256	0.0812	1081	0.0898	887	0.1293
Ti3	1256	0.0997	1077	0.1148	887	0.1738
Ti5	1255	0.1067	1071	0.1284	888	0.1949
Ti7	1246	0.1186	-	-	888	0.2458

3.3.2. X-ray diffraction

3.3.2.1. Ambient X-ray diffraction

The XRD patterns for the original as-prepared glass samples are shown in Figure 3.2. All the XRD patterns were free from any detectable crystalline phases and a broad peak was observed in each spectrum at 2θ values of around 20–40°.

(a)

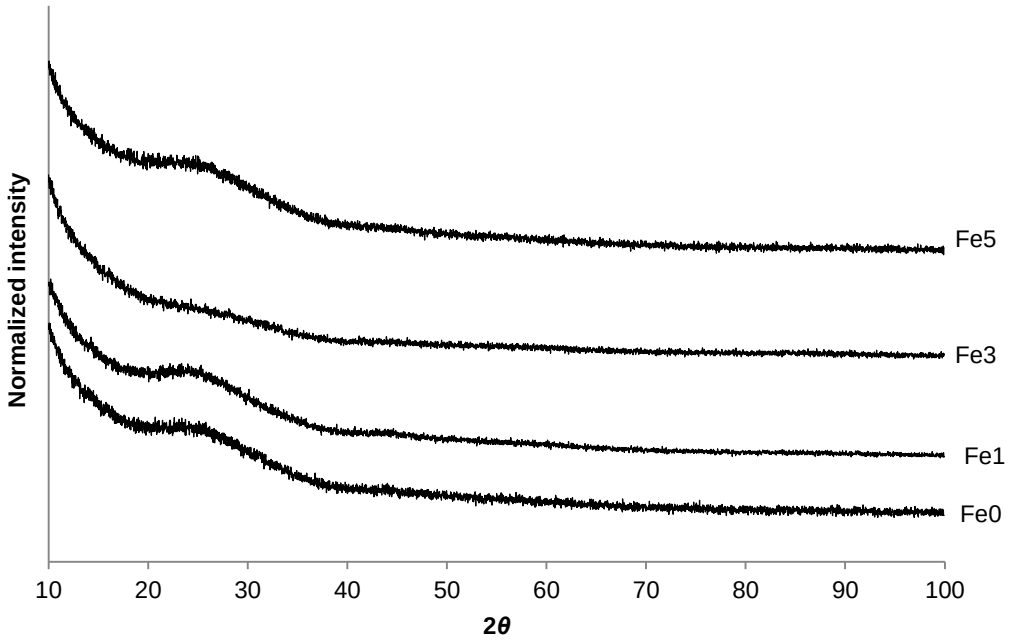

(b)

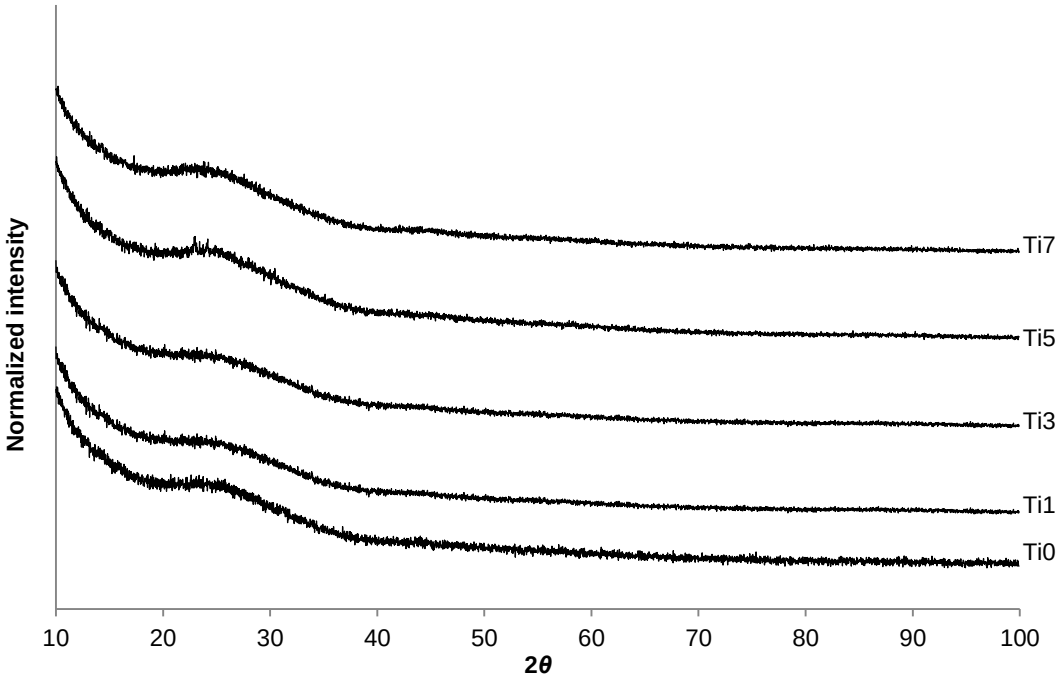

Figure 3.2. Ambient XRD plots of as-prepared glass powder samples of (a) iron and (b) titanium phosphate glasses. All the spectra are free from any detectable crystalline phases.

The X-ray diffraction patterns of the crystallised glass samples revealed that with an increase in the metal oxide content of the glasses, the intensities of peaks related to specific phases underwent changes, as indicated by dotted lines 1–5 in Figure 3.3(a) and 1–7 in Figure 3.3(b). In both the iron and titanium phosphate glasses, analysis using CSM software showed that at low metal oxide contents, (Fe0/Ti0, Fe1 and Ti1) the glasses comprised sodium calcium phosphate [$NaCa(PO_3)_3$; ICDD no.: 23-669] as the main phase with calcium phosphate [CaP_2O_6; ICDD no.: 11-39] as the secondary phase (Table 3.2). However, at higher metal oxide contents (Fe3–5 and Ti3–7), the main phase experienced a transition from $NaCa(PO_3)_3$ to CaP_2O_6. In the iron phosphate glasses, at Fe_2O_3 contents of 3 and 5 mol%, a metallic sodium iron phosphate [$NaFeP_2O_7$; ICDD no: 36-1454] phase appeared as the secondary phase. Similarly, at TiO_2 contents of 5 and 7 mol% in the titanium phosphate glasses, a metallic titanium phosphate [TiP_2O_7; ICDD no.: 34-1468] phase was observed as the secondary phase.

The transition between the phases as evidenced by software analysis could explain the variation in the intensities of certain peaks in the XRD spectra. For example, in the titanium phosphate glasses, the peaks denoted by dotted lines 2 and 3 in Figure 3.3(b) occur at 2θ values of approximately 13.4° and 18.3° respectively. From the software analysis, it was found that these peaks correspond to the spectra for $NaCa(PO_3)_3$. Thus, the decrease in intensity of this peak from Ti0 to Ti7 was consistent with the disappearance of $NaCa(PO_3)_3$ as the main phase in the glass. Similarly, the peaks corresponding to dotted lines 1, 4, 6 and 7 at approximately 12.6°, 19.4°, 23.9° and 31.1° respectively are found to belong to CaP_2O_6, and the increased intensity of this peak from Ti0 to Ti7 helped to identify the emergence of CaP_2O_6 as the dominant phase in the glass. The emergence of metal-containing phases in the glass such as $NaFeP_2O_7$ and TiP_2O_7 (lines 3 and 5 in Figures 3.3(a) and (b) respectively) could also be identified in the same way.

(a)

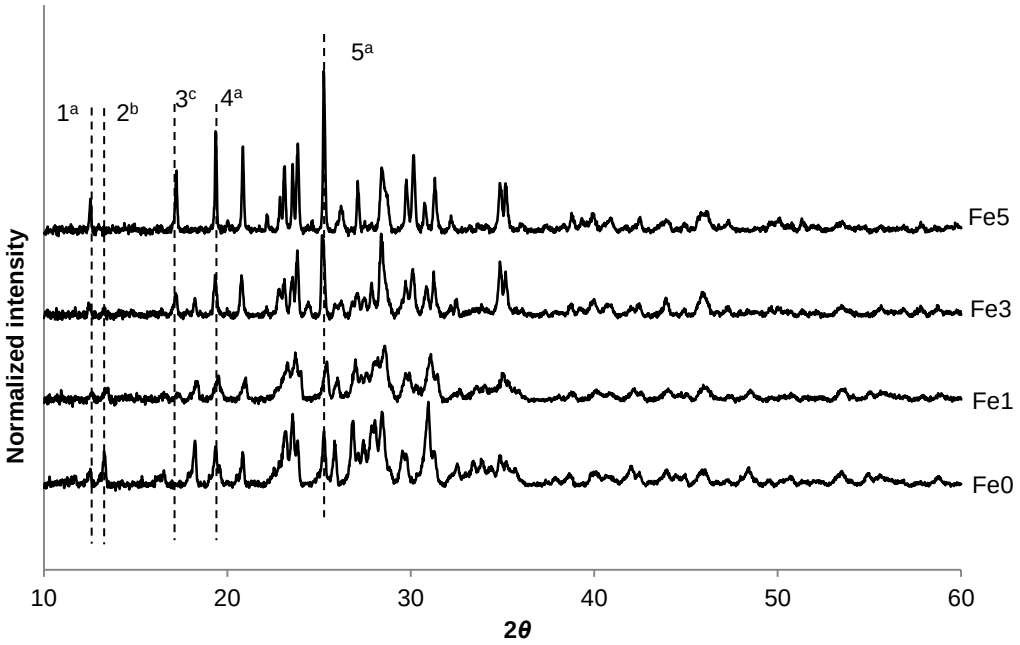

(b)

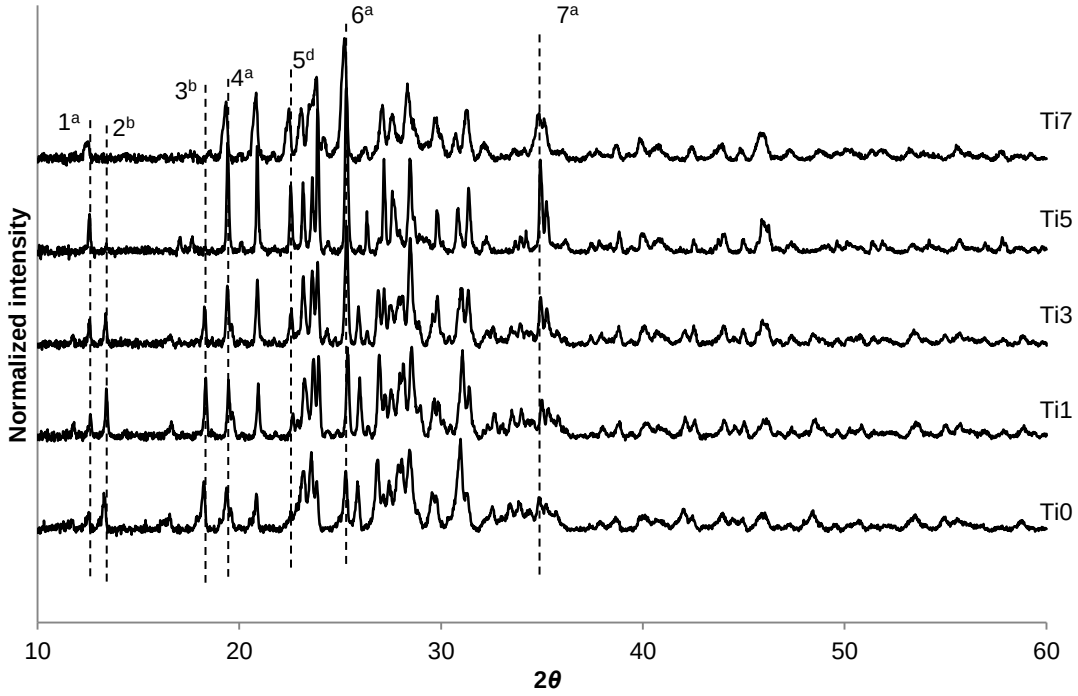

Figure 3.3. Ambient XRD plots of crystallised samples of (a) iron and (b) titanium phosphate glasses. Peaks 1–5 in (a) and 1–7 in (b) correspond to different phases in the glass. [a] Calcium phosphate, [b] sodium calcium phosphate, [c] sodium iron phosphate and [d] titanium phosphate. As the metal oxide content of the glass is increased, the intensities of the peaks undergo changes.

Table 3.2. Phases present in crystalline XRD samples as identified by Crystallographica Search-Match software in conjunction with ICDD database volumes 1 to 42.

Glass	Phase 1	Phase 2
Fe0/Ti0	Sodium calcium phosphate [$NaCa(PO_3)_3$; ICDD no: 23-669]	Calcium phosphate [CaP_2O_6; ICDD no: 11-39]
Fe1	Sodium calcium phosphate [$NaCa(PO_3)_3$; ICDD no: 23-669]	Calcium phosphate [CaP_2O_6; ICDD no: 11-39]
Fe3	Calcium phosphate [CaP_2O_6; ICDD no: 11-39]	Sodium iron phosphate [$NaFeP_2O_7$; ICDD no: 36-1454]
Fe5	Calcium phosphate [CaP_2O_6; ICDD no: 11-39]	Sodium iron phosphate [$NaFeP_2O_7$; ICDD no: 36-1454]
Ti1	Sodium calcium phosphate [$NaCa(PO_3)_3$; ICDD no: 23-669]	Calcium phosphate [CaP_2O_6; ICDD no: 11-39]
Ti3	Calcium phosphate [CaP_2O_6; ICDD no: 11-39]	Sodium calcium phosphate [$NaCa(PO_3)_3$; ICDD no: 23-669]
Ti5	Calcium phosphate [CaP_2O_6; ICDD no: 11-39]	Titanium phosphate [TiP_2O_7; ICDD no: 38-1468]
Ti7	Calcium phosphate [CaP_2O_6; ICDD no: 11-39]	Titanium phosphate [TiP_2O_7; ICDD no: 38-1468]

3.3.2.2. High temperature X-ray diffraction

Figures 3.4 and 3.5 show combination plots for iron and titanium phosphate glasses respectively where the DTA trace, ambient XRD spectrum and contour HTXRD plot have been included in the same graph. The HTXRD contours at 29° and 39° and shifting towards lower 2θ values can be attributed to the underlying platinum electrode and can be used for thermal expansion correction; the peaks for the platinum electrode are not always present due to the overlying glass powder sample sometimes being thicker.

The plots reveal close correlations between three distinct sets of experimental data, namely DTA, XRD and HTXRD. To illustrate using the Fe0/Ti0 plot (Figure 3.5(a)), the crystallisation peak in the DTA trace occurred at 593°C, which corresponded to a series of peaks at 2θ values of 20.5°, 23.2°, 25.5°, 27.3°, 27.9°, 29.1°, 29.3° and 34.4°. Analysis of the ambient XRD spectrum obtained for the sample crystallised at a temperature of 600°C revealed that $NaCa(PO_3)_3$ is formed at approximately the same 2θ values. Thus, we could reasonably demonstrate that the crystallisation peak at 593°C corresponds to the formation of $NaCa(PO_3)_3$ as the dominant phase in the glass. Using the same approach for the Ti1 glass (Figure 3.5(b)), it could be determined that the first and second crystallisation peaks, which significantly

overlap with each other, correspond to sodium calcium phosphate [$NaCa(PO_3)_3$; ICDD no.: 23-669] and calcium phosphate [CaP_2O_6; ICDD no.: 11-39] respectively. Similar results were obtained for the Fe1–5 and Ti3–7 glasses, although it should be noted that an increase in the TiO_2 content resulted in HTXRD plots with events occurring at higher temperatures; also, fewer such events were recorded in the HTXRD spectra and the correspondence between the sets of data was less clear. It should be noted that the T_m (in some cases more than one melting event) seen can be correlated to a particular crystalline phase melting and going back into solution; however, the complexity of the traces makes it difficult to interpret the sequence of events.

(a)

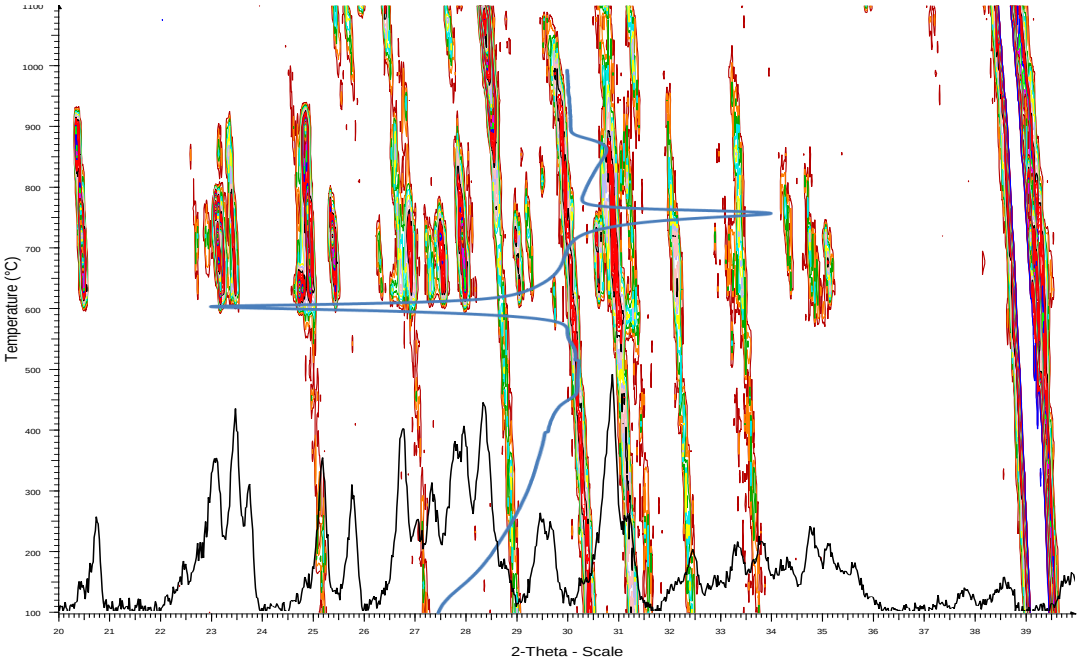

(b)

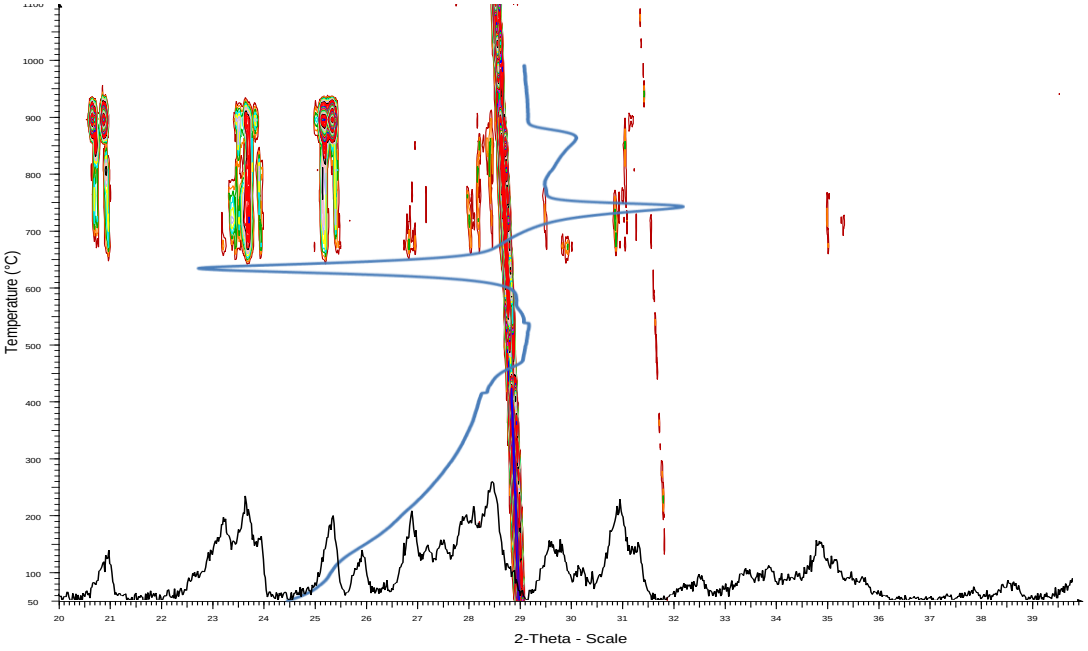

(c)

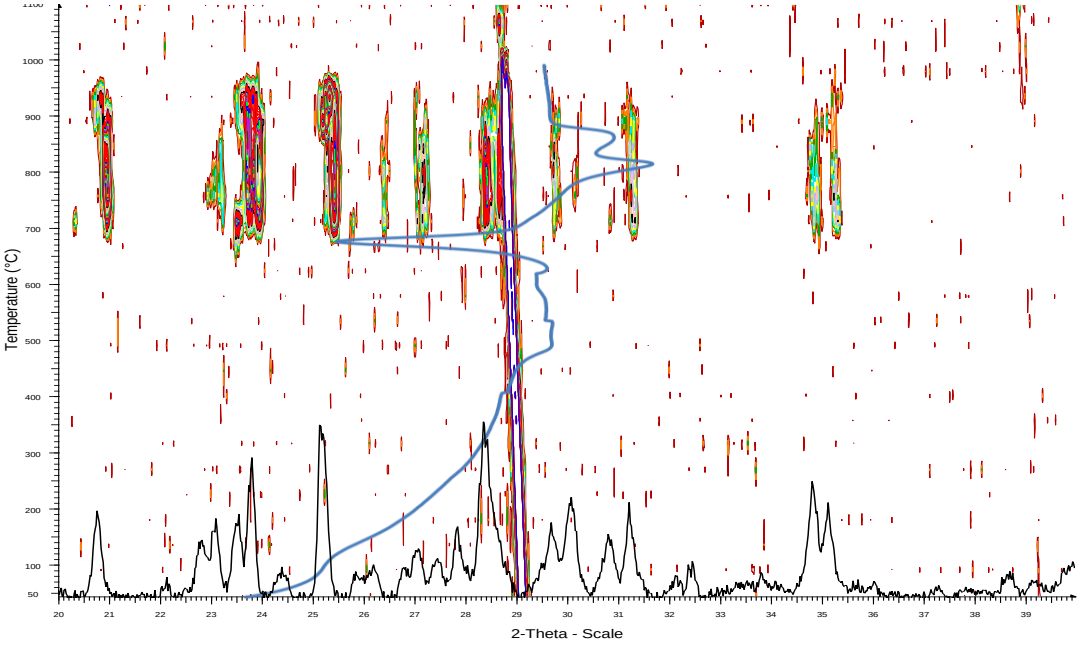

(d)

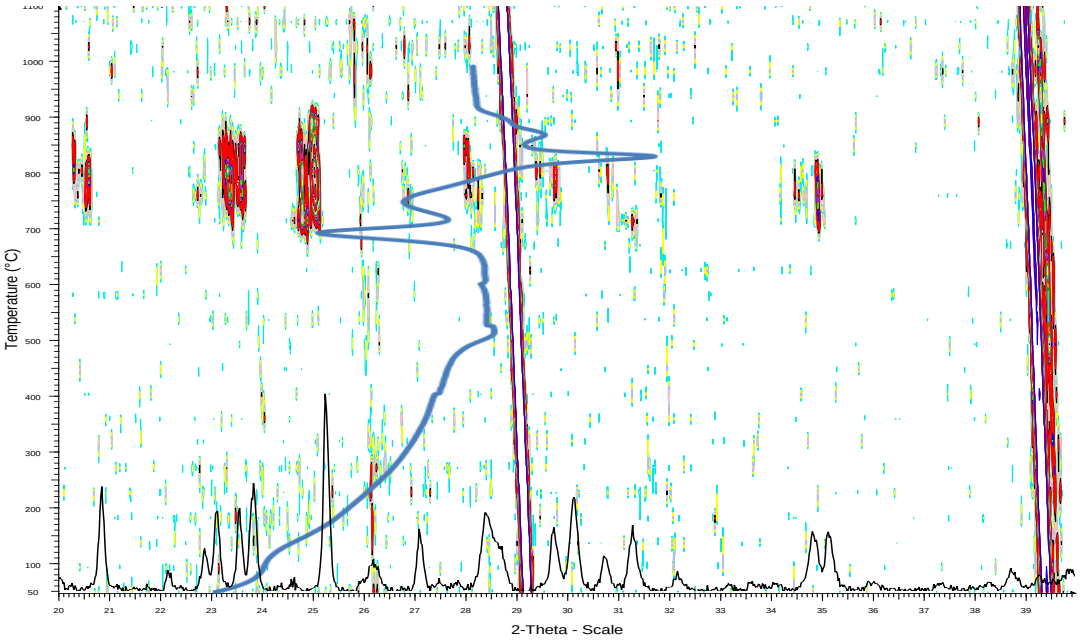

Figure 3.4. Combination plots of (a) Fe0, (b) Fe1, (c) Fe3 and (d) Fe5 glasses where DTA trace, ambient XRD spectrum and contour HTXRD plot are included in the same graph. The correlation between three distinct sets of experimental data can be observed. As the Fe_2O_3 content is increased, the HTXRD peaks are observed at higher temperatures and are fewer in number.

(a)

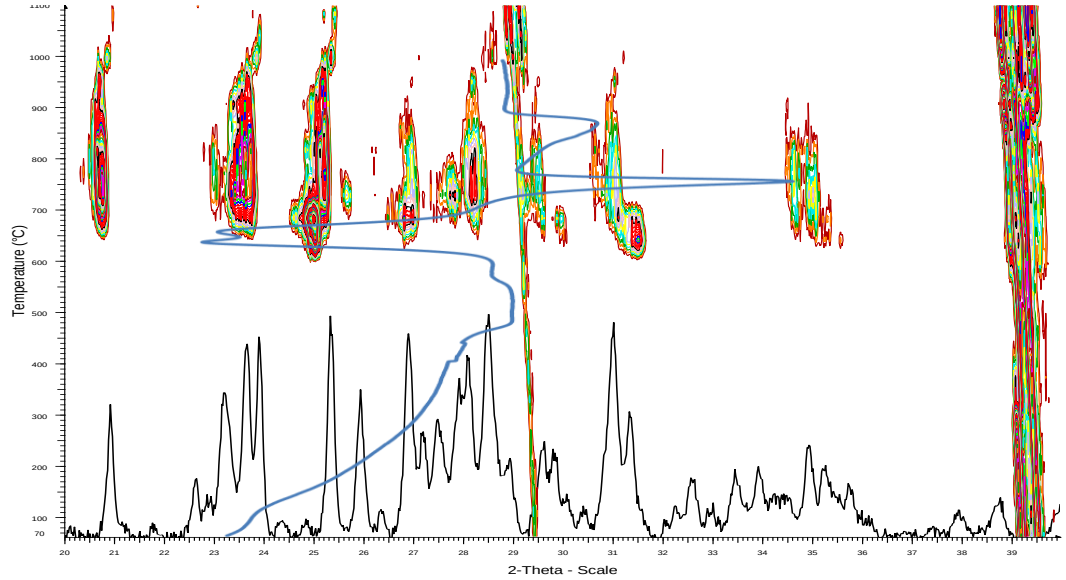

(b)

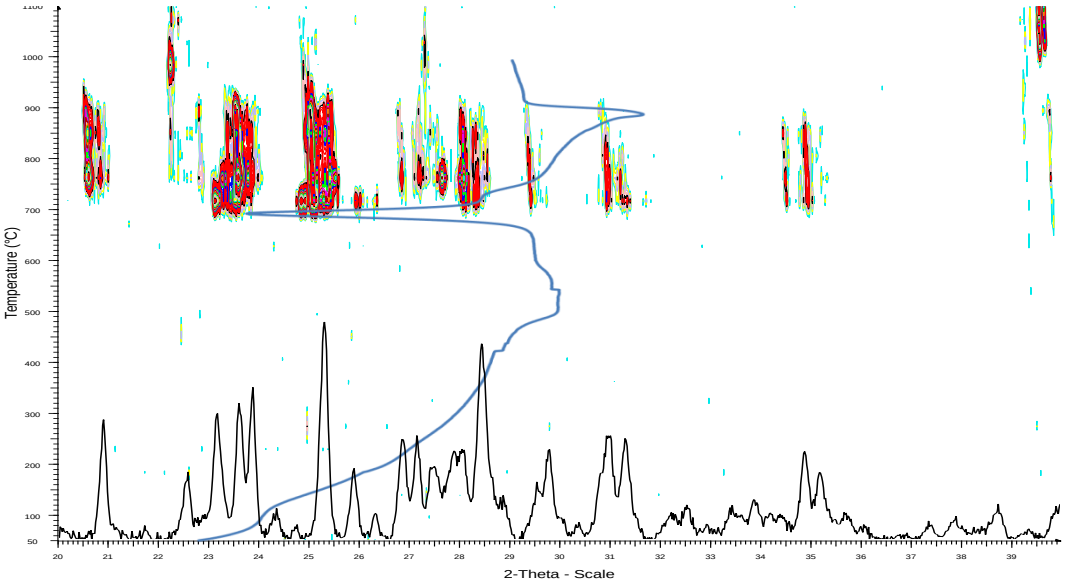

(c)

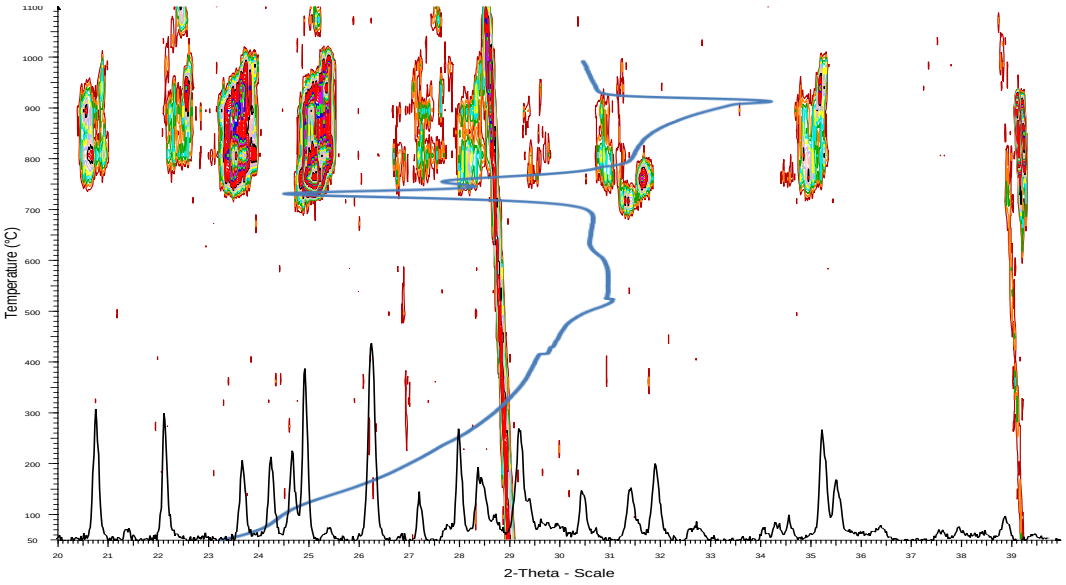

(d)

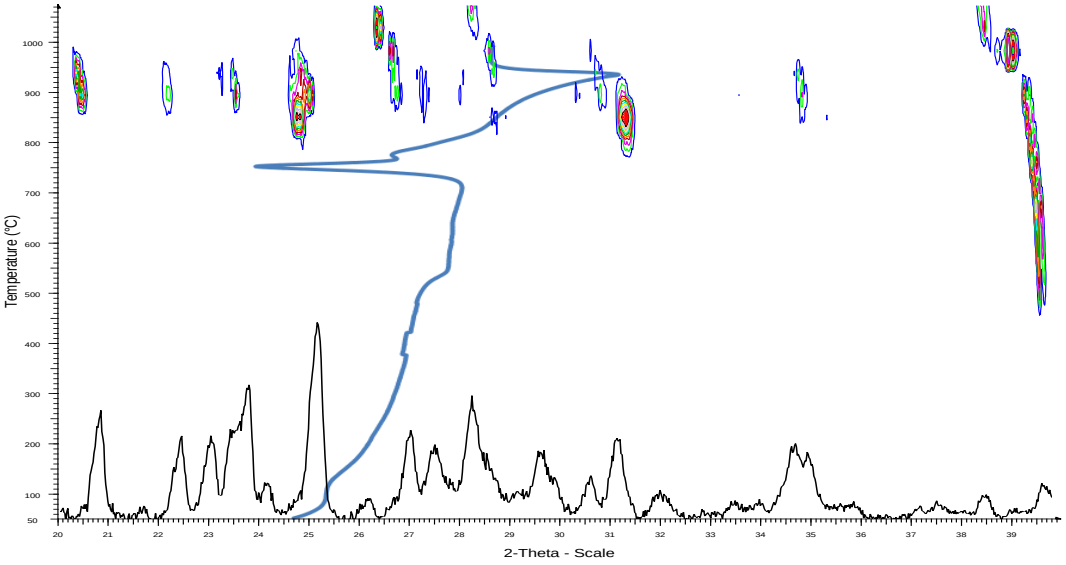

Figure 3.5. Combination plots of (a) Ti1, (b) Ti3, (c) Ti5 and (d) Ti7 glasses where DTA trace, ambient XRD spectrum and contour HTXRD plot are included in the same graph. As with the iron phosphate glasses, the correlation between three distinct sets of experimental data can be observed, with an increase in the TiO_2 content leading to a decrease in the number of HTXRD peaks which are observed at higher temperatures.

3.3.3. Solid state magic angle spinning nuclear magnetic resonance

3.3.3.1. ^{31}P MAS NMR

Figure 3.6 shows the ^{31}P MAS NMR spectra obtained for the investigated titanium phosphate glasses; asterisks denote spinning sidebands obtained in the spectrum. The ^{31}P MAS NMR spectra revealed that with increasing TiO_2 incorporation, no apparent significant change in the spectra could be observed. Spectral deconvolutions were performed using DmFit software, in which the ratio of the two resonances assigned as Q^1 and Q^2 was obtained by performing a fit of the observed resonance with Gaussian lineshapes and summing the intensities of the isotropic peaks and the full span of corresponding spinning sidebands. This deconvolution procedure provided information on the relative abundances (or relative intensities) of the Q^1 and Q^2 species present in the glasses (Figure 3.7) along with the associated chemical shifts (Figure 3.8) and linewidths (Figure 3.9). All these values are further tabulated in Table 3.3. The relative intensities of the Q^1 and Q^2 species were in the range of 0.97–1.49% and 98.51–99.03% respectively (Figure 3.7). Thus, the structural network of the investigated titanium phosphate glasses was predominantly comprised of Q^2 units. No significant trend could be discerned in the relative intensities with an increase in the TiO_2 content of the glass.

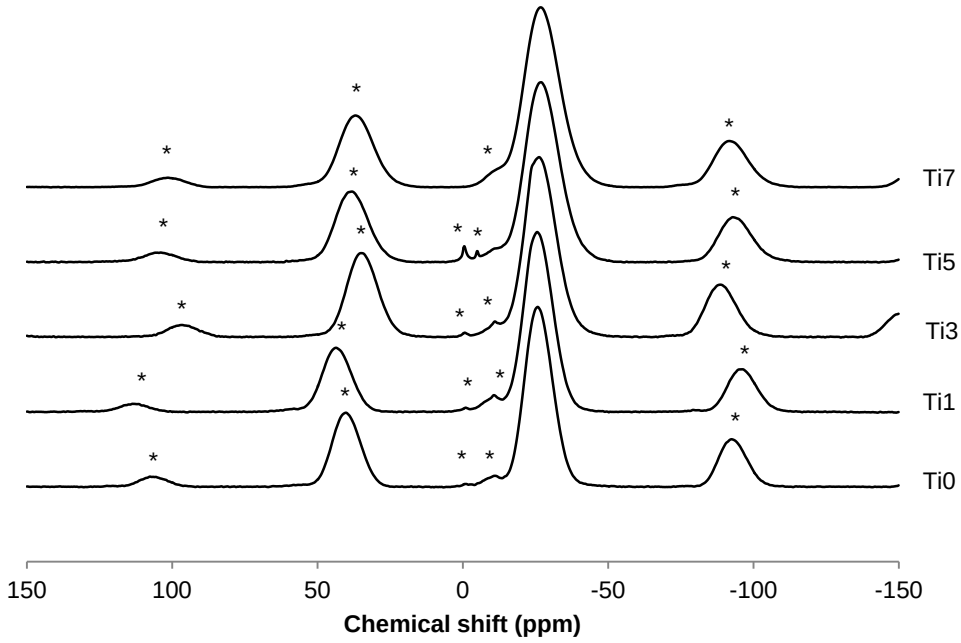

Figure 3.6. ^{31}P MAS NMR spectra obtained for the investigated titanium phosphate glass samples. Spinning sidebands are indicated by asterisks. No significant changes in the spectra can be discerned with an increase in the TiO_2 content.

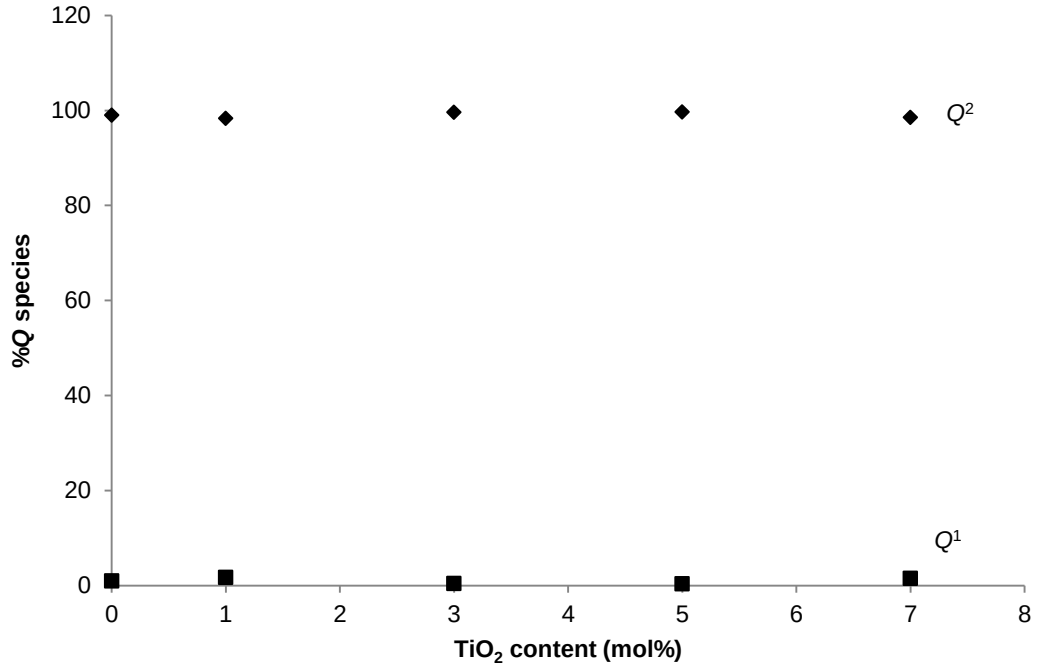

Figure 3.7. Relative abundance of Q^1 and Q^2 units in titanium phosphate glasses as a function of the TiO_2 content. Squares (■) denote Q^1 species and diamonds (♦) denote Q^2 species. Errors in Q^1 and Q^2 relative intensities are ±1% for all compositions as obtained from multiple fits of the ^{31}P NMR data using Dmfit software. Irrespective of the TiO_2 content, the glass structure is predominantly comprised of Q^2 species.

The chemical shifts associated with the Q^1 and Q^2 species showed upfield movement towards more negative values with an increase in the TiO_2 content of the glass (Figure 3.8). Thus, from Ti0 to Ti7, the Q^1 chemical shift moved from –8.66 ppm to –10.11 ppm while the Q^2 chemical shift moved from –25.57 ppm to –26.81 ppm (Table 3.3); it was observed that the Q^2 chemical shift was approx. 2–3 times greater than the Q^1 chemical shift. In addition, the linewidths associated with the Q^1 and Q^2 groups generally increased with the TiO_2 content (Figure 3.9). Consequently, from Ti0 to Ti7, the Q^1 linewidth increased from 3.19 ppm to 3.94 ppm, although it should be noted that a decrease in linewidth was observed from Ti1 to Ti3; further, the Q^2 linewidth increased from 10.56 ppm to 13.81 ppm. Thus, the Q^2 linewidth was approx. 3–4 times greater than the Q^1 linewidth.

(a)

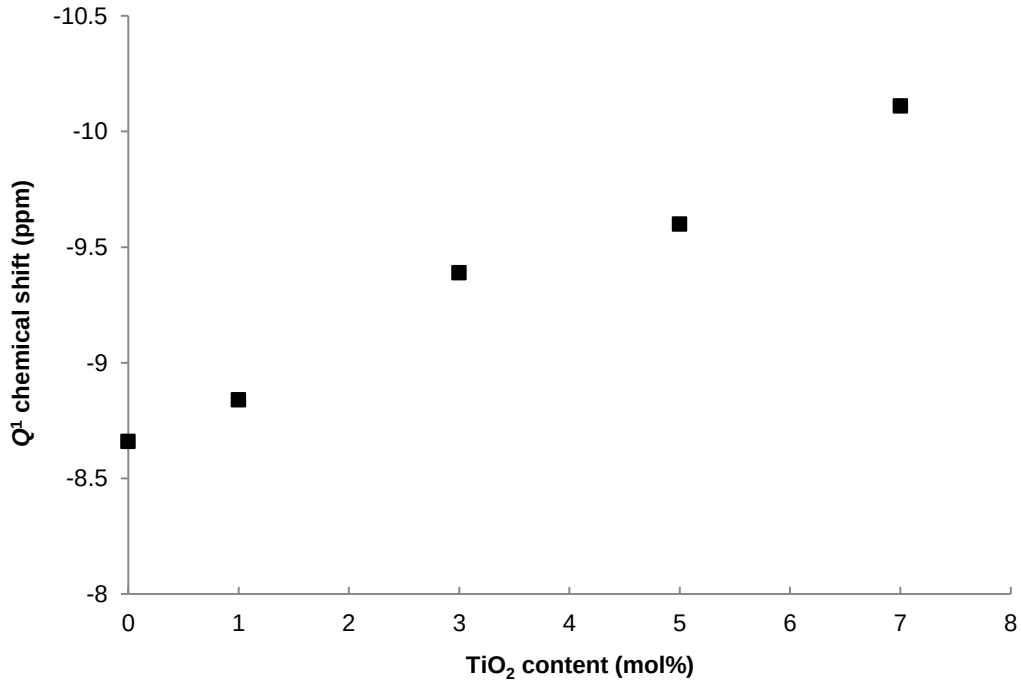
-10.5
-10
-9.5
-9
-8.5
-8
Q1 chemical shift (ppm)
0
1
2
3
4
5
6
7
8
TiO2 content (mol%)

(b)

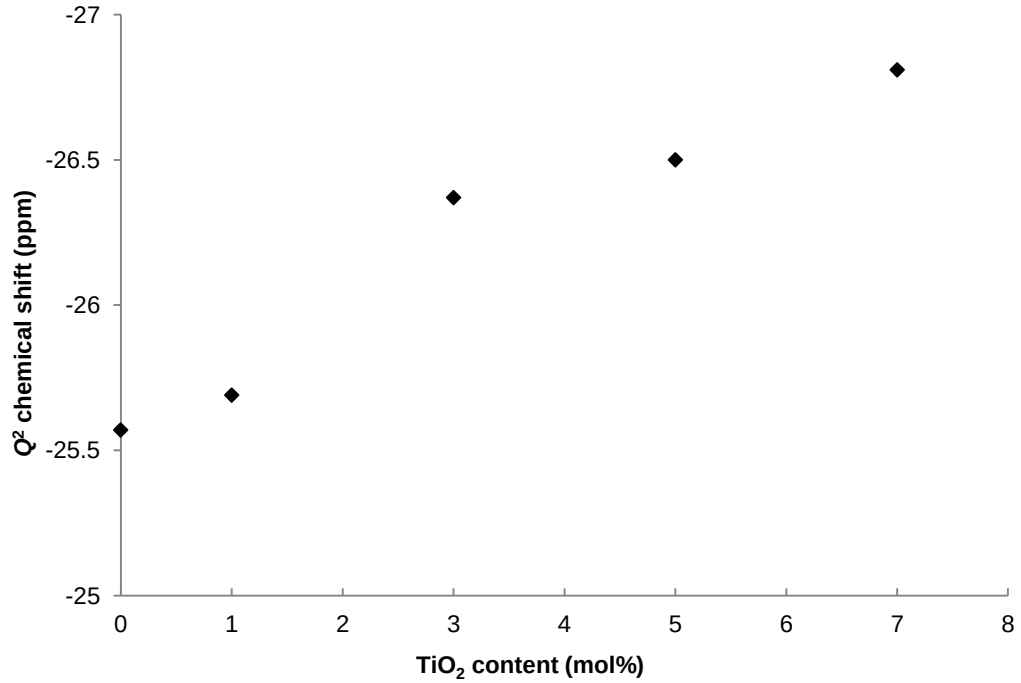
-27
-26.5
-26
-25.5
-25
Q2 chemical shift (ppm)
0
1
2
3
4
5
6
7
8
TiO2 content (mol%)

(c)

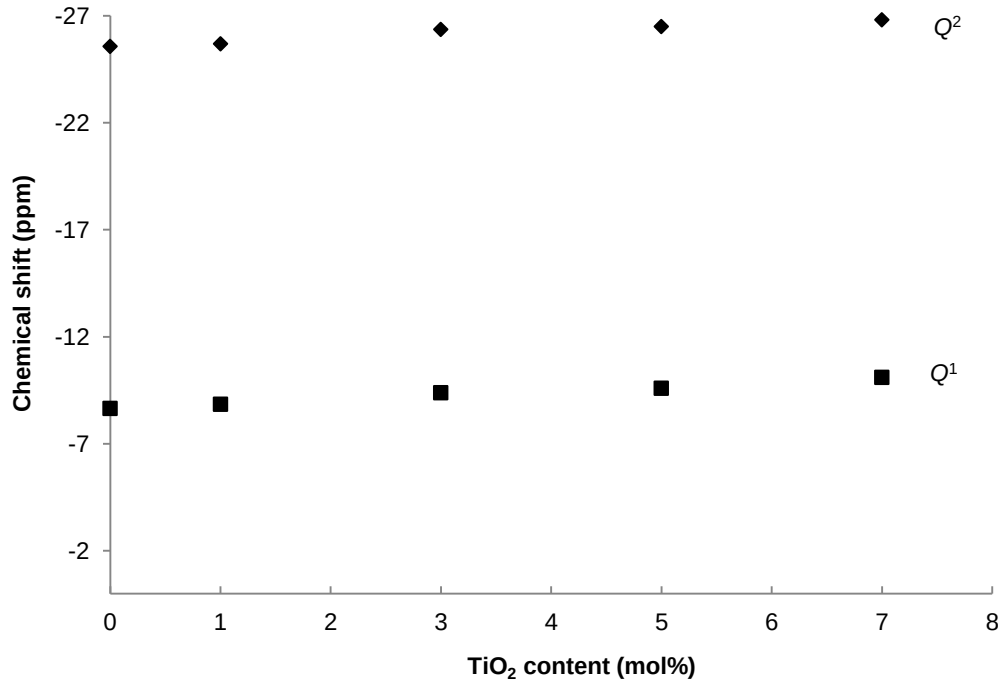

Figure 3.8. Isotropic chemical shift of (a) Q^1 and (b) Q^2 species as a function of the TiO_2 content of the investigated titanium phosphate glasses. (c) Relative isotropic chemical shift of Q species. Squares (■) denote Q^1 species and diamonds (♦) denote Q^2 species. Errors in Q^1 and Q^2 chemical shifts are ±0.5 ppm for all compositions as obtained from multiple fits of the ^{31}P NMR data using Dmfit software. The chemical shifts associated with both Q^1 and Q^2 species show upfield movement towards more negative values as the TiO_2 content is increased.

(a)

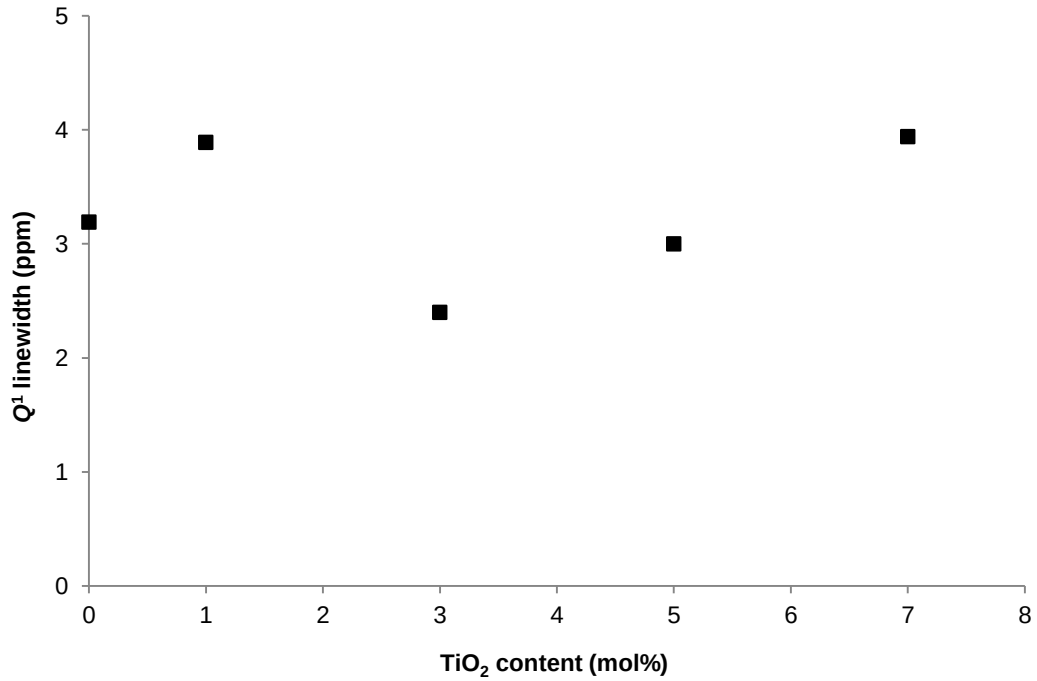
5
4
3
2
1
0
0
1
2
3
4
5
6
7
8
Q1 linewidth (ppm)
TiO2 content (mol%)

(b)

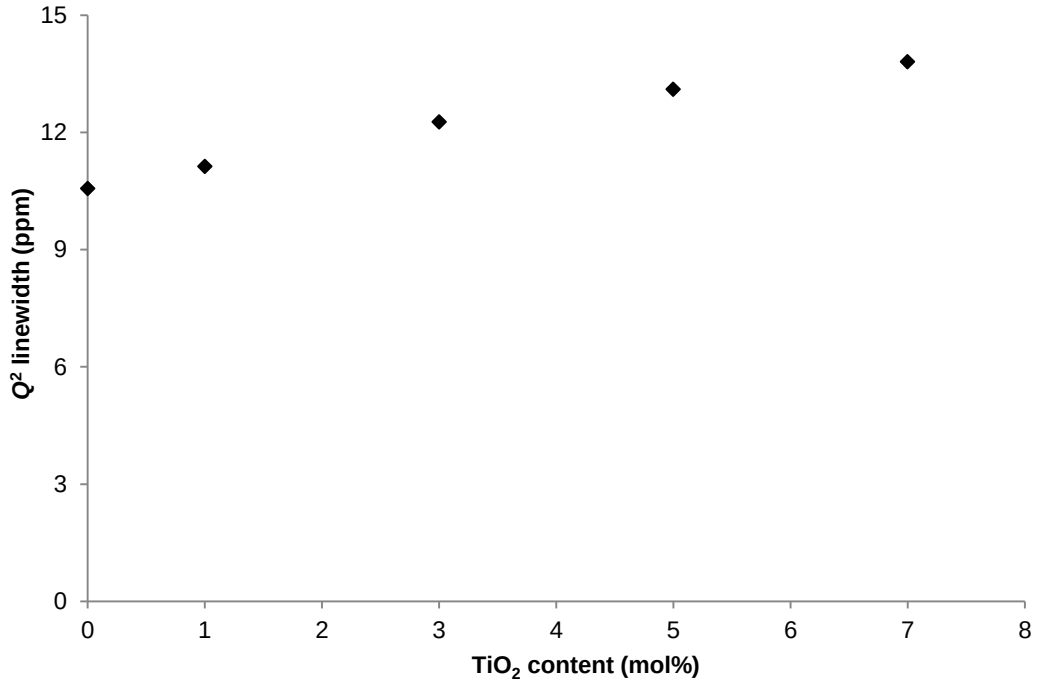
15
12
9
6
3
0
0
1
2
3
4
5
6
7
8
Q2 linewidth (ppm)
TiO2 content (mol%)

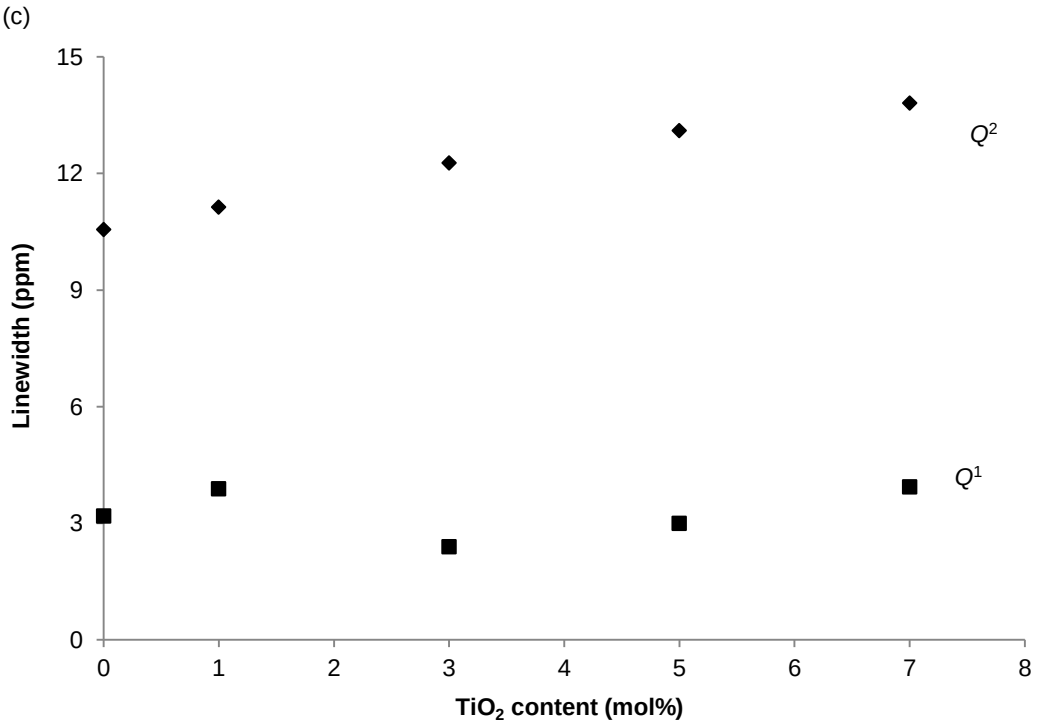

Figure 3.9. Variation in linewidth of (a) Q^1 and (b) Q^2 species as a function of the TiO_2 content of the investigated titanium phosphate glasses. (c) Relative variation in linewidth of Q species. Squares (■) denote Q^1 species and diamonds (♦) denote Q^2 species. Errors in linewidth values are ±0.5 ppm for all compositions as obtained from multiple fits of the ^{31}P NMR data using Dmfit software. The linewidths associated with the Q^1 and Q^2 groups generally increase with the TiO_2 content.

Table 3.3. Values of ^{31}P isotropic chemical shifts, linewidths and relative intensities for the investigated titanium phosphate glasses.

Glass	Q^1			Q^2		
	Chemical Shift (ppm)*	Linewidth (ppm)*	Relative intensity (%)**	Chemical Shift (ppm)	Linewidth (ppm)	Relative intensity (%)
Ti0	–8.66	3.19	0.97	–25.57	10.56	99.03
Ti1	–8.84	3.89	1.66	–25.69	11.13	98.34
Ti3	–9.39	2.40	0.41	–26.37	12.27	99.59
Ti5	–9.6	3.00	0.33	–26.50	13.10	99.67
Ti7	–10.11	3.94	1.49	–26.81	13.81	98.51

***Errors in Q^1 and Q^2 chemical shifts and linewidths are ±0.5 ppm for all compositions as obtained from multiple fits of the ^{31}P NMR data using Dmfit software.**
****Errors in Q^1 and Q^2 relative intensities are ±1% for all compositions as obtained from multiple fits of the ^{31}P NMR data using Dmfit software.**

One of the major objectives of the study was to compare the ^{31}P MAS NMR data obtained from the present study carried out on metaphosphate glasses (50 mol% P_2O_5) with corresponding data obtained from previous studies on quaternary P_2O_5–Na_2O–CaO–TiO_2 pyrophosphate glasses (45 mol% P_2O_5; (Kiani et al., 2010)) and ultraphosphate glasses (55 mol% P_2O_5; (Kiani et al., 2012a)) so as to obtain a more

comprehensive overview of titanium phosphate glass structure variations. Figure 3.10 shows the variation in the chemical shift and relative intensity of Q^1 species as a function of the TiO_2 content of the glass for quaternary P_2O_5–Na_2O–CaO–TiO_2 glasses containing 45 and 50 mol% P_2O_5. Note that data on Q^1 species in 55 mol% P_2O_5 glasses was not available since it was found that the structure of P_2O_5–Na_2O–CaO–TiO_2 glasses containing 55 mol% P_2O_5 was comprised of only Q^2 and Q^3 species (Kiani et al., 2012a). It was observed that both the 45 and 50 mol% P_2O_5 glasses showed an upfield movement in the Q^1 chemical shift towards more negative values as the TiO_2 content of the glass was increased. Thus, the Q^1 chemical shift in the 45 mol% P_2O_5 glass varied from –6.6 ppm at 0 mol% TiO_2 to –9.0 ppm at 5 mol% TiO_2 (and subsequently to –10.2 ppm at 15 mol% TiO_2; data not shown in graph), while that in the 50 mol% P_2O_5 glass varied from –8.6 ppm at 0 mol% TiO_2 to –9.6 ppm at 5 mol% TiO_2 (and subsequently to –10.11 ppm at 7 mol% TiO_2; data not shown). The magnitude of upfield Q^1 chemical shift in was greater in the 45 mol% P_2O_5 glass than in the 50 mol% P_2O_5 glass (54% vs. 17%). With regard to the relative abundance of Q^1 units, with an increase in the glass TiO_2 content, the Q^1 relative intensity showed a net downward trend in the 45 mol% P_2O_5 glass from 22% at 0 mol% TiO_2 to 16% at 5 mol% TiO_2 (and thereafter to 5% at 15 mol% TiO_2; data not shown in graph), while it remained relatively constant in the 50 mol% P_2O_5 glass within a narrow range of 0.9–2.5%.

(a)

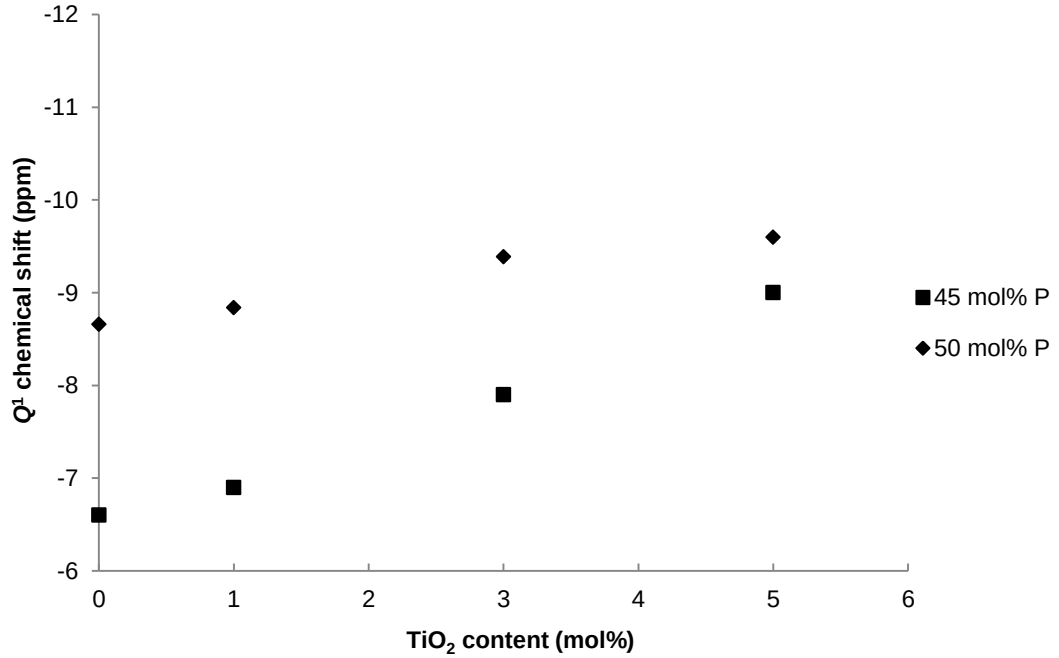

(b)

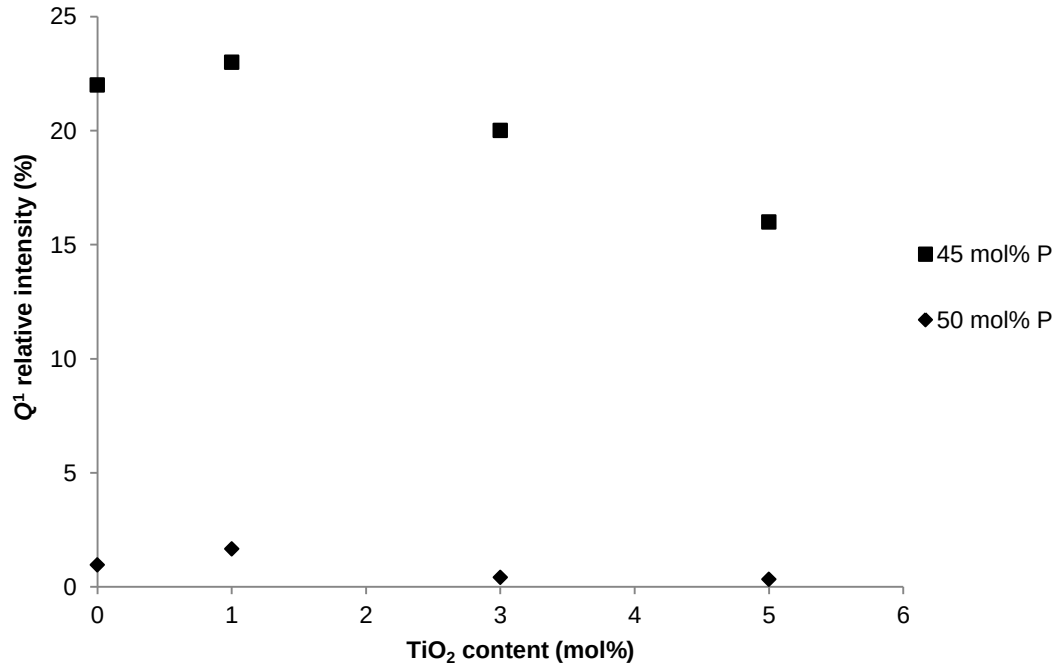

Figure 3.10. Variation in (a) chemical shift and (b) relative intensity of Q^1 species as a function of the TiO_2 content for titanium phosphate glasses containing 45 and 50 mol% P_2O_5 (data for 45 mol% P_2O_5 glass obtained from (Kiani et al., 2010); errors not shown for clarity). Both glass series show an upfield movement in the Q^1 chemical shift towards more negative values as the TiO_2 content is increased. The Q^1 relative intensity shows a net downward trend in the 45 mol% P_2O_5 glass but remains relatively constant in the 50 mol% P_2O_5 glass.

Figure 3.11 shows the variation in chemical shift and relative intensity of Q^2 species as a function of the TiO_2 content for titanium phosphate glasses containing 45, 50 and 55 mol% P_2O_5. With regard to the Q^2 chemical shift, all three glass series showed a steady upfield movement in the chemical shift towards more negative values with an increase in the TiO_2 content. Thus, the changes in the Q^2 chemical shift were as follows: (a) from –22.2 ppm at 0 mol% TiO_2 to –22.7 ppm at 5 mol% TiO_2 (and thereafter to –23.9 ppm at 15 mol% TiO_2; data not shown) in the 45 mol% P_2O_5 glass; (b) from –25.6 ppm at 0 mol% TiO_2 to –26.5 ppm at 5 mol% TiO_2 (and subsequently to –26.8 ppm at 7 mol% TiO_2; data not shown) in the 50 mol% P_2O_5 glass; and (c) from –25.7 ppm at 0 mol% TiO_2 to –26.1 ppm at 5 mol% TiO_2 in the 55 mol% P_2O_5 glass. All three glass series showed contrasting behaviour in terms of the abundance of Q^2 units in the glass structure as the TiO_2 content of the glass was increased. The 45 mol% P_2O_5 glass showed a net increase in the Q^2 relative intensity from 78% at 0 mol% TiO_2 to 84% at 5 mol% TiO_2 (and thereafter to 95% at 15 mol% TiO_2; data not shown). The Q^2 relative intensity values remained almost constant in the 50 mol% P_2O_5 glass within the range of 98–99%. A net decrease in the Q^2 relative intensity was observed in the 55 mol% TiO_2 glass from 72% at 0 mol% TiO_2 to 60% at 5 mol% TiO_2.

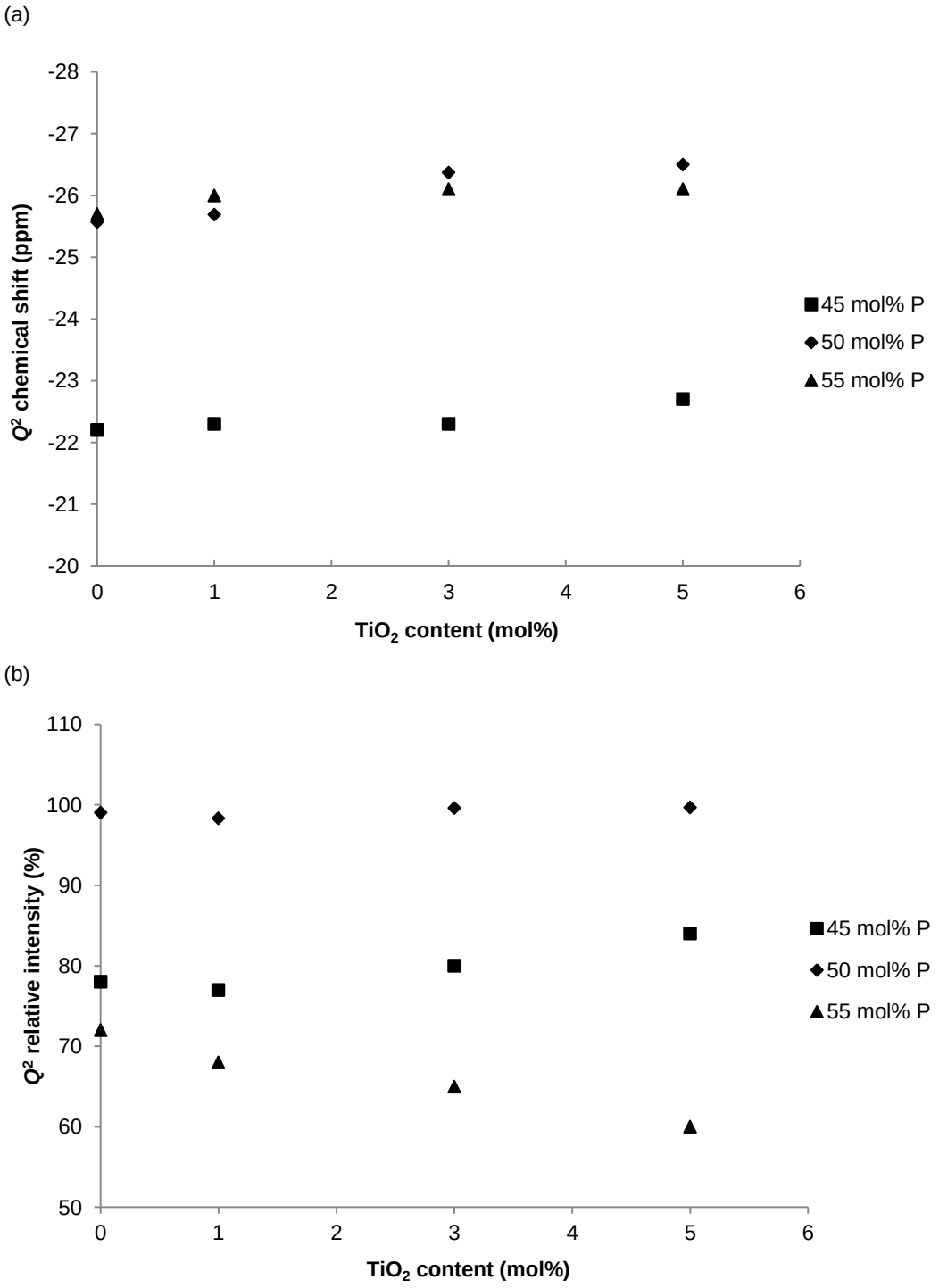

Figure 3.11. Variation in (a) chemical shift and (b) relative intensity of Q^2 species as a function of the TiO_2 content for titanium phosphate glasses containing 45, 50 and 55 mol% P_2O_5 (data for 45 and 55 mol% P_2O_5 glass obtained from (Kiani et al., 2010) and (Kiani et al., 2012a) respectively; errors not shown for clarity). As the TiO_2 content of the glass is increased, all three glass series exhibit upfield movement in the Q^2 chemical shift towards more negative values but show contrasting behaviour in terms of the abundance of Q^2 units in the glass structure.

3.3.3.2. ^{23}Na MAS NMR

Figure 3.12 shows the ^{23}Na MAS NMR spectra and simulations acquired for the investigated titanium phosphate glasses at two magnetic field strengths, 9.4 T and 14.1 T. The values of the chemical shift and quadrupolar coupling constant at the two magnetic field strengths are listed in Table 3.4. The spectra of all the investigated glasses revealed a single broad peak that was slightly asymmetric in nature, with a tail on the low frequency side (i.e. towards more negative ppm values). The spectra were lacking in any recognisable resolution and an increase in the TiO_2 content did not cause an appreciable change in the spectra. When the magnetic field strength was increased from 9.4 T to 14.1 T, the chemical shift underwent an upfield movement towards more negative values (Table 3.4). For instance, the chemical shift value for Ti0 changed from –4.98 ppm at 9.4 T to –8.35 ppm at 14.1 T. At both 9.4 and 14.1 T field strengths, an increase in the TiO_2 content of the glass was associated with an upfield movement of the chemical shift. Thus, the chemical shift changed from –4.98 ppm in Ti0 to –7.35 ppm in Ti7 when a field strength of 9.4 T was used, while it changed from –8.35 ppm in Ti0 to –10.75 ppm in Ti7 when a field strength of 14.1 T was used. Deconvolution procedures carried out using QuadFit software enabled the calculation of the quadrupolar coupling constant value. The quadrupolar coupling constant value revealed a net decrease with an increase in the TiO_2 content of the glass from 2.58 for the Ti0 glass to 2.16 for the Ti7 glass (Table 3.4).

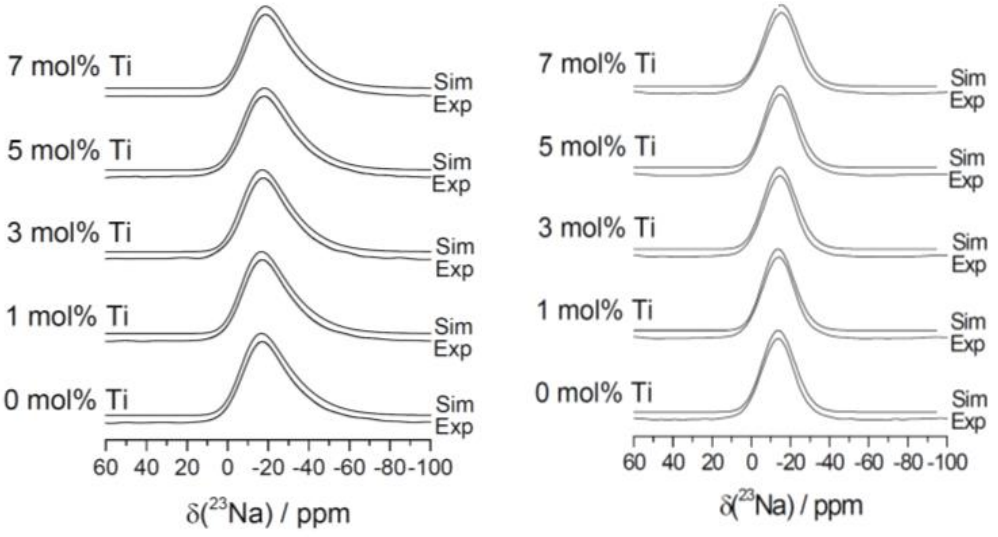

Figure 3.12. ^{23}Na MAS NMR spectra and simulations acquired for the investigated titanium phosphate glasses at (a) 9.4 T and (b) 14.1 T. The simulations were performed using QuadFit. All the spectra show a single, broad, slightly asymmetric peak lacking in any recognisable resolution with no appreciable change as the TiO_2 content is increased.

Table 3.4. Summary of chemical shift and quadrupolar coupling constant values for the investigated titanium phosphate glasses.

Glass	Chemical shift (ppm)		Quadrupolar coupling constant
	Field strength = 9.4 T	Field strength = 14.1 T	
Ti0	–4.98	–8.35	2.58
Ti1	–5.21	–8.51	2.55
Ti3	–5.92	–9.62	2.44
Ti5	–6.40	–10.10	2.46
Ti7	–7.35	–10.75	2.39

3.3.4. Ti *K*-edge X-ray near edge absorption

Figure 3.13 shows a normalised plot of the Ti *K*-edge XANES spectra of the investigated titanium phosphate glasses along with a magnified view of the pre-peak between energies of 4965 and 4980 eV. The normalised spectra for the glasses were similar in appearance regardless of the TiO_2 content of the glass. The pre-edge data for all of the samples comprised two small peaks at 4968 and 4970 eV with normalized intensities of 0.08 and 0.05 respectively. These results were consistent with Ti occupying a six-fold coordinated (TiO_6) environment.

One of the objectives of the XANES study was to compare the Ti local environments in glasses with different P_2O_5 contents. For this purpose, a constant TiO_2 content of 5 mol% was considered. In addition to the present XANES study on 50 mol% P_2O_5 glasses, XANES experiments were carried out on two quaternary P_2O_5–CaO–Na_2O–TiO_2 glasses with 45 and 55 mol% P_2O_5, each containing 5 mol% TiO_2. Data obtained from these additional samples was compared with the Ti5 XANES data (Figure 3.14). As in the earlier XANES results, two small peaks at 4968 and 4970 eV with normalized intensities of 0.08 and 0.05 respectively were observed in the pre-edge data, which implied the existence of a six-fold coordinated Ti environment in the glasses.

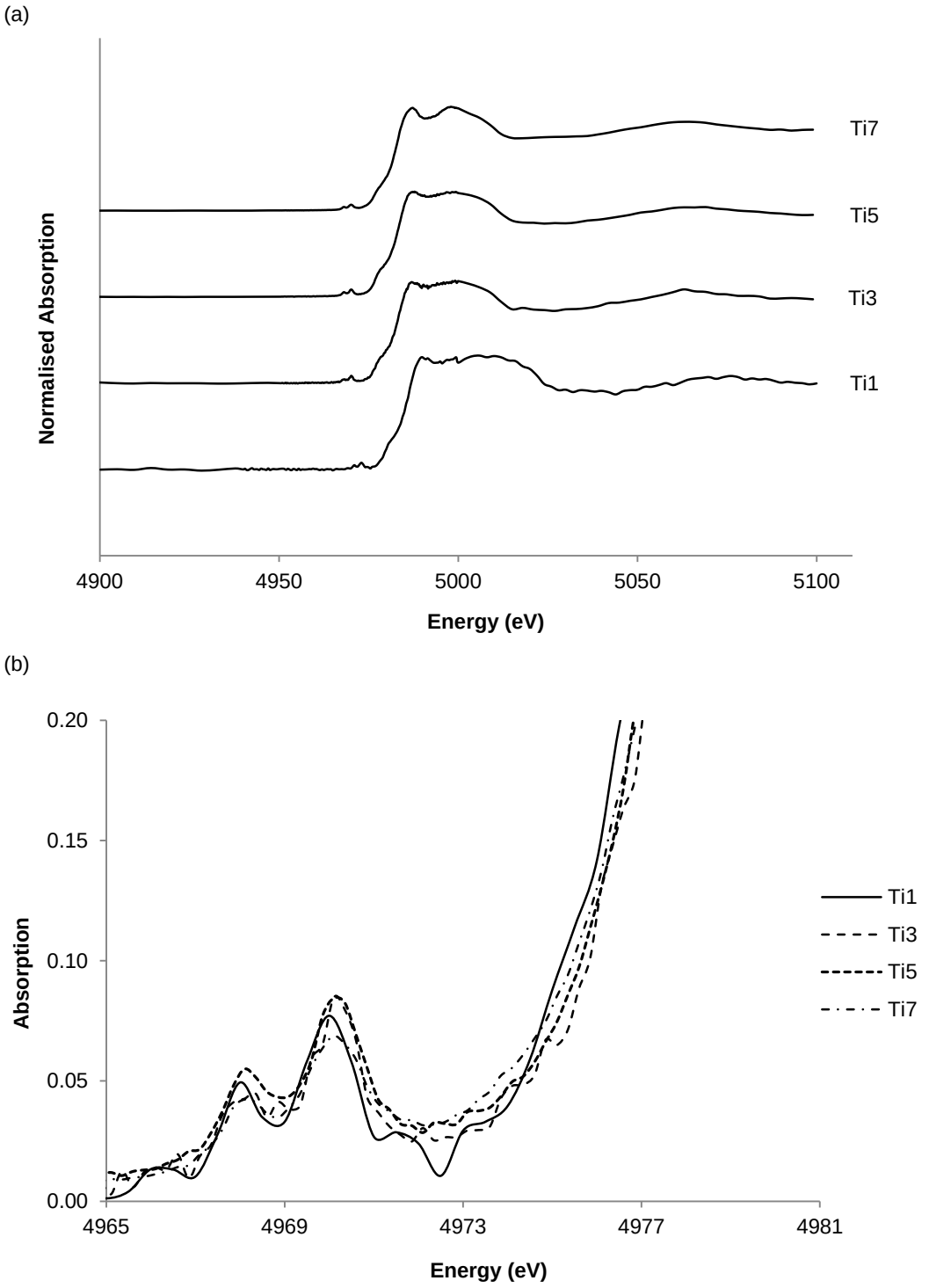

Figure 3.13. (a) Titanium *K*-edge X-ray absorption near edge structure spectra of the investigated titanium phosphate glasses (the data sets are offset for clarity). (b) Magnified view of pre-peak between 4965 and 4980 eV. Two small peaks are observed at 4968 and 4970 eV with normalized intensities of 0.08 and 0.05 respectively, indicating the Ti atom occupies a six-fold coordinated (TiO_6) environment in all the glasses.

(a)

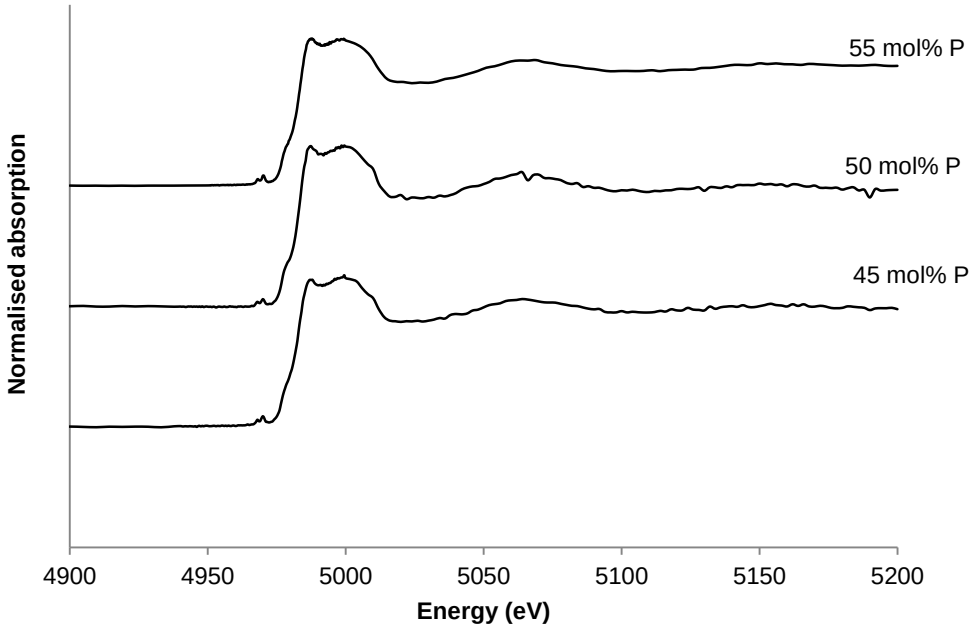

(b)

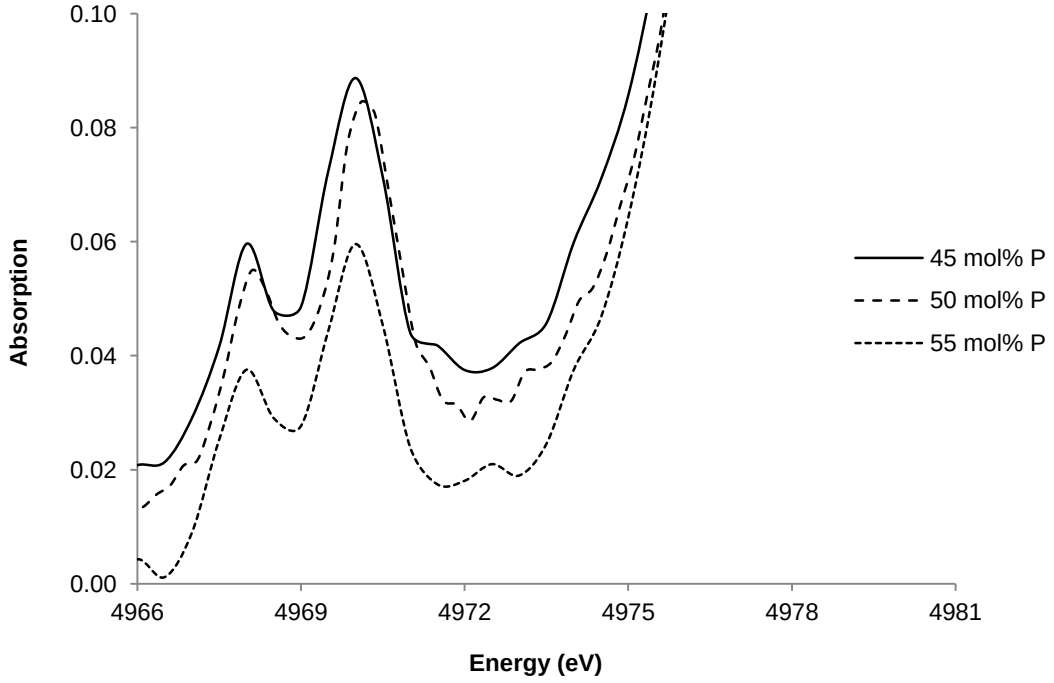

Figure 3.14. (a) Titanium *K*-edge X-ray absorption near edge structure spectra of titanium phosphate glasses having P_2O_5 contents of 45, 50 and 55 mol% and constant TiO_2 content of 5 mol% (the data sets are offset for clarity). (b) Magnified view of pre-peak between 4965 and 4980 eV. The peaks at 4968 and 4970 eV with normalized intensities of 0.08 and 0.05 respectively imply a six-fold coordinated (TiO_6) environment for the Ti atom in all the glasses.

3.4. Discussion

The objectives of this chapter were two-fold. The first objective was to probe the structure of the investigated glasses using progressively powerful techniques such as FTIR, XRD, MAS NMR and XANES so as to gain a deeper understanding of the glass structural features that underpin the glass physicochemical properties that were studied in the previous chapter. The second objective, which focused on the titanium phosphate glasses, was to correlate the glass structural variations for three different quaternary P_2O_5–CaO–Na_2O–TiO_2 glass series where the P_2O_5 content was varied from pyrophosphate (45 mol% P_2O_5; results obtained from (Kiani et al., 2010)) to metaphosphate (50 mol% P_2O_5; results obtained from the present study) and finally to ultraphosphate (55 mol% P_2O_5; results obtained from (Kiani et al., 2012a)).

In the case of the titanium phosphate glasses, the FTIR results are broadly in agreement with those obtained in previous studies by Abou Neel et al. that focused on similar compositions (Abou Neel et al., 2009a); similar results were obtained for the iron phosphate glasses as well, which implies similar effects of metal oxide addition in general on the FTIR spectra. The presence of peaks associated only with phosphate groups in the FTIR spectra—or in other words the absence of groups other than phosphate species—is to be expected since phosphate species comprise the greatest proportion of the glass network; the maximum metal oxide content of the investigated glasses is 5 mol% Fe_2O_3 or 7 mol% TiO_2, which is not considered sufficiently high for groups other than phosphates to be visible in the spectra. This also explains why the changes in the FTIR spectra with metal oxide addition are subtle in nature. From a general perspective, the incorporation of Fe_2O_3 or TiO_2 in the glass structure at the expense of Na_2O should increase the O/P ratio and lead to more Q^1 units being introduced in the glass structure in place of Q^2 units; however, as observed in the ^{31}P NMR results, the changes in the Q^1 and Q^2 proportions are so small that it can safely be considered that the glass maintains its metaphosphate character for all the investigated glasses.

With regard to the ambient XRD results obtained for the as-prepared samples, the absence of crystalline phases and the presence of broad peaks at 2θ values of around 20–40° are expected results and they indicate that all the prepared glasses are amorphous in nature, thereby demonstrating the success of the glass preparation process. In the XRD spectra of the crystallised samples, the transition in the main phase from $NaCa(PO_3)_3$ to CaP_2O_6 as the metal oxide content is increased

is in agreement with previous studies (Abou Neel et al., 2009a, Kiani et al., 2012a) and is attributable to the changes in the relative proportions of Na_2O and CaO in the glass. This is because in the investigated phosphate glasses, the Na_2O content of the glasses decreases from 10 mol% to 3–5 mol% as Fe_2O_3 or TiO_2 is incorporated into the glass at the expense of Na_2O, whereas the P_2O_5 and CaO contents remain constant at 50 mol% and 40 mol% respectively.

The DTA/XRD/HTXRD combination plots provide useful correlations between three sets of distinct but complementary experimental results. Such correlations have been reported previously in studies on phosphate glasses (Lakhkar et al., 2010, Pickup et al., 2007b). In the study by Lakhkar et al. (Lakhkar et al., 2010), one of the reported advantages of this approach was the ability to identify phases at higher temperatures (i.e. above the T_{c1} value); however, it was difficult to carry out such an identification for the glasses in the present study on account of an insufficient number of events in the HTXRD contour plot that could correspond to the XRD peaks in Figures 3.4 and 3.5 and also because of the overlap between the crystallisation peaks in most of the DTA graphs. There was also significant shift due to thermal expansion which further complicated the pattern analysis. However, it was in general possible to correlate the peaks in the HTXRD with thermal events seen in the DTA data.

^{31}P MAS NMR data are of particular significance in understanding the titanium phosphate glass structure since they provide valuable information about the local phosphorus environment; furthermore, the chemical shifts exhibit high sensitivity to changes in glass composition. It should be noted that in the present study, ^{31}P MAS NMR spectra have been obtained for the titanium phosphate glasses only; it is difficult to obtain NMR data for iron phosphate glasses because of the paramagnetic nature of these glasses. The investigated titanium phosphate glasses are dominated by Q^2 species (98–99%) with very little Q^1 species present (1–2%) (Figure 3.7). This result has been reported previously both for quaternary P_2O_5–CaO–Na_2O–TiO_2 glasses (Abou Neel et al., 2009a) and, at a more fundamental level, for binary P_2O_5–Na_2O glasses (Brow et al., 1990) and it has been attributed to the metaphosphate composition of these glasses wherein the P_2O_5 content of the glasses is 50 mol%.

At 50 mol% P_2O_5, it is considered that the glass comprises infinitely long chains of phosphate tetrahedra, although a small proportion of the tetrahedra may be linked

to form chain-limiting ring structures; however, the overall *Q* species distribution remains unaffected by the type of arrangement of tetrahedra. As the TiO_2 content of the glass is increased, the relative proportions of *Q* species do not undergo any significant change, which implies that the phosphorus environment in metaphosphate glasses remains unaffected by TiO_2 incorporation. From a quantitative perspective, the average P–O–P coordination (N_{P-O-P}) is defined as follows:

$$N_{P-O-P} = f_Q^1 + 2f_Q^2 \quad (1)$$

where f_Q^n denotes the fraction of the Q^n group.

The N_{P-O-P} value serves as a measure of the glass connectivity; for instance, a value of 2 means that the glass is composed entirely of polymerised chains of Q^2 species. As the TiO_2 content of the investigated glasses is increased, the N_{P-O-P} value remains relatively constant within the narrow range of 1.98–1.99. Thus, the quantitative results lend credence to the observation of a structure that is strongly dominated by Q^2 units such that the P–O–P connectivity is negligibly affected by TiO_2 incorporation.

^{31}P isotropic chemical shifts provide information regarding the local bonding arrangements in the glass in terms of both the covalent bonding and the ionic interactions with cations such as Na^+, Ca^{2+} and Ti^{4+}. There are three possible factors that can help explain the Q^1 and Q^2 chemical shifts: (a) the number of bonded ligands and their electronegativities, (b) the P–O–P bond angles and (c) the covalent (π bond) character of the phosphate-ligand bond (Brow et al., 1990). It is considered that the contribution from factors (a) and (b) are not sufficient to fully explain the difference, especially the 2–3 fold difference between the Q^1 and Q^2 chemical shift values for the same composition. It is believed that the increase in the π bond character provides a better explanation for the chemical shift behaviour.

In the present study, incorporation of increasing amounts of TiO_2 in the glass leads to a monotonic upfield movement of the chemical shift towards more negative values (Figure 3.8) as well as an increase in the linewidth (Figure 3.9). Several previous studies have observed this trend (Franks et al., 2000, Brow, 2000, Carta et al., 2007a, Carta et al., 2007b, Pickup et al., 2007a, Kiani et al., 2010, Kiani et al., 2012a, Walter et al., 2001) and have attributed it to the formation of P–O–Ti bonds in the glass network. These P–O–Ti bonds serve to increase the extent of cross-

linking in the glass structure and are, in effect, responsible for the glass structural densification and associated degradation rate reduction observed in the previous chapter. To elaborate, Ti^{4+} ions in quaternary P_2O_5–CaO–Na_2O–TiO_2 glasses are able to form cross-links between several oxygen sites present in the glass network; in contrast, the Na^+ ions in ternary P_2O_5–CaO–Na_2O glasses can only interact with non-bonding oxygen atoms while the Ca^{2+} ions cannot form cross-links to the same extent as Ti^{4+} ions because of their lower charge. Increasing incorporation of TiO_2 causes the phosphate network to become more condensed and rigid. Under these conditions, the charge on the oxygen atoms is displaced away from the P–O bonds (i.e. their covalent character increases) and the nuclei become more shielded (in other words, displaced towards a lower frequency), thus resulting in the upfield movement of the chemical shift.

The linewidth associated with the ^{31}P MAS NMR resonances is a measure of the level of disorder in the glass system. The increase in the linewidth of both Q^1 and Q^2 species with the TiO_2 content has been observed previously (Franks et al., 2000, Abou Neel et al., 2009a, Kiani et al., 2010, Kiani et al., 2012a). It indicates the increased disorder in the glass structure as increasing amounts of TiO_2 are added to the system. A low TiO_2 content in the glass corresponds to a lower degree of cross-linking, which leads to the formation of small structural arrangements which permit a greater degree of local ordering. The addition of increasing amounts of Ti^{4+} ions to the system gives rise to more possible bonding arrangements and thus a more rigid and condensed network.

The comparison of the results of the present study on metaphosphate glasses (containing 50 mol% P_2O_5) with those previously obtained from pyrophosphate glasses and ultraphosphate glasses (containing 45 and 55 mol% P_2O_5 respectively) gives rise to several interesting observations that facilitate an overall understanding of the way in which the titanium phosphate glass structure evolves as the phosphate content is varied. All three glass series are mainly comprised of Q^2 units, with the 45 and 50 mol% P_2O_5 series glasses consisting of additional Q^1 units and the 55 mol% P_2O_5 series glasses consisting of additional Q^3 units. This observation is in agreement with those of Brow et al. who focused on varying the P_2O_5 content of binary P_2O_5–Na_2O glasses between 44 and 75 mol% (Brow et al., 1990). In the Q^1 species, the upfield movement of the chemical shift is stronger for the 45 mol% glasses than for the 50 mol% glasses (Figure 3.10(a)), indicating a stronger effect of interactions with the Ti^{4+} ion in the pyrophosphate glasses. The most interesting

result is the trend of variation in the Q^2 relative intensity for the three glass series (Figure 3.11(b)). As mentioned previously for binary P_2O_5–Na_2O glasses (Brow, 2000, Brow et al., 1990), the addition of modifier oxides (in this case TiO_2) is associated with structural disruption arising from the breaking of bridging oxygen bonds to form non-bridging oxygens so that the cation and extra oxygen can be accommodated. In the case of the 55 mol% P_2O_5 glasses, this structural disruption (or depolymerisation) causes cross-linked Q^3 units to be converted to chain-like Q^2 units, whereas in the 45 mol% P_2O glasses, the Q^2 units are converted to depolymerised Q^1 units. The Q^1 and Q^2 intensities remain fairly constant in the metaphosphate 50 mol% P_2O_5 glass series; it seems that the metaphosphate glass series lies along a compositional boundary, and glass series on either side of this boundary exhibit significant variations in Q speciation with TiO_2 playing the role of a network former. TiO_2 evidently does not play the same role in the metaphosphate glasses as it does in the pyrophosphate and ultraphosphate glasses, and further research is required to elucidate the reasons for this.

With regard to the ^{23}Na NMR spectra, the presence of a single broad resonance lacking in resolution with a tailed distribution towards lower frequency is in agreement with previous results on titanium phosphate glasses as well on metal oxide–doped phosphate glasses in general (Smith and van Eck, 1999, MacKenzie and Smith, 2002a, Valappil et al., 2008, Abou Neel et al., 2009a, Kiani et al., 2010, Kiani et al., 2012a) and is expected for second-order quadrupolar lineshapes which are commonly observed in glasses. The lack of any change in the spectra with variations in the TiO_2 content suggests that TiO_2 incorporation has no significant effect on the local Na environment even though Ti^{4+} ions are introduced in the glass structure at the expense of Na^+ ions. As the strength of the magnetic field is increased, the resonance peaks become narrower and are shifted towards more negative values. It is considered that an increase in the magnetic field strength leads to a decrease in the second-order quadrupolar effect, thereby implying that the ^{23}Na resonances have a significant quadrupolar contribution. The quadrupolar interactions also provide an explanation for the tailed distribution at lower frequencies, which indicate the existence of a range of sodium local environments in the glasses. The upfield movement in the isotropic chemical shift values with the increase in the TiO_2 content can be explained by the spatial condensation of the glass network whereby the average Na–O bond length decreases; the decrease in the bond length leads to an increase in the shielding effect, resulting in the movement of the isotropic shift towards more negative values (i.e. lower

frequencies) (Xue and Stebbins, 1993, Koller et al., 1994).

The Ti *K*-edge XANES results are largely in agreement with those of a previous study carried out on melt-quenched and sol-gel derived titanium phosphate glasses (Pickup et al., 2008a) wherein all the investigated glass compositions exhibit a six-fold coordinated Ti environment comprising TiO_6 units. Previous studies have shown that the relative height of the pre-peak is ~0.9(1) for 4-fold Ti and ~0.4 to 0.7 for 5-fold Ti (Farges et al., 1996). The absence of this sharp pre-edge feature at ~4970 eV in the present study therefore excludes the possibility of a significant proportion of Ti occupying either a 4- or 5-fold coordinated environment. This is observed for the 45 and 55 mol% P_2O_5 glasses as well, thereby revealing that the nature of Ti coordination in the glasses is independent of either the TiO_2 content or the P_2O_5 content. In fact, it has also been revealed that the Ti environment is resilient even to degradation processes that occur when the glasses are immersed in deionised water over a period of several weeks (Pickup et al., 2008a).

Thus, the results presented in this chapter provide an analysis of the structure of the investigated iron and titanium phosphate glasses and offer very useful correlations between the glass physicochemical properties on the one hand and the glass structure on the other. Such correlations are important for biomaterials scientists who can then use the knowledge thus obtained to make informed decisions regarding the suitability of particular glass compositions for specific clinical applications. As will be described in the next chapter, the results obtained thus far have important implications for the interactions between glass microspheres and cells under different *in vitro* environments.

Chapter 4. Interactions between microspheres and MG63 osteosarcoma cells

4.1. Introduction

This chapter focused on initial cell culture experiments to investigate the interactions between the developed phosphate glass microspheres (PGMs) and MG63 osteosarcoma cells under both static and dynamic environments. MG63 cells were selected since these cells have been commonly used in order to establish at least the preliminary aspects of biocompatibility for a wide range of phosphate glasses and other materials (Clover and Gowen, 1994, Bachle and Kohal, 2004, Abou Neel et al., 2009d, Kiani et al., 2012b). Cell culture in static environments was performed using two different types of systems, namely permeable mesh well inserts and ultra-low attachment multiwell tissue culture plates. Cell culture under dynamic environments was carried out using spinner flask bioreactors. In both cases, cell culture was carried out over a 7 day period with time points of 1, 4 and 7 days in most instances. Imaging of the cultured samples was carried out using scanning electron microscopy (SEM) and confocal laser scanning microscopy (CLSM), while cell proliferation was quantified using a Cell Counting Kit-8 (CCK-8) cell proliferation assay. The major objectives of the study were (1) to determine the biocompatibility of the materials, (2) to investigate the cell–microsphere interactions for microspheres of all the investigated compositions (Fe0/Ti0, Fe1, Fe3, Fe5, Ti1, Ti3, Ti5 and Ti7) so as to select one composition that would elicit the most favourable response from MG63 cells and (3) to compare the cell–microsphere interactions in microspheres belonging to the selected composition with those on commercially available silica glass microspheres (Polysciences Inc., USA). (Note that the average size of adherent MG63 osteosarcoma cells is approximately 1000 μm^2 (PAUTKE et al., 2004); considering that the diameters of the microspheres used in all the experiments are in the 50–100 µm range, it can be calculated that each microsphere can accommodate approximately 30–60 cells on its surface.)

4.2. Materials and methods

4.2.1. Preparation of MG63 cells

MG63 osteoblast-type cells were obtained from in-house stocks at Eastman Dental Institute of University College London. The cells, which were stored in cryotubes in liquid nitrogen, were resuscitated by thawing in a water bath at 37°C and then introduced into a 75 cm^2 flask containing low-glucose Dulbecco Modified Eagles'

Medium (DMEM) to which 10% foetal bovine serum (FBS) and 1% penicillin–streptomycin had been added (note that unless mentioned otherwise, all reagents were procured from Gibco®, Life Technologies Ltd., Paisley, UK). The growth process was carried out in a 37°C/5% CO_2 incubator till the cells were 80–90% confluent, as visualised by phase contrast microscopy. At 80–90% confluency, the cells were washed with phosphate buffer solution (PBS) and trypsinised by adding 3 ml of 0.025% trypsin-EDTA to the flask and incubating at 37°C/5% CO_2 for 3–4 minutes to detach the cells from the flask surface. Proper detachment and floating of cells in the medium was ensured by visual observation using phase contrast microscopy. Trypsinisation was then inhibited by adding 7 ml of fresh media to the trypsinised live cells; the cell suspension was then added to a 15 ml falcon tube and centrifuged at 1000 rpm for 3 minutes, followed by careful removal of 8 ml of supernatant to avoid disturbing the cell pellet. Finally, 8 ml of media was added prior to cell counting, the procedure for which is based on the Trypan blue dye protocol (Strober, 2001).

4.2.2. Cell culture on microspheres under static conditions

The static culturing of cells on the microspheres was carried out using one of two different systems: (1) permeable mesh well inserts in conventional 24 well tissue culture test plates and (2) ultra-low attachment multiwell tissue culture plates. In either case, the microspheres to be cultured were sterilised prior to use. The required quantities of microspheres—40 mg for the inserts and 200 mg for the ultra-low attachment plates—were weighed and then added to glass vials; note that the weight of microspheres to be used was determined on the basis of the minimum quantity of microspheres required to cover the microsphere support surface with a thin layer of microspheres and had been quantified prior to the experiment. The open end of each glass vial was then sealed with aluminium foil and autoclave tape. The sealed vials were subsequently placed in a drying oven and the contents were sterilised under dry heat at a temperature of 180°C for 3 hours before leaving to cool overnight.

4.2.2.1. Seeding in mesh well inserts

Seeding of cells on the microspheres was carried out on Transwell® polyester inserts (Corning, USA) placed in conventional 24 well tissue culture test plates. These inserts comprise a permeable mesh that allows improved distribution of medium and nutrients within the system; furthermore, they can be detached from the cell culture well to carry out additional processing steps for assays and imaging.

The sterilised microspheres (approx. 40 mg weight) were carefully transferred to the inserts such that the entire surface of the mesh was covered by a thin layer of microspheres. Pre-warmed cell medium at 37°C was added to each well containing the microspheres, and the plate was then placed in a 37°C/5% CO_2 incubator for 1 hour to equilibrate the microsphere surface with respect to the medium. The cells were then seeded on the equilibrated microspheres at a seeding density of 10,000 cells per well followed by incubation at 37°C in an atmosphere of 5% CO_2. Care was taken to avoid loss of either microspheres or cell suspension from the insert into the bottom of the well. In all experiments (unless otherwise noted), 50% of the medium was removed and replaced with fresh medium at intervals of 2 days.

4.2.2.2. Seeding in ultra-low attachment plates

In several experiments, seeding of cells on the microspheres was carried out in Corning Costar® ultra-low attachment 24 well cell culture plates (Corning, USA). These plates possess a coating of a covalently bound hydrogel layer that serves to inhibit cellular attachment on the plate surface, so that the cells can attach only to the microsphere surface. The sterilised microspheres (approx. 200 mg weight) were carefully transferred to the ultra-low attachment plates such that the entire surface of the well was covered with a thin microsphere layer. As with the inserts, pre-warmed cell medium at 37°C was added to each well, followed by equilibration at 37°C/5% CO_2 for 1 hour and cell seeding at a density of 50,000 cells per well. The plate was then incubated at 37°C in an atmosphere of 5% CO_2. In all experiments (unless otherwise noted), 50% of the medium was replaced at intervals of 2 days.

4.2.3. Cell culture on microspheres under dynamic conditions

The dynamic culturing of cells on the microspheres was carried out in spinner flask bioreactors (4500 series, Corning, USA) with a capacity of 125 ml. Prior to the experiment, the inner surfaces of the bioreactor were siliconised by treating with 1 ml Sigmacote (Sigma–Aldrich, UK) for 2–3 hours so as to inhibit the attachment of cells to the bioreactor surface; after the siliconising step, the bioreactors were rinsed in distilled water and then sterilised by autoclaving.

To carry out cell culture in the bioreactors, the cells were initially seeded on microspheres in ultra-low attachment 24 well cell culture plates as per the method outlined in section 4.2.2.2. After seeding cells on the microspheres at a density of 50,000 cells per well, the cell culture plate was (1) placed in a 37°C/5% CO_2 incubator for 1 hour, then (2) placed on a plate shaker operating at 100 rpm for 5

minutes so as to enhance initial cell attachment and ensure uniform distribution of cells and microspheres in the well and then (3) replaced in the incubator for 1 hour. Meanwhile, 40 ml of pre-warmed DMEM was added to the bioreactors. The contents of each well of the ultra-low attachment plate were then added to the bioreactor using Pasteur pipettes; the well was washed 3–4 times with approx. 10 ml medium and the wash medium was subsequently added to the bioreactor to bring the total medium volume to 50 ml.

The bioreactors were then placed on a Variomag Biosystem magnetic stirrer plate (Thermo Scientific, USA) inside a 37°C/5% CO_2 incubator, with agitation achieved via a polytetrafluoroethylene paddle fitted with a magnetic stirring bar; the stirrer plate was connected to a Cimarec Biomodul 40B control unit (Thermo Scientific, Germany) placed outside the incubator so that the stirring speed could be controlled externally. The stirring speed was maintained at 20 rpm for 1 day. Subsequently, 50 ml DMEM was added to the bioreactor to bring the working volume within the bioreactor to 100 ml and the stirring speed was increased to 40 rpm and maintained for the remainder of the experiment. At intervals of 3 days, 50% of the bioreactor medium was replaced with fresh medium. At each time point of the experiment, approx. 90 ml of medium from the bioreactor was discarded and the solid contents (microspheres along with adherent cells) were transferred to a conventional 24 well cell culture plate using Pasteur pipettes. The bioreactor bottom surface was washed 2–3 times with cell culture medium so as to dislodge any remaining microspheres which were then transferred to the well; at each step, excess medium in the wells was discarded. After the entire solid contents were transferred to the cell culture plate, 1 ml of fresh cell culture medium was added to each well containing microspheres and adherent cells.

4.2.4. Scanning electron microscopy imaging

At specific time points depending on the experiment, the medium from the wells was removed and replaced with 3% glutaraldehyde in 0.14 M sodium cacodylate buffer (pH 7.3; both Sigma–Aldrich, UK) so as to fix the specimens. The samples were kept at 4°C overnight and then the glutaraldehyde fixative was replaced with a graded series of alcohols according to the following regimen for sample dehydration: 50% EtOH for 10 minutes, 70% EtOH for 10 minutes, 90% EtOH for 10 minutes and 100% EtOH for 10 minutes (3 times). The final concentration of alcohol was replaced with hexamethyldisilazane (HMDS; TAAB Laboratories, Aldermaston, UK) for 1–2 minutes so as to accomplish critical point drying, after which the HMDS

was removed and the plate was left to dry overnight in a desiccator. During all these steps, the samples were handled as carefully as possible to minimise the detachment of cells from the microspheres. For cell culture inside the Transwell® inserts, each insert was taken out of the well and the entire mesh was carefully cut out from the insert along the edge using a scalpel. The meshes with the cell-cultured microspheres on them were mounted onto carbon adhesive discs attached to aluminium SEM specimen stubs. For cell culture inside ultra-low attachment plates, the adhesive disc fixed to the specimen stub was dipped into the well containing the dried sample so as to form a sample layer on the disc; excess material was blown off using a compressed air duster spray. The specimens were then sputter-coated with gold/palladium by means of a Polaron E5100 coating device (Polaron CVT, Milton Keynes, UK). The coated samples were observed with a scanning electron microscope (model JSM 5410LV, JEOL, Japan) using various magnifications at an operating voltage of 10 kV.

4.2.5. Confocal laser scanning microscopy imaging

Confocal laser scanning microscopy images were obtained using Alexa Flour 488 phalloidin (Invitrogen, UK) to stain the actin filaments of the cytoskeleton and propidium iodide (BD Biosciences, UK) to stain the nucleus. For cell culture in ultra-low attachment plates, the staining process was carried out *in situ*, whereas for cell culture in Transwell® inserts, the mesh was carefully cut out from the insert along the edge using a scalpel and transferred to a fresh cell culture plate prior to staining. Initially, the samples were processed by fixing in 4% paraformaldehyde until required for imaging. The fixed samples were then washed twice with phosphate buffered saline (PBS) and permeabilised using a solution of 0.1 vol% Triton-X in PBS for 3–5 minutes. A solution of 2.5 vol% phalloidin methanolic stock solution in PBS was then added to each sample well and the samples were maintained for 20 minutes in a dark atmosphere to minimise evaporation and photobleaching. After washing again with PBS, the samples were counterstained with 1 µg/ml of propidium iodide for 10 minutes. The stained samples were visualised at different magnifications by a confocal microscope (Biorad, USA).

4.2.6. Cell proliferation assay

Cell proliferation on the microspheres was quantitatively determined using the CCK-8 cell proliferation assay kit (Sigma–Aldrich, UK). Commercially available silica glass microspheres (Polysciences Inc., USA) with sizes of 50–100 µm were used as the control. For all the assay experiments, the time points used were 1, 4 and 7

days and data was obtained on duplicate samples (i.e. n = 2); separate specimens of each composition and the control were used for each time point and were discarded after the assay measurement data were obtained. At predetermined time points, 10% $v.v^{-1}$ of culture medium was removed from all the wells and replaced with CCK-8 reagent, followed by incubation at 37°C for 4 hours in a humidified atmosphere containing 5% CO_2. Aliquots of 100 µl from each well were then transferred to a 96 well plate (8 aliquots per sample/control well), and absorption detection was accomplished by means of a Tecan Infinite® 200 PRO microplate reader (Tecan, Switzerland) with the absorption value set to 450 nm. The microplate reader provided absorbance data, so to plot the data in terms of the number of cells, a standard calibration curve was plotted separately. For the standard curve, cell populations in multiples of 10,000 (i.e. 0, 10000, 20000, 50000 and 100000 cells) were cultured over a 1 day period in a 24 well plate and absorbance measurements were carried out using the same microplate reader.

4.2.7. Statistical analysis

All statistical analyses were carried out using IBM SPSS version 21 (SPSS Inc., USA). Initial normality tests (one-sample Kolmogorov-Smirnov test) revealed the data did not have a normal distribution, so non-parametric tests were used, specifically the Kruskall-Wallis H test and Mann-Whitney U test. Multiple pairwise comparisons were corrected using the Bonferroni correction method. The assumed levels of significance for the statistical tests was 0.05 unless Bonferroni corrections were used, in which case it was either 0.008 or 0.016. Note that because the data do not have a normal distribution, the presence (or absence) of statistically significant differences may not always be visually apparent in some of the graphs. A more accurate representation of the data would be in the form of box-and-whisker plots, which are shown in Appendix A.2. Bar charts were used for ease of comparison of the data.

4.3. Results

4.3.1. Initial screening: static MG63 cell–microsphere interactions for Fe- and Ti-PGMs

The initial objective of the study was to investigate the interactions between cells and microspheres for all the investigated iron and titanium phosphate glasses so as to identify compositions that would elicit the most favourable cellular responses with regard to cell adhesion and proliferation. Microspheres belonging to all eight investigated compositions (Fe0/Ti0, Fe1, Fe3, Fe5, Ti1, Ti3, Ti5 and Ti7) were

selected, with commercially available silica microspheres (Polysciences Inc., USA) used as the control for some of the experiments. The Fe- and Ti-PGMs had sizes in the range of 63–75 μm, whereas the control microspheres were in the size range of 50–100 μm.

4.3.1.1. Scanning electron microscopy imaging

The first cell culture experiments involved SEM imaging of MG63 cells cultured on the investigated Fe- and Ti-PGMs over a 7 day period. Figure 4.1 shows SEM images of MG63 cells growing on Fe-PGMs in Transwell® inserts at time points of 1 and 7 days. The images show that at day 1 itself, it was evident that no cell growth was occurring on the Fe0 and Fe1 microspheres, whereas cells were visibly attached to the Fe3 and Fe5 glass microspheres. The Fe0/Ti0 glass microspheres showed considerable degradation *in vitro* on day 1 and had almost completely disintegrated by day 7. The Fe1 microspheres showed less degradation than the Fe0 microspheres, yet major changes in surface morphology were observed in the form of irregular cracks on the surface, and no adherent cells could be discerned. In contrast, many of the microspheres belonging to the Fe3 and Fe5 compositions showed significant numbers of cells on their surface. On day 1, the cells on both Fe3 and Fe5 microspheres were either flattened or somewhat rounded and a countable number of cells could be observed on the microspheres; however, by day 7, the Fe3 and Fe5 microspheres appeared to be covered by aggregates of cells that enveloped the microsphere surface. In many cases, cells on different microspheres appeared to be joined to each other by means of processes. Thus, the Fe3 and Fe5 microspheres clearly supported cell attachment and cell proliferation on their surface whereas the Fe0 and Fe1 microspheres did not. At the same time, it should be noted that not all the Fe3 and Fe5 microspheres were covered with cells; many of the microspheres had no cells covering the surface even though the microspheres did not show any apparent signs of degradation.

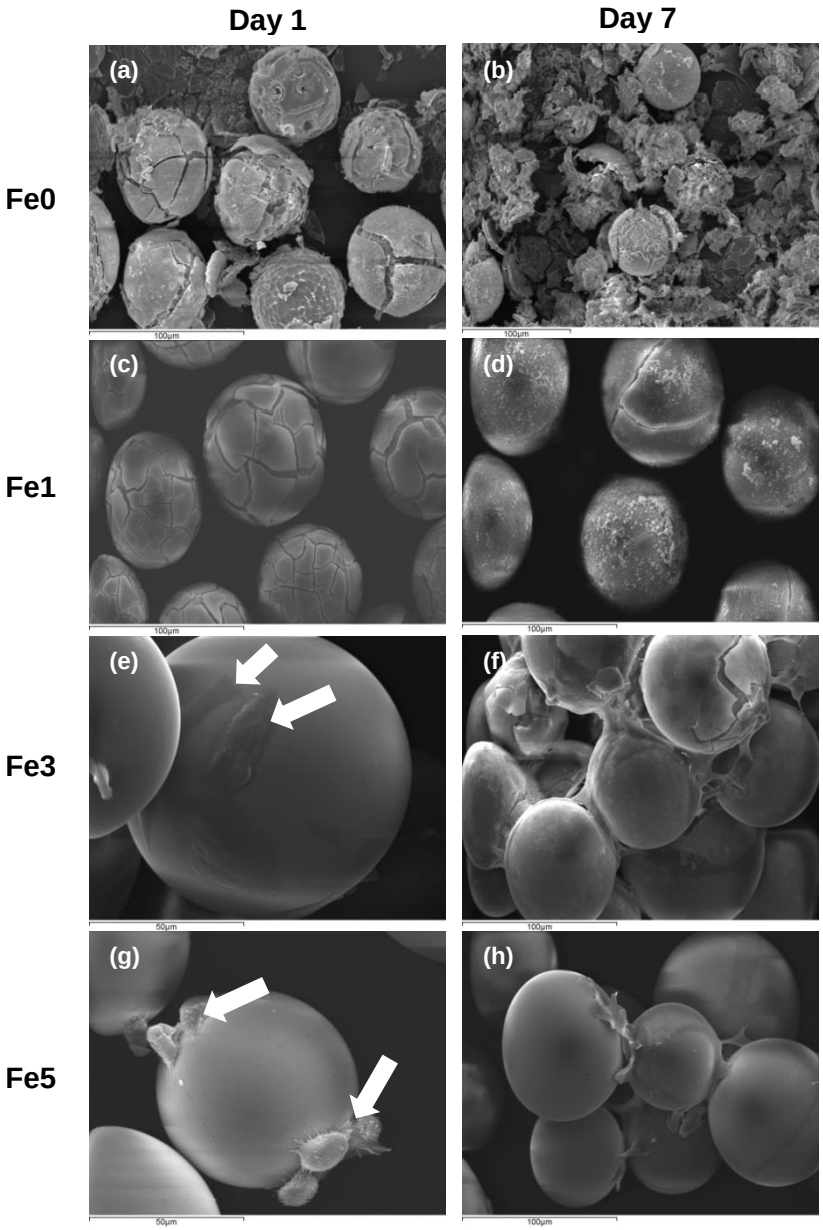

Figure 4.1. Scanning electron microscopy images showing MG63 cells growing on iron phosphate glass microspheres in Transwell® inserts at time points of 1 and 7 days. The Fe0 microspheres (a, b) and Fe1 microspheres (c, d) show no cell growth on account of excessive degradation. The Fe3 and Fe5 microspheres show individual cells (sometimes with flat morphology) growing on the surface at day 1 (e, g). Higher magnifications are used to view these cells more clearly; the positions of cells are denoted by arrows. By day 7, the cells have formed aggregates around groups of microspheres (f, h).

Figure 4.2 shows SEM images of MG63 cells growing on Ti-PGMs in Transwell® inserts at 7 days post culture; images for day 1 are not included since they are similar to the day 1 images obtained for the Fe-PGMs. The Ti1 microspheres, similar to the Fe1 microspheres, showed major changes in surface morphology through crack formation and no cells were discernible. In contrast, the Ti3, Ti5 and Ti7 microspheres all showed significant numbers of cells attached to the surface. As with the Fe3 and Fe5 microspheres, many of the cells showed a flattened

morphology on the microsphere surface. The cells exhibited a tendency to form extensive linkages on individual microspheres as well as on groups of adjacent microspheres by means of processes spreading across the microsphere surface, although this was not true for all the Ti3–7 microspheres, with several microspheres being completely devoid of cells in spite of showing no apparent signs of degradation.

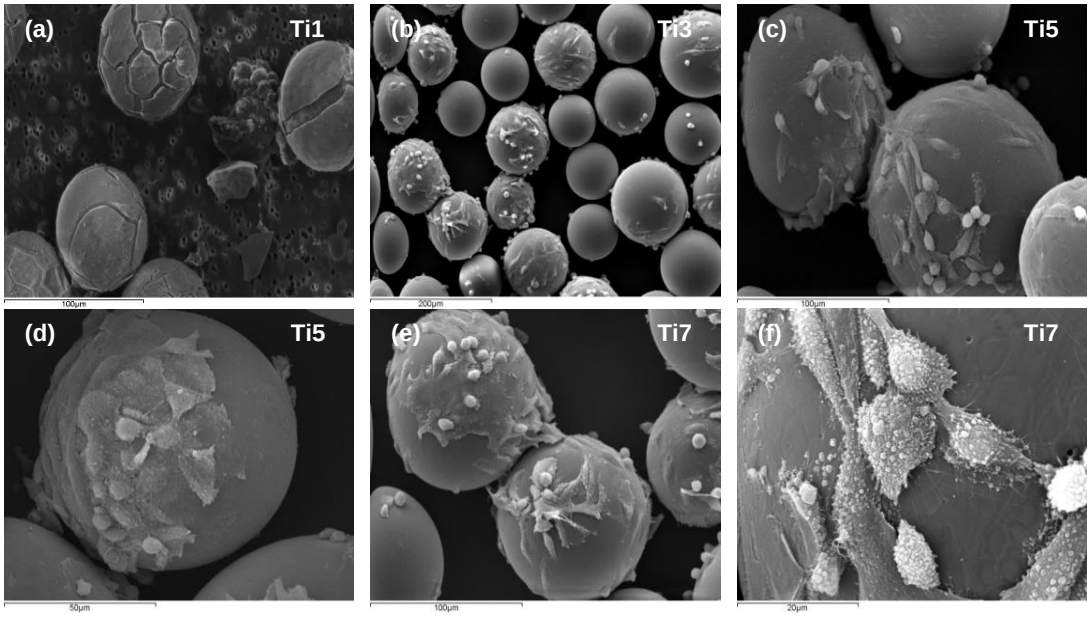

Figure 4.2. Scanning electron microscopy images showing MG63 cells growing on titanium phosphate glass microspheres in Transwell® inserts at 7 days post seeding (images for day 1 not shown since the images obtained are similar to those obtained for iron phosphate glass microspheres in terms of cell attachment). Similar to the Fe1 microspheres, the Ti1 microspheres show considerable surface degradation with no cells visible on the surface (a). The Ti3, Ti5 and Ti7 microspheres show similar cell growth features. A non-uniform distribution of cells on different microspheres is observed with some microspheres showing no cell growth while other microspheres show many cells growing on the surface (Ti3 microspheres in (b)). At higher magnifications, the proliferation of cells on the microspheres and the linkages between cells by means of processes can be more clearly discerned (Ti5 microspheres in (c, d) and Ti7 microspheres in (e, f)).

4.3.1.2. Confocal laser scanning microscopy imaging

The favourable nature of the cell–microsphere interactions was further confirmed by means of CLSM images of MG63 cells attached to the Ti3–7 microsphere at 7 days post culture (Figure 4.3). The phalloidin-stained actin filaments showed alignment along the microsphere surface curvature, thereby implying good adhesion characteristics. The cells tended to completely cover individual microspheres, and multiple microspheres were joined to each other by means of processes, thereby forming fragments of cell–microsphere aggregates.

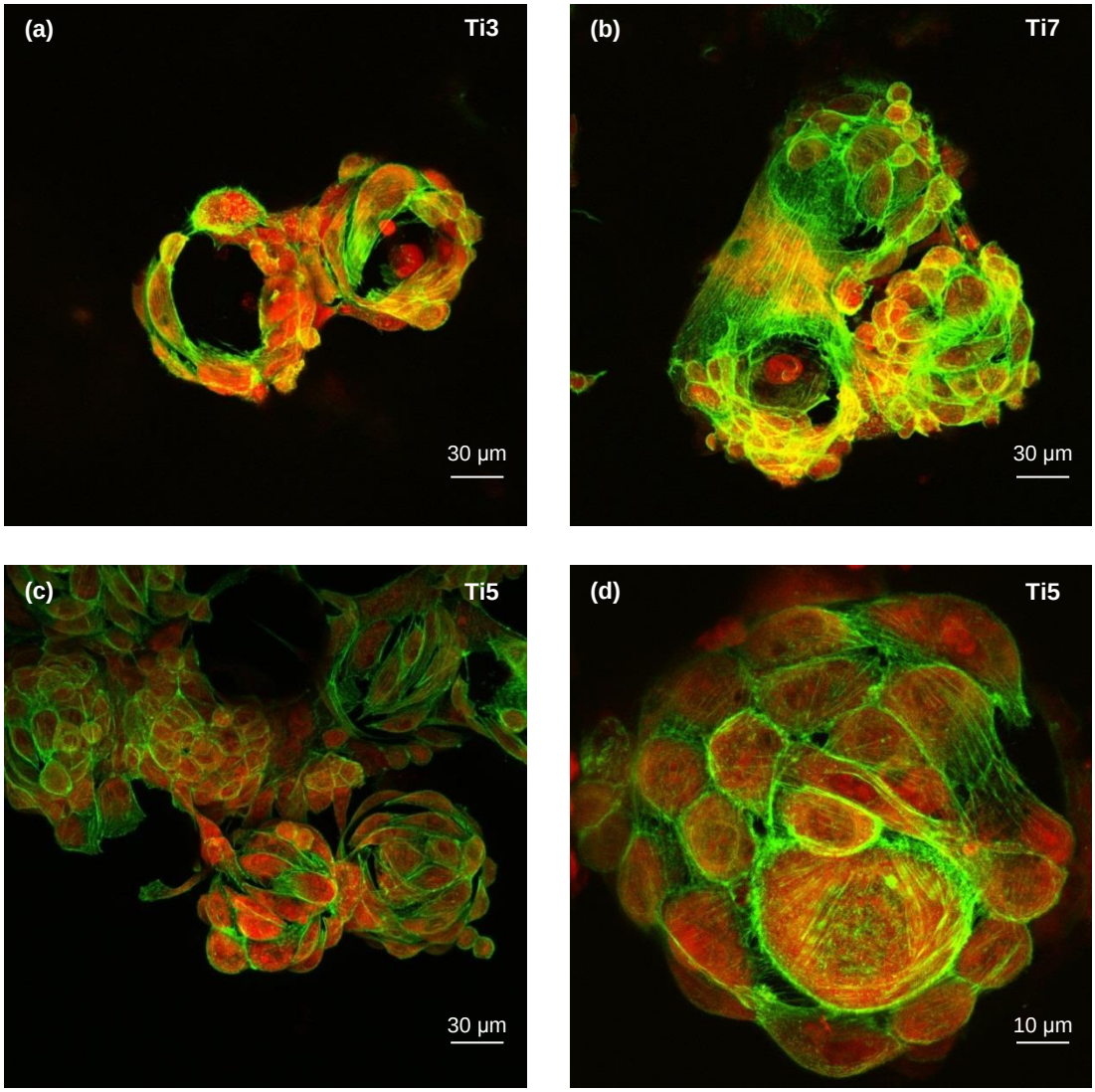

Figure 4.3. Confocal laser scanning microscopy images of MG63 cells attached to titanium phosphate glass microspheres in Transwell® inserts at 7 days post culture. Phalloidin stains the actin filaments of the cytoskeleton green while propidium iodide stains the nuclei red. As in the case of the SEM micrographs, the CLSM images of Ti3 (a), Ti7 (b) and Ti5 (c, d) microspheres show similar cell growth features. The actin filaments align themselves along the curved surface, indicating good cell adhesion. Cells on two or more microspheres are joined to each other and form larger sized fragments of cell–microsphere aggregates (a–c). Individual microspheres are also completely covered by a layer of cells (d).

4.3.1.3. Cell proliferation assays

The proliferation of the cells on the Fe- and Ti-PGMs was quantitatively assessed by means of the CCK-8 cell proliferation assay. Prior to the actual assay, a standard curve of the microplate absorbance values as a function of the number of cells was plotted as shown in Figure 4.4.

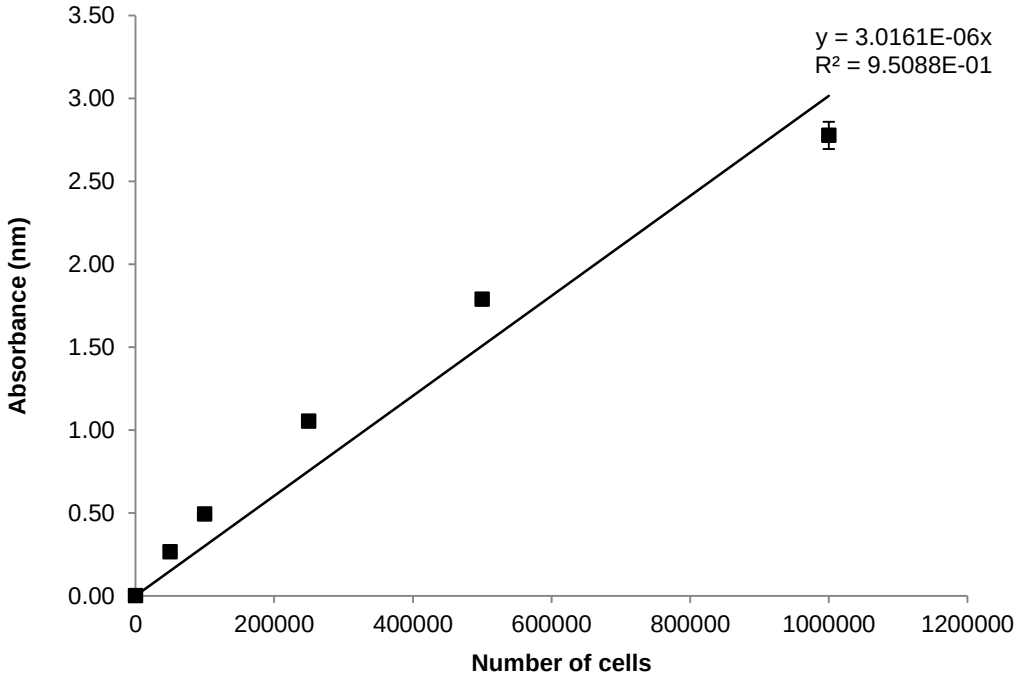

Figure 4.4. Standard curve of MG63 cell growth plotted as absorbance values versus number of cells after carrying out a CCK-8 assay at 1 day post seeding. The absorbance values are obtained at a wavelength of 450 nm. Error bars represent ±SD (n = 6).

Figure 4.5 shows the results of the CCK-8 cell proliferation assay carried out over time points of 1, 4 and 7 days on the Fe-PGMs, with commercially available silica glass microspheres used as the control. Note that the Fe0 and Fe1 microspheres were not included in the assays in accordance with the results of the SEM study (Figure 4.1) which showed no evidence of cell attachment on the excessively degraded microspheres. As shown in Figure 4.5(a), the results revealed that for all the compositions studied and the control, there was a significant increase in cell growth over the culture period (chi-square values = 28.044, 29.744 and 15.693 at days 1, 4 and 7 respectively with 2 degrees of freedom), and the differences in cell populations were highly significant between days 1, 4 and 7 (*** $p < 0.001$). The Fe3 and Fe5 compositions showed 3.5-fold and 2.7-fold increases in cell numbers respectively from day 1 to day 7, whereas the control microspheres showed a 2.9-fold increase over the same period (*** $p < 0.001$). As shown in Figure 4.5(b), at each time point, the cell numbers corresponding to Fe3 were significantly lower than those of the control, while those of Fe5 were significantly lower than those of the control only at day 7 (** $p < 0.01$). The Fe3 microspheres also showed lesser cell proliferation than the Fe5 microspheres at days 1 and 4 (*** $p < 0.001$).

(a)

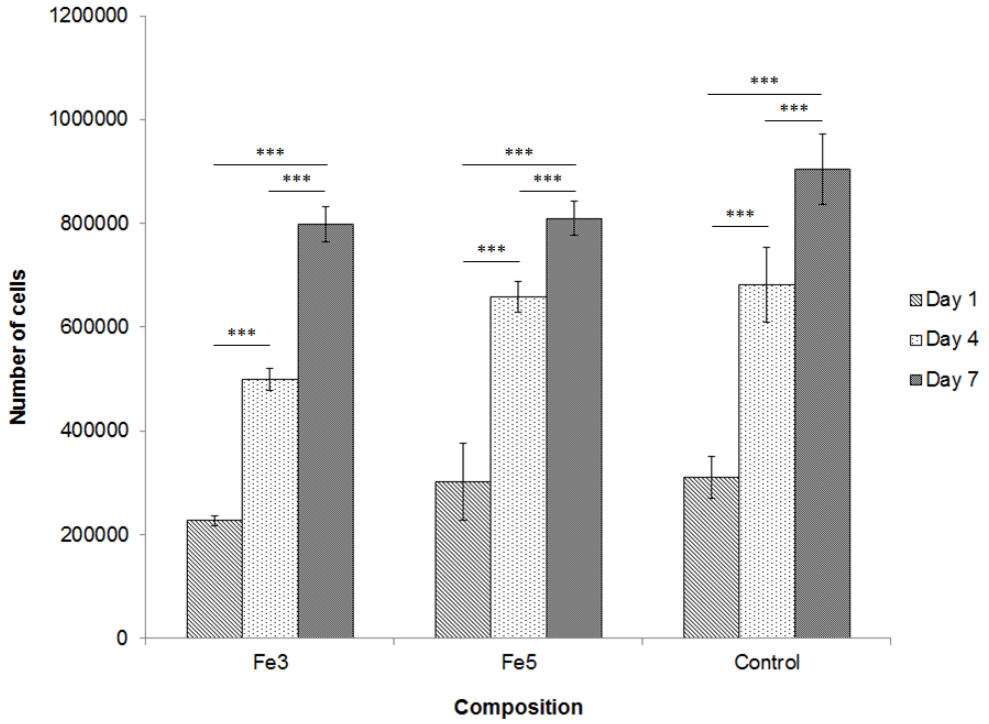

(b)

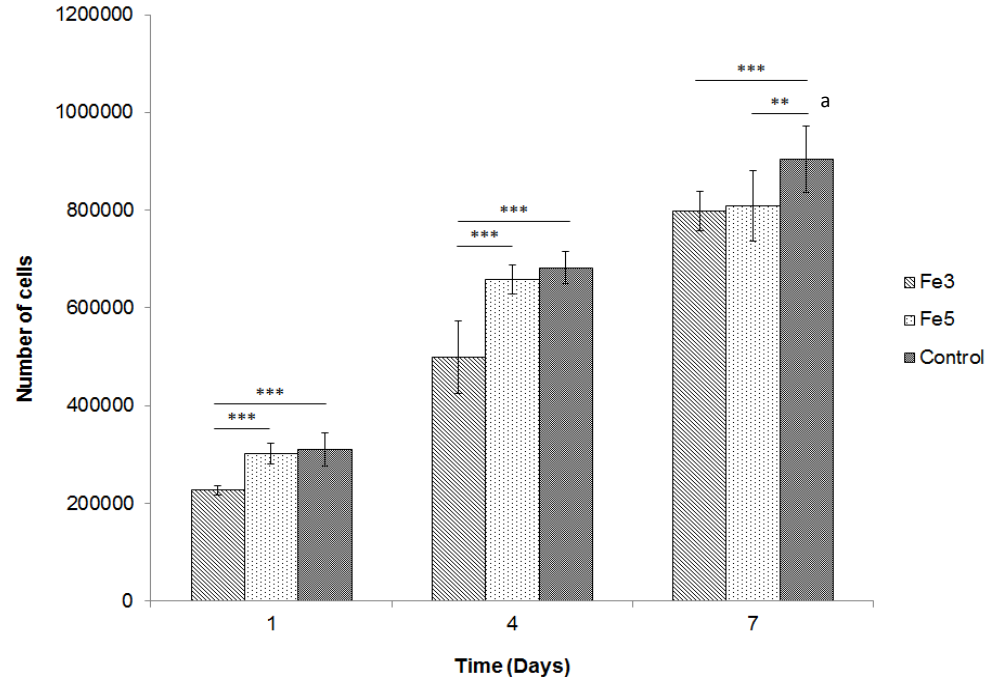

Figure 4.5. Bar charts showing the proliferation of MG63 cells on iron phosphate glass microspheres in ultra-low attachment cell culture plates at time points of 1, 4 and 7 days as determined using the CCK-8 assay. The control comprises silica glass microspheres (Polysciences Inc.). Error bars represent ±SD and n = 2. The symbols ** and * indicate $p < 0.01$ and $p < 0.001$ respectively. (a) For all the compositions and the control, a significant increase in cell numbers is observed between all the time points (*** $p < 0.001$). (b) At all the time points, the cell populations of Fe3 are significantly lower than those of the control, while those of Fe5**

are significantly lower than those of the control only at day 7; further, Fe5 shows significantly greater cell numbers than Fe3 at days 1 and 4 (* $p < 0.001$). [a]Note that the statistically significant differences shown in this bar chart are based on non-parametric statistical analysis, which was necessary because the data was not normally distributed. The presence of statistically significant differences is not always visually apparent because while the bar chart shows the mean values and standard deviations, statistical significance is calculated based on the sum of the ranks of the data points in each data set. The box-and-whisker plot in Figure A.2 of Appendix A.2 provides a more visually accurate representation of the statistically significant differences between the data sets. Also note that certain data points were found to be outliers during the statistical analysis and have therefore been excluded from the plotted data.**

The CCK-8 cell proliferation assay results obtained for Ti-PGMs over 1, 4 and 7 days are shown in Figure 4.6. As in the case of the Fe0 and Fe1 microspheres in the previous assay results, the Ti1 microspheres were excluded from the assay experiments on account of the SEM imaging results (Figure 4.2) which showed no evidence of cell attachment on the excessively degraded microspheres. As shown in Figure 4.6(a), similar to the Fe-PGMs, all the Ti-PGM compositions and the control showed a significant increase in cell growth over the culture period (chi-square values = 40.894, 38.139, 38.139 and 29.038 for Ti3, Ti5, Ti7 and control respectively with 2 degrees of freedom), and the differences in cell numbers between days 1, 4 and 7 were all highly significant (*** $p < 0.001$). The increases in cell numbers for the Ti3, Ti5 and Ti7 microspheres were 2.9-fold, 3.1-fold and 2.9-fold respectively from day 1 to day 7; the control microspheres showed a 2.6-fold increase over the same period (*** $p < 0.001$). Figure 4.6(b) shows that at days 1 and 7, the cell numbers on the Ti3–7 microspheres were significantly higher than those on the control (*** $p < 0.001$); however, the differences at day 4 were not statistically significant ($p > 0.008$, Bonferroni correction). Comparisons among the compositions Ti3, Ti5 and Ti7 revealed no statistically significant differences except at day 1 between Ti3 and Ti5 and at day 7 between Ti5 and Ti7 (** $p < 0.01$).

(a)

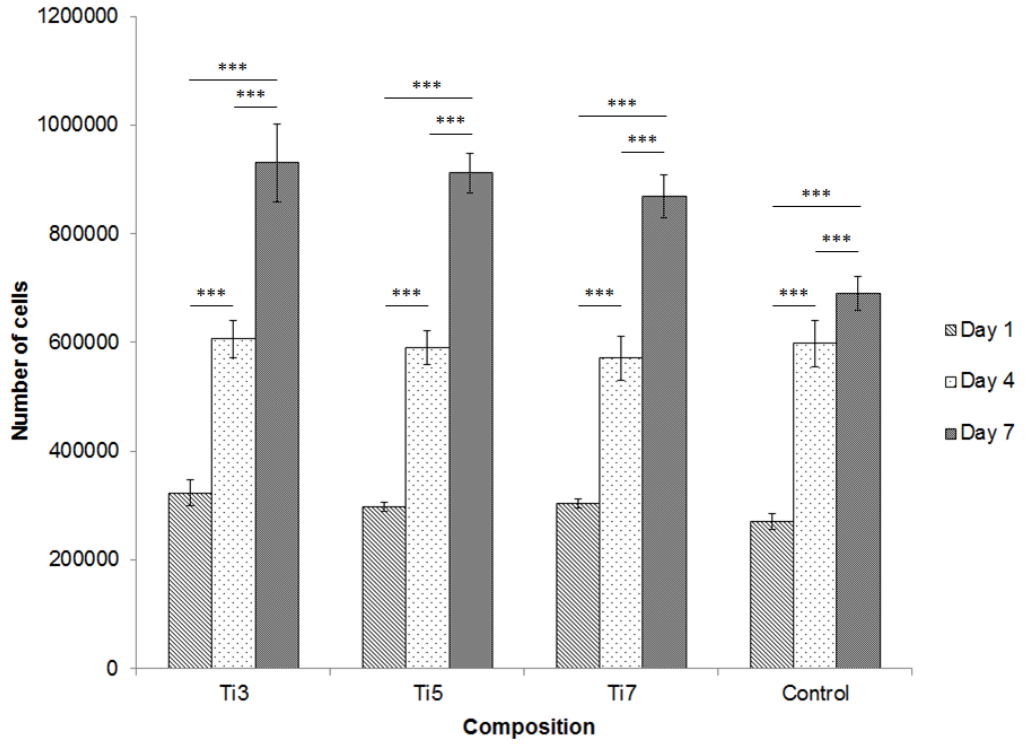

(b)

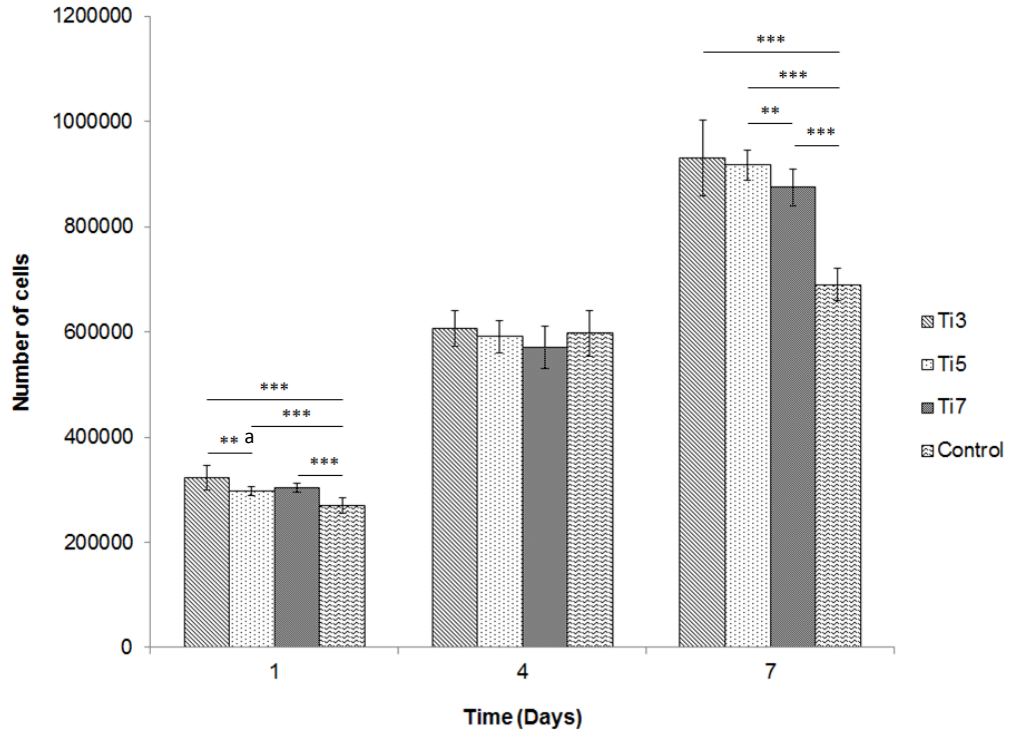

Figure 4.6. Bar charts representing MG63 cell proliferation on titanium phosphate glass microspheres in ultra-low attachment cell culture plates at time points of 1, 4 and 7 days as determined using the CCK-8 assay. The control comprises silica glass microspheres (Polysciences Inc.). Error bars represent ±SD and n = 2. The symbols ** and * indicate p < 0.01**

and p < 0.001 respectively. (a) As with the iron phosphate glass microspheres, statistically significant increases in cell growth between days 1, 4 and 7 can be observed for all the compositions and the control (* p < 0.001). (b) At days 1 and 7, the cell populations of all the compositions are significantly higher than the control (*** p < 0.001), but no statistically significant differences in cell populations can be observed on day 4 (p > 0.008, Bonferroni correction). [a]Note that the statistically significant differences shown in this bar chart are based on non-parametric statistical analysis, which was necessary because the data was not normally distributed. The presence of statistically significant differences is not always visually apparent because while the bar chart shows the mean values and standard deviations, statistical significance in this case is calculated based on the sum of the ranks of the data points in each data set. The box-and-whisker plot in Figure A.3 of Appendix A.2 provides a more visually accurate representation of the statistically significant differences between the data sets. Also note that certain data points were found to be outliers during the statistical analysis and have therefore been excluded from the plotted data.**

4.3.2. Bioreactor-mediated MG63 cell proliferation: dynamic MG63 cell–microsphere interactions for titanium PGMs

The interactions between MG63 cells and microspheres under the influence of dynamic environments found in spinner flask bioreactors were investigated. In order to quantify the effects of the bioreactor-induced dynamic environment on MG63 cell proliferation, the results obtained from dynamic culture in spinner flasks were compared with those from static culture in ultra-low attachment plates for the same experimental conditions in terms of (a) weights of microspheres used (200 mg), (b) seeding density (50,000 cells per well), (c) medium replacement interval (every 3 days) and (d) time points (1, 4 and 7 days). For this part of the study, the Ti5 microspheres were selected from amongst all the investigated compositions and commercially available silica glass microspheres were used as the control; the size ranges of both the Ti5 and control microspheres were 50–100 μm. Note that day 0 in the static culture experiments was considered to be the day on which the cells were seeded on the microspheres within ultra-low attachment 24 well plates, whereas day 0 in the dynamic culture experiments was considered to be the day on which the medium volume in the bioreactor was increased to the final working volume of 100 ml and the stirring speed was increased to 40 rpm (i.e. 1 day after the seeding of cells on the microspheres as described in section 4.2.3).

4.3.2.1. Scanning electron microscopy and confocal laser scanning microscopy imaging

Figure 4.7 shows SEM images at days 4 and 7 of MG63 cells cultured on Ti5 and control microspheres under dynamic conditions in spinner flask bioreactors. At both time points, the Ti5 microspheres exhibited greater cell coverage on the surface in comparison with the control microspheres. In the case of the Ti5 microspheres, more cells were observed on the surface on day 7 than on day 4. In most cases, the

cells exhibited a ‘torn’ appearance as they adhered to the surfaces of both the Ti5 and control microspheres. At the same time, it was possible to discern individual cells with a flattened morphology on the microspheres as well as groups of cell–microsphere aggregates with groups of cells on adjacent microspheres joined to each other. Similar observations were made from CLSM images of bioreactor-mediated MG63 culture on Ti5 and control microspheres at days 4 and 7 post seeding (Figure 4.8).

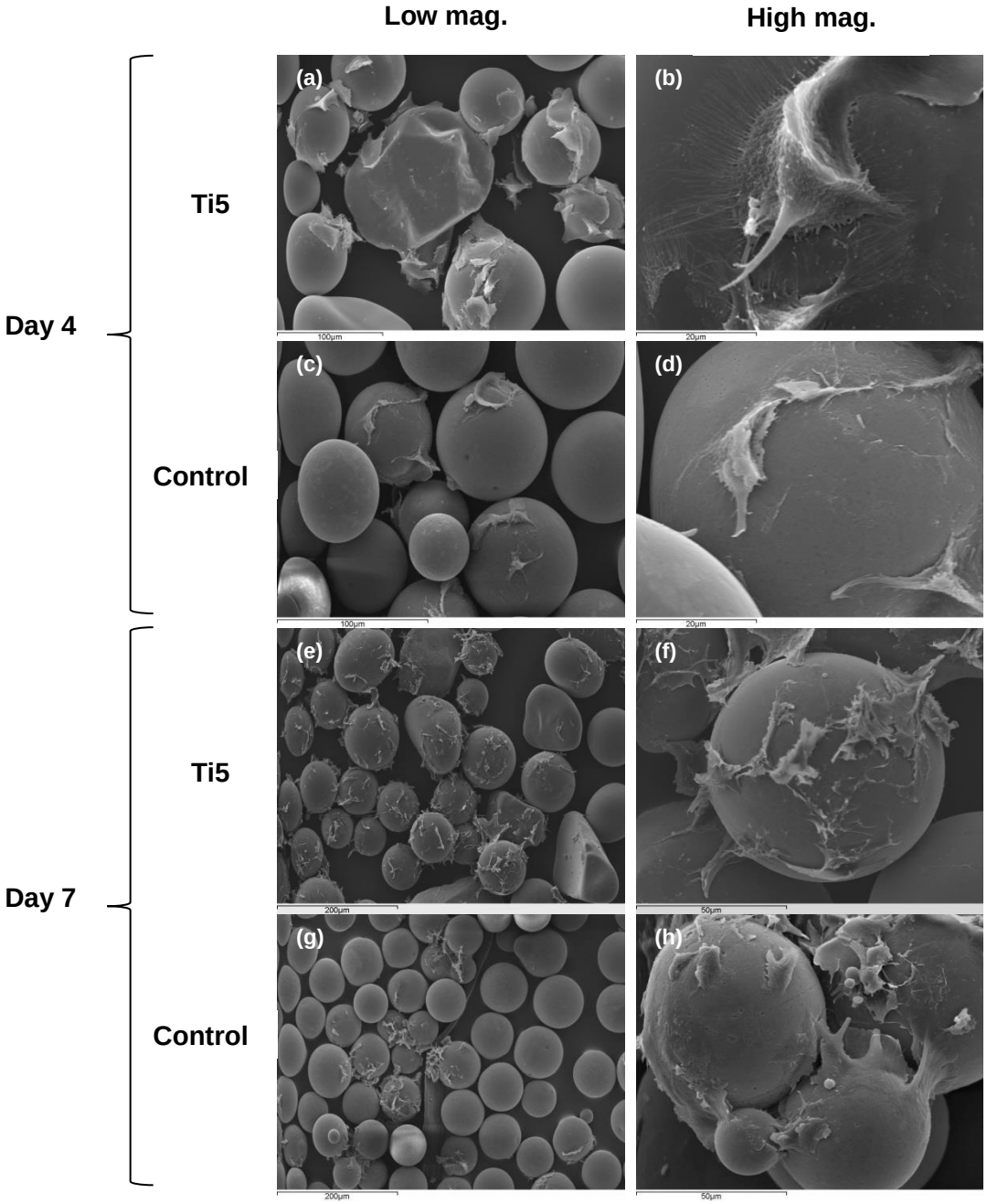

Figure 4.7. Scanning electron microscopy images showing MG63 cells attached to (a, b) Ti5 and (c, d) control glass microspheres at 4 days post seeding as well as (e, f) Ti5 and (g, h) control glass microspheres at 7 days post seeding after culture under dynamic conditions in spinner flask bioreactors. Left images are at lower magnifications (100x or 200x) while right images are

at higher magnifications (1500x or 2000x). Fewer MG63 cells are observed to be attached to the control microspheres in comparison with the Ti5 microspheres at both time points. Furthermore, with regard to the Ti5 microspheres, more cells are observed at day 7 (e) than at day 4 (b). Mostly individual cells with a 'torn' appearance are visible on both the Ti5 and control microspheres, although cells with a flattened morphology are visible (b, d), as are groups of cells on adjacent microspheres which are joined to each other by means of processes (h).

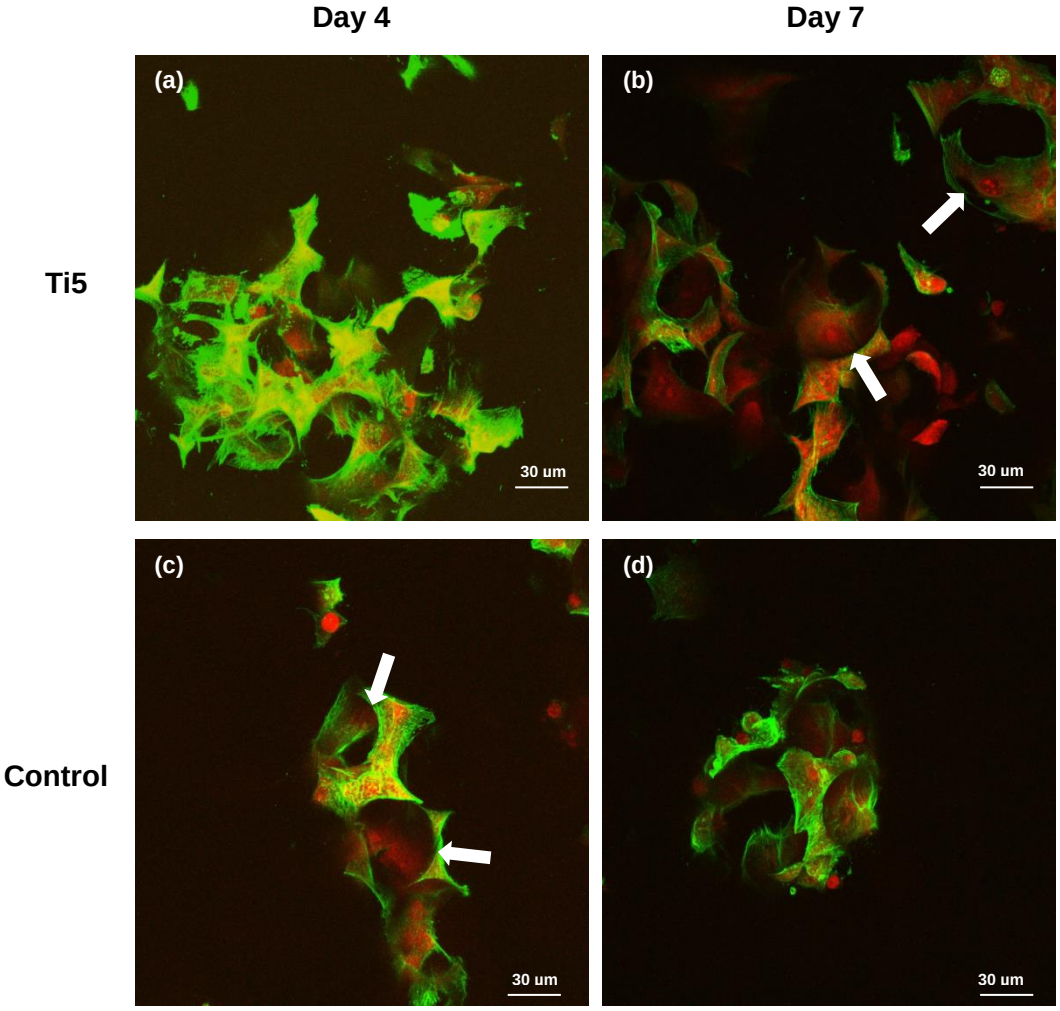

Figure 4.8. Confocal laser scanning microscopy images of MG63 cells growing on Ti5 and control microspheres in spinner flask bioreactors at 4 days post culture (a, c) and 7 days post culture (b, d) respectively. Phalloidin stains the actin filaments of the cytoskeleton green while propidium iodide stains the nuclei red. As with the SEM images in Figure 4.7, more cells are visible on the Ti microspheres (a, b) than on the control microspheres (c, d) at both time points. The cells mostly exhibit a 'torn' appearance on the surfaces of both the Ti5 and control microspheres, although the alignment of cytoskeletal filaments along the surface curvature can be discerned in some cases (as indicated by white arrows in the images).

4.3.2.2. Cell proliferation assays

Figures 4.9 and 4.10 show the results of cell proliferation assays carried out on Ti5 and control microspheres when cultured with MG63 cells under both static and dynamic conditions respectively over a 7 day period. In the static culture system (Figure 4.9), both the Ti5 and control microspheres showed significant changes in

cell numbers over the course of the 7 day study period (chi-square value = 12.626 and 24.024 for control and Ti5 microspheres respectively with 2 degrees of freedom). The differences in cell numbers between the Ti5 and control microspheres were not significant at any of the time points ($p > 0.016$, Bonferroni correction). The Ti5 microspheres showed a 30% increase in cell numbers from day 1 to day 4 and an overall 29% increase from day 1 to day 7 (*** $p < 0.001$); the cell numbers decreased slightly from day 4 to day 7 but the difference was statistically insignificant ($p > 0.016$, Bonferroni correction). The control microspheres showed an 18% increase in cell numbers from day 1 to day 4, but the cell numbers underwent a significant 25% decrease from day 4 to day 7 (** $p < 0.01$ in both cases). For an initial seeding density of 50,000 cells per well, the increase in the cell population by day 7 was approx. 8-fold on the Ti5 microspheres and approx. 6-fold on the control microspheres.

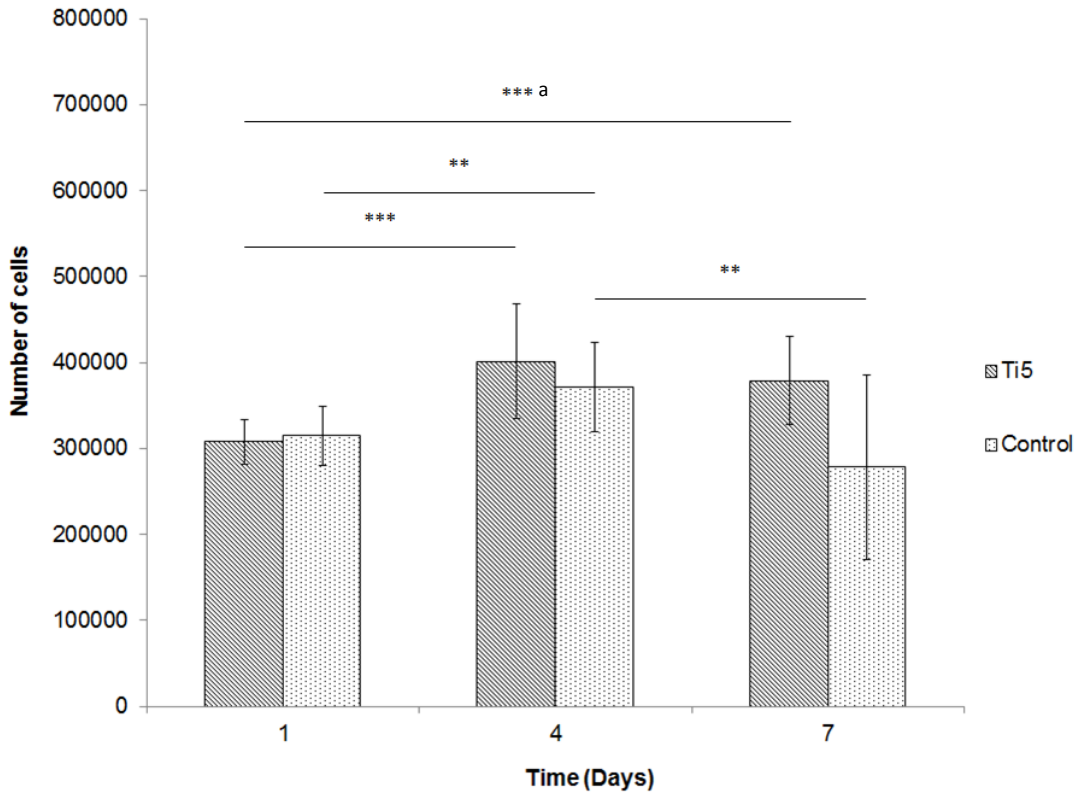

Figure 4.9. Bar chart showing the proliferation of MG63 cells on Ti5 and control glass microspheres at time points of 1, 4 and 7 days in ultra-low attachment cell culture plates under static conditions, as determined using the CCK-8 assay. The control comprises silica glass microspheres (Polysciences Inc.). Error bars represent ±SD where n = 2. The symbols ** and * indicate $p < 0.01$ and $p < 0.001$ respectively. Note the difference in the growth profile of Ti5 and control microspheres between this figure and Figure 4.6. The differences in cell growth between the Ti5 and control microspheres are not statistically significant on days 1, 4 or 7 ($p > 0.016$, Bonferroni correction). Ti5 microspheres show significantly greater cell proliferation on days 4 and 7 in comparison with day 1 (*** $p < 0.001$). The difference in cell numbers on control microspheres is statistically significant between days 1 and 4 and between days 4 and 7 (** $p < 0.01$). With reference to an initial seeding density of 50,000 cells per well, the increase in cell numbers for the Ti5 microspheres is 8-fold. [a]Note that the statistically significant**

differences shown in this bar chart are based on non-parametric statistical analysis, which was necessary because the data was not normally distributed. The presence of statistically significant differences is not always visually apparent because while the bar chart shows the mean values and standard deviations, statistical significance in this case is calculated based on the sum of the ranks of the data points in each data set. The box-and-whisker plot in Figure A.4 of Appendix A.2 provides a more visually accurate representation of the statistically significant differences between the data sets. Also note that certain data points were found to be outliers during the statistical analysis and have therefore been excluded from the plotted data.

In the dynamic culture system, the cell numbers for the Ti5 microspheres were considerably higher than those for the control microspheres at all the time points (62% higher on day 1, 87% on day 4 and 314% on day 7; *** $p < 0.001$). The cells cultured on the control microspheres underwent an increase in number of 88% between days 1 and 4 (*** $p < 0.001$), but the number of cells on the control microspheres at days 4 and 7 was almost equivalent with only a 3% difference that was statistically insignificant ($p > 0.016$, Bonferroni correction). In contrast, the cell numbers on the Ti5 microspheres increased by 117% between days 1 and 4 and 127% between days 4 and 7 (*** $p < 0.001$). Importantly, for an initial seeding density of 50,000 cells per well, the number of cells on the Ti5 microspheres underwent an approx. 24-fold increase over the 7 day culture period, whereas the control microspheres showed only an approx. 6-fold increase in cell numbers over the same period.

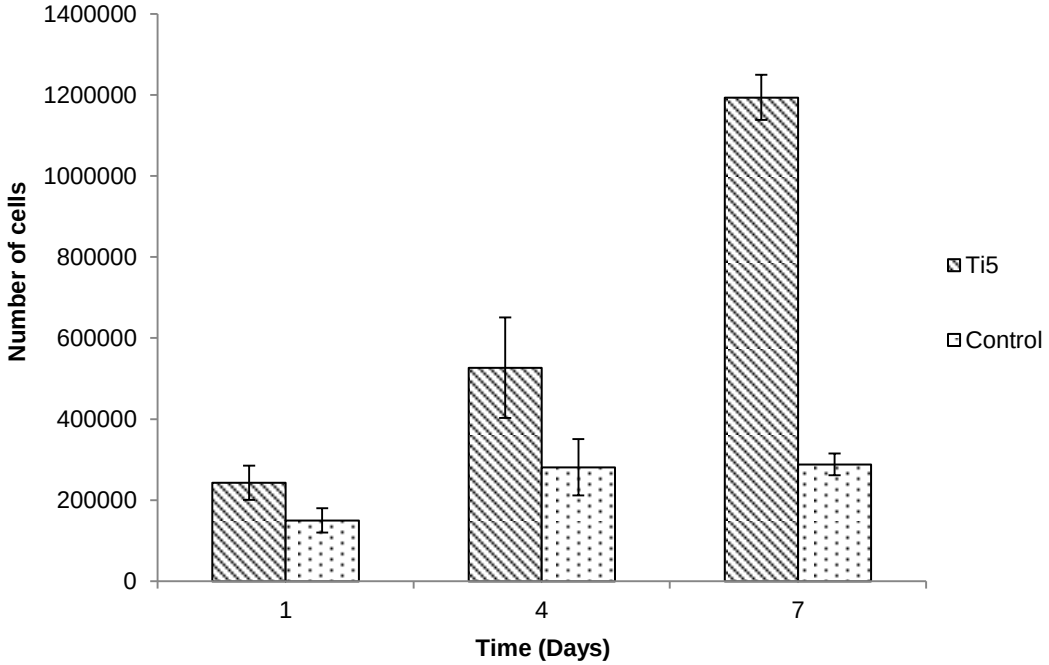

Figure 4.10. Bar chart showing the proliferation of MG63 cells on Ti5 and control glass microspheres at time points of 1, 4 and 7 days in spinner flask bioreactors under dynamic conditions, as determined using the CCK-8 assay. The control comprises silica glass microspheres (Polysciences Inc.). Error bars represent ±SD where n = 2 (note that for simplicity, statistical significance is not shown in the graph). In the dynamic environment, the

difference in cell growth between the Ti5 and control microspheres at all the investigated time points is highly significant (* $p < 0.001$). The Ti5 microspheres show a considerable increase in cell numbers between days 1, 4 and 7 (*** $p < 0.001$). In the control microspheres, the cell numbers at days 4 and 7 are significantly higher than at day 1 (*** $p < 0.001$) but the difference between days 4 and 7 is not statistically significant ($p > 0.016$, Bonferroni correction). With reference to an initial seeding density of 50,000 cells per well, the increase in cell numbers for the Ti5 microspheres is 24-fold under dynamic culture.**

4.4. Discussion

The present investigation examined the interactions between metal oxide-doped PGMs and MG63 osteosarcoma cells under two types of environments: (1) static environments via culture in Transwell® inserts or ultra-low attachment cell culture plates and (2) dynamic environments via culture in spinner flask bioreactors. The major objectives were to identify the PGM composition that would provide the most favourable surface for the attachment and proliferation of MG63 cells and then to compare the cell culture characteristics of the selected microspheres under both static and dynamic environments with those of commercially available glass microspheres that are marketed as substrate microcarriers for cell and tissue culture applications. The results obtained thus far provide detailed insights into the biocompatibility of the investigated PGMs and present several avenues for the next part of the research.

Initially, the biocompatibility of microspheres belonging to all the investigated compositions was assessed by means of culture with MG63 cells under static conditions in Transwell® inserts followed by imaging via SEM. Among the 8 studied compositions (Fe0/Ti0, Fe1, Fe3, Fe5, Ti1, Ti3, Ti5 and Ti7), microspheres belonging to three compositions, namely Fe0/Ti0, Fe1 and Ti1, were found to be unsuitable for cell culture applications on account of their excessive degradation over the 7 day culture period and the absence of cells on the surface as evidenced in the SEM micrographs (Figures 4.1 and 4.2). These results are in clear agreement with the results of studies on degradation (both short-term time lapse and long-term weight loss model studies) as well as ion release and pH measurements and are also concurrent with previous work (Ahmed et al., 2004a, Abou Neel et al., 2007a). As demonstrated in section 2.3.4 (see Table 2.4), among all the investigated Fe- and Ti-PGMs, the Fe0/Ti0, Fe1 and Ti1 microspheres show (1) the highest short-term degradation rates, (2) the highest long-term degradation rates, (3) the highest release rates of most ions and (4) the steepest decrease in pH over time spans of approx. 7 days. The pH changes associated with such degradation would have deleterious effects on cells; furthermore, the lack of a stable surface for attachment in these microspheres, as has been observed in the time lapse images in Figures

2.6 and 2.7 of section 2.3.4, would preclude the successful attachment of the cells to the microsphere surface. All these factors would be unfavourable for the survival of MG63 cells, which are known to be anchorage-dependent cells, and thus cells were not visible on the surfaces of the Fe0/Ti0, Fe1 and Ti1 microspheres.

In contrast, the Fe3–5 and Ti3–7 microspheres clearly showed cells attached to the microsphere surface, as evidenced by both SEM and CLSM imaging (Figures 4.1–4.3). The presence of greater cells on day 7 than on day 1 in Figure 4.1 showed that the cells were proliferating on the microsphere surface; thus, these microspheres were considered suitable candidates for quantitative cell proliferation assays. At this stage, it is worth noting that in the Fe3–5 and Ti3–7 microspheres samples, not all the microspheres showed cells on the surface i.e. many of the microspheres were devoid of any cell growth. To some extent, this is an expected result that can probably be attributed to the processing steps involved in preparing the samples for SEM imaging; this aspect will be discussed in greater detail later.

Subsequently, MG63 cell proliferation on the Fe3–5 and Ti3–7 microspheres was quantitatively assessed by means of a CCK-8 cell proliferation assay carried out at time points of 1, 4 and 7 days in ultra-low attachment cell culture plates, with the aforementioned commercially available silica glass microspheres used as the control. At this stage, it is worth noting that the cell proliferation assays were carried out in the ultra-low attachment plates instead of the Transwell® inserts that were used for the SEM imaging studies (although Transwell® inserts have been used in this research to carry out an alamarBlue® assay; see Appendix A.3 for details). Transwell® inserts are a useful means to carry out cell culture because of advantages in terms of handling and nutrient distribution, but they are not particularly suited for experiments involving quantitative measurements such as cell proliferation or ELISA assays. This is because the membrane surface in the Transwell® insert is specially treated to encourage high levels of cell attachment and proliferation. Thus, in the case of microsphere culture on such inserts, the cells could attach either to the microspheres or to the insert membrane and any assay results would indicate the combined effects of the microsphere surface and the membrane surface on the cells; consequently, the inserts would not be able to provide an accurate quantitative estimate of the capacity of the microspheres alone to support cells on their surface. Ultra-low attachment culture surfaces are advantageous in this respect because they possess a coating of a covalently bound hydrogel layer that serves to inhibit cellular attachment on the plate surface, so that

the cells can attach only to the microsphere surface. Therefore, ultra-low attachment plates were used so as to accurately quantify the effects of microspheres alone on the cells since the microspheres would provide the only surface on which the cells could attach and proliferate. Another aspect worth considering is the use of the Cell Counting Kit-8 cell proliferation assay, which has been employed extensively in the present study. As per the instructions of the manufacturer (Sigma-Aldrich, UK), the main component of the assay kit is a water-soluble tetrazolium salt WST-8, which produces a water-soluble formazan dye upon reduction in the presence of an electron carrier through cell dehydrogenase activity; the amount of formazan dye generated is directly proportional to the number of living cells. WST-8 belongs to the second generation of tetrazolium dyes, which on account of their net negative charge are largely cell-impermeable (Berridge et al., 2005). The mechanism of action of these dyes involves reduction at the cell surface by trans-plasma membrane electron transport. This is in contrast to earlier generations of tetrazolium dyes such as MTT which have a net positive charge and which undergo reduction associated with the mitochondria, cytoplasm and non-mitochondrial membranes post cellular uptake. It is therefore considered that whereas assays such as MTT may be measuring the cell metabolic activity as opposed to the number of living cells present, the CCK-8 assay does measure the number of living cells present in the sample.

The CCK-8 cell proliferation assays on the Fe3–5 and Ti3–7 microspheres revealed that all five compositions showed a significant increase in cell numbers over a 7 day culture period. The increase in the cell population for all the investigated Fe- and Ti-PGMs as well as the control from day 1 to day 7 was in the 2.7–3.5 fold range; the highest cell numbers at day 7 were obtained for the Ti3 and Ti5 microspheres (approx. 930,000). At day 7, the cell numbers for Ti-PGMs of different compositions were significantly greater than those for the control microspheres, indicating the superior ability of the Ti-PGMs to nurture cells on their surface. However, comparisons in cell numbers among the Ti3–7 microspheres at all the time points generally revealed no significant differences, indicating that the Ti3, Ti5 and Ti7 microspheres all provided a uniformly favourable surface for MG63 cell attachment and proliferation. It is interesting to note that the medium replacement frequency may have played a role in this result. In the assay experiments, 50% of the medium was replaced at intervals of 2 days throughout the 7 day study period. As observed in Figure 4.9, increasing the medium replacement interval from 2 days to 3 days can have significantly different effects on cell proliferation on both Ti5 and control

microspheres whereby the cell numbers at day 7 are either approx. equal to or lower than those at day 4, and the results in general have greater variability with high error values. Two possible influencing factors for this result could be the build-up of waste from cell metabolic processes and the effects of cell confluency on the microsphere surface. For subsequent experiments, the Ti5 microspheres were chosen from among all the investigated Fe- and Ti-PGMs. As will be discussed later, the reasons for selecting Ti5 as the candidate PGMs for comparison with commercially available microspheres are not entirely linked to the results of the biological tests, and there are several other factors involved.

Next, the interactions between the microspheres (Ti5 and control) and MG63 cells in a dynamic environment were studied by means of culture within spinner flask bioreactors. The spinner flask bioreactors were chosen mainly because these types of bioreactors, although simple in design, provide dynamic 3D *in vitro* environments that are capable of replicating *in vivo* conditions more accurately than static cell culture well environments; thus, they can provide valuable information not only for the *in vitro* growth of tissue substitutes but also for researching the responses of cells and tissues to various stimuli of mechanical and biochemical origin. With regard to the SEM and CLSM images of MG63 cells cultured on the Ti5 and control microspheres in the bioreactors (Figures 4.7 and 4.8), the torn appearance of the cells on the microspheres can be attributed to the forces exerted on the microsphere–cell aggregates when they were pipetted out of the bioreactors at each time point using Pasteur pipettes. Although images of the cell–microsphere aggregates were not taken at the time, macroscopic structures comprising groups of microspheres covered by confluent layers of cells were clearly visible on the bioreactor bottom surface. The pipetting steps involved in transferring the cell–microsphere aggregates from the bioreactors to cell culture plates for imaging/assaying purposes would probably have caused some of the confluent cells to be dislodged from the microsphere surface and led to morphological disruption of the remaining attached cells. It is anticipated that when harvesting the expanded cells for use in cell therapy applications, cell washout and/or tearing should not constitute a major concern because the attached cells would need to be trypsinised to detach them from the microsphere surfaces prior to for further use or, depending on the application, not removed from the substrate at all. Fewer cells were found attached to the control microspheres than the Ti5 microspheres at both 4 and 7 days post seeding, thereby indicating the superior adhesion of MG63 cells on the Ti5 microspheres in comparison with the control under dynamic conditions.

One of the major highlights of the entire research is the considerably superior MG63 cell proliferation on the Ti5 microspheres in spinner flask bioreactors in comparison with that on the control microspheres in the bioreactors; furthermore, the Ti5 bioreactor cell populations are considerably higher than the cell numbers obtained for both the Ti5 and control microspheres under static conditions. The results shown in Figures 4.9 and 4.10 clearly demonstrate the potential of the investigated titanium phosphate glass microspheres to function as stable microcarrier surfaces for bone tissue engineering applications. Also clear is the efficacy of the bioreactor approach employed in the study; the fact that a simple bioreactor system where the main forces exerted on the cells arise from gentle agitation at a speed of 40 rpm can have such a positive impact on MG63 cell growth, with a 24-fold increase in numbers from an initial seeding density of 50,000 cells per well, demonstrates the considerable effect of low-level mechanical forces on MG63 cell proliferation. The effects of the mechanical forces exerted in bioreactors on bone cells have been studied previously, and it has been demonstrated that the presence of such forces can significantly benefit bone cell differentiation, mineral matrix formation and phenotypic expression *in vitro* (Bancroft et al., 2002, Sikavitsas et al., 2003, Meinel et al., 2004). The higher errors and lower cell numbers on day 7 observed for static culture in Figure 4.9 can be attributed to the previously mentioned issue of medium replacement frequency; the replacement of 50% of the medium at intervals of 3 days, while sufficient for bioreactor culture with a working volume of 100 ml, is clearly not adequate for maintaining cell numbers in static culture with a working volume of 1 ml.

Thus, the results obtained from studies of MG63 cell–microsphere interactions under static and dynamic environments demonstrate the potential of the developed glass microspheres to serve as microcarrier substrates for bone tissue engineering applications. The next and final step in the research is to study the interactions between the microspheres and human mesenchymal stem cells (hMSCs). Such a study permits the investigation of the microspheres as substrates that can guide the differentiation of hMSCs along osteogenic pathways. Furthermore, one of the major objectives is to replicate the favourable results obtained for MG63 cells in bioreactor culture with hMSCs as well, which could then offer exciting possibilities for application of metal-doped PGMs to the development of small-sized bone tissue *in vitro*.

Chapter 5. Interactions between microspheres and human mesenchymal stem cells

5.1. Introduction

In this chapter, the interactions between the developed microspheres and human mesenchymal stem cells (hMSCs) were investigated under both static and dynamic conditions. Among all the investigated phosphate glass microsphere compositions (Fe0, Fe1, Fe3, Fe5 and Ti0, Ti1, Ti3, Ti5, Ti7), the Ti5 microspheres were selected and their performance in the experiments was compared with that of commercially available non-degradable silica glass microspheres (Polysciences Inc., USA). A size range of 50–100 μm was chosen for both the Ti5 and control microspheres so as to minimize the effect of microsphere size on the experimental results. For the static culture studies, two types of cell culture media—low glucose Dulbecco's Modified Eagle's Medium (DMEM; supplemented with 10% foetal bovine serum (FBS) and 1% penicillin–streptomycin) and the commercially available mesenchymal stem cell medium DXF (Promocell GmbH, Germany)—were used and the effects of the use of two different media on hMSC proliferation were assessed. In addition to quantification of hMSC proliferation on the microspheres, which was performed using the Cell Counting Kit-8 (CCK-8) cell proliferation assay, the differentiation of hMSCs along osteogenic pathways was studied using an Alizarin Red S assay, and the expression of two proteins, namely bone morphogenetic protein-2 (BMP-2) and osteopontin (OPN), was quantified by means of ELISA assays. Dynamic culture of hMSCs on the investigated microspheres was carried out using spinner flask bioreactors. Only Ti5 microspheres were used for hMSC bioreactor culture experiments so as to gain a preliminary understanding of hMSC interactions with glass microspheres under dynamic conditions. The effects of two different types of media—DMEM and osteogenic medium—on hMSC proliferation were assessed. Furthermore, the effect of increasing the culture time from 7 days to 15 days on cell proliferation was studied. (Note that from previous experience in the author's group, the average size of adherent human mesenchymal stem cells used in the study is approximately 2500 μm^2; considering that the diameters of the microspheres used in all the experiments are in the 50–100 μm range, it can be calculated that each microsphere can accommodate approximately 12–25 cells on its surface.)

5.2. Materials and methods

5.2.1. Preparation of hMSCs

Human mesenchymal stem cells were obtained from in-house stocks and grown in the same way as described previously for MG63 cells in section 4.2.1. The hMSCs were additionally grown by a slightly different method when the commercially available mesenchymal stem cell growth medium DXF (PromoCell GmbH, Germany) was used. This medium does not contain cell attachment and spreading factors. Therefore, as per the manufacturer instructions, the surface of the flask was treated with a 10 µg/ml solution of bovine fibronectin (PromoCell GmbH, Germany) in phosphate buffered saline (PBS) for 1 hour prior to introduction of medium and cells so as to introduce a fibronectin coating on the flask surface and facilitate the attachment and cytoplasmic spreading of the cells. The remaining steps were performed in the same way as in section 4.2.1 with DXF being used in place of DMEM (low glucose Dulbecco's Modified Eagle Medium; 10% FBS and 1% penicillin–streptomycin added).

5.2.2. Cell culture on microspheres under static conditions

The static culturing of cells on the microspheres was carried out using ultra-low attachment plates only. The same protocol as that described in section 4.2.2 was followed for sterilisation of microspheres and culturing of hMSCs on the microspheres. However, for experiments involving hMSCs in which the DXF medium was used, an additional microsphere coating step was employed prior to pre-warmed medium addition, in which 1 ml of a 10 µg/ml solution of bovine fibronectin in PBS was added to each well containing sterilised microspheres and left as is for 1 hour before it was removed and replaced with pre-warmed medium. This step was carried out so as to investigate whether the presence of a fibronectin coating on the microsphere surface would enhance hMSC attachment.

5.2.3. Cell culture on microspheres under dynamic conditions

The methods used for dynamic culturing of hMSCs on the microspheres in spinner flask bioreactors was carried out using the same methods as those described in section 4.2.3 with some modifications in terms of the media used and the culturing time (these are highlighted in section 5.3.2).

Prior to conducting the bioreactor experiments, it was necessary to carry out a time course experiment in order to determine the time for which initial static culture of

hMSCs on the microspheres should be carried out before transfer of microspheres and attached cells to the bioreactor. For this purpose, 200 mg per well of sterilised microspheres were seeded with hMSCs in a 24 well ultra-low attachment cell culture plate at a seeding density of 50,000 cells per well. The plate was then placed in a 37°C/5% CO_2 incubator for 30 minutes so as to allow sedimentation of the microspheres and cells. The plate was then placed on a plate shaker operating at a speed of 100 rpm for 5 minutes, after which it was replaced in the incubator for durations of 2, 4, 6 and 8 hours. At each time point, the contents of each well were pipetted out using Pasteur pipettes into a 50 ml centrifuge tube fitted with a cell strainer (BD Biosciences, Oxford, UK) having a pore size of 40 µm so as to separate the microspheres with attached cells (that were immobilised on the strainer mesh surface) from the unattached cells (that passed through the mesh into the centrifuge tube). The well was washed 2-3 times with medium and the contents were passed through the strainer each time so as to ensure that all the microspheres with bound/unbound cells had been transferred. The number of unbound cells in the centrifuge tube was then determined using a Vi-CELL cell viability analyser (Beckman Coulter, High Wycombe, UK), and the data was plotted as percentage of unattached cells versus time.

5.2.4. Scanning electron microscopy and confocal laser scanning microscopy imaging

Both scanning electron microscopy (SEM) and confocal laser scanning microscopy (CLSM) imaging techniques were carried out in accordance with the methods described in sections 4.2.4 and 4.2.5 respectively.

5.2.5. Cell proliferation assay

Cell proliferation on the microspheres was quantified using the CCK-8 assay as per the protocol provided in section 4.2.6.

5.2.6. Alizarin Red S assay

The Alizarin Red S assay was carried out in accordance with the protocol as described by Gregory et al. (Gregory et al., 2004) with some modifications. The medium used for cell culturing was osteogenic medium, which comprised DMEM containing (by volume) 10% FBS, 1% penicillin–streptomycin and 0.1% Fungizone along with 0.1 µM dexamethasone, 0.2 mM ascorbic acid 2-phosphate and 10 mM glycerol 2-phosphate (the last three chemicals were procured from Sigma–Aldrich, UK). The procedure used to prepare the osteogenic medium has been described

previously (de Girolamo et al., 2007). Assay measurements were carried out on duplicate samples (i.e. n = 2); for each time point, separate samples of each composition and the control (commercially available silica microspheres) were seeded and all samples were discarded post measurement. The sample and control microspheres were cultured with hMSCs (seeding density of 50,000 cells per well) in ultra-low attachment 24 well plates over a 21 day period with sampling time points of 7, 14 and 21 days. At each time point, the contents in each well were washed with PBS and fixed with 10% formalin (Sigma–Aldrich, UK) for 1 hour at room temperature. The fixative was then aspirated and further washing was carried out 1–2 times with distilled water. Then, 0.5 ml of 2% Alizarin Red S dye in water (pH 4.2) was added to each well and the plate was maintained at room temperature for 20 minutes. The dye was then aspirated and the wells were allowed to dry overnight at room temperature. For quantification of staining, 0.5 ml of 10% w/v cetyl pyridinium chloride (Sigma–Aldrich, UK) in 10 mM sodium phosphate buffer (pH 7.0) was added to each well and the plate was kept at room temperature for 2 hours. Then, 100 µl aliquots were transferred to a 96 well plate and absorbance was measured in a microplate reader at 540 nm.

5.2.7. ELISA assays for bone morphogenetic protein-2 and osteopontin

ELISA assays for detection of BMP-2 and OPN release were carried out as per protocols specified by the manufacturer (mammalian Quantikine ELISA kits, R&D Systems, Abingdon, UK). Assay measurements were carried out on duplicate samples (i.e. n = 2) and osteogenic medium was used for the cell culture procedures. The sample microspheres and controls (commercially available silica microspheres) were cultured with hMSCs in ultra-low attachment 24 well plates over a 21 day period with sampling time points of 7, 14 and 21 days. At each time point, the cell culture supernatant from each well was collected and replaced with fresh medium. The collected supernatant was centrifuged at 1500 rpm for 10 minutes at a temperature of 4°C so as to remove any particulates; the supernatant was then stored at –20°C until required. Following the assay procedure, optical density was measured at 450 nm with respect to a reference wavelength of 540 nm. In order to convert the optical density values to protein concentrations in ng/ml or pg/ml, a standard curve of protein concentration versus optical density was plotted according to the manufacturer instructions.

5.2.8. Statistical analysis

All statistical analyses were carried out using IBM SPSS version 21 (SPSS Inc., USA). As was the case in chapter 4, initial tests for normality (one-sample Kolmogorov-Smirnov test) revealed the data did not have a normal distribution, so it was necessary to use non-parametric tests such as the Kruskall-Wallis H test and Mann-Whitney U test. Multiple pairwise comparisons were corrected using the Bonferroni correction method. The assumed levels of significance for the statistical tests was 0.05 unless Bonferroni corrections were used, in which case it was either 0.008 or 0.016. Note that because the data do not have a normal distribution, the presence (or absence) of statistically significant differences may not always be visually apparent in some of the graphs. A more accurate representation of the data would be in the form of box-and-whisker plots, which are shown in Appendix A.4. Bar charts were used for ease of comparison of the data.

5.3. Results

5.3.1. Investigating stem cell growth and differentiation potential: static hMSC–microsphere interactions for Ti-PGMs

5.3.1.1. Scanning electron microscopy imaging

Figure 5.1 shows SEM images at day 7 of hMSCs cultured on Ti5 and control microspheres under static conditions in ultra-low attachment plates using DMEM as the culture medium. It was observed that in comparison with the number of MG63 cells found attached to and growing on the microspheres (Figures 4.1 and 4.2 in section 4.3.1), much fewer hMSCs were visible on the microspheres surface; most of the microspheres in the sample and control had no cells attached. At a preliminary level, visual examination revealed that the hMSCs that were attached to the microspheres appeared to be larger than the MG63 cells. Furthermore, on both the Ti5 and control microspheres, it appeared that the cells were either somewhat flattened and seem to be spreading out on the surface or they had a torn appearance and seemed to be peeling off the microspheres. Mostly individual cells were seen on the Ti5 microspheres, whereas groups of cells could be seen on the control microspheres. Cell-microsphere aggregates comprising groups of microspheres covered with cells joined to each other by means of processes could also be discerned in the control microspheres.

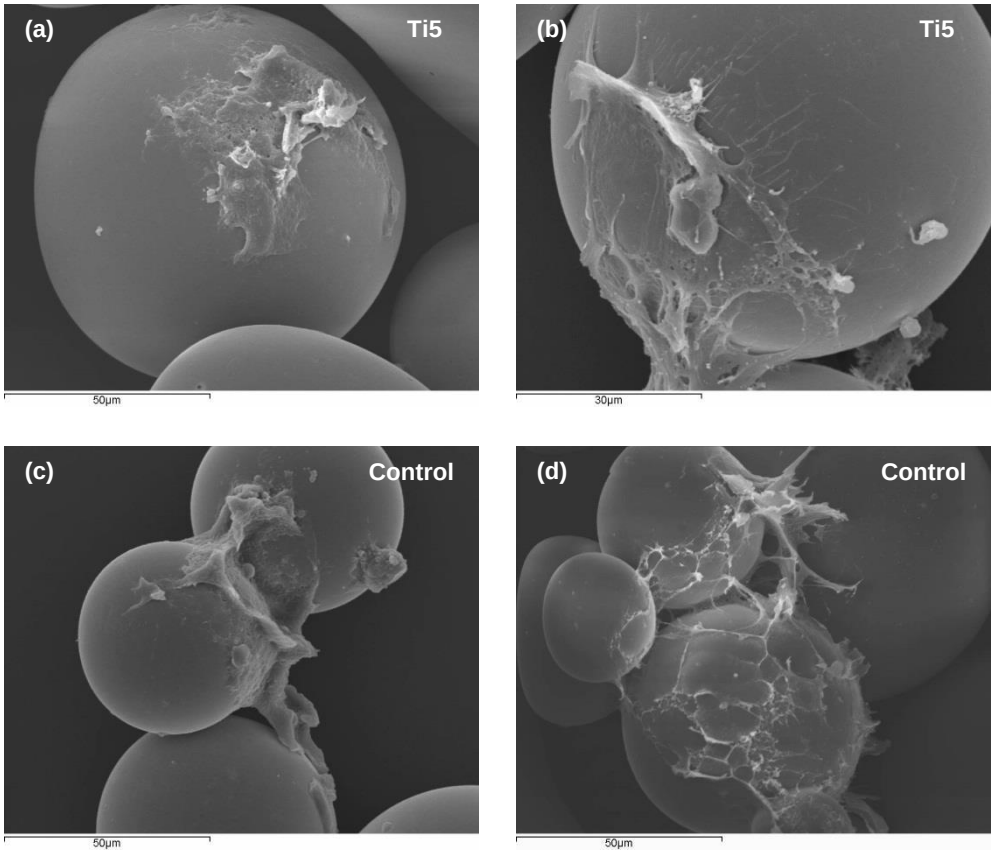

Figure 5.1. Scanning electron microscopy images showing hMSCs attached to (a, b) Ti5 and (c, d) control glass microspheres when cultured in ultra-low attachment plates at 7 days post seeding (DMEM is used as the culture medium). In comparison with the number of MG63 cells attached to the microspheres in earlier experiments, much fewer hMSCs are found attached to both the Ti5 and control microspheres, with most microspheres not covered with cells. Individual cells are visible on the Ti5 microspheres, which have either a torn appearance (a) or a reasonably flattened morphology with spread out features (b). The control microspheres show groups of cells on adjacent microspheres that are joined together by means of processes. As with the cells on the Ti5 microspheres, those on the control have either a somewhat flattened structure (c) or a torn appearance (d).

5.3.1.2. Confocal laser scanning microscopy imaging

Figure 5.2 shows CLSM images of hMSCs at 7 days when cultured on Ti5 and control microspheres under static conditions in ultra-low attachment plates using DMEM as the culture medium. In general, more cells were observed adhering to the microspheres in the CLSM images than in the SEM images (Figure 5.1). Furthermore, more cells were observed growing on the control microspheres as compared to the Ti5 microspheres. Favourable cell adhesion could be inferred from the alignment of the green actin filaments along the microsphere curvature. Similar to the SEM images (Figure 5.1), clusters of cells on groups of microspheres seemed to be attached by means of processes in the control microspheres, whereas the Ti5 microspheres seemed to be attached to individual cells.

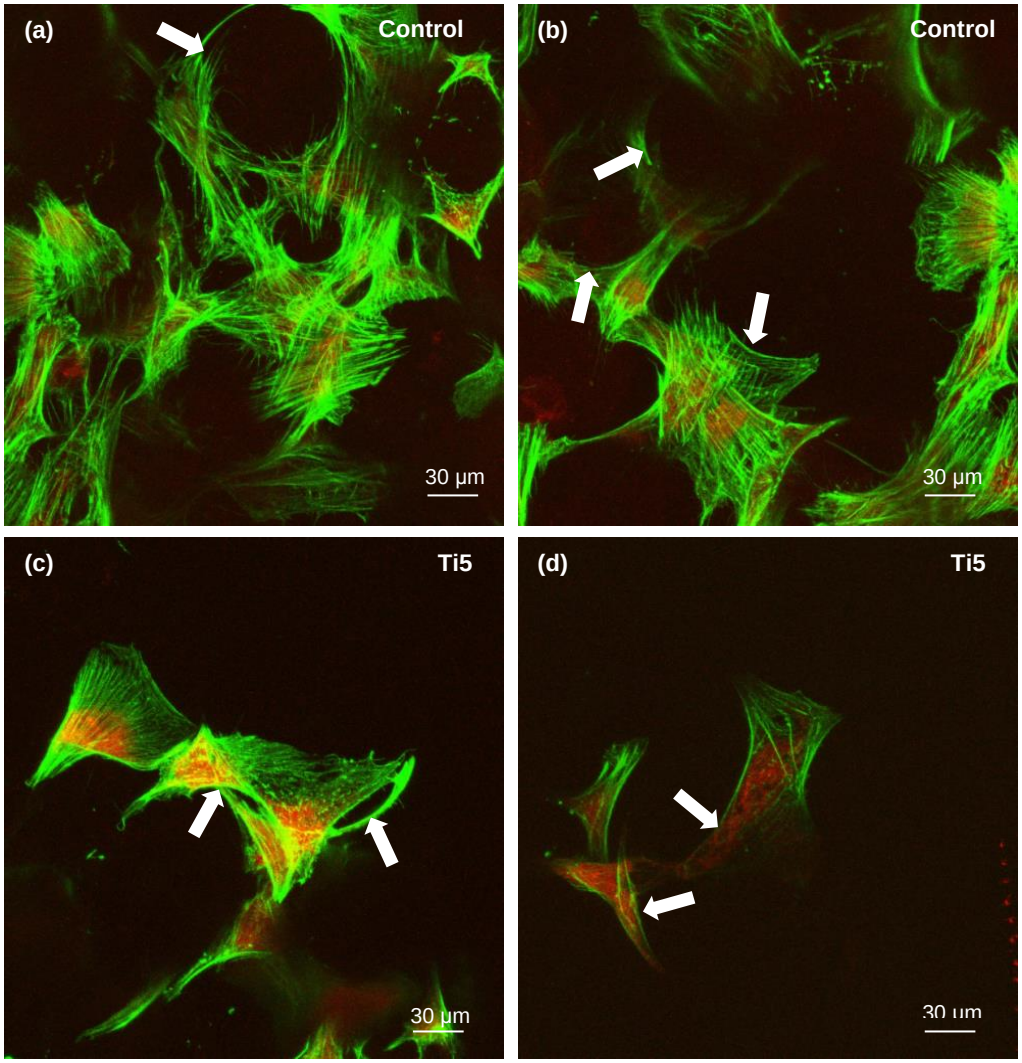

Figure 5.2. Confocal laser scanning microscopy images of hMSCs growing on the control microspheres (a, b) and Ti5 microspheres (c, d) in ultra-low attachment plates at 7 days post culture. DMEM is used as the culture medium. Phalloidin stains the actin filaments of the cytoskeleton green while propidium iodide stains the nuclei red. More cells are visible on the control microspheres than on the Ti microspheres. The alignment of the actin filaments along the microsphere curvature is visible (indicated by white arrows in the images), which implies favourable cell adhesion. Clusters of cells covering groups of microspheres are observed in the control microspheres (a, b), whereas smaller clusters or individual cells are found to cover the Ti5 microsphere (c, d).

5.3.1.3. Cell proliferation assays

Human mesenchymal stem cell proliferation on the Ti5 and control microspheres was quantitatively determined using the CCK-8 cell proliferation assay. Prior to the actual assay, a standard curve of the microplate absorbance values as a function of the number of cells was plotted as shown in Figure 5.3.

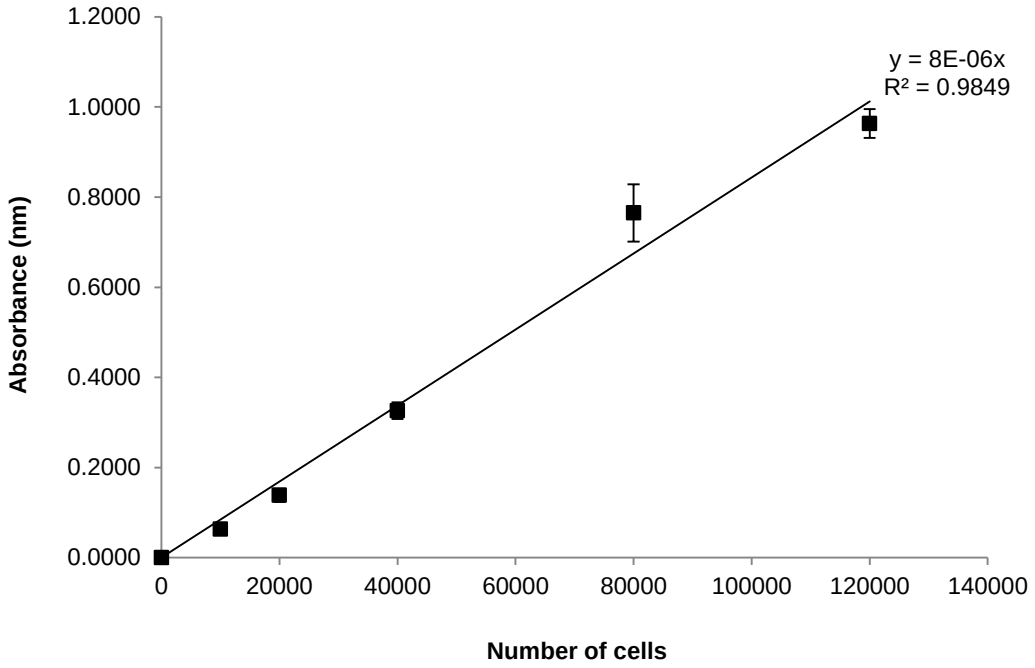

Figure 5.3. Standard curve of hMSC growth plotted as absorbance values versus number of cells after carrying out a CCK-8 assay at 1 day post seeding. The absorbance values are obtained at a wavelength of 450 nm. Error bars represent ±SD (n = 6).

Figure 5.4 shows the overall results of the CCK-8 assay performed to quantify the proliferation of hMSCs on the surfaces of Ti5 and control microspheres in ultra-low attachment cell culture plates over a 7 day period when DMEM and a commercially available mesenchymal stem cell growth medium DXF (Promocell GmbH) are used as the culture medium. It was observed that among the four sample/medium combinations that were investigated i.e. Ti5-DMEM, Ti5-DXF, control-DMEM and control-DXF, all the combinations showed statistically significant differences in cell numbers over the 7 day study period (chi-square values = 36.752, 21.470, 41.798 and 33.067 respectively with 2 degrees of freedom); furthermore, all the combinations except Ti5-DXF showed a significant increase in cell population from day 1 to day 7 of the culture period (*** $p < 0.001$). To elaborate, when DMEM was used as the culture medium, the cell numbers on the Ti5 microspheres increased by 26% from day 1 to day 4 (*** $p < 0.001$) and by 17% from day 4 to day 7 (*** $p < 0.01$), leading to an overall increase of 48% (*** $p < 0.001$) from day 1 to day 7 and a 4.5-fold increase from an initial seeding density of 50,000 cells per well. The

corresponding numbers for the control microspheres cultured in DMEM were 18% from day 1 to day 4 (*** $p < 0.001$) and 25% from day 4 to day 7 (*** $p < 0.001$), with an overall increase of 47% (*** $p < 0.001$) from day 1 to day 7 and a 3.3-fold increase for an initial seeding density of 50,000 cells per well. When the DXF medium was used, the cell growth trends for the control microspheres were roughly similar to the trends obtained when DMEM was used. However, in contrast to all the other results, the Ti5 microspheres showed a statistically significant decrease in cell population. The number of cells reduced by 5% from day 1 to day 4 but the difference was statistically insignificant ($p > 0.016$, Bonferroni correction). However, the number of cells decreased by 3% from day 4 to day 7 (** $p < 0.01$), resulting in an overall decrease of 7% from day 1 to day 7 (*** $p < 0.001$) but a 3.4-fold increase for a 50,000 cells per well initial seeding density.

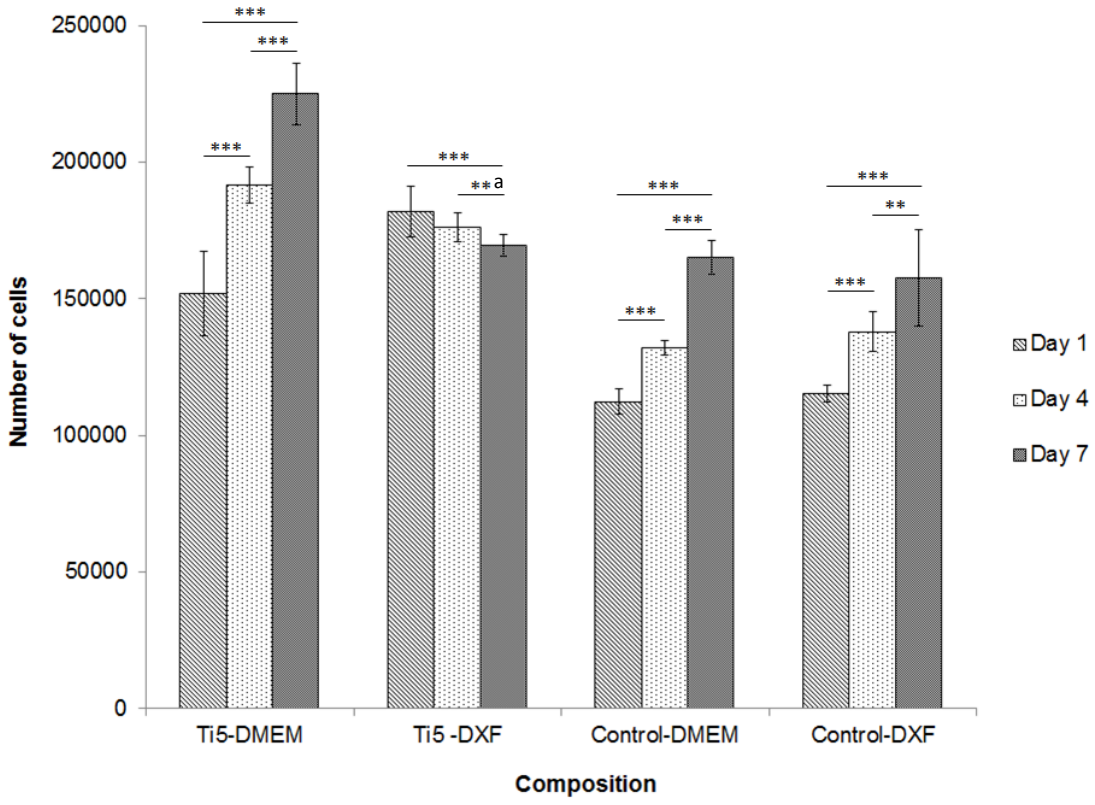

Figure 5.4. Bar chart representing the results of a CCK-8 assay to quantify hMSC proliferation on Ti5 and control microspheres in ultra-low attachment cell culture plates at time points of 1, 4 and 7 days when DMEM and a commercially available mesenchymal stem cell growth medium DXF (Promocell GmbH, Germany) are used as the culture medium. The control comprises silica glass microspheres (Polysciences Inc.). Error bars represent ±SD and n = 2. The symbols ** and * indicate $p < 0.01$ and $p < 0.001$ respectively. DMEM produces a significant increase in cell numbers on both the Ti5 and control microspheres between day 1 and day 7 (*** $p < 0.001$). DXF produces a significant increase in cell numbers on the control microspheres but causes a significant decrease in cell numbers on the Ti5 microspheres from day 1 to day 7 (*** $p < 0.001$). [a]Note that the statistically significant differences shown in this bar chart are based on non-parametric statistical analysis, which was necessary because the data was not normally distributed. The presence of statistically significant differences is not always visually apparent because while the bar chart shows the mean values and standard deviations, statistical**

significance in this case is calculated based on the sum of the ranks of the data points in each data set. The box-and-whisker plots in Figure A.7 of Appendix A.4 provide a more visually accurate representation of the statistically significant differences between the data sets. Also note that certain data points were found to be outliers during the statistical analysis and have therefore been excluded from the plotted data.

Figure 5.5 compares the differences in hMSC proliferation between the Ti5 and control microspheres when (a) DMEM and (b) DXF are used as the cell culture medium. In the presence of DMEM as the culture medium, the Ti5 microspheres showed significantly greater cell proliferation than the control microspheres at all the investigated time points; thus, the differences in cell numbers between the Ti5 and control microspheres were 26, 31 and 26% at days 1, 4 and 7 (*** $p < 0.001$). When DXF was used as the culture medium, significantly greater cell proliferation was found on the Ti5 microspheres in comparison with the control microspheres at days 1 and 4 (40% difference at day 1; 24% difference at day 4; *** $p < 0.001$); however, the differences were not statistically significant at day 7 ($p > 0.05$).

(a)

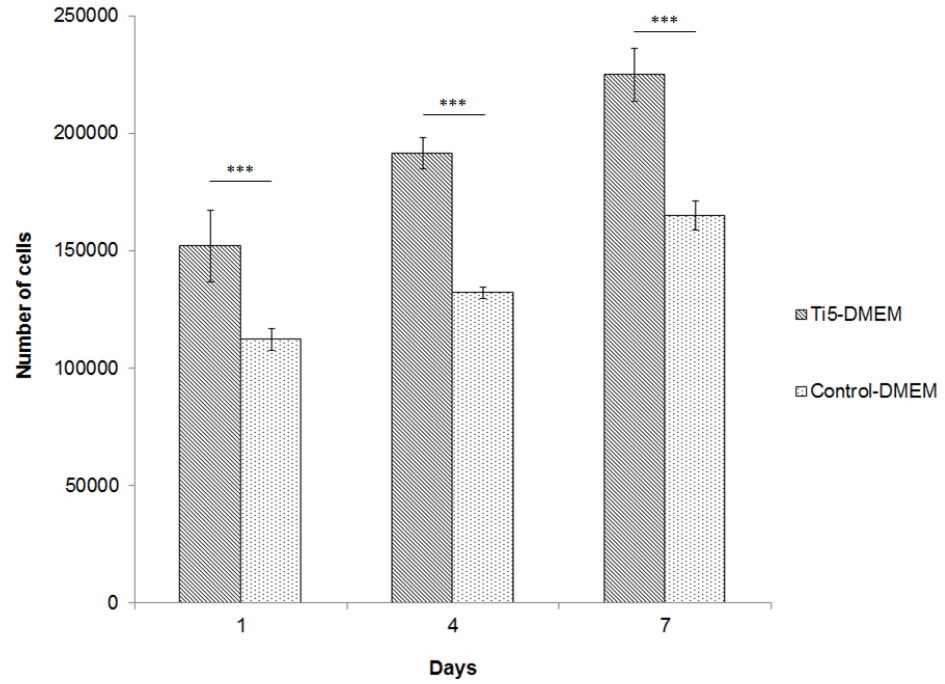

(b)

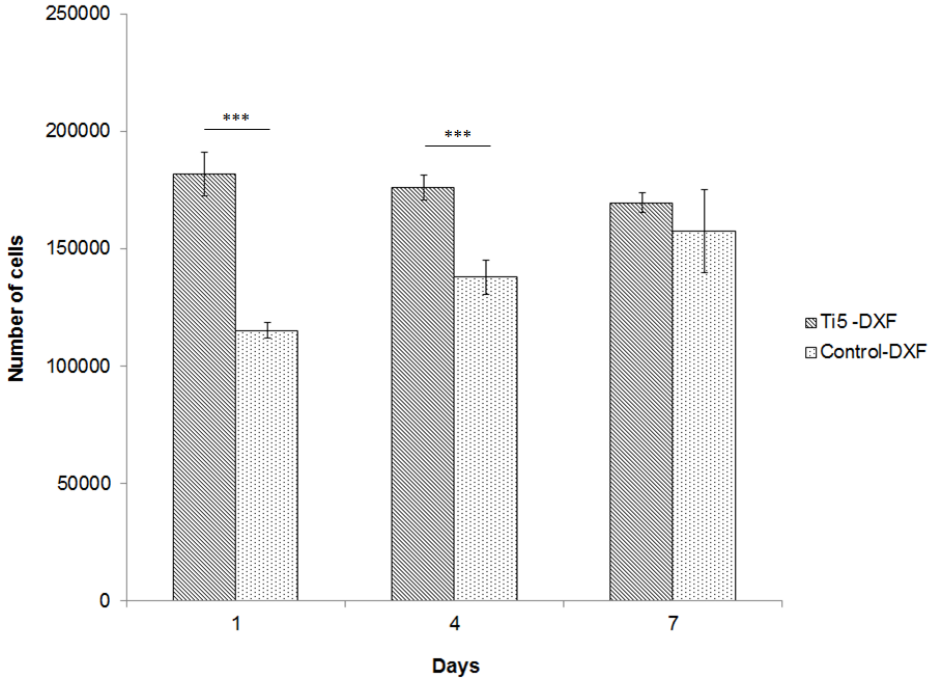

Figure 5.5. Bar chart comparing hMSC proliferation on Ti5 and control microspheres in ultra-low attachment cell culture plates at time points of 1, 4 and 7 days when (a) DMEM and (b) DXF are used as the culture medium. The control comprises silica glass microspheres (Polysciences Inc.). Error bars represent ±SD and n = 2. The symbols ** and * indicate $p < 0.01$ and $p < 0.001$ respectively. When DMEM is used, the Ti5 microspheres show significantly greater cell proliferation than the control microspheres at all the time points (*** $p < 0.001$). When commercial DXF is used, the Ti5 microspheres show significantly greater cell proliferation than the control microspheres at days 1 and 4 (*** $p < 0.001$) but not at day 7 where the difference is statistically insignificant ($p > 0.05$).**

Figure 5.6 compares the effects of DMEM and DXF media on hMSC proliferation in the case of (a) Ti5 and (b) control microspheres. It was observed that in the case of the Ti5 microspheres, DMEM resulted in 19% lower cell proliferation than commercially available DXF on day 1 (*** $p < 0.001$); however, DMEM subsequently outperformed DXF with 8% higher cell proliferation on day 4 and 25% higher proliferation on day 7 (*** $p < 0.001$). In the case of the control microspheres, no statistically significant difference was found between the DMEM and DXF media at any of the time points ($p > 0.05$ throughout).

(a)

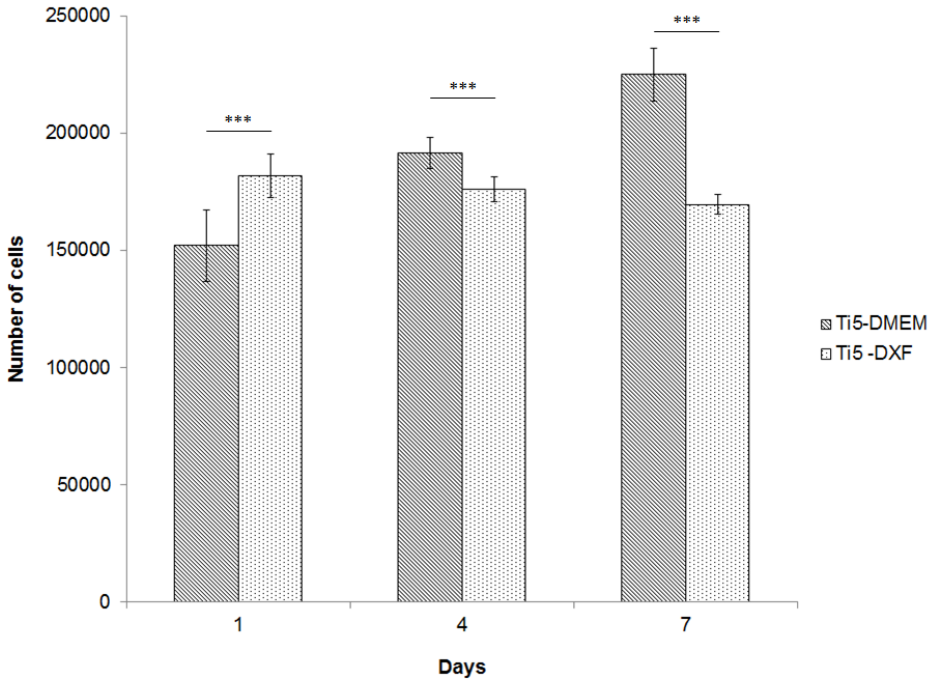

(b)

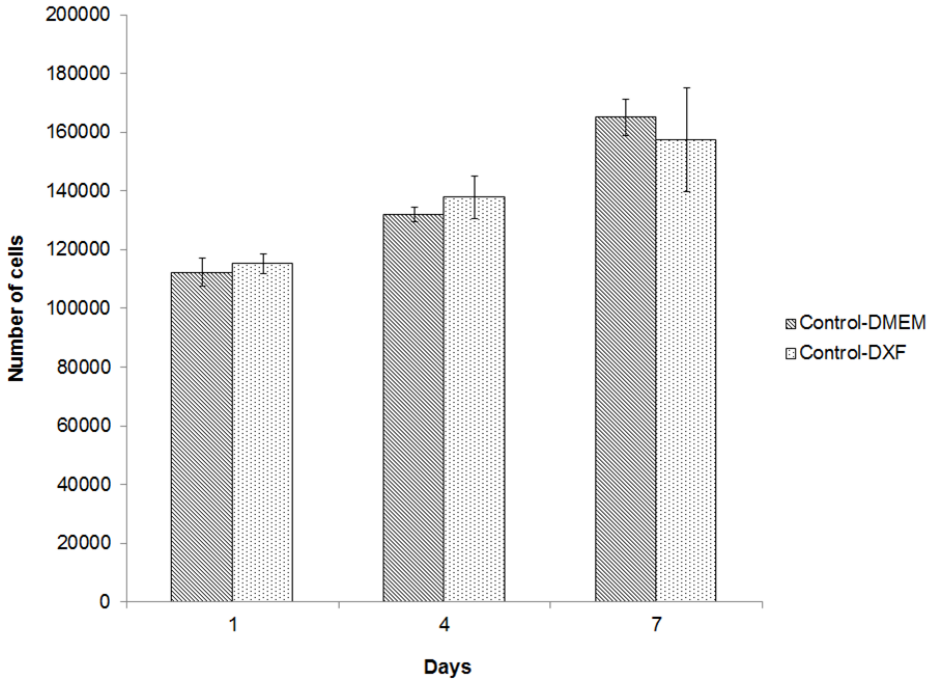

Figure 5.6. Bar charts comparing the effects of DMEM and commercial DXF cell culture media on hMSC proliferation in the case of (a) Ti5 and (b) control microspheres in ultra-low attachment cell culture plates at time points of 1, 4 and 7 days. The control comprises silica glass microspheres (Polysciences Inc.). Error bars represent ±SD and n = 2. The symbols ** and * indicate $p < 0.01$ and $p < 0.001$ respectively. Ti5 microspheres exhibit a positive effect towards DMEM but a negative effect towards commercial DXF with statistically significant differences at all the time points (*** $p < 0.001$). Control microspheres exhibit a positive effect towards both DMEM and DXF but the differences are statistically insignificant ($p > 0.05$).**

5.3.1.4. Alizarin Red S assay

Figure 5.7 shows the results of the Alizarin Red S assay carried out for hMSCs cultured on Ti5 and control glass microspheres over time points of 7, 14 and 21 days. Over the 21 day experimental period, the changes in the absorbance values were found to be statistically significant for the control microspheres (chi-square value = 18.656 with 2 degrees of freedom) but not for the Ti5 microspheres. The level of mineralisation on the control microspheres was found to be significantly greater than that on the Ti5 microspheres at all the investigated time points (** $p < 0.01$; *** $p < 0.001$). The absorbance values underwent an increase for the control microspheres over the duration of the experiment, with the differences between days 7 and 14 and between days 7 and 21 being statistically significant (*** $p < 0.001$). However, for the Ti5 microspheres, the differences among the absorbance values at all the investigated time points were not statistically significant ($p > 0.016$, Bonferroni correction).

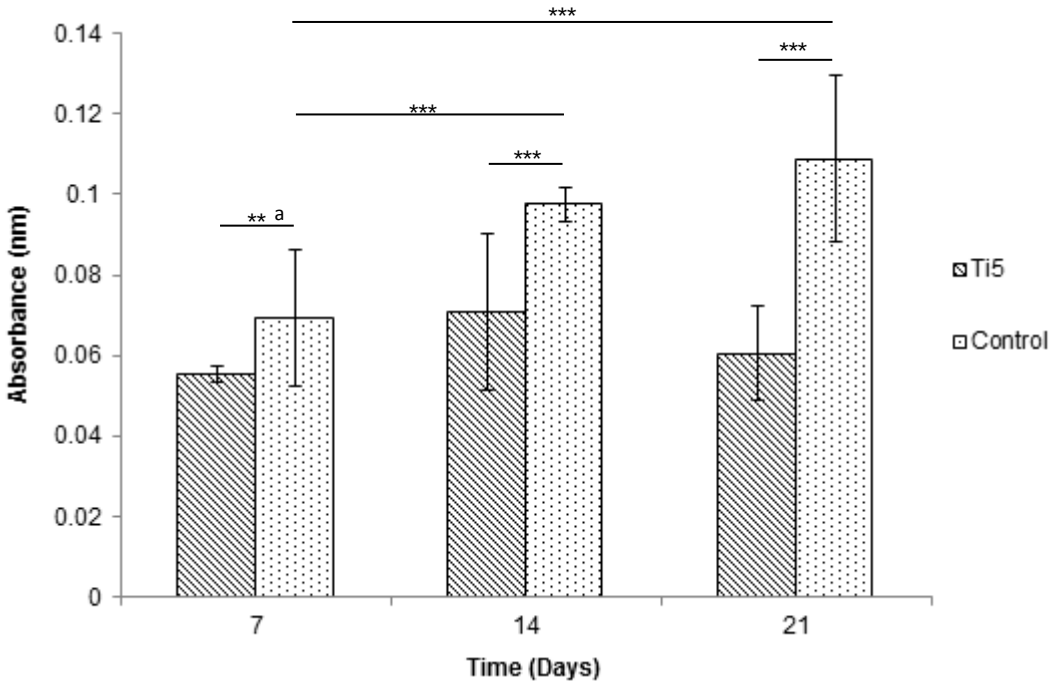

Figure 5.7. Bar chart representing the differentiation of hMSCs into bone cells on Ti5 and control glass microspheres as quantified by the extent of mineralisation on the microsphere surface using an Alizarin Red S assay. The assay was carried out at time points of 7, 14 and 21 days and absorbance measurements were carried out at 540 nm. Error bars represent ±SD where n = 2. The symbols ** and * indicate $p < 0.01$ and $p < 0.001$ respectively. Significantly higher absorbance values are obtained for the control microspheres in comparison with the Ti5 microspheres at every time point (** $p < 0.01$; *** $p < 0.001$). Statistically significant differences are observed in the control microspheres between days 7 and 14 and between days 7 and 21 (*** $p < 0.001$). For the Ti5 microspheres, the differences in the absorbance values are not statistically significant between any of the time points ($p > 0.016$, Bonferroni correction). [a]Note that the statistically significant differences shown in this bar chart are based on non-parametric statistical analysis, which was necessary because the data was not normally distributed. The presence of statistically significant differences is not always visually apparent because while**

the bar chart shows the mean values and standard deviations, statistical significance is calculated based on the median values. For a more visually accurate representation of the statistically significant differences, refer to the box-and-whisker plot in Figure A.8 of Appendix A.4.

5.3.1.5 ELISA assays for bone morphogenetic protein-2 and osteopontin

Figure 5.8(b) shows the results of the BMP-2 ELISA assay carried out for hMSCs cultured using osteogenic medium on Ti5 and control microspheres over a 21 day study period. Before conducting the assay, a calibration curve of optical density versus BMP-2 concentration had been plotted using serially diluted solutions of the BMP-2 standard supplied by the manufacturer (Figure 5.8(a)). (Note that statistical analysis of the ELISA results was not possible since only two measurements per sample were obtained.) It was observed that BMP-2 production was significantly higher on the Ti5 microspheres than on the control microspheres across all the time points. The difference in BMP-2 secretion between the Ti5 and control microspheres at time points of 7, 14 and 21 days was 13.6, 12.1 and 15.7%. Thus, consistently higher BMP-2 production was observed for the Ti5 microspheres as compared to the control microspheres.

(a)

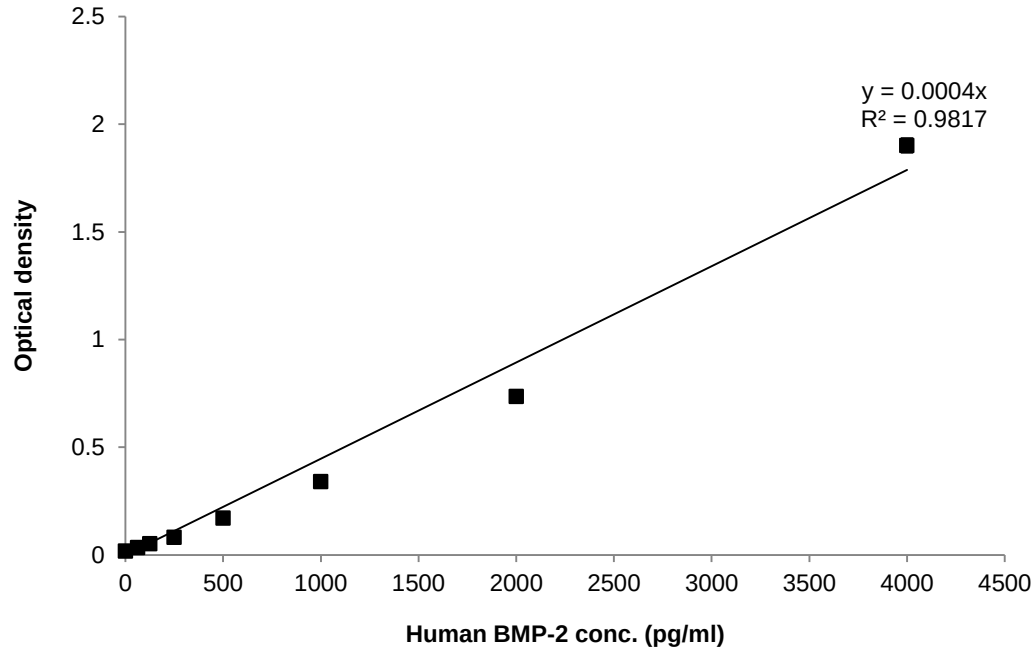

(b)

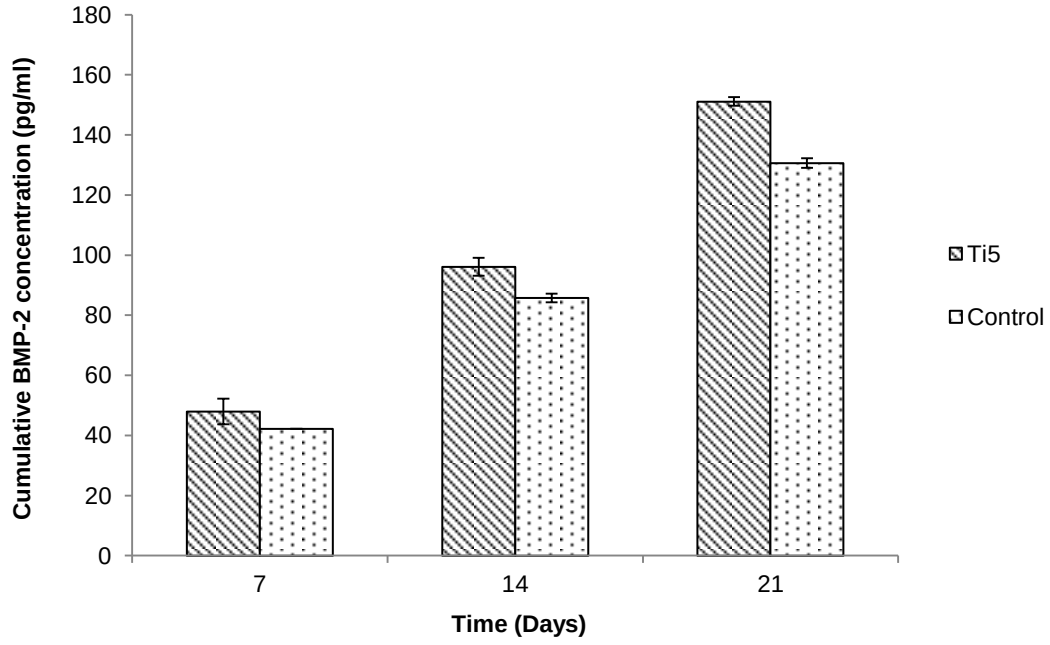

Figure 5.8. Bar chart showing the variation in the cumulative secretion of human bone morphogenetic protein–2 (BMP-2) by hMSCs at time points of 7, 14 and 21 days when cultured on Ti5 and control microspheres in osteogenic medium, as quantified using a mammalian BMP-2 ELISA assay. Prior to the assay, a standard curve of optical density versus human BMP-2 concentration (pg/ml) was plotted (a). Error bars represent ±SD where n = 2. hMSCs cultured on Ti5 microspheres secrete higher levels of BMP-2 at all the investigated time points in comparison with those cultured on control microspheres.

Figure 5.9(b) shows the results obtained when the OPN ELISA assay was carried out for the same experimental conditions (the calibration curve is shown in Figure

5.9(a)). Considerably higher levels of OPN production were found for the Ti5 microspheres in comparison with the control microspheres over the 21 day study period. OPN secretion from the Ti5 microspheres at days 7, 14 and 21 was 15.2-, 18.3- and 11.8-fold higher than that from the control microspheres. It is also worth noting that whereas the measured BMP-2 levels were approx. in the 42–151 pg/ml range, the measured OPN levels were approx. in the 0.2–7.1 ng/ml range i.e. the 200–7100 pg/ml range. As shown in Figure 5.10, which compares the production levels of both BMP-2 and OPN from the Ti5 and control microspheres over the 21 day study period, hMSCs generally produced OPN at higher levels than BMP-2 when cultured on the Ti5 and control microspheres. This was especially true for the Ti5 microspheres. To illustrate, at day 21, the amount of OPN produced by the cells on the Ti5 microspheres was 7154 ng/ml whereas that on the control microspheres was 605 ng/ml; the amounts of BMP-2 produced by the same cells on the Ti5 and control microspheres were only 151 and 130 ng/ml.

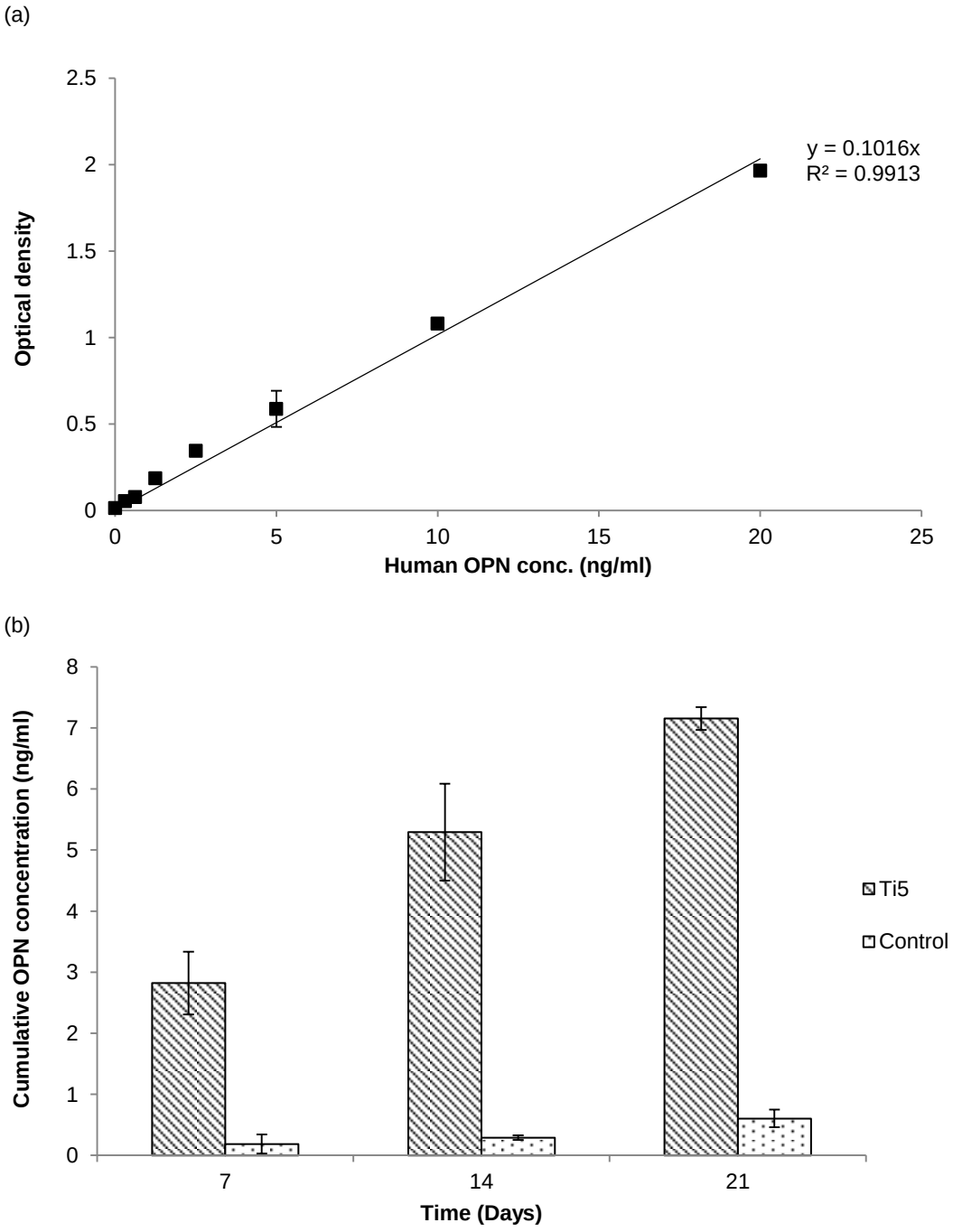

Figure 5.9. Bar chart showing the variation in the cumulative secretion of human osteopontin (OPN) by hMSCs at time points of 7, 14 and 21 days when cultured on Ti5 and control microspheres in osteogenic medium, as quantified using a mammalian OPN ELISA assay. Prior to the assay, a standard curve of optical density versus human OPN concentration (ng/ml) was plotted (a). Error bars represent ±SD where n = 2. hMSCs cultured on Ti5 microspheres produce considerably higher levels of OPN than those cultured on the control at all the investigated time points.

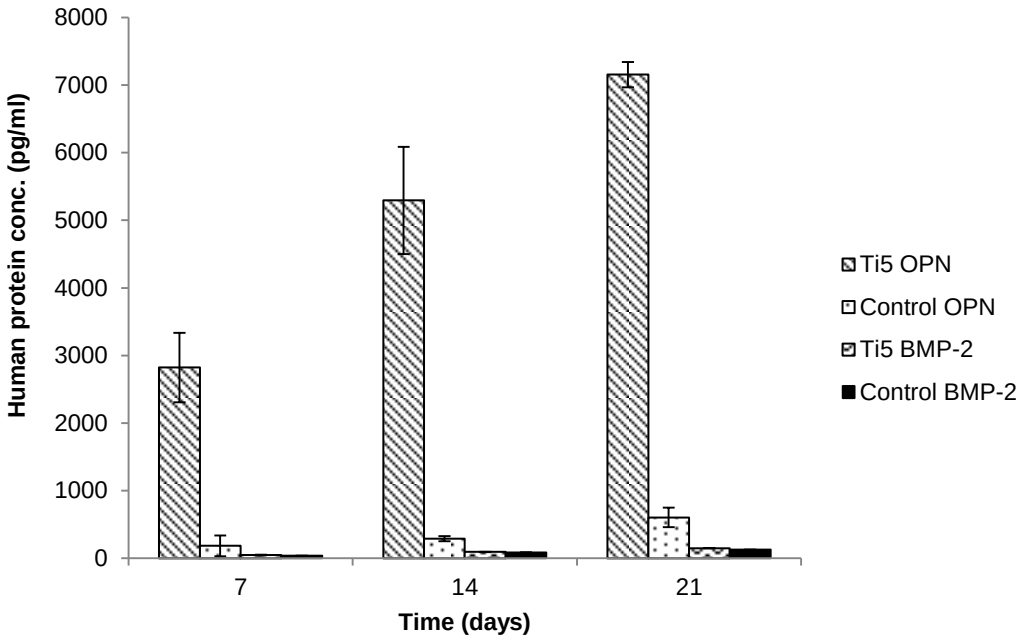

Figure 5.10. Bar chart comparing the variations in the secretion of human BMP-2 and OPN by hMSCs as obtained from Figures 5.8 and 5.9. Error bars represent ±SD where n = 2. The secretion of OPN from the Ti5 microspheres is considerably higher than that from the control microspheres or the secretion of BMP-2 from the Ti5 and control microspheres.

5.3.2. Investigating bioreactor-mediated hMSC proliferation: dynamic hMSC–microsphere interactions for Ti-PGMs

5.3.2.1. Time course experiment

Figure 5.11 shows the results of the time course experiment involving culture of hMSCs on Ti5 and control microspheres over a period of 8 hours. It was observed that at 2 hours post seeding, approx. 24% of the hMSCs on the Ti5 microspheres and 18% of the hMSCs on the control microspheres remained unattached to the microspheres. By 4 hours post seeding, approx. 8–10% of the hMSCs on both the Ti5 and control microspheres remained unattached. The percentage of unattached cells remained almost constant at 7–8% at 6 and 8 hours post seeding. The results implied that cell attachment of up to 90% and above had been achieved by 4 hours post seeding, after which the number of attached cells was independent of the static culture time for both the Ti5 and control microspheres. Thus, an initial static culture time of 4 hours was considered to be sufficient for attachment of hMSCs to the Ti5 and control microspheres prior to transfer of the microspheres and attached cells to the spinner flask bioreactors.

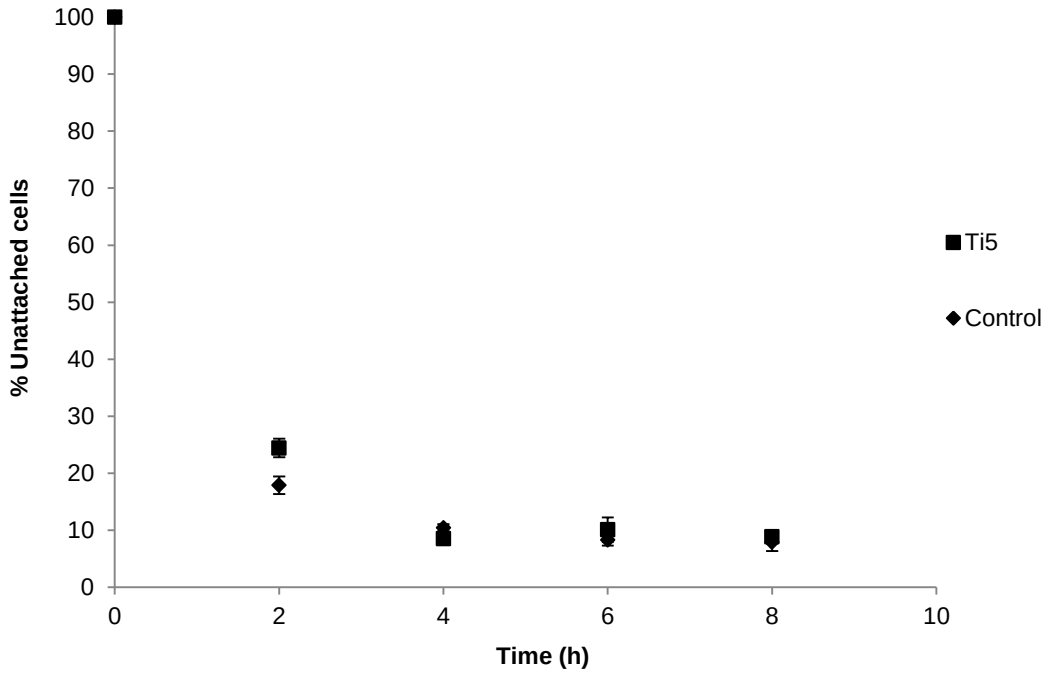

Figure 5.11. Scatter plot showing the percentage of unattached cells remaining at time points of 2, 4, 6 and 8 hours after culture of Ti5 and control microspheres with hMSCs; the number of unattached cells was determined using a Vi-CELL cell viability analyser. Error bars represent ±SD and n = 2. By 4 hours post seeding, approx. 10% unattached cells remain for both the Ti5 and control microspheres, indicating that approx. 90% of the seeded cells have attached to the microsphere surface.

5.3.2.2. Cell proliferation assays

Figure 5.12 shows the results of the CCK-8 cell proliferation assay carried out for hMSCs cultured on Ti5 microspheres when cultured under dynamic conditions in spinner flask bioreactors using DMEM over time points of 4 and 7 days. It was observed that from day 4 to day 7, a 12% increase in cell numbers occurred on the Ti5 microspheres; however, the difference was not statistically significant ($p > 0.05$). With reference to an initial seeding density of 50,000 cells per well, the increase in cell numbers by day 7 was approx. 1.7 fold i.e. around 71%. Thus, the level of cell proliferation obtained for hMSCs was far lower than that obtained for MG63 cells (approx. 24 fold) over the same time period.

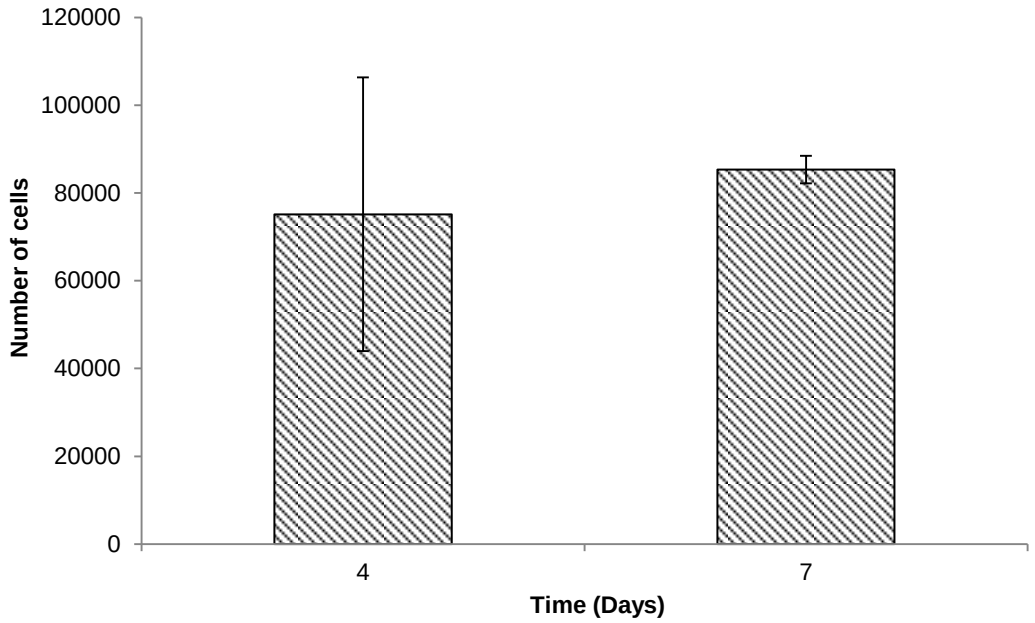

Figure 5.12. Bar chart showing the number of hMSCs on Ti5 microspheres at time points of 4 and 7 days in spinner flask bioreactors under dynamic conditions, as determined using the CCK-8 cell proliferation assay. DMEM is used as the culturing medium. Error bars represent ±SD where n = 2. The Ti5 microspheres show greater cell proliferation at day 7 than at day 4 but the difference is not statistically significant ($p > 0.05$).

In order to further increase the proliferation of hMSCs on the Ti5 microspheres, the effect of using longer culture times as well as an osteogenic medium was investigated. Figure 5.13 shows the results of a CCK-8 cell proliferation assay carried out for hMSCs cultured on Ti5 microspheres in bioreactors using osteogenic medium over time points of 10 and 15 days. It was observed that increasing the culturing time and using a different medium did not positively impact on the number of hMSCs on the Ti5 microspheres. From day 10 to day 15, a significant decrease in the cell population of about 30% occurred on the microspheres (*** $p < 0.001$). The number of cells on the Ti5 microspheres decreased by about 8% with reference to the initial seeding density of 50,000 cells per well.

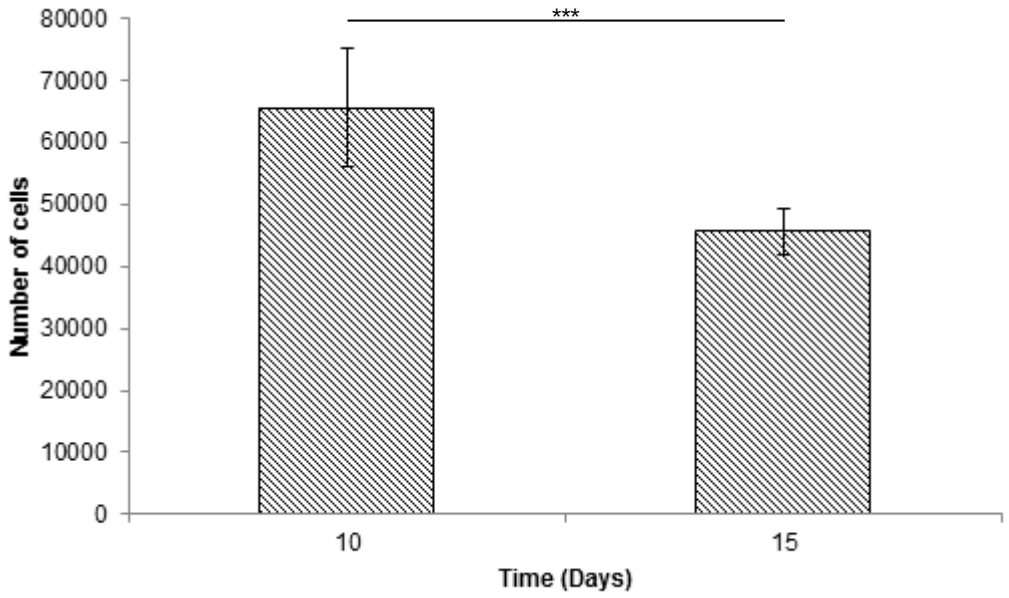

Figure 5.13. Bar chart showing the number of hMSCs on Ti5 microspheres at time points of 10 and 15 days in spinner flask bioreactors under dynamic conditions, as determined using the CCK-8 cell proliferation assay. Osteogenic inductive medium is used as the culturing medium. Error bars represent ±SD where n = 2. The symbol * indicates $p < 0.001$. The Ti5 microspheres show significantly lesser numbers of cells at day 15 than at day 10 (*** $p < 0.001$).**

5.3.2.3. Scanning electron microscopy imaging

Figure 5.14 shows SEM images of hMSCs cultured on Ti5 microspheres under dynamic conditions in spinner flask bioreactors at days 10 and day 15 when osteogenic medium was used as the culture medium. Very few cells, if at all, could be discerned on the microsphere surface at both time points and most of the microspheres remained uncovered. Fragments which may correspond to cell layers were visible on a few microspheres; these fragments appeared to be peeling off the microspheres. No differences were visible between the Ti5 microspheres on day 10 and day 15 with regard to the number of cells or their appearance.

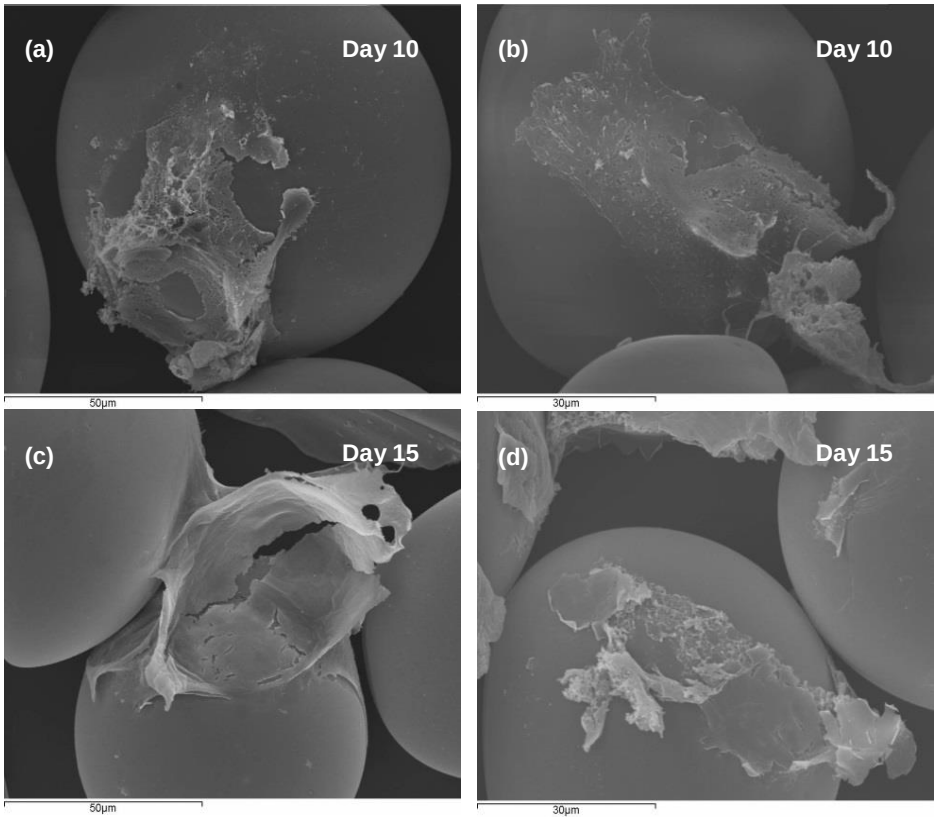

Figure 5.14. Scanning electron microscopy images showing hMSCs attached to Ti5 microspheres at (a, b) 10 days and (c, d) 15 days post seeding when cultured in a dynamic environment within spinner flask bioreactors. Osteogenic inductive medium is used as the culture medium. Very few hMSCs, if at all, are found attached to the Ti5 microspheres, with almost all the microspheres showing no signs of cell coverage. Some fragments, which may correspond to cells, are visible on the Ti5 microspheres; the fragments seem to be peeling off the microspheres. No differences can be observed between the microspheres on days 10 and 15 with regard to the number of cells or their morphology.

5.4. Discussion

In this final part of the research, the interactions between Ti5/control microspheres and hMSCs were investigated from the perspectives of cell adhesion, proliferation and differentiation, and an attempt was made to replicate the outstanding bioreactor-mediated proliferation of MG63 cells on Ti5 microspheres with hMSCs as well. It is worth noting at the outset that understanding the interactions between PGMs and hMSCs is one of the cornerstones of the entire research project for two reasons. First, the scale up of MSCs, and of stem cells in general, without loss of multipotency, phenotype or senescence is one of the foremost areas of biomedical research, whereby it is envisaged that the cells thus obtained can be used for a whole host of applications ranging from regenerative cell-based therapies on the one hand to high throughput screening technologies for utilization in many different fields from theranostics to drug discovery on the other (Dominici et al., 2006, Yu et al., 2007). Second, it is considered that the developed PGMs may serve as suitable

microcarrier substrates for the guided differentiation of MSCs down the osteogenic pathway to form bone cells (Müller et al., 2008); combining this strategy with a suitable tissue engineering approach could lead to the *in vitro* development of bone tissue structures for replacement of critical-sized bone defects (Langer and Vacanti, 1993).

The SEM images of hMSCs adhering to the Ti5 and control microspheres following culture over a 7 day period showed some differences between the attachment characteristics of MG63 cells and hMSCs on glass microsphere surfaces. In comparison with MG63 cell attachment to the microspheres, the presence of fewer cells on the surfaces of both the Ti5 and control microspheres at 7 days post culture, with many microspheres devoid of cells on their surfaces, and the torn or peeled appearance of the cells that are found attached indicate that the adhesion of hMSCs to the microsphere surfaces is weaker than that of MG63 cells. It is possible that the various processing steps involved in preparing the samples (in this case, microspheres with attached cells) for SEM imaging, such as fixing, dehydration and critical point drying—all of which involve pipetting of solvents into the cell culture wells—may be causing large numbers of cells to become detached from the microsphere surface. More hMSCs are observed to be adherent to the Ti5 and control microspheres in the CLSM images, which is again attributable to the fewer and less forceful processing steps involved in sample preparation for CLSM imaging. In both the SEM and CLSM images, aggregates of cells were found attached to the control microspheres whereas only individual cells were found on the Ti5 microspheres. The reason for this observation is not entirely clear; however, the authors consider that it would be erroneous to infer superior cell adhesion on the control microspheres from this observation because the number of adherent hMSCs on both the Ti5 and control microspheres in comparison with the initial seeding density does not seem sufficient to come to such a conclusion.

The factors influencing the adhesion of hMSCs to glass surfaces have been researched previously (Curran et al., 2005), and the beneficial effects on stem cell adhesion and differentiation of the presence of particular functional groups such as $–NH_2$ on the glass surface has been highlighted. Thus, the incorporation of functional groups on the glass surface may be one way to strengthen the attachment of hMSCs to the microsphere surface. Biomolecular functionalization of the microsphere surface may be another way to accomplish the same objective. The use of the commercially available MSC culture medium DXF was explored from

this perspective. This medium, which is marketed as a specially designed medium for the efficient proliferation of MSCs and robust differentiation of undifferentiated multipotent MSCs, does not contain attachment or spreading factors. Thus, it was considered that applying a two-pronged approach, which would involve (a) the use of DXF medium for improved proliferation of hMSCs on the Ti5 microspheres and (b) coating the microsphere surfaces with fibronectin so as to provide the necessary attachment factors for improved cell adhesion, would be the best approach (even if not a cost-effective one) to obtain effective hMSC proliferation on the microspheres.

The comparison of the performance of DMEM with DXF in terms of hMSC proliferation on Ti5 and control microsphere surfaces yielded surprising results. As shown in Figure 5.4, among the four investigated sample–medium systems (Ti5-DMEM, Ti5-DXF, control-DMEM and control-DXF), the highest cell numbers at day 7 were obtained when Ti5 microspheres were cultured in DMEM. On the other hand, culturing the Ti5 microspheres in DXF led to a statistically significant decrease in cell numbers from day 1 to day 7, indicating the superior performance of commonly used DMEM over the specially designed DXF medium in the investigated systems. Clearly, using the DXF medium has not had the desired impact on the proliferation of hMSCs on the Ti5 microsphere surface.

The major point to be discussed in this context is the medium replacement regime followed in the experiment. According to commonly used protocols, both the DMEM and DXF media were replaced at intervals of 2 days. However, in the case of the DXF medium (which does not contain attachment factors), the fibronectin coating was applied only once to the microspheres prior to introduction of medium into the culture wells. It is possible that the fibronectin layer on the Ti5 microsphere surface was washed away with time so that timely replacement of the fibronectin coating is required in order to maintain the increase in the cell population, although it is not clear how such a replacement can be efficiently accomplished once the microspheres have been cultured with hMSCs. Comparison of the cell proliferation capacities of the Ti5 and control microspheres reveals that the Ti5 microspheres show greater cell numbers than the control microspheres when using both DMEM and DXF (although the difference is no longer statistically significant towards the end of the 7 day study period when using DXF) (Figure 5.5). These findings are in contrast to the results of the SEM/CLSM studies where more cells were observed on the control microspheres than on the Ti5 microspheres (Figures 5.1 and 5.2).

DMEM and DXF have similar effects on cell proliferation in the case of the control microspheres, which suggests that the effect of the medium on the silica-based control microspheres is not as pronounced as it is in the phosphate glass microspheres (Figure 5.6).

From an overall perspective, the suboptimal findings of the present research vis-à-vis use of commercially available culture media to aid hMSC adhesion and proliferation on substrate materials are in agreement with observations by other research groups engaged in similar research. As reviewed by Jung et al., several companies have developed specially designed media for the accelerated expansion of hMSCs (Jung et al., 2012). However, a major concern in the use of such media is that the underlying formulations are not disclosed by the manufacturer in most cases. This raises problems because several studies cited in the review have reported contradictory results in terms of media performance for the same culture media—often because of differences in the substrate used—which means that the so-called “one size fits all” approach to stem cell media development is not suitable. As such, careful evaluation of the available media, particularly with regard to specific medium or serum components that could significantly affect hMSC adhesion and proliferation, is vital. The high costs of such media also limit their utility in hMSC research, clinical studies or industrial applications. Commercially available stem cell media with clearly defined compositions have a significant advantage in this regard since they allow researchers to assess the effects of different media components and to alter the media composition according to the end application (Parker et al., 2007, Jung et al., 2010, Mimura et al., 2011).

The Alizarin Red S assay and BMP-2 ELISA assay were performed in order to assess the potential of the Ti5 microspheres to function as platforms for guided differentiation of hMSCs along osteogenic pathways. The Alizarin Red S assay provides a quantitative measure of mineral deposition by cells (Gregory et al., 2004); thus, it was considered that if hMSCs are induced to differentiate into bone cells using osteogenic medium, the extent of differentiation of the cells could be quantified indirectly by measuring the mineral deposition of the bone cells formed as a result of the differentiation process. The Alizarin Red S assay results (Figure 5.7) showed that at all the time points, the control microspheres showed significantly greater mineral formation than the Ti5 microspheres. There are two major considerations to be discussed in this context. First, it is possible that the forces involved in the processing steps for the assay may have inevitably disrupted the

mineral deposits formed on the microspheres in some of the samples; the relatively high error values suggest this may be the case. Another possible governing factor may be the effect of the microsphere geometry on the mineralisation processes and products. The spherical geometry of the microspheres may have led to displacement of the mineralisation products from the microsphere surface as they were being produced by the cells. Second, it is possible that the mineral deposits formed on the surface of the silica glass control microspheres may be intrinsic to the material itself and may not be entirely indicative of the differentiation potential of the hMSCs. Silica-based glasses such as Bioglass® 45S5 and ceramics such as sintered hydroxyapatite have been observed to form a calcium-rich mineral layer when implanted *in vivo* or immersed in solutions such as simulated biological fluid or Tris buffer (Kokubo and Takadama, 2006). On the other hand, titanium phosphate glasses elicit a favourable biological response from bone cells in spite of the absence of such a calcium rich layer on the glass surface (Abou Neel et al., 2007a). Also to date, no evidence of mineral formation has been seen with these types of phosphate glasses. Therefore, it cannot be accurately concluded that the mineral deposits quantified by the Alizarin Red S assay in the present study are indicative of hMSC differentiation on the microsphere surfaces.

Bone morphogenetic protein-2 has been implicated to be a key protein in the regulation of such diverse cellular processes as growth, differentiation, chemotaxis and apoptosis in various cell types including mesenchymal, epithelial, hematopoietic and neuronal cells (Hogan, 1996). The expression of BMP-2 by hMSCs when cultured on the Ti5 and control microsphere surfaces was thus considered to be an indicator of the capacity of hMSCs to differentiate along the osteogenic pathway under such environments. The results showed that the Ti5 microspheres elicited greater BMP-2 expression than the control microspheres at every time point over the 21 day study period (Figure 5.8(b)), thereby suggesting that Ti5 microspheres have a more positive influence on hMSCs in terms of differentiation to bone cells. At the same time, it should be noted that the overall amounts of BMP-2 secreted were in the 42–151 pg/ml range, which is a very small value; to illustrate, the 42–151 pg/ml range is closer to the lowermost values of the calibration curve of optical density versus human BMP-2 concentration (Figure 5.8(a)).

Osteopontin is considered to play a role in bone metabolism; it has been shown to stimulate the adhesion of osteoclasts to bone *in vitro* (Reinholt et al., 1990) and also to influence the regulation of mineral crystal formation and growth both *in vitro* and

in vivo (Boskey et al., 1993). The OPN ELISA test for hMSCs cultured on the Ti5 and control microspheres over a 21 day study period yielded unexpected results. The expression of OPN from hMSCs cultured on Ti5 microspheres was 12–15 fold higher than that on the control microspheres (Figure 5.9(b)). This suggests that hMSCs are far more metabolically active on the Ti5 microspheres than on the control, although the reason for this is unclear. It is also interesting to note that when OPN and BMP-2 expression on both the Ti5 and control microspheres are compared (Figure 5.10), OPN expression on the Ti5 microspheres far outweighs that on the control microspheres, which in turn is higher than the BMP-2 expression on both microsphere types. Perhaps the cellular processes related to bone metabolism are more active than those related to differentiation on the microspheres, but further research is definitely required in order to understand the exact mechanisms involved.

Considering the success of the bioreactor culture approach for MG63 cell proliferation on the Ti5 microspheres, it was considered that a similar approach with some modifications would facilitate the achievement of similar results with hMSC proliferation. Taking into account the previously observed weaker cell adhesion of hMSCs on the microspheres, one of the modifications that was considered necessary was the period of initial static culture of the cells on the microspheres prior to transfer to the bioreactors. The static culture time of 4 hours, as obtained from Figure 5.11, was considered to be a sufficient period to ensure reasonable attachment of hMSCs to the microsphere surfaces. However, the results of the bioreactor culture proliferation assays and SEM imaging were not encouraging. The preliminary results carried out for bioreactor culture over a 7 day period yielded a 1.7-fold increase in cell numbers with respect to the initial seeding density (Figure 5.12). However, the number of cells obtained from bioreactor culture on the Ti5 microspheres was approx. 62% lower than that obtained from static culture over a 7 day period (Figure 5.4), indicating that bioreactor culture was exerting a less positive effect on cell numbers. Excessive cell washout during transfer of microspheres and attached cells to cell culture plates at each time point was considered to be the main cause for these findings.

It was then thought that increasing the culture time from 7 days to 15 days and changing the medium from DMEM to osteogenic medium could possibly lead to improvements in hMSC numbers, but as shown in Figure 5.13, this led to a pronounced decrease in the cell numbers, again possibly due to excessive cell

washout. SEM images of the microspheres with attached cells from this system showed that almost all the Ti5 microspheres were devoid of cells on the surface, with only a few cellular fragments being visible on a very small number of microspheres (Figure 5.14). Weak hMSC adhesion to the microsphere surface was identified to be the main reason for these findings.

In summary, a range of data sets have been obtained from studies on hMSC–microsphere interactions under both static and dynamic environments. On the one hand, the Ti5 microspheres have demonstrated their ability to serve as viable microcarrier substrates for hMSC proliferation and guided differentiation along osteogenic pathways under static conditions. On the other hand, the suboptimal results obtained from dynamic studies of hMSC–microsphere interactions imply that further work is required in order to optimise the glass microsphere surface in order for improving hMSC adhesion and proliferation under dynamic conditions. Several areas of further research have been identified in this regard, which will be discussed in the next chapter.

Chapter 6. Summary: General discussion and future directions

To reiterate the hypotheses of the present research which were outlined in chapter 1, an attempt was made to demonstrate that (a) phosphate glass microspheres (PGMs) of different compositions can be successfully produced using an inexpensive, rapid and easily scalable process; (b) the physicochemical properties of the developed microspheres vary systematically with the glass composition, in particular the metal oxide content; (c) the microsphere properties are closely linked to the glass chemistry and structure; and (d) the microspheres interact favourably with bone cells and human mesenchymal stem cells (hMSCs) and can be used as carriers for bone tissue engineering applications. The following paragraphs summarise the findings obtained from experimental studies and also discuss directions for future work to overcome the various challenges encountered.

With regard to the first objective, a flame spheroidisation apparatus was designed and the methodology for preparing PGMs was optimised so that microspheres in the size range of approx. 10–210 µm were successfully prepared from glasses of two different compositional series: (a) $0.5P_2O_5$–0.4CaO–(0.1 – *x*)Na_2O–*x*Fe_2O_3 where x = 0.00, 0.01, 0.03 and 0.05 mole fraction and (b) $0.5P_2O_5$–0.4CaO–(0.1 – *x*)Na_2O–*x*TiO_2 where x = 0.00, 0.01, 0.03, 0.05 and 0.07 mole fraction. The main challenge encountered here was the restriction in the effective size range (within which almost all the particles were spheroidised to form microspheres) to approximately 45–105 µm. A larger blowtorch connected to a gas–oxygen source was suggested as a possible solution to obtain larger microspheres as well as higher throughput. In terms of selecting the type of blow torch, it is suggested that a powder spray torch may be an optimal solution. Powder spray torches are equipped with a cylindrical canister to hold the powder and feed it directly into the flame, so that an external feed system is not required (Figure 6.1). Suitable modifications to the torch so as to ensure an optimum flame residence time will facilitate the production of microspheres with sizes in excess of 100 µm.

At the other end of the scale (for particles with sizes of <45 µm), dispersion of the glass powder in a suitable dispersant was considered a possible way to obtain smaller-sized microspheres. The choice of dispersant to be used may need to be determined empirically as it will depend on various factors such as, for instance, the

contact angle for particle wetting, concentration of particles in the dispersant, type of dispersant to be used (considering that phosphate glass surfaces are generally hydrophilic in nature (Abou Neel et al., 2008a, Lee et al., 2013a)), zeta potential of the microsphere surface, safety considerations (particularly when volatile organic solvents are used) and so on. The ISO 14887 standard provides a comprehensive set of procedures for determining the dispersant to be used, which would be a useful guide in this case. However, even with the use of a dispersant, it may be difficult to obtain large quantities of glass particles in the size range of 5 μm or less, especially in the sub-micron range. To obtain sub-micron sized glass microspheres, it is more suitable to use a different approach involving electrospraying of sol-gel derived glasses in the solution state; work in this direction is currently in progress.

Figure 6.1. A conventional powder spray torch. The use of a powder canister above the torch eliminates the need for an external feed.

The second and third objectives were respectively to investigate the physicochemical properties of the developed microspheres and to correlate the microsphere properties to the underlying glass structural arrangements. A variety of previously reported techniques (e.g. differential thermal analysis, density and pH measurements, ion chromatography, inductively coupled plasma–mass spectroscopy etc.) were used along with a novel time lapse imaging technique to visualise and quantify microsphere degradation in deionised water, thereby providing comprehensive series of results that essentially correlated increased metal oxide addition with increased densification of the glass structure and reduced microsphere solubility and ion release. The underlying glass structural arrangements were probed by commonly used techniques such as Fourier

transform infrared spectroscopy and X-ray diffraction as well as state-of-the-art techniques such as ^{31}P and ^{23}Na magic angle spinning nuclear magnetic resonance and Ti *K*-edge X-ray absorption near edge structure spectroscopies. The results obtained in terms of the variations in the functional groups; crystalline phases; and local environments of P, Na and Ti atoms could all be explained in the context of variations in the glass chemistry. The findings of the present study (which was focused on metaphosphate glasses containing 50 mol% P_2O_5) were compared with those of previous studies on polyphosphate glasses (containing 45 mol% P_2O_5) and ultraphosphate glasses (containing 55 mol% P_2O_5), which provided an overall perspective of glass structural variations with changes in both the metal oxide content and the P_2O_5 content on both sides of the metaphosphate boundary. One possible avenue of further structural research in these glasses would be to carry out X-ray and neutron scattering experiments which, although quite expensive, can potentially provide valuable information about every atomic correlation in the glass structure and thus provide a detailed interpretation of the structure.

The final objective was to investigate the interactions between the developed microspheres and MG63 cells as well as hMSCs under static and dynamic conditions. Initial tests under static conditions on microspheres of all the studied compositions (Fe0/Ti0, Fe1, Fe3, Fe5, Ti1, Ti3, Ti5 and Ti7) showed favourable MG63 cell adhesion and proliferation on microspheres of glasses containing 3–7 mol% metal oxides (Fe_2O_3 or TiO_2). Out of these compositions, the Ti5 microspheres were selected for further tests with hMSCs under static conditions and with both MG63 cells and hMSCs under dynamic conditions, even though the cell culture results for the Ti5 microspheres were comparable to those of the Fe3, Fe5, Ti3 and Ti7 microspheres. There are several reasons for this selection. The preference for titanium phosphate glasses over iron phosphate glasses is mainly empirical, considering that titanium phosphate glasses have been studied for biomedical applications to a far greater extent than iron phosphate glasses, although it is considered that both Fe^{3+} and Ti^{4+} ions can possibly play positive roles in bone formation (Walsh et al., 2003, Lakhkar et al., 2013). There also appears to be some evidence for increased bioactivity of certain titanium containing compositions (Abou Neel et al., 2007a, Abou Neel and Knowles, 2008). Among the five Ti-PGM compositions studied (Ti0, Ti1, Ti3, Ti5 and Ti7), the physicochemical properties of the Ti5 and Ti7 microspheres in terms of degradation and ion release are considered the most suitable for these microspheres to provide a stable surface for cell adhesion and proliferation under *in vitro* environments. Finally, although the

Ti5 and Ti7 microspheres have similar physicochemical properties, the production of the Ti5 glasses requires a lower temperature (1300°C vs. 1400°C for the Ti7 glasses) and less time (3 hours vs. 5 hours for Ti7); also it is observed that that the Ti7 glasses have a higher propensity towards crystallisation as the molten glass is cooled rapidly to room temperature. They also require a longer residence time during the flame spheroidisation process.

In comparison with commercially available silica glass microspheres, which are marketed by the manufacturer for applications related to cell scale up and tissue engineering, the Ti5 microspheres showed similar MG63 cell proliferation under static culture conditions, but remarkably greater cell proliferation under dynamic conditions in spinner flask bioreactors. Indeed, the 24-fold increase in cell numbers on the Ti5 microspheres under dynamic conditions over a 7 day culture period is a major highlight of the research since it is considerably greater than the 6-fold increase exhibited by control microspheres under the same conditions or the 8-fold increase exhibited by the Ti5 microspheres under static conditions. It was therefore anticipated that replication of the results with hMSCs in place of MG63 cells would provide breakthroughs in applications for cell-based therapies and bone tissue engineering.

Initial results of static hMSC culture on the Ti5 and control microspheres showed relatively weaker physical cell adhesion and proliferation on the microsphere surface. Therefore, it was envisaged that using a commercially available MSC medium together with fibronectin coating of the microsphere surface would lead to improved adhesion and proliferation characteristics. However, this was not found to be the case; in fact, the specially designed stem cell medium led to a significant decrease in cell numbers on the Ti5 microspheres. In addition, dynamic culture of hMSCs on Ti5 microspheres using conventional DMEM or osteogenic medium revealed significant levels of cell washout, again presumably due to weak cell adhesion to the microsphere surface. Studies on the potential of the developed microspheres to serve as microcarriers for guided differentiation of hMSCs along osteogenic pathways showed that the Ti5 microspheres cause increased expression of bone morphogenetic protein-2 in comparison with the control microspheres. It was also found that hMSC osteopontin expression on the Ti5 microspheres is particularly high, implying considerably higher cell metabolism on the Ti5 microspheres, although further research is required to understand the exact reason for this finding.

The hMSC culture results, although not entirely positive, offer several avenues for further research. For instance, considering that the use of specially designed media with complex and costly formulations is not cost-effective or practicable, several research groups have investigated the use of so-called ‘home-made’ mesenchymal stem cell media using a combination of high-glucose Dulbecco’s Modified Eagle medium, foetal bovine serum, penicillin–streptomycin and recombinant human fibroblast growth factor (Steigman and Fauza, 2007, Hudson et al., 2011, Jung et al., 2012). Such media can be prepared in the laboratory at a fraction of the cost of the commercially available media and the formulations can be varied so as to suit specific end applications. Another major avenue of research is functionalization of the microsphere surface. Although the coating of a fibronectin layer was not successful in increasing hMSC adhesion on the microspheres in the present study, it is expected that selecting an appropriate biofunctionalisation strategy and optimising the functionalisation protocol will provide a solution to this issue. Work in this area of research is currently underway.

Figure 6.2. Schematic diagram of a perfusion bioreactor system. Media is perfused in a closed loop through a growth chamber containing substrate material and seeded cells (Yeatts and Fisher, 2011).

Another major avenue of further research is the use of different bioreactor types for culture of hMSCs on the developed microspheres. In this context, the use of

perfusion bioreactors is a heavily researched area that offers interesting possibilities for the development for small-sized bone tissue that can be used to combat bone loss caused by injuries, congenital deformities or disease (Yeatts and Fisher, 2011, El Haj and Cartmell, 2010, Rauh et al., 2011, Salter et al., 2012). Basic perfusion bioreactor systems generally comprise a substrate material (either a scaffold or microparticles) placed along with cells inside a chamber. Cell culture medium flows through the chamber in a closed loop via tubes passing through a peristaltic pump that controls the medium perfusion rate (Figure 6.2). Perfusion bioreactor systems allow a laminar flow of medium and mass transport of nutrients and oxygen throughout the entire volume of the construct and are therefore able to overcome the diffusional limitations associated with other bioreactor types (e.g. rotating wall bioreactors). By varying the perfusion rate using the peristaltic pump, the fluid shear stresses exerted on the tissue can be optimised to provide the environment for optimal growth of small-sized bone tissue. Although only preliminary work on using perfusion bioreactors with Ti5 microspheres has been carried out in the author's present laboratory, it is expected that the selection of an appropriately sized perfusion chamber and optimisation of the seeding and culturing protocol, together with on-going developments in microsphere surface functionalization and specialised stem cell medium production, will in the long term lead to the realisation of the main objective of the research, which is to develop viable bone tissue *in vitro* for use in bone replacement therapies.

References

ABOU NEEL, E. A., AHMED, I., BLAKER, J. J., BISMARCK, A., BOCCACCINI, A. R., LEWIS, M. P., NAZHAT, S. N. & KNOWLES, J. C. 2005a. Effect of iron on the surface, degradation and ion release properties of phosphate-based glass fibres. *Acta Biomaterialia,* 1**,** 553-63.

ABOU NEEL, E. A., AHMED, I., PRATTEN, J., NAZHAT, S. N. & KNOWLES, J. C. 2005b. Characterisation of antibacterial copper releasing degradable phosphate glass fibres. *Biomaterials,* 26**,** 2247-2254.

ABOU NEEL, E. A., CHRZANOWSKI, W. & KNOWLES, J. C. 2008a. Effect of increasing titanium dioxide content on bulk and surface properties of phosphate-based glasses. *Acta Biomaterialia,* 4**,** 523-534.

ABOU NEEL, E. A., CHRZANOWSKI, W., VALAPPIL, S. P., O'DELL, L. A., PICKUP, D. M., SMITH, M. E., NEWPORT, R. J. & KNOWLES, J. C. 2009a. Doping of a high calcium oxide metaphosphate glass with titanium dioxide. *Journal of Non-Crystalline Solids,* 355**,** 991-1000.

ABOU NEEL, E. A. & KNOWLES, J. C. 2008. Physical and biocompatibility studies of novel titanium dioxide doped phosphate-based glasses for bone tissue engineering applications. *Journal of Materials Science-Materials in Medicine,* 19**,** 377-386.

ABOU NEEL, E. A., KNOWLES, J. C., CHRZANOWSKI, W., PICKUP, D. M., O'DELL, L. A., MORDAN, N. J., NEWPORT, R. J. & SMITH, M. E. 2009b. Structure and properties of strontium-doped phosphate-based glasses. *Journal of the Royal Society Interface,* 6**,** 435-446.

ABOU NEEL, E. A., MIZOGUCHI, T., ITO, M., BITAR, M., SALIH, V. & KNOWLES, J. C. 2007a. In vitro bioactivity and gene expression by cells cultured on titanium dioxide doped phosphate-based glasses. *Biomaterials,* 28**,** 2967-2977.

ABOU NEEL, E. A., O'DELL, L. A., CHRZANOWSKI, W., SMITH, M. E. & KNOWLES, J. C. 2009c. Control of Surface Free Energy in Titanium Doped Phosphate Based Glasses by Co-Doping With Zinc. *Journal of Biomedical Materials Research Part B-Applied Biomaterials,* 89B**,** 392-407.

ABOU NEEL, E. A., O'DELL, L. A., SMITH, M. E. & KNOWLES, J. C. 2008b. Processing, characterisation, and biocompatibility of zinc modified metaphosphate based glasses for biomedical applications. *Journal of Materials Science-Materials in Medicine,* 19**,** 1669-1679.

ABOU NEEL, E. A., PICKUP, D. M., VALAPPIL, S. P., NEWPORT, R. J. & KNOWLES, J. C. 2009d. Bioactive functional materials: a perspective on phosphate-based glasses. *Journal of Materials Chemistry,* 19**,** 690-701.

ABOU NEEL, E. A., YOUNG, A. M., NAZHAT, S. N. & KNOWLES, J. C. 2007b. A facile synthesis route to prepare microtubes from phosphate glass fibres. *Advanced Materials,* 19**,** 2856-+.

AHMED, I., ABOU NEEL, E. A., VALAPPIL, S. P., NAZHAT, S. N., PICKUP, D. M., CARTA, D., CARROLL, D. L., NEWPORT, R. J., SMITH, M. E. & KNOWLES, J. C. 2007. The structure and properties of silver-doped phosphate-based glasses. *Journal of Materials Science,* 42**,** 9827-9835.

AHMED, I., COLLINS, C. A., LEWIS, M. P., OLSEN, I. & KNOWLES, J. C. 2004a. Processing, characterisation and biocompatibility of iron-phosphate glass fibres for tissue engineering. *Biomaterials,* 25**,** 3223-3232.

AHMED, I., LEWIS, M., OLSEN, I. & KNOWLES, J. C. 2004b. Phosphate glasses for tissue engineering: Part 1. Processing and characterisation of a ternary-based P2O5-CaO-Na2O glass system. *Biomaterials,* 25**,** 491-499.

AHMED, I., LEWIS, M., OLSEN, I. & KNOWLES, J. C. 2004c. Phosphate glasses for tissue engineering: Part 2. Processing and characterisation of a ternary-based P2O5-CaO-Na2O glass fibre system. *Biomaterials,* 25**,** 501-507.

AHMED, I., LEWIS, M. P. & KNOWLES, J. C. 2005a. Quantification of anions and cations from ternary phosphate based glasses with fixed 50 and 55 mol% P2O5 using ion chromatography. *Physics and Chemistry of Glasses,* 46**,** 547-552.

AHMED, I., LEWIS, M. P., NAZHAT, S. N. & KNOWLES, J. C. 2005b. Quantification of anion and cation release from a range of ternary phosphate-based glasses with fixed 45 mol% P2O5. *Journal of Biomaterials Applications,* 20**,** 65-80.

AHMED, I., LEWIS, M. P., NAZHAT, S. N. & KNOWLES, J. C. 2005c. Quantification of anion and cation release from a range of ternary phosphate-based glasses with fixed 45 mol% P(2)O(5). *J Biomater Appl,* 20**,** 65-80.

AHMED, I., PARSONS, A., JONES, A., WALKER, G., SCOTCHFORD, C. & RUDD, C. 2010. Cytocompatibility and Effect of Increasing MgO Content in a Range of Quaternary Invert Phosphate-based Glasses. *Journal of Biomaterials Applications,* 24**,** 555-575.

AHMED, I., PARSONS, A. J., RUDD, C. D., NAZHAT, S. N., KNOWLES, J. C., GUERRY, P. & SMITH, M. E. 2008. Comparison of phosphate-based glasses in the range 50P(2)O(5)-(50-x)CaO-xNa(2)O prepared using different precursors. *Glass Technology-European Journal of Glass Science and Technology Part A,* 49**,** 63-72.

AHMED, I., READY, D., WILSON, M. & KNOWLES, J. C. 2006. Antimicrobial effect of silver-doped phosphate-based glasses. *Journal of Biomedical Materials Research Part A,* 79A**,** 618-626.

ANSELME, K. 2000. Osteoblast adhesion on biomaterials. *Biomaterials,* 21**,** 667-681.

ARCOS, D., LOPEZ-NORIEGA, A., RUIZ-HERNANDEZ, E., TERASAKI, O. & VALLET-REGI, M. 2009. Ordered Mesoporous Microspheres for Bone Grafting and Drug Delivery. *Chemistry of Materials,* 21**,** 1000-1009.

ASHBROOK, S. E. & SMITH, M. E. 2006. Solid state O-17 NMR - an introduction to the background principles and applications to inorganic materials. *Chemical Society Reviews,* 35**,** 718-735.

BACHLE, M. & KOHAL, R. J. 2004. A systematic review of the influence of different titanium surfaces on proliferation, differentiation and protein synthesis of osteoblast-like MG63 cells. *Clinical Oral Implants Research,* 15**,** 683-692.

BALUYOT, E. S. & HARTFORD, C. G. 1996. Comparison of polyphosphate analysis by ion chromatography and by modified end-group titration. *Journal of Chromatography A,* 739**,** 217-222.

BANCROFT, G. N., SIKAVITSAST, V. I., VAN DEN DOLDER, J., SHEFFIELD, T. L., AMBROSE, C. G., JANSEN, J. A. & MIKOS, A. G. 2002. Fluid flow increases mineralized matrix deposition in 3D perfusion culture of marrow stromal osteloblasts in a dose-dependent manner. *Proceedings of the National Academy of Sciences of the United States of America,* 99**,** 12600-12605.

BERRIDGE, M. V., HERST, P. M. & TAN, A. S. 2005. Tetrazolium dyes as tools in cell biology: new insights into their cellular reduction. *Biotechnology annual review,* 11**,** 127-152.

BITAR, M., KNOWLES, J. C., LEWIS, M. P. & SALIH, V. 2005. Soluble phosphate glass fibres for repair of bone-ligament interface. *Journal of Materials Science-Materials in Medicine,* 16**,** 1131-1136.

BOROICA, L., SAVA, B. A., SAVA, M. & ELISA, M. 2013. Structure and properties of phosphate glasses containing Mo, B, V and Fe. *Journal of Optoelectronics and Advanced Materials,* 15**,** 187-192.

BOSKEY, A. L., MARESCA, M., ULLRICH, W., DOTY, S. B., BUTLER, W. T. & PRINCE, C. W. 1993. Osteopontin-hydroxyapatite interactions in vitro: inhibition of hydroxyapatite formation and growth in a gelatin-gel. *Bone and mineral,* 22**,** 147-59.

BOYAN, B. D., HUMMERT, T. W., DEAN, D. D. & SCHWARTZ, Z. 1996. Role of material surfaces in regulating bone and cartilage cell response. *Biomaterials,* 17**,** 137-146.

BRAUER, D. S., RUSSEL, C., LI, W. & HABELITZ, S. 2006. Effect of degradation rates of resorbable phosphate invert glasses on in vitro osteoblast proliferation. *Journal of Biomedical Materials Research Part A,* 77A**,** 213-219.

BRAUER, D. S., RUSSEL, C., VOGT, S., WEISSER, J. & SCHNABELRAUCH, M. 2008. Degradable phosphate glass fiber reinforced polymer matrices: mechanical properties and cell response. *Journal of Materials Science-Materials in Medicine,* 19**,** 121-127.

BROW, R. K. 2000. Review: the structure of simple phosphate glasses. *Journal of Non-Crystalline Solids,* 263**,** 1-28.

BROW, R. K., KIRKPATRICK, R. J. & TURNER, G. L. 1990. The Short-Range Structure of Sodium-Phosphate Glasses .1. Mas Nmr-Studies. *Journal of Non-Crystalline Solids,* 116**,** 39-45.

BUNKER, B. C., ARNOLD, G. W. & WILDER, J. A. 1984. Phosphate-Glass Dissolution in Aqueous-Solutions. *Journal of Non-Crystalline Solids,* 64**,** 291-316.

BURNIE, J., DOHERTY, R. J., GILCHRIST, T., DUFF, S. R. I., MALCOLM, A. J. & DRAKE, C. F. 1983. CONTROLLED RELEASE GLASS AS A POTENTIAL BONE-GRAFT SUBSTITUTE. *Journal of Bone and Joint Surgery-British Volume,* 65**,** 364-365.

BURNIE, J., GILCHRIST, T., DUFF, S. R. I., DRAKE, C. F., HARDING, N. G. L. & MALCOLM, A. J. 1981. CONTROLLED RELEASE GLASSES (CRG) FOR BIOMEDICAL USES. *Biomaterials,* 2**,** 244-246.

CACAINA, D., YLANEN, H., HUPA, M. & SIMON, S. 2006. Study of yttrium containing bioactive glasses behaviour in simulated body fluid. *Journal of Materials Science-Materials in Medicine,* 17**,** 709-716.

CACAINA, D., YLANEN, H., SIMON, S. & HUPA, M. 2008. The behaviour of selected yttrium containing bioactive glass microspheres in simulated body environments. *Journal of Materials Science-Materials in Medicine,* 19**,** 1225-1233.

CARTA, D., KNOWLES, J. C., SMITH, M. E. & NEWPORT, R. J. 2007a. Synthesis and structural characterization of P2O5-CaO-Na2O sol-gel materials. *Journal of Non-Crystalline Solids,* 353**,** 1141-1149.

CARTA, D., PICKUP, D. M., KNOWLES, J. C., AHMED, I., SMITH, M. E. & NEWPORT, R. J. 2007b. A structural study of sol-gel and melt-quenched phosphate-based glasses. *Journal of Non-Crystalline Solids,* 353**,** 1759-1765.

CHEN, M. Q., WANG, X., YE, Z. Y., ZHANG, Y., ZHOU, Y. & TAN, W. S. 2011. A modular approach to the engineering of a centimeter-sized bone tissue construct with human amniotic mesenchymal stem cells-laden microcarriers. *Biomaterials,* 32**,** 7532-7542.

CLOVER, J. & GOWEN, M. 1994. Are MG-63 and HOS TE85 human osteosarcoma cell lines representative models of the osteoblastic phenotype? *Bone,* 15**,** 585-591.

COZIEN-CAZUC, S., PARSONS, A. J., WALKER, G. S., JONES, I. A. & RUDD, C. D. 2008. Effects of aqueous aging on the mechanical properties of P40Na20Ca16Mg24 phosphate glass fibres. *Journal of Materials Science,* 43**,** 4834-4839.

COZIEN-CAZUC, S., PARSONS, A. J., WALKER, G. S., JONES, I. A. & RUDD, C. D. 2009. Real-time dissolution of P40Na20Ca16Mg24 phosphate glass fibers. *Journal of Non-Crystalline Solids,* 355**,** 2514-2521.

CURRAN, J. M., CHEN, R. & HUNT, J. A. 2005. Controlling the phenotype and function of mesenchymal stem cells in vitro by adhesion to silane-modified clean glass surfaces. *Biomaterials,* 26**,** 7057-7067.

DE GIROLAMO, L., SARTORI, M. F., ALBISETTI, W. & BRINI, A. T. 2007. Osteogenic differentiation of human adipose-derived stem cells: comparison of two different inductive media. *Journal of Tissue Engineering and Regenerative Medicine,* 1**,** 154-157.

DEFFONTAINES, B., MONTAGNE, L., VAST, P. & PALAVIT, G. 1991. Characterisation od Crystalline Species During the PReparation of Phosphate Ceramics in the NA2O-CAO-P2O5 System. *Comptes Rendus De L Academie Des Sciences Serie Ii,* 312**,** 1123-1127.

DEL VALLE, L. J., NAVARRO, M., SEPULCRE, F., GINEBRA, M. P. & PLANELL, J. A. 2003. Growth and differentiation of osteogenic cells on calcium phosphate glasses. *European Biophysics Journal,* 32**,** 269.

DEVI, A. V. G., RAJENDRAN, V. & RAJENDRAN, N. 2010. Structure, solubility and bioactivity in TiO2-doped phosphate-based bioglasses and glass-ceramics. *Materials Chemistry and Physics,* 124**,** 312-318.

DIAS, A. G., LOPES, M. A., CABRAL, A. T. T., SANTOS, J. D. & FERNANDES, M. H. 2005. In vitro studies of calcium phosphate glass ceramics with different solubility with the use of human bone marrow cells. *Journal of Biomedical Materials Research Part A,* 74A**,** 347-355.

DIAS, A. G., LOPES, M. A., SANTOS, J. D., AFONSO, A., TSURU, K., OSAKA, A., HAYAKAWA, S., TAKASHIMA, S. & KURABAYASHI, Y. 2006. In vivo performance of biodegradable calcium phosphate glass ceramics using the rabbit model: Histological and SEM observation. *Journal of Biomaterials Applications,* 20**,** 253-266.

DOMINICI, M., LE BLANC, K., MUELLER, I., SLAPER-CORTENBACH, I., MARINI, F. C., KRAUSE, D. S., DEANS, R. J., KEATING, A., PROCKOP, D. J. & HORWITZ, E. M. 2006. Minimal criteria for defining multipotent mesenchymal stromal cells. The International Society for Cellular Therapy position statement. *Cytotherapy,* 8**,** 315-317.

DRAKE, A. F. 1994. Optical Spectroscopy. *In:* TOTOWA, N. J. (ed.) *Methods in Molecular Biology, Vol. 22: Microscopy, Optical Spectroscopy, and Macroscopic Techniques. .* Humana Press Inc.

DU, Y. A., LO, E., ALI, S. & KHADEMHOSSEINI, A. 2008. Directed assembly of cell-laden microgels for fabrication of 3D tissue constructs. *Proceedings of the National Academy of Sciences of the United States of America,* 105**,** 9522-9527.

DVIR-GINZBERG, M., GAMLIELI-BONSHTEIN, I., AGBARIA, R. & COHEN, S. 2003. Liver tissue engineering within alginate scaffolds: Effects of cell-seeding density on hepatocyte viability, morphology, and function. *Tissue Engineering,* 9**,** 757-766.

EHRHARDT, G. J. & DAY, D. E. 1987. Therapeutic use of 90Y microspheres. *International Journal of Radiation Applications and Instrumentation. Part B. Nuclear Medicine and Biology,* 14**,** 233-242.

EL HAJ, A. J. & CARTMELL, S. H. 2010. Bioreactors for bone tissue engineering. *Proc Inst Mech Eng H,* 224**,** 1523-32.

ELBATAL, H. A., KHALIL, E. M. A. & HAMDY, Y. M. 2009. In vitro behavior of bioactive phosphate glass-ceramics from the system P2O5-Na2O-CaO containing titania. *Ceramics International,* 35**,** 1195-1204.

ERBE, E. M. & DAY, D. E. 1993. CHEMICAL DURABILITY OF Y2O3-AL2O3-SIO2 GLASSES FOR THE IN-VIVO DELIVERY OF BETA-RADIATION. *Journal of Biomedical Materials Research,* 27**,** 1301-1308.
FARGES, F., BROWN, G. E. & REHR, J. J. 1996. Coordination chemistry of Ti(IV) in silicate glasses and melts .1. XAFS study of titanium coordination in oxide model compounds. *Geochimica Et Cosmochimica Acta,* 60**,** 3023-3038.
FARGES, F., BROWN, G. E. & REHR, J. J. 1997. Ti K-edge XANES studies of Ti coordination and disorder in oxide compounds: Comparison between theory and experiment. *Physical Review B,* 56**,** 1809-1819.
FERNANDEZ, J. G. & KHADEMHOSSEINI, A. 2010. Micro-Masonry: Construction of 3D Structures by Microscale Self-Assembly. *Advanced Materials,* 22**,** 2538-2541.
FRANKS, K., ABRAHAMS, I. & KNOWLES, J. C. 2000. Development of soluble glasses for biomedical use Part I: In vitro solubility measurement. *Journal of Materials Science-Materials in Medicine,* 11**,** 609-614.
FRANKS, K., SALIH, V., KNOWLES, J. C. & OLSEN, I. 2002. The effect of MgO on the solubility behavior and cell proliferation in a quaternary soluble phosphate based glass system. *Journal of Materials Science-Materials in Medicine,* 13**,** 549-556.
FRONZONI, G., FRANCESCO, R., STENER, M. & CAUSA, M. 2006. X-ray absorption spectroscopy of titanium oxide by time dependent density functional calculations. *Journal of Physical Chemistry B,* 110**,** 9899-9907.
GAO, H. S., TAN, T. N. & WANG, D. H. 2004. Effect of composition on the release kinetics of phosphate controlled release glasses in aqueous medium. *Journal of Controlled Release,* 96**,** 21-28.
GILCHRIST, T., HEALY, D. M. & DRAKE, C. 1991. Controlled Silver-Releasing Polymers and Their Potential for Urinary-Tract Infection Control. *Biomaterials,* 12**,** 76-78.
GILL, I. & BALLESTEROS, A. 2000. Bioencapsulation within synthetic polymers (Part 1): sol-gel encapsulated biologicals. *Trends in Biotechnology,* 18**,** 282-296.
GOH, Y.-F., ALSHEMARY, A. Z., AKRAM, M., KADIR, M. R. A. & HUSSAIN, R. 2014. In-vitro characterization of antibacterial bioactive glass containing ceria. *Ceramics International,* 40**,** 729-737.
GREGORY, C. A., GRADY GUNN, W., PEISTER, A. & PROCKOP, D. J. 2004. An Alizarin red-based assay of mineralization by adherent cells in culture: comparison with cetylpyridinium chloride extraction. *Analytical biochemistry,* 329**,** 77-84.
GU, Y. W., YAP, A. U. J., CHEANG, P. & KUMAR, R. 2004. Spheroidization of glass powders for glass ionomer cements. *Biomaterials,* 25**,** 4029-4035.
GUMBINER, B. M. 1996. Cell adhesion: the molecular basis of tissue architecture and morphogenesis. *Cell,* 84**,** 345-357.
HADLOCK, T., SUNDBACK, C., HUNTER, D., CHENEY, M. & VACANTI, J. P. 2000. A polymer foam conduit seeded with Schwann cells promotes guided peripheral nerve regeneration. *Tissue Engineering,* 6**,** 119-127.
HAQUE, P., AHMED, I., PARSONS, A., FELFEL, R., WALKER, G. & RUDD, C. 2013a. Degradation properties and microstructural analysis of 40P2O5–24MgO–16CaO–16Na2O–4Fe2O3 phosphate glass fibres. *Journal of Non-Crystalline Solids,* 375**,** 99-109.
HAQUE, P., AHMED, I., PARSONS, A., FELFEL, R., WALKER, G. & RUDD, C. 2013b. Degradation properties and microstructural analysis of 40P(2)O(5)-24MgO-16CaO-16Na(2)O-4Fe(2)O(3) phosphate glass fibres. *Journal of Non-Crystalline Solids,* 375**,** 99-109.
HASAN, M. S., AHMED, I., PARSONS, A. J., WALKER, G. S. & SCOTCHFORD, C. A. 2012. Material characterisation and cytocompatibility assessment of

quinternary phosphate glasses. *Journal of Materials Science-Materials in Medicine,* 23**,** 2531-2541.
HENCH, L. L. 1991. BIOCERAMICS - FROM CONCEPT TO CLINIC. *Journal of the American Ceramic Society,* 74**,** 1487-1510.
HENCH, L. L. 2006. The story of Bioglass (R). *Journal of Materials Science-Materials in Medicine,* 17**,** 967-978.
HENCH, L. L., SPLINTER, R. J., ALLEN, W. C. & GREENLEE, T. K. 1972. BONDING MECHANISM AT THE INTERFACE OF CERAMIC PROSTHETIC MATERIALS. *Journal of Biomedical Materials Research Biomedical Materials Symposium,* 2**,** 117-141.
HESARAKI, S., ALIZADEH, M., NAZARIAN, H. & SHARIFI, D. 2010. Physico-chemical and in vitro biological evaluation of strontium/calcium silicophosphate glass. *Journal of Materials Science-Materials in Medicine,* 21**,** 695-705.
HO, S., LAU, W. Y., LEUNG, T. W. & JOHNSON, P. J. 1998. Internal radiation therapy for patients with primary or metastatic hepatic cancer: a review. *Cancer,* 83**,** 1894-907.
HOGAN, B. L. M. 1996. Bone morphogenetic proteins: Multifunctional regulators of vertebrate development. *Genes & Development,* 10**,** 1580-1594.
HOLMES, T. C., DE LACALLE, S., SU, X., LIU, G. S., RICH, A. & ZHANG, S. G. 2000. Extensive neurite outgrowth and active synapse formation on self-assembling peptide scaffolds. *Proceedings of the National Academy of Sciences of the United States of America,* 97**,** 6728-6733.
HOLY, C. E., SHOICHET, M. S. & DAVIES, J. E. 2000. Engineering three-dimensional bone tissue in vitro using biodegradable scaffolds: Investigating initial cell-seeding density and culture period. *Journal of Biomedical Materials Research,* 51**,** 376-382.
HOPPE, U. 1996. A structural model for phosphate glasses. *Journal of Non-Crystalline Solids,* 195**,** 138-147.
HUDGENS, J. J., BROW, R. K., TALLANT, D. R. & MARTIN, S. W. 1998. Raman spectroscopy study of the structure of lithium and sodium ultraphosphate glasses. *Journal of Non-Crystalline Solids,* 223**,** 21-31.
HUDSON, J. E., MILLS, R. J., FRITH, J. E., BROOKE, G., JARAMILLO-FERRADA, P., WOLVETANG, E. J. & COOPER-WHITE, J. J. 2011. A Defined Medium and Substrate for Expansion of Human Mesenchymal Stromal Cell Progenitors That Enriches for Osteo- and Chondrogenic Precursors. *Stem Cells and Development,* 20**,** 77-87.
HULL, A. W. 1919. A new method of chemical analysis. *Journal of the American Chemical Society,* 41**,** 1168-1175.
HUNZIKER, E. B. 2002. Articular cartilage repair: basic science and clinical progress. A review of the current status and prospects. *Osteoarthritis and Cartilage,* 10**,** 432-463.
HUTMACHER, D. W. 2000. Scaffolds in tissue engineering bone and cartilage. *Biomaterials,* 21**,** 2529-2543.
ISHAUG-RILEY, S. L., CRANE-KRUGER, G. M., YASZEMSKI, M. J. & MIKOS, A. G. 1998. Three-dimensional culture of rat calvarial osteoblasts in porous biodegradable polymers. *Biomaterials,* 19**,** 1405-1412.
ISHAUG, S. L., CRANE, G. M., MILLER, M. J., YASKO, A. W., YASZEMSKI, M. J. & MIKOS, A. G. 1997. Bone formation by three-dimensional stromal osteoblast culture in biodegradable polymer scaffolds. *Journal of Biomedical Materials Research,* 36**,** 17-28.
JAKAB, K., NOROTTE, C., DAMON, B., MARGA, F., NEAGU, A., BESCH-WILLIFORD, C. L., KACHURIN, A., CHURCH, K. H., PARK, H., MIRONOV, V., MARKWALD, R., VUNJAK-NOVAKOVIC, G. & FORGACS, G. 2008.

Tissue engineering by self-assembly of cells printed into topologically defined structures. *Tissue Engineering Part A,* 14**,** 413-421.
JUNG, S., PANCHALINGAM, K. M., ROSENBERG, L. & BEHIE, L. A. 2012. Ex Vivo Expansion of Human Mesenchymal Stem Cells in Defined Serum-Free Media. *Stem Cells International*.
JUNG, S., SEN, A., ROSENBERG, L. & BEHIE, L. A. 2010. Identification of growth and attachment factors for the serum-free isolation and expansion of human mesenchymal stromal cells. *Cytotherapy,* 12**,** 637-657.
KARABULUT, M., METWALLI, E., DAY, D. E. & BROW, R. K. 2003. Mossbauer and IR investigations of iron ultraphosphate glasses. *Journal of Non-Crystalline Solids,* 328**,** 199-206.
KASUGA, T., SAWADA, M., NOGAMI, M. & ABE, Y. 1999. Bioactive ceramics prepared by sintering and crystallization of calcium phosphate invert glasses. *Biomaterials,* 20**,** 1415-1420.
KAWASHITA, M., TODA, S., KIM, H. M., KOKUBO, T. & MASUDA, N. 2003. Preparation of antibacterial silver-doped silica glass microspheres. *Journal of Biomedical Materials Research Part A,* 66A**,** 266-274.
KELM, J. M., DJONOV, V., ITTNER, L. M., FLURI, D., BORN, W., HOERSTRUP, S. P. & FUSSENEGGER, M. 2006. Design of custom-shaped vascularized tissues using microtissue spheroids as minimal building units. *Tissue Engineering,* 12**,** 2151-2160.
KEMP, T. F. & SMITH, M. E. 2009a. QuadFit-A new cross-platform computer program for simulation of NMR line shapes from solids with distributions of interaction parameters. *Solid State Nuclear Magnetic Resonance,* 35**,** 243-252.
KEMP, T. F. & SMITH, M. E. 2009b. QuadFit—A new cross-platform computer program for simulation of NMR line shapes from solids with distributions of interaction parameters. *Solid State Nuclear Magnetic Resonance,* 35**,** 243-252.
KENNEDY, A. S., NUTTING, C., COLDWELL, D., GAISER, J. & DRACHENBERG, C. 2004. Pathologic response and microdosimetry of (90)Y microspheres in man: review of four explanted whole livers. *Int J Radiat Oncol Biol Phys,* 60**,** 1552-63.
KHOR, S. F., TALIB, Z. A., DAUD, W. M. & SIDEK, H. A. A. 2011. Degradation study on ternary zinc magnesium phosphate glasses. *Journal of Materials Science,* 46**,** 7895-7900.
KIANI, A., CAHILL, L. S., ABOU NEEL, E. A., HANNA, J. V., SMITH, M. E. & KNOWLES, J. C. 2010. Physical properties and MAS-NMR studies of titanium phosphate-based glasses. *Materials Chemistry and Physics,* 120**,** 68-74.
KIANI, A., HANNA, J. V., KING, S. P., REES, G. J., SMITH, M. E., ROOHPOUR, N., SALIH, V. & KNOWLES, J. C. 2012a. Structural characterization and physical properties of P2O5-CaO-Na2O-TiO2 glasses by Fourier transform infrared, Raman and solid-state magic angle spinning nuclear magnetic resonance spectroscopies. *Acta Biomaterialia,* 8**,** 333-340.
KIANI, A., LAKHKAR, N. J., SALIH, V., SMITH, M. E., HANNA, J. V., NEWPORT, R. J., PICKUP, D. M. & KNOWLES, J. C. 2012b. Titanium-containing bioactive phosphate glasses. *Philosophical Transactions of the Royal Society a-Mathematical Physical and Engineering Sciences,* 370**,** 1352-1375.
KIRKPATRICK, R. J. & BROW, R. K. 1995a. NUCLEAR-MAGNETIC-RESONANCE INVESTIGATION OF THE STRUCTURES OF PHOSPHATE AND PHOSPHATE-CONTAINING GLASSES - A REVIEW. *Solid State Nuclear Magnetic Resonance,* 5**,** 9-21.

KIRKPATRICK, R. J. & BROW, R. K. 1995b. Nuclear-Magnetic-Resonance Investigation of the Structures of Phosphate and Phosphate-Containing Glasses - A Review. *Solid State Nuclear Magnetic Resonance,* 5**,** 9-21.
KNOWLES, J. C. 2003. Phosphate based glasses for biomedical applications. *Journal of Materials Chemistry,* 13**,** 2395-2401.
KOHN, S. C., DUPREE, R. & SMITH, M. E. 1989. A Multinuclear Magnetic-Resonance Study of the Strucutre of Hydrous Albite Glasses. *Geochimica Et Cosmochimica Acta,* 53**,** 2925-2935.
KOHN, S. C., SMITH, M. E., DIRKEN, P. J., VAN ECK, E. R. H., KENTGENS, A. P. M. & DUPREE, R. 1998. Sodium environments in dry and hydrous albite glasses: Improved Na-23 solid state NMR data and their implications for water dissolution mechanisms. *Geochimica Et Cosmochimica Acta,* 62**,** 79-87.
KOKUBO, T., KIM, H. M. & KAWASHITA, M. 2003. Novel bioactive materials with different mechanical properties. *Biomaterials,* 24**,** 2161-2175.
KOKUBO, T. & TAKADAMA, H. 2006. How useful is SBF in predicting in vivo bone bioactivity? *Biomaterials,* 27**,** 2907-2915.
KOLLER, H., ENGELHARDT, G., KENTGENS, A. P. M. & SAUER, J. 1994. Na-23 Nmr-Spectroscopy of Solids - Interpretation of Quadrupole Interaction Parameters and Chemical-Shifts. *Journal of Physical Chemistry,* 98**,** 1544-1551.
KREIDL, N. J. & WEYL, W. A. 1941. Phosphates in ceramic ware: IV, Phosphate glasses. *Journal of the American Ceramic Society,* 24**,** 372-378.
LAFLAMME, M. A. & MURRY, C. E. 2005. Regenerating the heart. *Nature Biotechnology,* 23**,** 845-856.
LAKHKAR, N., ABOU NEEL, E. A., SALIH, V. & KNOWLES, J. C. 2010. Titanium and Strontium-doped Phosphate Glasses as Vehicles for Strontium Ion Delivery to Cells. *Journal of Biomaterials Applications*.
LAKHKAR, N. J., ABOU NEEL, E. A., SALIH, V. & KNOWLES, J. C. 2009. Strontium oxide doped quaternary glasses: effect on structure, degradation and cytocompatibility. *Journal of Materials Science-Materials in Medicine,* 20**,** 1339-1346.
LAKHKAR, N. J., LEE, I. H., KIM, H. W., SALIH, V., WALL, I. B. & KNOWLES, J. C. 2013. Bone formation controlled by biologically relevant inorganic ions: role and controlled delivery from phosphate-based glasses. *Adv Drug Deliv Rev,* 65**,** 405-20.
LAKHKAR, N. J., PARK, J. H., MORDAN, N. J., SALIH, V., WALL, I. B., KIM, H. W., KING, S. P., HANNA, J. V., MARTIN, R. A., ADDISON, O., MOSSELMANS, J. F. & KNOWLES, J. C. 2012. Titanium phosphate glass microspheres for bone tissue engineering. *Acta Biomaterialia,* 8**,** 4181-90.
LANGER, R. & VACANTI, J. P. 1993. TISSUE ENGINEERING. *Science,* 260**,** 920-926.
LAO, J., JALLOT, E. & NEDELEC, J.-M. 2008. Strontium-delivering glasses with enhanced bioactivity: A new biomaterial for antiosteoporotic applications? *Chemistry of Materials,* 20**,** 4969-4973.
LE SAOUT, G., SIMON, P., FAYON, F., BLIN, A. & VAILLS, Y. 2002. Raman and infrared study of (PbO)(x)(P2O5)((1-x)) glasses. *Journal of Raman Spectroscopy,* 33**,** 740-746.
LEE, I. H., SHIN, S. H., FOROUTAN, F., LAKHKAR, N. J., GONG, M. S. & KNOWLES, J. C. 2013a. Effects of magnesium content on the physical, chemical and degradation properties in a Mgo-CaO-Na2O-P2O5 glass system. *Journal of Non-Crystalline Solids,* 363**,** 57-63.
LEE, I. H., YU, H. S., LAKHKAR, N. J., KIM, H. W., GONG, M. S., KNOWLES, J. C. & WALL, I. B. 2013b. Development, characterisation and biocompatibility testing of a cobalt-containing titanium phosphate-based glass for

engineering of vascularized hard tissues. *Materials Science & Engineering C-Materials for Biological Applications,* 33**,** 2104-2112.
LEE, K. Y., PARK, M., KIM, H. M., LIM, Y. J., CHUN, H. J., KIM, H. & MOON, S. H. 2006. Ceramic bioactivity: progresses, challenges and perspectives. *Biomedical Materials,* 1**,** R31-R37.
LEI, B., CHEN, X. F., WANG, Y. J., ZHAO, N. R., MIAO, G. H., LI, Z. M. & LIN, C. 2010. Fabrication of porous bioactive glass particles by one step sintering. *Materials Letters,* 64**,** 2293-2295.
LI, S. Y., NGUYEN, L., XIONG, H. R., WANG, M. Y., HU, T. C. C., SHE, J. X., SERKIZ, S. M., WICKS, G. G. & DYNAN, W. S. 2010. Porous-wall hollow glass microspheres as novel potential nanocarriers for biomedical applications. *Nanomedicine-Nanotechnology Biology and Medicine,* 6**,** 127-136.
LIU, B., LIU, Y., LEWIS, A. K. & SHEN, W. 2010. Modularly assembled porous cell-laden hydrogels. *Biomaterials,* 31**,** 4918-4925.
LIVAGE, J., BARBOUX, P., VANDENBORRE, M. T., SCHMUTZ, C. & TAULELLE, F. 1992. SOL-GEL SYNTHESIS OF PHOSPHATES. *Journal of Non-Crystalline Solids,* 147**,** 18-23.
LUCACEL, R. C., MAIER, M. & SIMON, V. 2010. Structural and in vitro characterization of TiO2-CaO-P2O5 bioglasses. *Journal of Non-Crystalline Solids,* 356**,** 2869-2874.
MACKENZIE, K. J. & SMITH, M. E. 2002a. *Multinuclear solid-state nuclear magnetic resonance of inorganic materials*, Access Online via Elsevier.
MACKENZIE, K. J. D. & SMITH, M. E. 2002b. *Multinuclear Solid State NMR of Inorganic Materials,* Oxford, Pergamon.
MARASINGHE, G. K., KARABULUT, M., RAY, C. S., DAY, D. E., SHUH, D. K., ALLEN, P. G., SABOUNGI, M. L., GRIMSDITCH, M. & HAEFFNER, D. 2000. Properties and structure of vitrified iron phosphate nuclear wasteforms. *Journal of Non-Crystalline Solids,* 263**,** 146-154.
MARTIN, Y., ELDARDIRI, M., LAWRENCE-WATT, D. J. & SHARPE, J. R. 2011. Microcarriers and Their Potential in Tissue Regeneration. *Tissue Engineering Part B-Reviews,* 17**,** 71-80.
MARTINELLI, J. R., SENE, F. F., KAMIKAWACHI, C. N., PARTITI, C. S. D. & CORNEJO, D. R. 2010. Synthesis and characterization of glass-ceramic microspheres for thermotherapy. *Journal of Non-Crystalline Solids,* 356**,** 2683-2688.
MASSIOT, D., FAYON, F., CAPRON, M., KING, I., LE CALVE, S., ALONSO, B., DURAND, J. O., BUJOLI, B., GAN, Z. H. & HOATSON, G. 2002. Modelling one- and two-dimensional solid-state NMR spectra. *Magnetic Resonance in Chemistry,* 40**,** 70-76.
MEINEL, L., KARAGEORGIOU, V., FAJARDO, R., SNYDER, B., SHINDE-PATIL, V., ZICHNER, L., KAPLAN, D., LANGER, R. & VUNJAK-NOVAKOVIC, G. 2004. Bone tissue engineering using human mesenchymal stem cells: Effects of scaffold material and medium flow. *Annals of Biomedical Engineering,* 32**,** 112-122.
MEYER, K. 1997. Characterization of the structure of binary zinc ultraphosphate glasses by infrared and Raman spectroscopy. *Journal of Non-Crystalline Solids,* 209**,** 227-239.
MEYER, K. 1998. Characterisation of the structure of binary calcium ultraphosphate glasses by infrared and Raman spectroscopy. *Physics and Chemistry of Glasses,* 39**,** 108-117.
MIKOS, A. G., HERRING, S. W., OCHAREON, P., ELISSEEFF, J., LU, H. H., KANDEL, R., SCHOEN, F. J., TONER, M., MOONEY, D., ATALA, A., VAN DYKE, M. E., KAPLAN, D. & VUNJAK-NOVAKOVIC, G. 2006. Engineering complex tissues. *Tissue Engineering,* 12**,** 3307-3339.

MIMURA, S., KIMURA, N., HIRATA, M., TATEYAMA, D., HAYASHIDA, M., UMEZAWA, A., KOHARA, A., NIKAWA, H., OKAMOTO, T. & FURUE, M. K. 2011. Growth factor-defined culture medium for human mesenchymal stem cells. *International Journal of Developmental Biology,* 55**,** 181-187.

MONEM, A. S., ELBATAL, H. A., KHALIL, E. M. A., AZOOZ, M. A. & HAMDY, Y. M. 2008. In vivo behavior of bioactive phosphate glass-ceramics from the system P2O5-Na2O-CaO containing TiO2. *Journal of Materials Science-Materials in Medicine,* 19**,** 1097-1108.

MOSS, R. M., ABOU NEEL, E. A., PICKUP, D. M., TWYMAN, H. L., MARTIN, R. A., HENSON, M. D., BARNEY, E. R., HANNON, A. C., KNOWLES, J. C. & NEWPORT, R. J. 2010. The effect of zinc and titanium on the structure of calcium-sodium phosphate based glass. *Journal of Non-Crystalline Solids,* 356**,** 1319-1324.

MÜLLER, P., BULNHEIM, U., DIENER, A., LÜTHEN, F., TELLER, M., KLINKENBERG, E. D., NEUMANN, H. G., NEBE, B., LIEBOLD, A. & STEINHOFF, G. 2008. Calcium phosphate surfaces promote osteogenic differentiation of mesenchymal stem cells. *Journal of cellular and molecular medicine,* 12**,** 281-291.

MULLIGAN, A. M., WILSON, M. & KNOWLES, J. C. 2003a. The effect of increasing copper content in phosphate-based glasses on biofilms of Streptococcus sanguis. *Biomaterials,* 24**,** 1797-1807.

MULLIGAN, A. M., WILSON, M. & KNOWLES, J. C. 2003b. Effect of increasing silver content in phosphate-based glasses on biofilms of Streptococcus sanguis. *Journal of Biomedical Materials Research Part A,* 67A**,** 401-412.

MUNOZ, F., PRITULA, O., SEDLACEK, J. & RUSSEL, C. 2008. A study on the anisotropy of phosphate glass fibres. *Glass Technology-European Journal of Glass Science and Technology Part A,* 49**,** 47-52.

MUSCHLER, G. E., NAKAMOTO, C. & GRIFFITH, L. G. 2004. Engineering principles of clinical cell-based tissue engineering. *Journal of Bone and Joint Surgery-American Volume,* 86A**,** 1541-1558.

NAVARRO, M., GINEBRA, M. P., CLEMENT, J., MARTINEZ, S., AVILA, G. & PLANELL, J. A. 2003a. Physicochemical degradation of titania-stabilized soluble phosphate glasses for medical applications. *Journal of the American Ceramic Society,* 86**,** 1345-1352.

NAVARRO, M., GINEBRA, M. P. & PLANELL, J. A. 2003b. Cellular response to calcium phosphate glasses with controlled solubility. *Journal of Biomedical Materials Research Part A,* 67A**,** 1009-1015.

NICHOL, J. W. & KHADEMHOSSEINI, A. 2009. Modular tissue engineering: engineering biological tissues from the bottom up. *Soft Matter,* 5**,** 1312-1319.

NODA, K., SAKAMOTO, W., KIKUTA, K., YOGO, T. & HIRANO, S. 1997. Effect of phosphorus sources on synthesis of KTiOPO4 thin films by sol-gel method. *Chemistry of Materials,* 9**,** 2174-2178.

O'DONNELL, M. D. & HILL, R. G. 2010. Influence of strontium and the importance of glass chemistry and structure when designing bioactive glasses for bone regeneration. *Acta Biomaterialia,* 6**,** 2382-2385.

OHASHI, K., YOKOYAMA, T., YAMATO, M., KUGE, H., KANEHIRO, H., IWATA, H., YANG, J., OKANO, T. & NAKAJIMA, Y. 2007. Engineering two-dimensional and three-dimensional functional hepatic tissues in vivo using cell sheet engineering technologies. *Xenotransplantation,* 14**,** 385-385.

OTT, H. C., MATTHIESEN, T. S., GOH, S.-K., BLACK, L. D., KREN, S. M., NETOFF, T. I. & TAYLOR, D. A. 2008. Perfusion-decellularized matrix: using nature's platform to engineer a bioartificial heart. *Nature Medicine,* 14**,** 213-221.

PARK, J. H., PEREZ, R. A., JIN, G. Z., CHOI, S. J., KIM, H. W. & WALL, I. B. 2013. Microcarriers Designed for Cell Culture and Tissue Engineering of Bone. *Tissue Engineering Part B-Reviews,* 19**,** 172-190.

PARKER, A. M., SHANG, H., KHURGEL, M. & KATZ, A. J. 2007. Low serum and serum-free culture of multipotential human adipose stem cells. *Cytotherapy,* 9**,** 637-646.

PAUTKE, C., SCHIEKER, M., TISCHER, T., KOLK, A., NETH, P., MUTSCHLER, W. & MILZ, S. 2004. Characterization of osteosarcoma cell lines MG-63, Saos-2 and U-2 OS in comparison to human osteoblasts. *Anticancer research,* 24**,** 3743-3748.

PEITL, O., ZANOTTO, E. D. & HENCH, L. L. 2001. Highly bioactive P2O5-Na2O-CaO-SiO2 glass-ceramics. *Journal of Non-Crystalline Solids,* 292**,** 115-126.

PEMBERTON, J. E., LATIFZADEH, L., FLETCHER, J. P. & RISBUD, S. H. 1991. Raman-Spectroscopy of Calcium-Phosphate Glasses with Varying Cao Modifier Concentrations. *Chemistry of Materials,* 3**,** 195-200.

PICKUP, D. M., ABOU NEEL, E. A., MOSS, R. M., WETHERALL, K. M., GUERRY, P., SMITH, M. E., KNOWLES, J. C. & NEWPORT, R. J. 2008a. TiK-edge XANES study of the local environment of titanium in bioresorbable TiO2-CaO-Na2O-P2O5 glasses. *Journal of Materials Science-Materials in Medicine,* 19**,** 1681-1685.

PICKUP, D. M., AHMED, I., GUERRY, P., KNOWLES, J. C., SMITH, M. E. & NEWPORT, R. J. 2007a. The structure of phosphate glass biomaterials from neutron diffraction and P-31 nuclear magnetic resonance data. *Journal of Physics-Condensed Matter,* 19.

PICKUP, D. M., GUERRY, P., MOSS, R. M., KNOWLES, J. C., SMITH, M. E. & NEWPORT, R. J. 2007b. New sol-gel synthesis of a (CaO)(0.3)(Na2O)(0.2)(P2O5)(0.5) bioresorbable glass and its structural characterisation. *Journal of Materials Chemistry,* 17**,** 4777-4784.

PICKUP, D. M., NEWPORT, R. J. & KNOWLES, J. C. 2012. Sol-gel phosphate-based glass for drug delivery applications. *J Biomater Appl,* 26**,** 613-22.

PICKUP, D. M., SPEIGHT, R. J., KNOWLES, J. C., SMITH, M. E. & NEWPORT, R. J. 2008b. Sol-gel synthesis and structural characterisation of binary TiO2-P2O5 glasses. *Materials Research Bulletin,* 43**,** 333-342.

PICKUP, D. M., VALAPPIL, S. P., MOSS, R. M., TWYMAN, H. L., GUERRY, P., SMITH, M. E., WILSON, M., KNOWLES, J. C. & NEWPORT, R. J. 2009. Preparation, structural characterisation and antibacterial properties of Ga-doped sol-gel phosphate-based glass. *Journal of Materials Science,* 44**,** 1858-1867.

POORBAYGI, H., AGHAMIRI, S., KAMALI-ASL, A., SHEIBANI, S. & MOHAGHEGHPOOR, E. 2011a. Study of Creation of Spect Imaging Possibility in Y-90 Glass Microsphere Using Adding a Gamma Emitter Impurity. *Internal Medicine Journal,* 41**,** 30-30.

POORBAYGI, H., AGHAMIRI, S. M. R., SHEIBANI, S., KAMALI-ASL, A. & MOHAGHEGHPOOR, E. 2011b. Production of glass microspheres comprising Y-90 and Lu-177 for treating of hepatic tumors with SPECT imaging capabilities. *Applied Radiation and Isotopes,* 69**,** 1407-1414.

POUMELLEC, B., DURHAM, P. J. & GUO, G. Y. 1991. Electronic-Strucutre and X-ray Absorption-Spectrum of Rutile TiO2. *Journal of Physics-Condensed Matter,* 3**,** 8195-8204.

QIU, D., GUERRY, P., KNOWLES, J. C., SMITH, M. E. & NEWPORT, R. J. 2008a. Formation of functional phosphosilicate gels from phytic acid and tetraethyl orthosilicate. *Journal of Sol-Gel Science and Technology,* 48**,** 378-383.

QIU, D., MOSS, R. M., PICKUP, D. M., AHMED, I., KNOWLES, J. C. & NEWPORT, R. J. 2008b. An X-ray absorption spectroscopy study of the local

environment of iron in degradable iron-phosphate glasses. *Journal of Non-Crystalline Solids,* 354**,** 5542-5546.
RADISIC, M., MARSANO, A., MAIDHOF, R., WANG, Y. & VUNJAK-NOVAKOVIC, G. 2008. Cardiac tissue engineering using perfusion bioreactor systems. *Nat Protoc,* 3**,** 719-38.
RAJENDRAN, V., DEVI, A. V. G., AZOOZ, M. & EL-BATAL, F. H. 2007. Physicochemical studies of phosphate based P2O5-Na2O-CaO-TiO2 glasses for biomedical applications. *Journal of Non-Crystalline Solids,* 353**,** 77-84.
RAUH, J., MILAN, F., GUNTHER, K. P. & STIEHLER, M. 2011. Bioreactor systems for bone tissue engineering. *Tissue Eng Part B Rev,* 17**,** 263-80.
RAVEL, B. & NEWVILLE, M. 2005. ATHENA, ARTEMIS, HEPHAESTUS: data analysis for X-ray absorption spectroscopy using IFEFFIT. *Journal of Synchrotron Radiation,* 12**,** 537-541.
REINHOLT, F. P., HULTENBY, K., OLDBERG, A. & HEINEGARD, D. 1990. Osteopontin--a possible anchor of osteoclasts to bone. *Proceedings of the National Academy of Sciences of the United States of America,* 87**,** 4473-5.
REIS, S. T., FARIA, D. L. A., JR, M., PONTUSCHKA, W. M., DAY, D. E. & PARTITI, C. S. M. 2002. Structural features of lead iron phosphate glasses. *Journal of Non-Crystalline Solids,* 304**,** 188-194.
REZWAN, K., CHEN, Q. Z., BLAKER, J. J. & BOCCACCINI, A. R. 2006. Biodegradable and bioactive porous polymer/inorganic composite scaffolds for bone tissue engineering. *Biomaterials,* 27**,** 3413-3431.
SAHOO, S., OUYANG, H., GOH, J. C. H., TAY, T. E. & TOH, S. L. 2006. Characterization of a novel polymeric scaffold for potential application in tendon/ligament tissue engineering. *Tissue Engineering,* 12**,** 91-99.
SALEM, R. & THURSTON, K. G. 2006. Radioembolization with yttrium-90 microspheres: a state-of-the-art brachytherapy treatment for primary and secondary liver malignancies: part 3: comprehensive literature review and future direction. *J Vasc Interv Radiol,* 17**,** 1571-93.
SALIH, V., FRANKS, K., JAMES, M., HASTINGS, G. W., KNOWLES, J. C. & OLSEN, I. 2000. Development of soluble glasses for biomedical use Part II: The biological response of human osteoblast cell lines to phosphate-based soluble glasses. *Journal of Materials Science-Materials in Medicine,* 11**,** 615-620.
SALIH, V., PATEL, A. & KNOWLES, J. C. 2007. Zinc-containing phosphate-based glasses for tissue engineering. *Biomedical Materials,* 2**,** 11-20.
SALTER, E., GOH, B., HUNG, B., HUTTON, D., GHONE, N. & GRAYSON, W. L. 2012. Bone tissue engineering bioreactors: a role in the clinic? *Tissue Eng Part B Rev,* 18**,** 62-75.
SAVA, B. A., BOROICA, L. & ELISA, M. 2013. SYNTHESIS OF RARE-EARTH-DOPED PHOSPHATE GLASSES WITH IMPROVED OPTICAL PROPERTIES. *Revista Romana De Materiale-Romanian Journal of Materials,* 43**,** 339-346.
SCHOTTNER, G. 2001. Hybrid sol-gel-derived polymers: Applications of multifunctional materials. *Chemistry of Materials,* 13**,** 3422-3435.
SENE, F. F., OKUNO, E. & MARTINELLI, J. R. 2008. Synthesis and characterization of phosphate glass microspheres for radiotherapy applications. *Journal of Non-Crystalline Solids,* 354**,** 4887-4893.
SHAH, R., SINANAN, A. C. M., KNOWLES, J. C., HUNT, N. P. & LEWIS, M. P. 2005. Craniofacial muscle engineering using a 3-dimensional phosphate glass fibre construct. *Biomaterials,* 26**,** 1497-1505.
SHAHARUDDIN, S. I. S., AHMED, I., FURNISS, D., PARSONS, A. J. & RUDD, C. D. 2012. Thermal properties, viscosities and densities of (50-x)Na2O-xCaO-

50P(2)O(5) glasses. *Glass Technology-European Journal of Glass Science and Technology Part A,* 53**,** 245-251.
SHAKESHEFF, K. 2007. Liver tissue engineering. *Tissue Engineering Using Ceramics and Polymers***,** 404-420.
SHANNON, R. D. 1976. Revised Effective Ionic-Radii and Systematic Studies of Interatomic Distances in Halides and Chalcogenides. *Acta Crystallographica Section A,* 32**,** 751-767.
SHASH, N. M. & AHMED, I. S. 2013. Structure and electrical properties of ZnO doped barium-metaphosphate glasses. *Materials Chemistry and Physics,* 137**,** 734-741.
SHIH, P. Y. 2003. Properties and FTIR spectra of lead phosphate glasses for nuclear waste immobilization. *Materials Chemistry and Physics,* 80**,** 299-304.
SHIH, P. Y. & SHIU, H. M. 2007. Properties and structural investigations of UV-transmitting vitreous strontium zinc metaphosphate. *Materials Chemistry and Physics,* 106**,** 222-226.
SHIH, P. Y., YUNG, S. W. & CHIN, T. S. 1998. Thermal and corrosion behavior of P2O5-Na2O-CuO glasses. *Journal of Non-Crystalline Solids,* 224**,** 143-152.
SHIH, P. Y., YUNG, S. W. & CHIN, T. S. 1999. FTIR and XPS studies of P2O5-Na2O-CuO glasses. *Journal of Non-Crystalline Solids,* 244**,** 211-222.
SIKAVITSAS, V. I., BANCROFT, G. N., HOLTORF, H. L., JANSEN, J. A. & MIKOS, A. G. 2003. Mineralized matrix deposition by marrow stromal osteoblasts in 3D perfusion culture increases with increasing fluid shear forces. *Proceedings of the National Academy of Sciences of the United States of America,* 100**,** 14683-14688.
SMITH, M. E. 2001. Recent progress in solid-state NMR of low-gamma nuclei. *Annual Reports on Nmr Spectroscopy, Vol 43.* London: Academic Press Ltd.
SMITH, M. E. & VAN ECK, E. R. H. 1999. Recent advances in experimental solid state NMR methodology for half-integer spin quadrupolar nuclei. *Progress in Nuclear Magnetic Resonance Spectroscopy,* 34**,** 159-201.
STEBBINS, J. F., FARNAN, I. & XUE, X. Y. 1992. The Structure and Dynamics of Alkali Silicate Liquids. A View From NMR-Spectroscopy. *Chemical Geology,* 96**,** 371-385.
STEIGMAN, S. A. & FAUZA, D. O. 2007. Isolation of Mesenchymal Stem Cells from Amniotic Fluid and Placenta. *Current Protocols in Stem Cell Biology.* John Wiley & Sons, Inc.
STEVENS, M. P. 1999. Evaluation, characterisation, and analysis of polymers. *Polymer Chemistry: An Introduction. .* New York: Oxford University Press.
STROBER, W. 2001. Trypan Blue Exclusion Test of Cell Viability. *Current Protocols in Immunology.* John Wiley & Sons, Inc.
SUH, J. K. F. & MATTHEW, H. W. T. 2000. Application of chitosan-based polysaccharide biomaterials in cartilage tissue engineering: a review. *Biomaterials,* 21**,** 2589-2598.
TANG, A. J., HASHIMOTO, T., NISHIDA, T., NASU, H. & KAMIYA, K. 2004. Structure study of binary titanophosphate glasses prepared by sol-gel and melting methods. *Journal of the Ceramic Society of Japan,* 112**,** 496-501.
TIWARI, B., SUDARSAN, V., DIXIT, A. & KOTHIYAL, G. P. 2011. Effect of TiO2 Addition on the Optical, Thermo-Physical, and Structural Aspects of Sodium Alumino-Phosphate Glasses. *Journal of the American Ceramic Society,* 94**,** 1440-1446.
URCIUOLO, F., IMPARATO, G., GUACCIO, A., MELE, B. & NETTI, P. A. 2012. Novel Strategies to Engineering Biological Tissue In Vitro. *Nanotechnology in Regenerative Medicine: Methods and Protocols,* 811**,** 223-244.
VALAPPIL, S. P., PICKUP, D. M., CARROLL, D. L., HOPE, C. K., PRATTEN, J., NEWPORT, R. J., SMITH, M. E., WILSON, M. & KNOWLES, J. C. 2007.

Effect of silver content on the structure and antibacterial activity of silver-doped phosphate-based glasses. *Antimicrobial Agents and Chemotherapy,* 51**,** 4453-4461.
VALAPPIL, S. P., READY, D., ABOU NEEL, E. A., PICKUP, D. M., CHRZANOWSKI, W., O'DELL, L. A., NEWPORT, R. J., SMITH, M. E., WILSON, M. & KNOWLES, J. C. 2008. Antimicrobial gallium-doped phosphate-based glasses. *Advanced Functional Materials,* 18**,** 732-741.
VALAPPIL, S. P., READY, D., ABOU NEEL, E. A., PICKUP, D. M., O'DELL, L. A., CHRZANOWSKI, W., PRATTEN, J., NEWPORT, R. J., SMITH, M. E., WILSON, M. & KNOWLES, J. C. 2009. Controlled delivery of antimicrobial gallium ions from phosphate-based glasses. *Acta Biomaterialia,* 5**,** 1198-1210.
VITALE-BROVARONE, C., NOVAJRA, G., LOUSTEAU, J., MILANESE, D., RAIMONDO, S. & FORNARO, M. 2012. Phosphate glass fibres and their role in neuronal polarization and axonal growth direction. *Acta Biomaterialia,* 8**,** 1125-1136.
VITALE-BROVARONE, C., NOVAJRA, G., MILANESE, D., LOUSTEAU, J. & KNOWLES, J. C. 2011. Novel phosphate glasses with different amounts of TiO2 for biomedical applications Dissolution tests and proof of concept of fibre drawing. *Materials Science & Engineering C-Materials for Biological Applications,* 31**,** 434-442.
WALSH, P. M., O'CONNOR, J. & STRAIN, J. 2003. The role of trace elements in bone health. *Nutritional aspects of bone health***,** 351-361.
WALTER, G., VOGEL, J., HOPPE, U. & HARTMANN, P. 2001. The structure of CaO-Na2O-MgO-P2O5 invert glass. *Journal of Non-Crystalline Solids,* 296**,** 212-223.
WARD, J. M., WU, Y. Q., KHALFI, K. & CHORMAIC, S. N. 2010. Short vertical tube furnace for the fabrication of doped glass microsphere lasers. *Review of Scientific Instruments,* 81.
WHITE, J. E. & DAY, D. E. 1994. Rare-Earth Aluminosilicate Glasses for in-Vivo Radiation Delivery. *Rare Elements in Glasses,* 94-9**,** 181-208.
WIESER, M. E., HOLDEN, N., COPLEN, T. B., BOHLKE, J. K., BERGLUND, M., BRAND, W. A., DE BIEVRE, P., GRONING, M., LOSS, R. D., MEIJA, J., HIRATA, T., PROHASKA, T., SCHOENBERG, R., O'CONNOR, G., WALCZYK, T., YONEDA, S. & ZHU, X. K. 2013. Atomic weights of the elements 2011 (IUPAC Technical Report). *Pure and Applied Chemistry,* 85**,** 1047-1078.
WOO, S. L. Y., HILDEBRAND, K., WATANABE, N., FENWICK, J. A., PAPAGEORGIOU, C. D. & WANG, J. H. C. 1999. Tissue engineering of ligament and tendon healing. *Clinical Orthopaedics and Related Research***,** S312-S323.
WU, C., FAN, W., GELINSKY, M., XIAO, Y., SIMON, P., SCHULZE, R., DOERT, T., LUO, Y. & CUNIBERTI, G. 2011. Bioactive SrO-SiO(2) glass with well-ordered mesopores: Characterization, physiochemistry and biological properties. *Acta Biomaterialia,* 7**,** 1797-1806.
WU, C. T., XIAO, Y., ZHANG, Y. F., KE, X. B., XIE, Y. X., ZHU, H. Y. & CRAWFORD, R. 2010. Bioactive mesopore-glass microspheres with controllable protein-delivery properties by biomimetic surface modification. *Journal of Biomedical Materials Research Part A,* 95A**,** 476-485.
XUE, X. Y. & STEBBINS, J. F. 1993. Na-23 Nmr Chemical-Shifts and Local Na Coordination Environments in Silicate Crystals, Melts and Glasses. *Physics and Chemistry of Minerals,* 20**,** 297-307.
YANAGAWA, F., KAJI, H., JANG, Y. H., BAE, H., DU, Y. A., FUKUDA, J., QI, H. & KHADEMHOSSEINI, A. 2011. Directed assembly of cell-laden microgels for

building porous three-dimensional tissue constructs. *Journal of Biomedical Materials Research Part A,* 97A**,** 93-102.
YANG, F., MURUGAN, R., RAMAKRISHNA, S., WANG, X., MA, Y. X. & WANG, S. 2004. Fabrication of nano-structured porous PLLA scaffold intended for nerve tissue engineering. *Biomaterials,* 2**5,** 1891-1900.
YANG, J., YAMATO, M., KOHNO, C., NISHIMOTO, A., SEKINE, H., FUKAI, F. & OKANO, T. 2005. Cell sheet engineering: Recreating tissues without biodegradable scaffolds. *Biomaterials,* 26**,** 6415-6422.
YEATTS, A. B. & FISHER, J. P. 2011. Bone tissue engineering bioreactors: Dynamic culture and the influence of shear stress. *Bone,* 48**,** 171-181.
YU, J. Y., VODYANIK, M. A., SMUGA-OTTO, K., ANTOSIEWICZ-BOURGET, J., FRANE, J. L., TIAN, S., NIE, J., JONSDOTTIR, G. A., RUOTTI, V., STEWART, R., SLUKVIN, II & THOMSON, J. A. 2007. Induced pluripotent stem cell lines derived from human somatic cells. *Science,* 318**,** 1917-1920.
YU, X., BOTCHWEY, E. A., LEVINE, E. M., POLLACK, S. R. & LAURENCIN, C. T. 2004. Bioreactor-based bone tissue engineering: the influence of dynamic flow on osteoblast phenotypic expression and matrix mineralization. *Proc Natl Acad Sci U S A,* 101**,** 11203-8.
ZACHARIASEN, W. H. 1932. The atomic arrangement in glass. *Journal of the American Chemical Society,* 54**,** 3841-3851.

Appendices

A.1. Procedure for carrying out the time lapse and image analysis studies for microsphere diameter measurements

A.1.1. Materials

Microspheres made from a glass of known density

A.1.2. Equipment

- Analytical balance (resolution of 0.1 mg)
- Alcohol wipes (Azowipe bactericidal wipes may be used)
- Beaker
- Brush
- Camera (TCA-10.0-N, Tucsen Image Technology Inc., China) (**Note:** A wide range of cameras equipped with software for capturing time lapse images are available and can be used for this experiment.)
- Desktop PC loaded with µManager microscopy open source software (version 1.4; Ron Vale Lab, University of California–San Francisco, USA) and ImageJ (version 1.47; National Institutes of Health, USA)
- Micro spatula
- Microscope incubator system (Solent Scientific, UK) (**Note:** The incubator system is used so as to carry out the time-lapse experiment at 37°C. If such an incubator system is not available, the same experiment can be carried out at room temperature; our previous experience shows that the lower temperature will not drastically affect the experimental results.)
- Optical microscope (DMIRB microscope, Leica Microsystems, Germany) (**Note:** This microscope was procured together with the incubator system, but conventional optical microscopes having a camera port and appropriate adapters can be used.)
- Pipette with a capacity of 10 ml (Finpipette, Thermo Scientific, UK)
- Pipette tips (10 ml, Thermo Scientific, UK)
- Tissue culture flask, 25 cm^2 (TPP, Helena Biosciences, UK)
- Type 1 ultrapure water purification system capable of dispensing water with a resistivity of 18.2 $M\Omega.cm^{-1}$ (Purelab UHQ-PS, Elga Labwater, UK)
- Weighing boats

A.1.3. Procedure

1. Switch on the incubator system about 2 hours prior to setting up the experiment and set the temperature to 37°C. Just before the experiment, switch on the desktop PC and load the µManager software.
2. Weigh 100 mg of glass microspheres on an analytical balance and pour into a T-25 cell culture flask. Add 10 ml of ultrapure water to the flask using a pipette. (**Tip:** Prior to the addition of microspheres and water, the bottom inner surface of the flask can be scraped with a brush in order to provide surface roughness so that the microspheres remain reasonably stationary during the experiment. If this step is performed, the flask should then be washed 2-3 times with ultrapure water in order to wash away any debris resulting from the scraping action.)
3. Place the flask on the microscope stage and adjust the vertical stage position so that the microspheres are brought into focus on the software display screen (the Live View window, which can be opened by clicking on the Live option on the software interface). Adjust the horizontal stage position so that the display screen shows approximately 8-10 microspheres. (**Tip:** It is advisable to focus on microspheres that do not touch each other so that the image processing software will count the microspheres as individual objects and provide diameter values for each microsphere; this is because microspheres touching each other may be interpreted by the software as a single object.)
4. To begin the time lapse sequence, click on Multi-D Acq. On the following window, tick the boxes for Time Points and Save Images (Figure X.3.). Below Time Points, list the number of images to be taken and the interval between images. Below Save Images, write the file pathway to be used to store the files. For Saving Format, click the option for Separate image files. Click on Acquire.

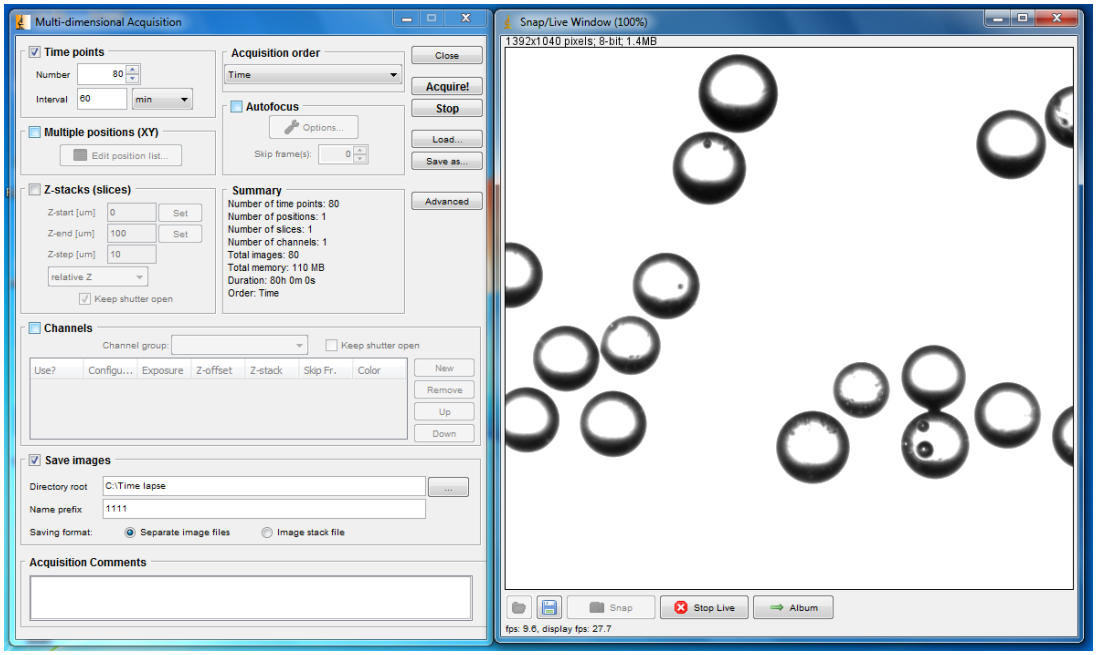

Figure A.1. Screenshots of Multi–dimensional Acquisition and Snap/Live windows in μManager software.

5. Carry out the following steps to obtain microsphere diameter values from the stored time lapse images using ImageJ version 1.47.
    a. **Open the time lapse images:** Go to File | Import | Image Sequence. Go to the folder containing the images. Click on the first image from your sequence and press Open. Press OK on the window that appears.
    b. **Binarise the images:** Go to Process | Binary | Make Binary and press OK on the window that appears.
    c. **Select a rectangular area around a microsphere:** Press on the rectangle icon and then draw a rectangle on the image wherever required by dragging the cursor (which looks like a '+' on the image) across the image with the left mouse button pressed. The position of the rectangle can be adjusted by keeping the cursor anywhere inside the rectangle (the '+' sign changes to a normal arrow) and dragging it over the image.
    d. **Exclude all objects other than the ones inside the rectangular area:** Go to File | Edit | Clear Outside, and press OK on the window that appears. Remove the rectangular area by clicking anywhere on the image. (**Tip:** Before excluding all other microspheres from each image, make sure that the bead of interest stays fully within the rectangle throughout all the images by moving the horizontal scroll bar from beginning to end. It is alright if parts of other microspheres are visible inside the rectangular area since the software will exclude them during the analysis.)

e. **Set the calibration scale:** Go to Analyse | Set Scale and input appropriate values for Distance in Pixels and Known Distance. Maintain Pixel Aspect Ratio = 1.0 and Unit of Length = micron. Make sure that the box next to Global is ticked. Press OK. (**Note:** If the calibration values are not known, use a micrometer calibration slide to measure a known distance in pixels. After proper focusing, draw a line on the screen between two divisions on the slide and measure the length in pixel units by going to Analyse | Measure. The output measurement is the Distance in Pixels and the distance between the divisions is the Known Distance in the Set Scale window.)

f. **Measure the diameters in the first and last images:** Measure the diameter of the microsphere in the first image of your sequence by pressing on the circle icon next to the rectangular icon, repeating step 3 to draw a circle roughly around the microsphere circumference, and going to Analyse | Measure. Make a mental note of the approximate area (say 22788.789). Repeat the same step for the last image to get the approximate area (say 20742.123). Approximations of both values are needed for the next step.

g. **Obtain the bead diameter:** Go to Analyze | Analyze Particles and use the following values: Size (micron^2) = 20000-25000, Circularity: 0.0-1.0, Show: Outlines (from drop-down menu). Tick the following boxes: Display Results, Summarize, Exclude on Edges, Include Holes, Record Starts. Press OK on the window that comes up. Three new windows will appear on the screen. Go to the Results window. Then go to Edit | Select All and Edit | Copy in order to paste the values in a suitable spread sheet software.

A.2. Box-and-whisker plots for bar charts provided in Chapter 4

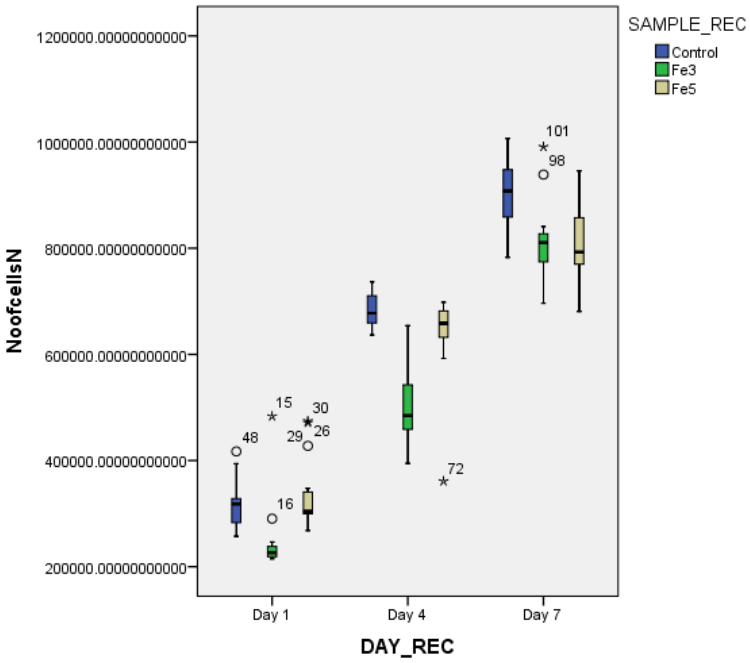

Figure A.2. Box-and-whisker plot representing MG63 cell proliferation on iron phosphate glass microspheres in ultra-low attachment cell culture plates at time points of 1, 4 and 7 days as determined using the CCK-8 assay (corresponding to bar charts in Figure 4.5). Note that circles indicate outliers (values more than the interquartile range) while asterisks indicate extreme outliers (values more than three times the interquartile range).

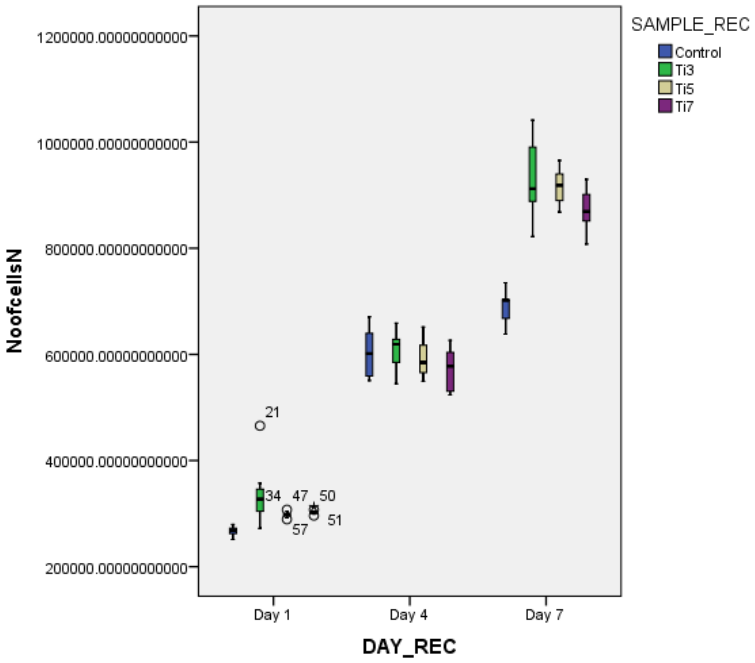

Figure A.3. Box-and-whisker plot representing MG63 cell proliferation on titanium phosphate glass microspheres in ultra-low attachment cell culture plates at time points of 1, 4 and 7 days as determined using the CCK-8 assay (corresponding to bar charts in Figure 4.6). Note that circles with numbers next to them indicate outliers.

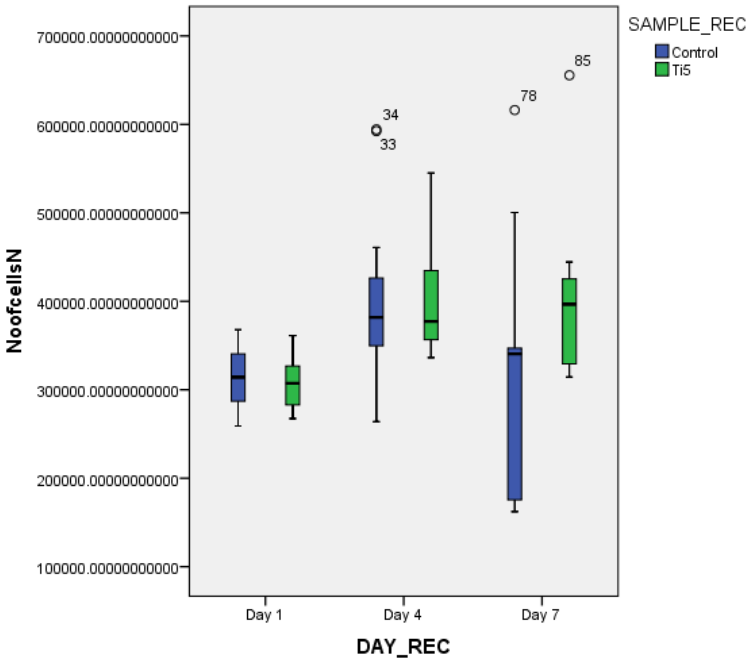

Figure A.4. Box-and-whisker plot showing the proliferation of MG63 cells on Ti5 and control glass microspheres at time points of 1, 4 and 7 days in ultra-low attachment cell culture plates under static conditions, as determined using the CCK-8 assay (corresponding to bar chart in Figure 4.9). Note that circles with numbers next to them indicate outliers.

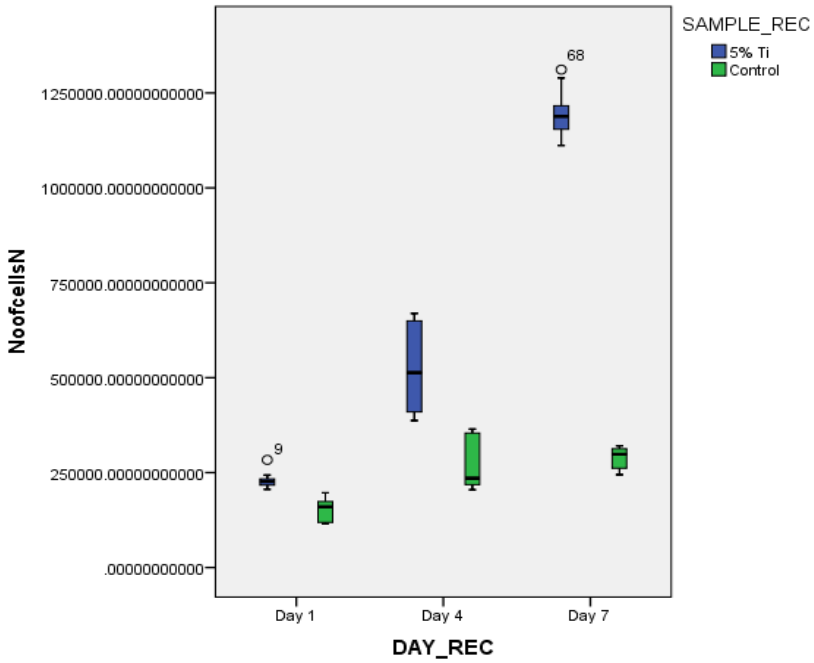

Figure A.5. Box-and-whisker plot showing the proliferation of MG63 cells on Ti5 and control glass microspheres at time points of 1, 4 and 7 days in spinner flask bioreactors under dynamic conditions, as determined using the CCK-8 assay (corresponding to bar chart in Figure 4.10). Note that circles with numbers next to them indicate outliers.

A.3. AlamarBlue® cell proliferation assay

A.3.1. Materials and methods

(Note: The procedure for seeding of MG63 cells on the microspheres in Transwell® inserts is given in section 4.2.2). The cell proliferation assay was conducted at time points of 1, 4 and 7 days. The control comprised the mesh of the cell culture insert with cells seeded on it. The MG63 cells were seeded on the glass discs and control mesh at a seeding density of 10,000 cells per well, followed by incubation at 37°C in an atmosphere of 5% CO_2. Cell proliferation at each time point was determined using the alamarBlue® assay (AbD Serotec, UK), for which 10% $v.v^{-1}$ of culture medium was removed from all the wells and replaced with 100 ml of alamarBlue® reagent, followed by incubation at 37°C for 4 hours in a humidified atmosphere containing 5% CO_2. Fluorescence detection was accomplished by means of a Fluoroskan fluorimeter (Thermo Scientific, UK) with absorption and emission values set to 560 nm and 590 nm, respectively. The fluorimeter provided absorbance data, so to plot the data in terms of the number of cells, a standard calibration curve was plotted separately. For the standard curve, cell populations in multiples of 10,000 (i.e. 0, 10000, 20000, 50000 and 100000 cells) were cultured over a 1-day period in a 24 well plate and fluorescence measurements were carried out using the same fluorimeter.

A.3.2. Results

Figure A.6(b) shows the results of the alamarBlue™ cell proliferation assay carried out over time points of 1, 4 and 7 days on the Ti3 and Ti5 glass microspheres (the standard curve is shown in Figure A.6(a)). The results revealed that for all the compositions studied and the control, cell growth increased over the culture period. At day 1, the cell numbers on the Ti3–7 microspheres were similar to those on the control. On day 4, the Ti3–7 microspheres showed comparable growth rates, while that of the control was noticeably higher. By day 7, a considerable increase in cell numbers in comparison with days 1 and 4 was observed for all the compositions as well as the control.

(a)

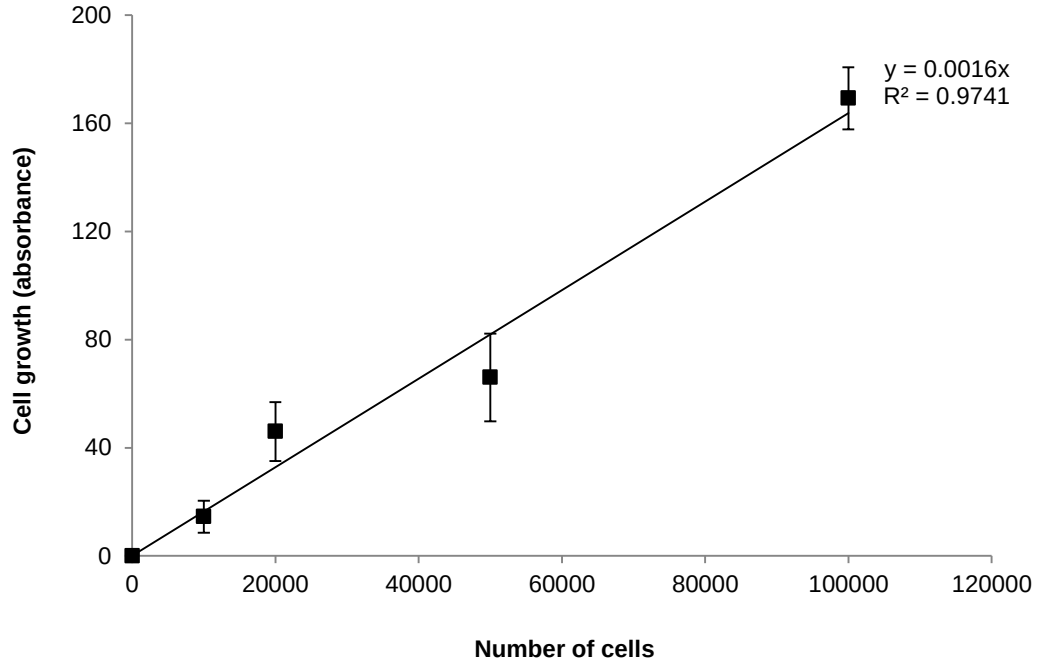

(b)

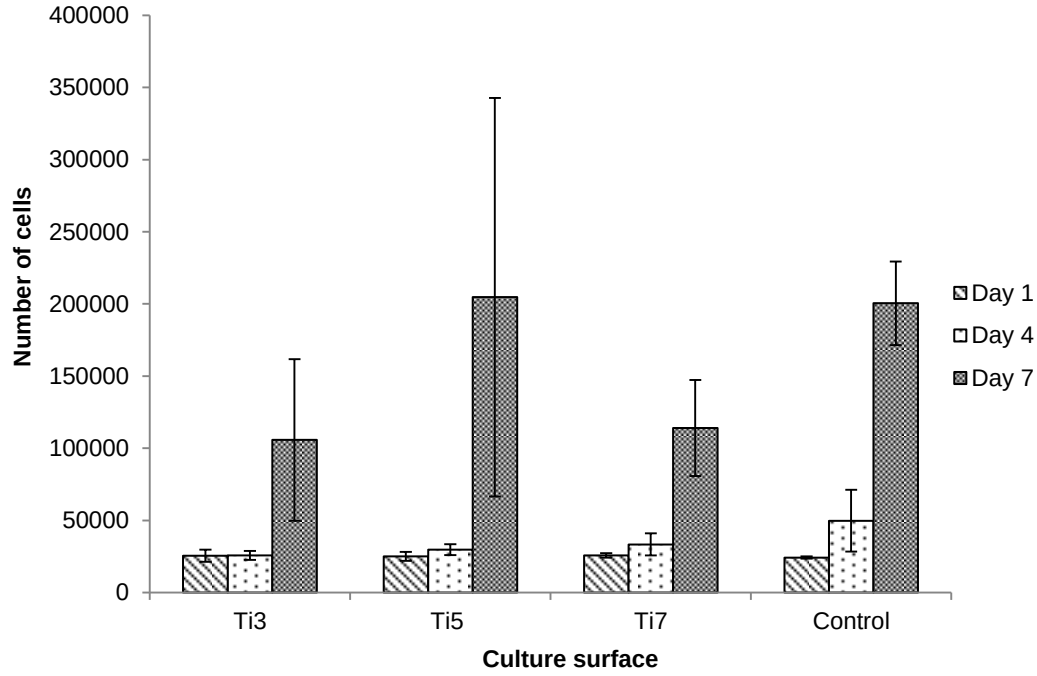

Figure A.6. (a) Standard curve of cell growth plotted as absorbance values versus number of cells. (b) Bar chart showing the proliferation of MG63 cells on titanium phosphate glass microspheres in Transwell® inserts at time points of 1, 4 and 7 days as determined using the alamarBlue® assay. The control comprises the mesh of the Transwell® insert. Error bars represent ±SD and n = 2. For all the compositions and the control, a significant increase in cell numbers is observed between day 1 and day 7.

A.4. Box-and-whisker plots for bar charts provided in Chapter 5

(a)

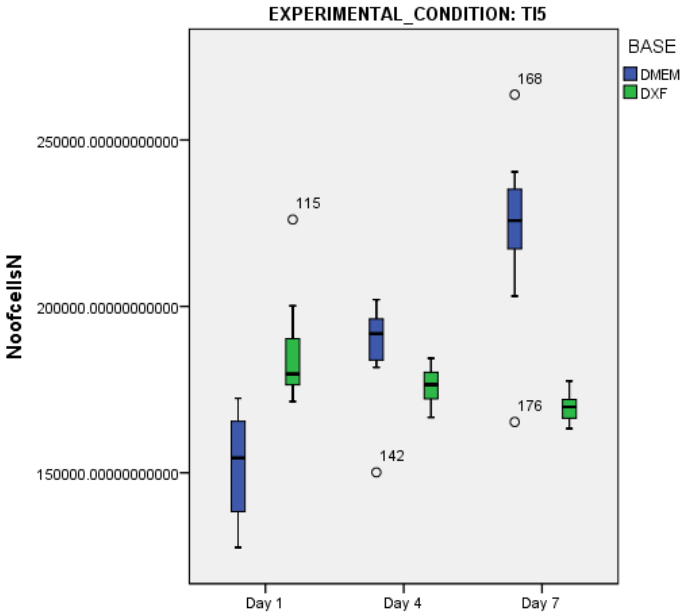

(b)

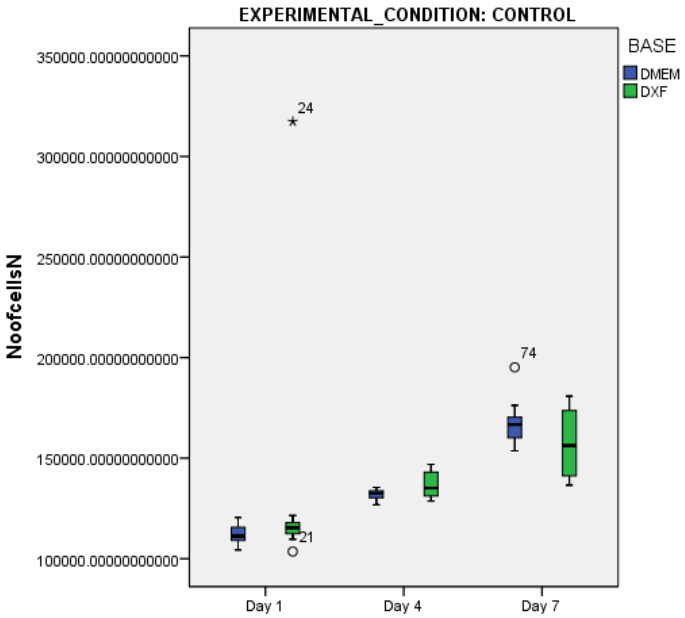

Figure A.7. Box-and-whisker plots representing the results of a CCK-8 assay to quantify hMSC proliferation on Ti5 and control microspheres in ultra-low attachment cell culture plates at time points of 1, 4 and 7 days when DMEM and a commercially available mesenchymal stem cell growth medium DXF (Promocell GmbH, Germany) are used as the culture medium. The control comprises silica glass microspheres (Polysciences Inc.). (a) and (b) correspond to bar charts in Figures 5.6(a) and 5.6(b) respectively. Note that circles indicate outliers (values more than the interquartile range) while asterisks indicate extreme outliers (values more than three times the interquartile range).

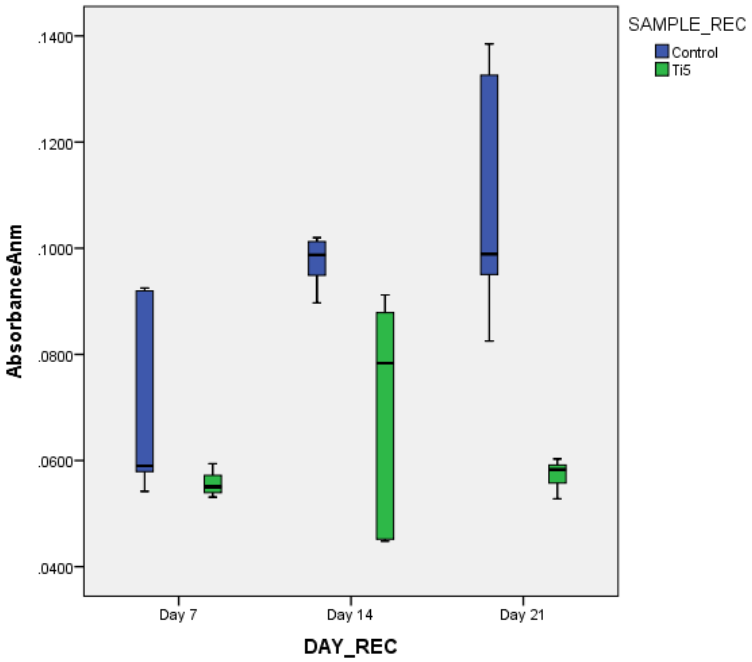

Figure A.8. Box-and-whisker plot representing the differentiation of hMSCs into bone cells on Ti5 and control glass microspheres at time points of 7, 14 and 21 days as quantified by the extent of mineralisation on the microsphere surface using an Alizarin Red S assay (corresponding to bar chart in Figure 5.7).

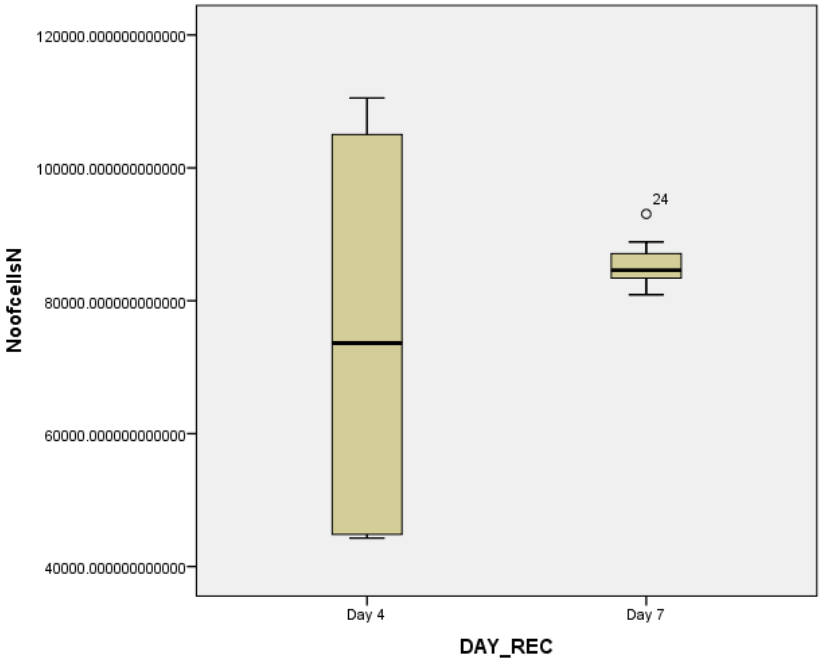

Figure A.9. Box-and-whisker plot showing the proliferation of hMSCs on Ti5 microspheres at time points of 4 and 7 days in spinner flask bioreactors under dynamic conditions, as determined using the CCK-8 cell proliferation assay (corresponding to bar chart in Figure 5.12). Note that circles with numbers next to them indicate outliers.

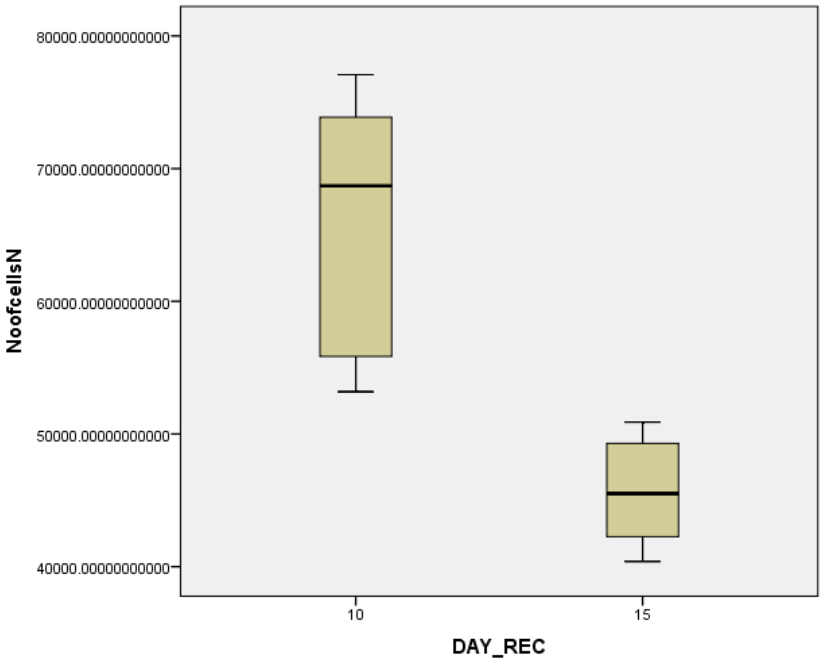

Figure A.10. Box-and-whisker plot showing the proliferation of hMSCs on Ti5 microspheres at time points of 10 and 15 days in spinner flask bioreactors under dynamic conditions when osteogenic inductive medium is used as the culturing medium, as determined using the CCK-8 cell proliferation assay (corresponding to bar chart in Figure 5.13).

A.5. List of publications

1. Lakhkar NJ, Abou Neel EA, Salih V, Knowles JC (2009). Strontium oxide doped quaternary glasses: Effects on structure, degradation and cytocompatibilty. *J. Mater. Sci. Mater. Med.* **20**, 1339–46.
2. Lakhkar NJ, Abou Neel EA, Salih V, Knowles JC (2011). Titanium and strontium-doped phosphate glasses as vehicles for strontium ion delivery to cells. *J. Biomater. Appl.* **25**, 877–93.
3. Lakhkar NJ, Salih V (2012). Heavy Metal: Perspectives on the controversy surrounding metal-on-metal hip implants. *Opticon1826* **12**, 7–8.
4. Lakhkar NJ, Park J-H, Mordan NJ, Salih V, Wall IB, Kim H-W, King SP, Hanna JV, Martin RA, Addison O, Mosselmans JFW, Knowles JC (2012). Titanium phosphate glass microspheres for bone tissue engineering. *Acta Biomater.* **8**, 4181–90.
5. Kiani A, Lakhkar NJ, Salih V, Smith ME, Hanna JV, Newport RJ, Pickup DM, Knowles JC (2012). Titanium-containing bioactive phosphate glasses. *Phil. Trans. R. Soc. A.* **370**, 1352–79.
6. Martin RA, Moss RM, Lakhkar NJ, Knowles JC, Cuello GJ, Smith ME, Hanna JV, Newport RJ (2012). Structural characterisation of titanium-doped Bioglass using isotopic substitution neutron diffraction. *Phys. Chem. Chem. Phys.* **14**, 15807–15.
7. Lakhkar NJ, Lee I-H, Kim H-W, Salih V, Wall IB, Knowles JC (2013). Bone formation controlled by biologically relevant inorganic ions: Role and controlled delivery from phosphate-based glasses. *Adv. Drug Del. Rev.* **65**, 405–20.
8. Guedes JC, Park J-H, Lakhkar NJ, Kim H-W, Knowles JC, Wall IB (2013). TiO_2-doped phosphate glass microcarriers: A stable bioactive substrate for expansion of adherent mammalian cells. *J. Biomater. Appl.* **28**, 3–11.
9. Lee I-H, Shin S-H, Foroutan F, Lakhkar NJ, Gong M-S, Knowles JC (2013). Effects of magnesium content on the physical properties in a MgO–CaO–Na_2O–P_2O_5 glass system. *J. Non-Cryst. Solids* **363**, 57–63.
10. Lee I-H, Foroutan F, Lakhkar NJ, Gong M-S, Knowles JC (2013). Sol-gel synthesis and structural characterisation of P_2O_5–CaO–Na_2O glasses. *Phys. Chem. Glasses* **54**, 115–20.
11. Lee I-H, Yu H-S, Lakhkar NJ, Kim H-W, Gong M-S, Knowles JC, Wall IB (2013). Development of a vascularization-promoting slow release glass: Effect of cobalt on bulk, surface and biocompatibility properties of titanium phosphate based glasses. *Mater. Sci. Eng. C* **33**, 2104–12.
12. Lakhkar NJ, Knowles JC (2013) Structural investigations of titanium metaphosphate glasses by ambient and high-temperature X-ray diffraction techniques. *Macromol. Sym.* **334**, 10–6.
13. Lakhkar NJ, Peticone C, De Silva-Thompson D, Wall IB, Salih V, Knowles JC (2014) Titanium phosphate glass microspheres as microcarriers for *in vitro* bone cell tissue engineering. In *Biointerfaces: Where Material Meets Biology.* Eds. Hutmacher DW, Chrzanowski W. RSC Publishing (in press)

A.6. List of conferences

1. Lakhkar NJ, Salih V, Knowles JC. Titanium phosphate glass microspheres as microcarriers for bone cell scale-up and differentiation. World Biomaterials Congress, Chengdu, China, 01–05 June 2012 (poster and oral presentations).
2. Lakhkar NJ, Park J-H, Salih V, Knowles JC. Titanium phosphate glass microspheres: novel microcarriers for bioreactor-mediated bone cell scale-up and differentiation. Tissue and Cell Engineering Society Meeting, Liverpool, UK, 04–06 July 2012 (poster presentation).
3. Lakhkar NJ, Salih V, Knowles JC. Titanium phosphate glass microspheres as microcarriers for bioreactor-mediated 3D culture of bone cells. BIND-12, Bangalore, India, 09–11 December 2012 (oral presentation).
4. Lakhkar NJ, Kiani A, King SP, Hanna JV, Martin RA, Knowles JC. Structural investigations of titanium phosphate glasses by XRD, solid-state ^{31}P NMR and Ti *k*-edge XANES. 533th WE-Heraeus-Seminar on Advanced Functional Polymers for Medicine, Bad Honnef, Germany, 27–29 May 2013 (poster presentation).